frontiers | Research Topics

Climatic and associated cryospheric and hydrospheric changes on the third pole,
volume II

Edited by
Lei Wang, Xiuping Li, Chunqiao Song, Tobias Conradt
and Mohamed Rasmy

Published in
Frontiers in Earth Science
Frontiers in Environmental Science

ISSN 1664-8714
ISBN 978-2-8325-3307-9
DOI 10.3389/978-2-8325-3307-9

About Frontiers

Frontiers is more than just an open access publisher of scholarly articles: it is a pioneering approach to the world of academia, radically improving the way scholarly research is managed. The grand vision of Frontiers is a world where all people have an equal opportunity to seek, share and generate knowledge. Frontiers provides immediate and permanent online open access to all its publications, but this alone is not enough to realize our grand goals.

Frontiers journal series

The Frontiers journal series is a multi-tier and interdisciplinary set of open-access, online journals, promising a paradigm shift from the current review, selection and dissemination processes in academic publishing. All Frontiers journals are driven by researchers for researchers; therefore, they constitute a service to the scholarly community. At the same time, the *Frontiers journal series* operates on a revolutionary invention, the tiered publishing system, initially addressing specific communities of scholars, and gradually climbing up to broader public understanding, thus serving the interests of the lay society, too.

Dedication to quality

Each Frontiers article is a landmark of the highest quality, thanks to genuinely collaborative interactions between authors and review editors, who include some of the world's best academicians. Research must be certified by peers before entering a stream of knowledge that may eventually reach the public - and shape society; therefore, Frontiers only applies the most rigorous and unbiased reviews. Frontiers revolutionizes research publishing by freely delivering the most outstanding research, evaluated with no bias from both the academic and social point of view. By applying the most advanced information technologies, Frontiers is catapulting scholarly publishing into a new generation.

What are Frontiers Research Topics?

Frontiers Research Topics are very popular trademarks of the *Frontiers journals series*: they are collections of at least ten articles, all centered on a particular subject. With their unique mix of varied contributions from Original Research to Review Articles, Frontiers Research Topics unify the most influential researchers, the latest key findings and historical advances in a hot research area.

Find out more on how to host your own Frontiers Research Topic or contribute to one as an author by contacting the Frontiers editorial office: frontiersin.org/about/contact

Climatic and associated cryospheric and hydrospheric changes on the third pole, volume II

Topic editors
Lei Wang — Institute of Tibetan Plateau Research, Chinese Academy of Sciences (CAS), China
Xiuping Li — Institute of Tibetan Plateau Research, Chinese Academy of Sciences (CAS), China
Chunqiao Song — Nanjing Institute of Geography and Limnology, Chinese Academy of Sciences (CAS), China
Tobias Conradt — Potsdam Institute for Climate Impact Research (PIK), Germany
Mohamed Rasmy — National Graduate Institute for Policy Studies, Japan

Citation
Wang, L., Li, X., Song, C., Conradt, T., Rasmy, M., eds. (2023). *Climatic and associated cryospheric and hydrospheric changes on the third pole, volume II*. Lausanne: Frontiers Media SA. doi: 10.3389/978-2-8325-3307-9

Table of contents

frontiers | Frontiers in Earth Science

TYPE Editorial
PUBLISHED 08 August 2023
DOI 10.3389/feart.2023.1255039

OPEN ACCESS

EDITED AND REVIEWED BY
Wouter Buytaert,
Imperial College London,
United Kingdom

*CORRESPONDENCE
Lei Wang,
✉ wanglei@itpcas.ac.cn

RECEIVED 08 July 2023
ACCEPTED 31 July 2023
PUBLISHED 08 August 2023

CITATION
Wang L, Song C, Li X, Conradt T and Rasmy M (2023), Editorial: Climatic and associated cryospheric and hydrospheric changes on the Third Pole - Volume II. *Front. Earth Sci.* 11:1255039.
doi: 10.3389/feart.2023.1255039

Editorial: Climatic and associated cryospheric and hydrospheric changes on the Third Pole - Volume II

Lei Wang[1,2]*, Chunqiao Song[3], Xiuping Li[1], Tobias Conradt[4] and Mohamed Rasmy[5]

[1]State Key Laboratory of Tibetan Plateau Earth System, Environment and Resources (TPESER), Institute of Tibetan Plateau Research, Chinese Academy of Sciences, Beijing, China, [2]College of Earth and Planetary Sciences, University of Chinese Academy of Sciences, Beijing, China, [3]Key Laboratory of Watershed Geographic Sciences, Nanjing Institute of Geography and Limnology (CAS), Nanjing, China, [4]Potsdam Institute for Climate Impact Research (PIK), Potsdam, Germany, [5]International Centre for Water Hazard and Risk Management (ICHARM), National Graduate Institute for Policy Studies, Tokyo, Japan

KEYWORDS

glacier, snow, permafrost, atmospheric ice, terrestrial water storage, lake, overflow risk, evapotranspiration

Editorial on the Research Topic
Climatic and associated cryospheric and hydrospheric changes on the Third Pole - Volume II

The Third Pole (TP) region refers to the high lands in Asia, including the Tibetan Plateau, Himalayas and their surrounding mountains, as well as the Pamir Plateau, the Tianshan Mountains and the Altai Mountains (Yao et al., 2022). It is home to more than 100,000 km^2 of glaciers, containing the largest volume of ice outside the Arctic and Antarctic (Yao et al., 2012).

The warming rate of the TP is twice the global average in the past half century (Chen et al., 2015; Pepin et al., 2015). Climate warming has altered the water vapor supply and regional climate characteristics of the TP (Yang et al., 2014). The changes in cryosphere such as glacier retreat, permafrost degradation, and snow-to-rain in precipitation (Kang et al., 2010) have also greatly changed the hydrological cycle (Yang et al., 2011) and land surface conditions (such as vegetation, soil, lake, and geomorphology), leading to prominent differences among major TP river basins in various components of changes, including actual evapotranspiration, terrestrial water storage, and river runoff (Bibi et al., 2018; Yao et al., 2019). Due to the complex land surface environment and the influence of atmospheric circulation in the TP, river runoff components (rainfall-runoff, ice and snow melting, soil freezing/thawing) could be also largely different. These changes have a profound impact on the regional water cycle, changing the spatiotemporal patterns of available freshwater supply (Immerzeel et al., 2010; Lutz et al., 2014). However, up to now, the quantification of the atmosphere, cryosphere, biosphere and hydrosphere over the TP still has large uncertainties, due to a lack of necessary ground-based observations (across a range of different hydrometeorology and cryosphere variables) and advanced satellite technology (e.g., new sensors for permafrost ice monitoring, and atmospheric ice monitoring).

This Research Topic aims to cover recent climate changes over the TP (or comparable cold regions) and its associated impacts on the cryosphere and hydrosphere. Different from "Climatic and Associated Cryospheric and Hydrospheric Changes on the Third Pole-Volume I," this Research Topic ("*Climatic and Associated Cryospheric and Hydrospheric Changes on the Third Pole-Volume II*") tends to quantify the atmosphere, cryosphere, biosphere and hydrosphere of the TP in different aspects with acceptable accuracies, based on *in situ* observations, satellite remote sensing, and numerical modeling. These studies address changes in atmospheric ice, seasonal snow cover, mountain glaciers, permafrost, lakes, vegetation, evapotranspiration, terrestrial water storage as well as water-related disasters, and examine how these changes are linked to climate change across different spatial scales (from a catchment to the whole TP). Results from these studies will improve our understanding of cryosphere–hydrosphere–atmosphere interactions over the TP.

This Research Topic includes nine original research articles and one brief research report. This is a multidisciplinary Research Topic bridging the gaps in cryosphere, climatology, hydrology, geomorphology, biogeochemistry, and remote sensing sciences.

Liu et al. present a low-cost approach by integrating remote sensing data and limited underwater surveys for lake volume estimation on the TP, by coupling the lake hypsometric curve and bottom elevation. Their studies on nine TP lakes with different sizes and geometric characteristics show an overall bias in volume estimate of about 15%. The method proposed by their paper is expected to provide a simplified but efficient solution for estimating the lake water volume on the TP and other ungauged areas.

Liu et al. examine the hydrological budgets and their driving forces of closed Chinese inland basins. In their study, trends and magnitudes of precipitation, terrestrial water storage, and actual evapotranspiration were detected by the rank-based non-parametric Mann–Kendall test method. Their results showed that both precipitation and actual evapotranspiration significantly increased in the Chinese inland basins. Moreover, the annual terrestrial water storage in the Chinese inland basins significantly decreased mainly due to the increased actual evapotranspiration, in which approximately 60% was attributed to increased irrigation diversions.

Yang et al. evaluate the total mass, spatial distributions, and long-term trends of atmospheric ice over the TP. Based on the estimations using multiple satellite datasets (Aqua, Terra, the Suomi National Polar-orbiting Partnership, and NOAA-20), they concluded that the total mass of atmospheric ice could be up to 0.26 ± 0.03 Gt over the TP from 2013 to 2020. In general, the southwest and northeast TP were the low-concentration areas (0. 05 kg/m^2 on average), while the southeast TP was the high-concentration area (0.09 kg/m^2 on average). The plentiful water vapor transported by the Southwest Summer Monsoon and steep topography could be the major contributors to the rapid growth and the higher ice concentration of atmospheric ice in southeast TP.

Half of the annual water discharge in the upper Indus Basin is contributed from the glacier and snow-fed basins in the Hindu Kush, Karakoram, and Himalayan regions, which are sensitive to climate change. Moazzam et al. indicates that the snow cover area in Astore (Western Himalayas) and Shigar (Karakoram region) has an increasing trend with a rate of 11.16 km^2/year and 4.27 km^2/year, respectively. The increasing annual precipitation and decreasing annual mean temperature also support the phenomenon of expanding snow cover area in these areas. Their further analyses on snow cover changes with elevation reveal that snow cover area was decreasing on foothills while increasing at the valley top.

Liu et al. explore the spatial-temporal changes in the lake area on the northeastern TP from 1988 to 2019 and their driving factors based on Landsat images, meteorological data, and glacier and permafrost data. It suggests that the lake areas increased at rates of 0.01–16.03 km^2/year from 1988 to 2019. In more detail, the change was featured by a decrease during 1988–2000, a moderate increase during 2000–2012, and an accelerated increase during 2012–2019. The precipitation (other than glacial meltwater) was the primary driving factor for this dramatic change in the lake area of this region, while the permafrost degradation further intensified the lake expansion.

Park et al. implement a water age calculation scheme into a coupled hydrological and biogeochemical model to assess the mechanisms through which climate warming affects the soil water storage–evapotranspiration–water age feedback cycle in a boreal forest. Their results suggest that permafrost warming (characterized by earlier soil thawing and later freezing) induced higher evapotranspiration, thereby shortening the residence time of precipitation-sourced water in the active layer and further rejuvenating water in soil layers and in evapotranspiration. Under future climate warming conditions, this effect is expected to intensify and the water cycle will be accelerated.

Deng et al. explore the relationship between changes in terrestrial water storage and vegetation on the TP to understand further the role of vegetation in the changes of water systems in alpine mountains. They combine terrestrial water storage anomalies data and vegetation indices to determine how they interact. Their results indicate a significant warming rate of 0.44°C/decade over the TP from 1980 to 2020, while evapotranspiration and precipitation trended upward significantly (12.9 and 15 mm/decade, respectively). Under the current climate change state (the increased rate of precipitation is faster than actual evapotranspiration), vegetation change has an insignificant impact on the changes in terrestrial water storage; in contrast, changes in terrestrial water storage (surplus/deficit) significantly affect vegetation changes (greening/browning) in parts of the TP.

Mountains glacier, as one of the most important components of terrestrial water storage, effectively regulates and stabilizes surface water resources. However, how much the mountain glacier mass balance contributes to terrestrial water storage changes around mountain regions is unknown. Li et al. combine multi-source datasets to quantify the contribution rate over high-elevation mountain regions. They find that the glacial melting mass loss is equivalent to about 49% of the total terrestrial water storage decline during 2006–2015 at a global scale. There are larger contributions in the regions with more glaciers. Glacier mass together with other storage components play diverse roles in changing terrestrial water storages across different mountain regions and watersheds, but factors with great influence are glaciers, groundwater, soil water, reservoirs, and lakes.

Gao et al. develop a multi-source data fusion snow cover dataset for the TP, and conduct snow zonation and comparative snow variability analysis. They find that from 2000 to 2021, 23.0% of TP has experienced a significant decrease in snow cover days (mainly in the southeast) and 4.9% has experienced a significant increase (mainly in the northwest). The contrasting change in the snowpack on the TP, with a large decrease at lower elevations and an increase at higher elevations, will bring new challenges to water resources management in the region.

Finally, a study of the water-related extreme disaster on the TP is reported by Wang et al. Global warming is inducing dramatic changes in fluvial geomorphology and reshaping the hydrological connections between rivers and lakes. The water level and area of the Salt Lake have increased rapidly since the Zonag Lake outburst in the Hoh Xil region of the TP in 2011, threatening the downstream infrastructure. Wang et al. extract the long time series of the Salt Lake areas and analyze its spatiotemporal variation from 1973 to 2021, and finally assess the overflow risk of Salt Lake that is a downstream closed lake. They found that, the area change of the Salt Lake was consistent with the variation in precipitation before the outburst event. After that, it showed a remarkable area expansion (circa 350%), especially in the southeast direction. Without the construction of the emergency drainage channel, their simulation results indicated that the earliest and latest times of the Salt Lake overflow event are predicted to occur in 2020 and 2031, respectively.

Author contributions

LW: Conceptualization, Funding acquisition, Investigation, Writing–original draft, Writing–review and editing. CS: Funding acquisition, Writing–review and editing. XL: Conceptualization, Writing–review and editing. TC: Writing–review and editing. MR: Writing–review and editing.

Funding

This study was supported by the National Natural Science Foundation of China (Grant Nos. 41988101 and 41971403), the Second Tibetan Plateau Scientific Expedition and Research Program (2019QZKK020604).

Acknowledgments

We warmly appreciate the Editorial Board and Editorial Office of Frontiers in Earth Science for the kind invitation to edit this Research Topic and their timely support during organizing and managing the Research Topic.

Conflict of interest

Publisher's note

References

Bibi, S., Wang, L., Li, X., Chen, D., and Yao, T. (2018). Climatic and associated cryospheric, biospheric, and hydrological changes on the Tibetan plateau: a review. *Int. J. Climatol.* 38 (1), e1–e17. doi:10.1002/joc.5411

Chen, D. L., Xu, B. Q., Yao, T. D., Guo, Z., Cui, P., Chen, F., et al. (2015). Assessment of past, present and future environmental changes on the Tibetan Plateau. *Chin. Sci. Bull.* 60, 3025–3035. doi:10.1360/N972014-01370

Immerzeel, W. W., Beek, L., and Bierkens, M. F. P. (2010). Climate change will affect the asian water towers. *Science* 328, 1382–1385. doi:10.1126/science.1183188

Kang, S., Xu, Y., You, Q., Flügel, W. A., Pepin, N., and Yao, T. (2010). Review of climate and cryospheric change in the Tibetan Plateau. *Environ. Res. Lett.* 5, 015101. doi:10.1088/1748-9326/5/1/015101

Lutz, A. F., Immerzeel, W. W., Shrestha, A. B., and Bierkens, M. F. P. (2014). Consistent increase in High Asia's runoff due to increasing glacier melt and precipitation. *Nat. Clim. Change* 4 (7), 587–592. doi:10.1038/nclimate2237

Pepin, N., BradleyDiaz, R. S. H. F., Baraer, M., Caceres, E. B., Forsythe, N., FowlerH., et al. (2015). Elevation-dependent warming in mountain regions of the world. *Nat. Clim. Change* 5, 424–430. doi:10.1038/nclimate2563

Yang, K., Wu, H., Qin, J., Lin, C., Tang, W., and Chen, Y. (2014). Recent climate changes over the Tibetan plateau and their impacts on energy and water cycle: a review. *Glob. Planet. Change* 112, 79–91. doi:10.1016/j.gloplacha.2013.12.001

Yang, K., Ye, B., Zhou, D., Wu, B., Foken, T., Qin, J., et al. (2011). Response of hydrological cycle to recent climate changes in the Tibetan Plateau. *Clim. Change* 109, 517–534. doi:10.1007/s10584-011-0099-4

Yao, T., Bolch, T., Chen, D., Gao, J., Immerzeel, W., Piao, S., et al. (2022). The imbalance of the Asian water tower. *Nat. Rev. Earth Environ.* 3, 618–632. doi:10.1038/s43017-022-00299-4

Yao, T., Thompson, L., Yang, W., Yu, W., Gao, Y., Guo, X., et al. (2012). Different glacier status with atmospheric circulations in Tibetan Plateau and surroundings. *Nat. Clim. Change* 2, 663–667. doi:10.1038/nclimate1580

Yao, T., Xue, Y., Chen, D., Chen, F., Thompson, L., Cui, P., et al. (2019). Recent Third Pole's rapid warming accompanies cryospheric melt and water cycle intensification and interactions between Monsoon and environment: multidisciplinary approach with observations, modeling, and analysis. *Bull. Amer. Meteor. Soc.* 100, 423–444. doi:10.1175/bams-d-17-0057.1

frontiers | Frontiers in Earth Science

ORIGINAL RESEARCH
published: 13 July 2022
doi: 10.3389/feart.2022.925944

A Low-Cost Approach for Lake Volume Estimation on the Tibetan Plateau: Coupling the Lake Hypsometric Curve and Bottom Elevation

Kai Liu, Chunqiao Song*, Pengfei Zhan, Shuangxiao Luo and Chenyu Fan

Key Laboratory of Watershed Geographic Sciences, Nanjing Institute of Geography and Limnology, Chinese Academy of Sciences, Nanjing, China

The widespread lakes on the Tibetan Plateau (TP) are key components of the water cycle, thus the knowledge of their spatial distribution and volume is crucial for understanding the hydrological processes under ongoing climate change. Many previous studies focus on investigating surface elevation, inundation area variations and water volume changes for these lakes. However, how much water is stored in lakes across the TP remains relatively unexplored. It is because of the incapacity of satellite remote sensing methods in lake depth measurements and the high cost of field bathymetric measurement. This study developed a low-cost approach by integrating remote sensing data and limited underwater surveys. The observed lake areas and surface elevations generated the elevation-area relationship. Underwater surveys were conducted to detect the potentially “maximum” lake depths using three optimized survey routes. With the constraint of lake-bottom elevation, the lake-bottom zone area could be estimated for calculating the lake volume. Experiments on nine TP lakes with different size and geometric characteristics demonstrate that the optimized survey line along the lake short axis is well balanced in efficiency and accuracy, with an overall volume bias of 15% approximately. The proposed hypsometric curve method coupled with the bottom elevation measurement is expected to provide a simplified but efficient solution for estimating the lake water volume on the TP, which could be applicable to ungauged lakes in other harsh environments.

Keywords: lake volume, Tibetan plateau (TP), hypsometric curve, water-depth survey, remote sensing

Edited by:
Frédéric Frappart,
INRAE Nouvelle-Aquitaine Bordeaux, France

Reviewed by:
Baojin Qiao,
Zhengzhou University, China
Yao Li,
Texas A&M University, United States

****Correspondence:***
Chunqiao Song
cqsong@niglas.ac.cn

Specialty section:
This article was submitted to Hydrosphere, a section of the journal Frontiers in Earth Science

Received: *22 April 2022*
Accepted: *15 June 2022*
Published: *13 July 2022*

Citation:
Liu K, Song C, Zhan P, Luo S and Fan C (2022) A Low-Cost Approach for Lake Volume Estimation on the Tibetan Plateau: Coupling the Lake Hypsometric Curve and Bottom Elevation.
Front. Earth Sci. 10:925944.
doi: 10.3389/feart.2022.925944

1 INTRODUCTION

Lakes play a critical part in the water cycle and provide wide-ranging ecosystem services (Pekel et al., 2016; Busker et al., 2019; Woolway et al., 2020; Liu et al., 2021b). Remote sensing observations indicated more than 100 million lakes worldwide with uneven distribution (Verpoorter et al., 2014). As one of the most concentrated areas of lake distribution, the Tibetan Plateau (TP) hosts more than 1330 lakes (>1 km^2) in 2020, with a total area of ~5×10^4 km^2 (Zhang et al., 2021a). Lakes on the TP are highly sensitive to climate change because of minimal disturbances from human activities. Many previous studies have examined the lake dynamics by using various remote sensing techniques (Lei et al., 2013; Yang et al., 2018; Yao et al., 2018; Li et al., 2019a; Qiao et al., 2019b; Liu et al., 2021a;

Cheng et al., 2022). However, the satellite remote sensing-based studies focus on investigating variations of surface elevation, inundation area and water storage for these lakes. Lack of the underwater depths for most of the Tibetan lakes is a major obstacle for calculating absolute lake volume of this region. Thus, to answer how much water is stored in the high-altitude deep lakes of the TP is still a very challenging task due to the harsh environment and high cost of field investigation (Zhang et al., 2020).

Field measurement using the onboard sonar is the most reasonable method for generating the bathymetric map (Bandini et al., 2018; Qiao et al., 2019a; Coggins and Ghadouani, 2019). However, the labor cost and low efficiency limited the large-scale underwater lake surveys over the TP. To overcome the disadvantage of the traditional survey, some researchers attempted to derive the bathymetric map using remote sensing technologies (Getirana et al., 2018; Li et al., 2019b, 2020). Both the optical images and satellite altimetry were used to derive the underwater topography of inland or coastal waterbodies (Armon et al., 2020; Xu et al., 2022), yet being restricted in deep or turbid water conditions (Saylam et al., 2017; Bandini et al., 2018). Some spatial prediction and modeling methods were gradually proposed to overcome such difficulties mentioned above by predicting underwater bathymetry using exposed lake-surrounding terrains (Hollister et al., 2011; Heathcote et al., 2015; Cael et al., 2017; Getirana et al., 2018). For example, Messager et al. (2016) developed a geo-statistical model based on available bathymetric data of 12,150 natural lakes to estimate the lake volume globally. This approach is believed to derive reasonable results on a global scale. However, the uncertainty for lake individuals varies considerably.

Given the high cost of field measurement in full coverage and the low accuracy of the spatial prediction method for local scale, this study aims to propose an efficient method for water volume estimation for lakes on the TP. Inspired by the application of the lake hypsometric curve method in monitoring lake volume change trajectory (Yigzaw et al., 2018; Fassoni-Andrade et al., 2020; Li et al., 2021), we tried to estimate the lake volume by extrapolating the hypsometric curve fitting to the near-bottom constrained by the minimized water depth surveys. The most commonly used hypsometric curve method is to combine the water area estimations from satellite imagery (e.g., Landsat and MODIS) with elevations from altimetry datasets (e.g., Hydroweb, G-REALM, and DAHITI) (Crétaux et al., 2011; Busker et al., 2019). Recently, Li et al. (2019a) developed a novel approach to establishing the lake elevation-area (E-A) relationship by projecting the lidar-based elevation profile (i.e., ICESat-2) onto the surface water occurrence generated from long-term water classifications, and this method has been applied to the global scale (Li et al., 2020). In this study, the hypsometric curve of the lake E-A relationship was derived from the satellite observation of the historically inundated areas and corresponding water levels. Subsequently, an optimized survey line over the lake was designed for determining the bottom depths (elevations) with limited underwater surveys. The lake-bottom elevation was further used for constraining the hypsometric curve to predict the near-bottom area. Finally, after obtaining the water depth and area of the bottom zone, the lake elevation-volume (E-V) curve can be generated along with the estimated lake water volume.

2 STUDY AREA AND DATASET

The Tibetan Plateau is the highest and most extensive highland worldwide, with an average elevation exceeding 4000 m above sea leave (Chen et al., 2020). The TP is widely acknowledged as the Asian Water Tower because more than ten large rivers originate from the TP and adjacent mountain ranges (Immerzeel and Bierkens, 2012), where are distributed with about 50,000 km^2 of lakes. The TP lakes are mainly concentrated in the endorheic basin and are sensitive to climate change. Many previous studies have investigated the long-term trend and spatial pattern of lake dynamics over the TP (Song et al., 2013; Li et al., 2019a). This study targets to demonstrate the approach of estimating absolute lake volume. Three items of criteria were considered in selecting the case lakes. First, the bathymetric data is available for evaluating the accuracy of lake water volume estimates. Currently, only nearly 30 lakes on the TP have open-access bathymetry. Second, the long-term satellite altimetry data can be accessed for deriving the lake level series. Last, the selected lakes should be roughly representative in the area, morphology, location, and surrounding topography. We eventually chose nine lakes based on the above-mentioned criteria, including Aksai Chin Lake, Bangda Co, Eling Lake, Manasarovar Lake, Kusai Lake, Pung Co, Tangra Yumco, Taro Co, and Zharinam Co. (**Figure 1**). The basic information about the case lakes is listed in **Table 1**.

We collected the bathymetric maps of the nine case lakes from the published literature, which were generated based on full-coverage measurements using the boat-mounted depth meter. The high-quality lake bathymetry data can provide the reference data for the performance assessment of volume estimation. The hypsometric curve construction requires the paired time series of lake areas and water levels in the (near-) synchronous measurement periods. Landsat-7 ETM+ and Landsat-8 OLI images were employed for lake extent mapping. Lake level series were derived from the satellite altimetry data, including ICESat/ICESat-2 and Hydroweb dataset. In addition, the digital elevation model (DEM), which depicts the lake surrounding terrains, was also used. Among all the available DEMs over the TP, MERIT, the improved version of the SRTM DEM was selected due to its high accuracy and early acquisition time (February 2000) (Yamazaki et al., 2017; Liu et al., 2019).

3 METHODS

This study proposes a low-cost and simplified method for lake volume estimation. As shown in **Figure 2**, the method includes four main steps. First, the hypsometric curve of the "Elevation-Area (E-A)" relationship was constructed based on the (near-) synchronous lake area and water level series. Next, the underwater survey was conducted along with the optimized survey line for determining the lake bottom elevation. Then,

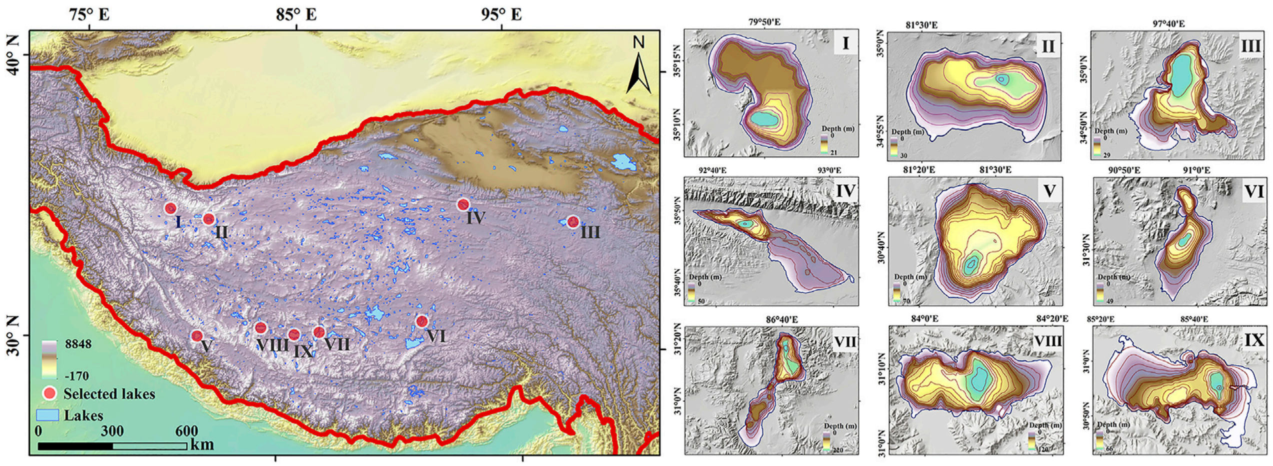

FIGURE 1 | Distribution of nine selected lakes and their bathymetric data. The lakes are in order as follows: Aksai Chin Lake, Bangda Co, Eling Lake, Kusai Lake, Manasarovar Lake, Pung Co, Tangra Yumco, Taro Co, and Zharinam Co.

TABLE 1 | Basic information of the selected lakes.

Lake name	Latitude/ longitude	Area* (km^2)	Lake level (m)	Circularity	Mean slope (1000m)	Mean depth (m)	Maximum depth (m)	*In-situ* data
Aksai Chin Lake	35.21°N/ 79.83°E	170.75 287.32	4846.43	0.18	2.63	9.18	20.78	Qiao et al. (2017)
Bangda Co	34.95°N/ 81.56°E	109.25 159.63	4904.74	0.44	2.26	11.56	29.83	Qiao et al. (2017)
Eling Lake	34.90°N/ 97.70°E	619.59 675.08	4269.67	0.31	3.47	13.08	28.89	Shen et al. (2016)
Kusai Lake	35.74°N/ 92.86°E	261.47 327.91	4475.48	0.16	2.93	12.24	49.77	Jia & Liu, (2019)
Manasarovar Lake	30.68°N/ 81.47°E	413.37 413.54	4585.32	0.80	4.46	35.79	70.35	Wang et al. (2013)
Pung Co	31.50°E/ 90.97°E	153.91 175.28	4530.77	0.23	3.66	18.69	49.04	Zhang et al. (2021b)
Tangra Yumco	31.07°N/ 86.61°E	834.23 850.45	4536.09	0.09	8.65	83.61	219.41	Wang et al. (2010)
Taro Co	31.14°N/ 84.12°E	482.04 492.91	4567.74	0.22	8.07	59.39	120.07	Ma et al. (2014)
Zharinam Co	30.93°N/ 85.62°E	967.77 1045.90	4613.14	0.26	3.97	18.30	65.92	Wang et al. (2010)

**We provided lake areas in 2000 and 2020, respectively. The other lake parameters were calculated based on the circa-2000 lake extent.*

with the constraint of the lake bottom, the lake-bottom area was predicted by extending the hypsometric curve to the permanently inundated area. Last, the year 2000 was selected as the benchmark, and the total lake volume in 2000 can be estimated by calculating the volume of a frustum based on the solid geometry formula. The details of the above four steps are as follows.

3.1 The E-A Relationship Construction

The E-A relationship is a widely-used metric for capturing the morphologic features of lakes and reservoirs, which is constructed by pairing up the lake areas and corresponding elevations (water levels) information from *in-situ* measurements or satellite observations. As all selected lakes are ungauged in this study, the ICESat/ICESat-2 measurements and the altimetry data provided by Hydroweb were jointly used for monitoring lake level changes. Our previous studies have revealed two-generation ICESat mission data coverage over the TP lakes (Luo et al., 2021), among which seven study lakes are included. The long-term change of these seven lakes was determined by integrating ICESat/GLAH14 and ICESat-2 ATL13 version 4 data. We collected the orthometric heights in the EGM96 datum by subtracting geoid heights from ellipsoidal heights. The other two lakes, Pung Co and Kusai Lake, have the altimetry data provided by the Hydroweb.

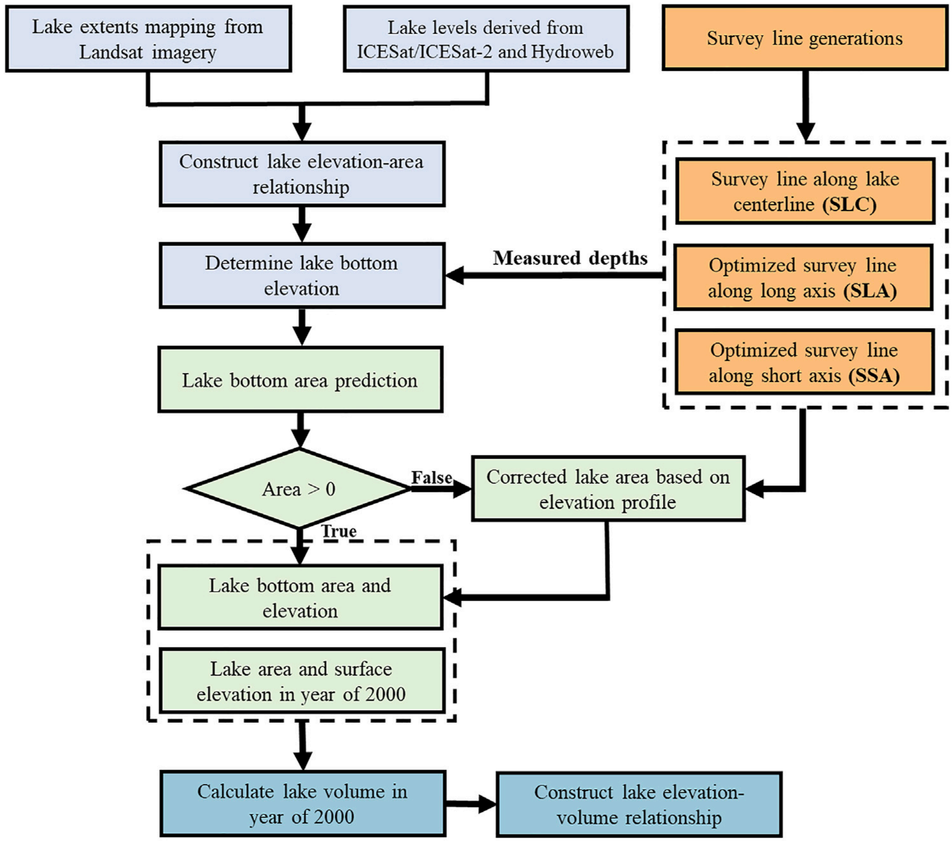

FIGURE 2 | Workflow of the proposed method.

According to the time slots of our obtained lake levels, we collected the temporally corresponding images for mapping the lake areas. We employed the Landsat-7 ETM+ and Landsat-8 OLI images to extract multi-temporal lake inundation extents. The common-used normalized difference water index (NDWI) was applied in this study along with a two-step threshold segmentation strategy to extract the water extent area based on our previous studies (Sheng et al., 2016; Song et al., 2018). Lake mapping was performed in the Google Earth Engine platform, reducing the time cost of preparing the source imagery. After generating long-term surface elevation and surface areas, the hypsometric curves of the E–A relationship can be derived for each lake.

3.2 Determination of the Optimized Survey Line for Searching the “Maximum” Lake Depth

Water-depth measurement is necessary for this method to determine the lake-bottom elevation. However, the full-coverage survey is not recommended due to its high cost and low efficiency. The key step of our proposed method is to design an optimal survey route that can go through the lake bottom zone using limited underwater surveys. Three strategies are considered and compared in this study, including the survey line along the lake centerline (SLC) and optimized survey lines along the lake long axis (SLA) or lake short axis (SSA). Lake centerline determination is initialized by searching the starting and ending points of the bathymetric survey, which are usually generated from the intersection points between the lake boundary and its bounding rectangle. The two points split the lake boundary into two arcs. Then, the Euclidean allocation algorithm is applied to allocate the cells to one side based on the closest proximity. After turning proximity regions into polygons, the lake centerline can be determined as the shared boundary.

The underlying assumption of the SLC is that the maximum lake depth is in the points farthest from shore. However, the spatial heterogeneity of the lake topography may cause an asymmetric distribution of the bathymetric map, and the deep-water zones tend to approach the shore with steep terrains. Thus, the lake shoreline topography is considered in the optimization of the survey line, which is implemented by two procedures. First, the vertical direction of each pixel along the lake shoreline is determined by aligning its adjacent pixels within a certain distance (ten pixels were used in this study) (**Figure 3A**). Second, the gradient value for each shoreline pixel is calculated for representing the vertical drop per mile of longitudinal reach. The default buffer size is set to 600 m in this study (**Figure 3B**) (The influences of different buffer sizes

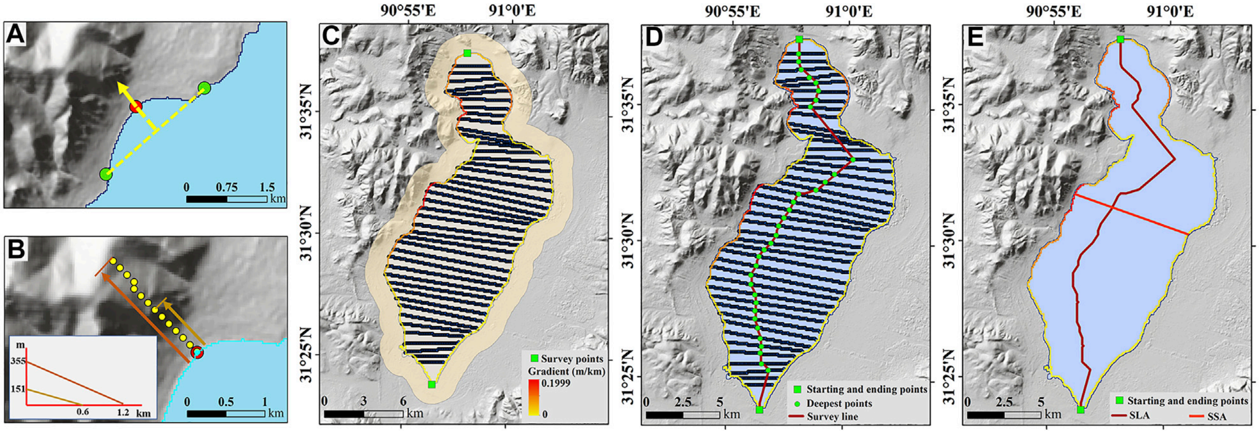

FIGURE 3 | Steps for generating the optimized survey lines along the major axis and minor axis. **(A)** Vertical angle of the center pixel (red point) is calculated using two adjacent points (green points). **(B)** Gradient calculation using different buffer sizes. **(C)** Cross sections generation. **(D)** The predicted deepest points in each cross section were used for creating the optimized survey line along the major axis. **(E)** The pixel along the lake shoreline with the largest gradient value was selected to develop the optimized survey line along the minor axis.

will be discussed below). The generated gradient map of the lake shoreline can indicate the difference in surrounding terrains. Subsequently, lake cross-sections that are approximately perpendicular to the lake's major axis were generated. As shown in **Figure 3C**, the starting and ending points split the lake boundary into the left and right sides. Each side is further sampled by a certain number, determining how many cross-sections need to be generated. Each selected pixel on the left side is connected to its corresponding pixel with the same relative distance on the right side. After connecting the two pixels, a cross-section is generated. The next step is to determine the possible deepest point in each cross-section. It can be roughly assumed that the steepness of the lake's exposed terrains is an extension of the inundated area within certain distances. The elevation profile is thus generated by extending the lakeside slope towards the underwater area. The deepest point along the cross-section is selected as the candidate point for creating the survey route. A distance threshold with the value of 1 km is suggested to remove the point close to the lake shoreline. Finally, the optimized survey line is created after connecting all the remaining deep points.

Both the SAC and SLA are along the lake's major axis, leading to a great deal of survey work, especially for the long-sharp lake. To improve the practicability of the proposed approach, whether the underwater surveys along the short axis can ensure the estimation accuracy is also investigated by using the SSA strategy. The SSA is easy to generate with a two-step process. The first step is to detect the lake-shoreline pixel with the highest gradient value. As the underwater topography is a spatial extension of the exposed terrains, the deepest zone of a lake is likely to be close to the lake shoreline with the steepest surrounding landscapes. Hence, the second step generates a perpendicular line to the lake boundary direction. As shown in **Figure 3E**, the created SSA is much shorter than SLA. Meanwhile, its straight direction is another advantage in practical application.

3.3 Lake Bottom Area Prediction and Volume Estimation

Both lake-bottom elevation and the corresponding lake area are essential for estimating the lake volume. Unfortunately, the lake-bottom site is hard to measure with limited underwater surveys. It is predicted using the constructed E-A relationship (**Figures 4A,B**) and the measured "maximum" lake depth (transferred to lake-bottom elevation). However, the differences in lake geometry and topography between water-fluctuated and underwater regions may cause the uncertainty of lake area prediction, even leading to a negative value. This study used an alternative method by referring to the ratio between survey length within the bottom zone and the total length. As shown in **Figure 4C**, after detecting the point with the maximum depth, all the points with a relative elevation of fewer than 1 m are labeled as the lake bottom. The ratio of the lake-bottom area is assumed to be approximately equal to the percentage of lake-bottom length. Hence, the lake bottom area can be calculated by multiplying the lake surface area and the bottom length ratio.

After obtaining the lake-bottom area and elevation (**Figure 4D**), the total lake volume can be estimated by calculating the difference value between the bottom zone and the referenced lake extent. Although the direct calculation is not infeasible due to the lack of lake bathymetry, we adopted the solid geometry method assuming that a lake can be simplified as a frustum (Abileah and Vignudelli, 2011). In this case, the volume between two conical surfaces can be calculated using the following equation: (**eq. 1**):

$$V = \frac{1}{3}\left(H_{ref} - H_{bottom}\right) \times \left(A_{ref} + A_{bottom} + \sqrt{A_{ref} \times A_{bottom}}\right) \tag{1}$$

where V is the lake volume, H_{ref} and H_{bottom} are the water levels in the referenced time and that of bottom area, respectively, and A_{ref} and A_{bottom} represent the lake areas. The accuracy of the adopted

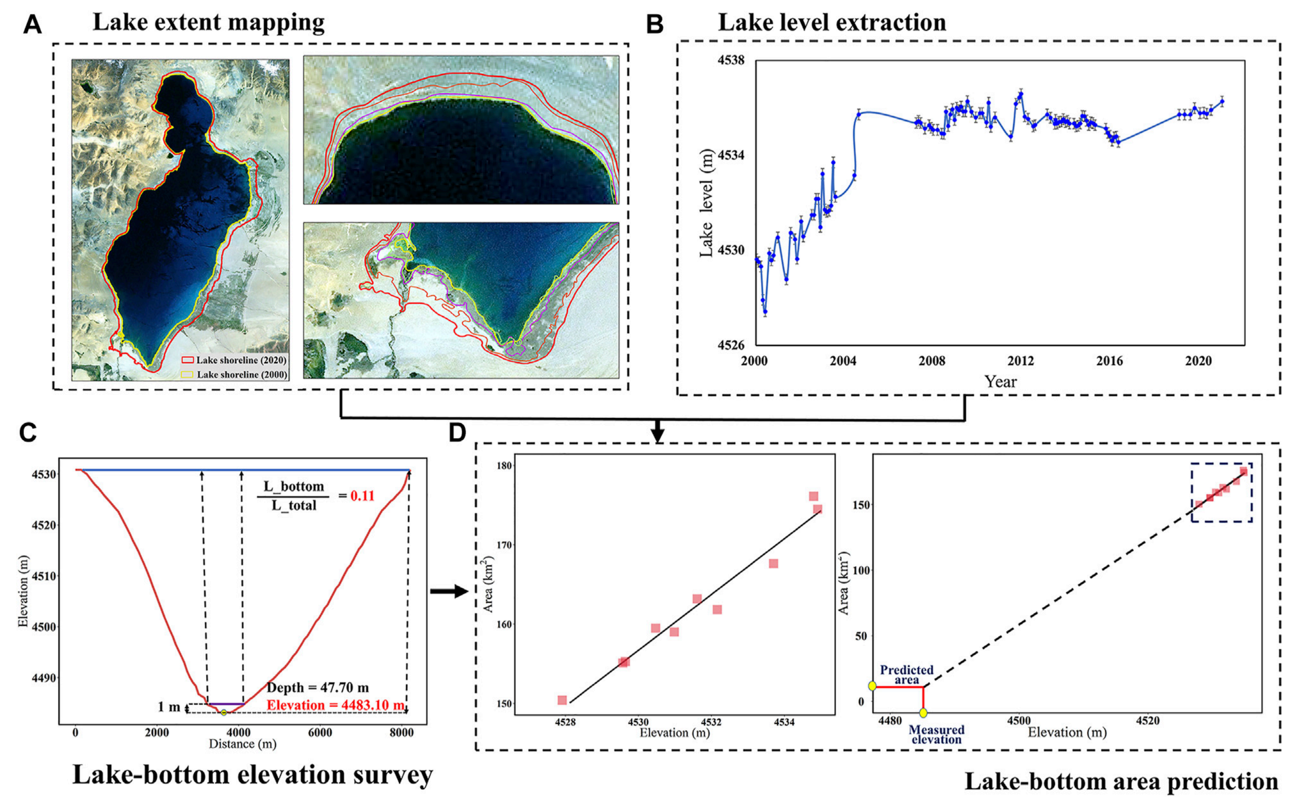

FIGURE 4 | Workflow for predicting the lake-bottom area **(A,B)** Lake extent mapping and lake level extraction are conducted to pair up E-A relationship. **(C)** Vertical profile along the survey line was generated as the lowest elevation was selected as the lake-bottom elevation. **(D)** Lake-bottom area was predicted by using the measured elevation and the E-A relationship.

hypsometric analysis has been proven by the comparation with *in-situ* measurement of lake volume change for Nam Co. (Zhang et al., 2011).

As most lakes on the TP experienced a rapid expansion trend in the 21st century, the newly inundated area can be captured by the SRTM DEM collected in February 2000. Hence, the total lake volume in 2000 is regarded as the benchmark data which remains to be estimated in this study.

4 RESULTS

4.1 Measured Lake-Bottom Elevation and Predicted Lake-Bottom Area

There are strong linear relations between lake levels and area changes, with R^2 values larger than 0.9 for all study lakes (**Figure 5**). To obtain the lake-bottom area by employing the constructed E-A relationship, a constraint value of lake depth is necessary based on the underwater measurements with the optimized survey lines. Both SLC and SLA are along the lake's major axis (**Figure 6**). SLA is more zigzagged and longer than the SLC because its generation considers the influence of surrounding topography. The depth bias is used to evaluate whether the survey line had gone through the deepest zone. **Table 2** indicates that the SLC is generally acceptable, with a bias of less than 10% in all cases except the Bangda Co. The SLA further reduces the depth bias in the case of Aksai Chin Lake, Bangda Co, Kusai Lake, and Pung Co. However, SLA even achieves a larger bias in another four lakes (Tangra Yumco, Manasarovar Lake, and Zharinam Co), although more complex and longer underwater surveys need to be conducted. There is no doubt that the SSA exhibits a huge advantage in reducing the survey work. For example, the length of the SSA in Kusai Lake is only 4.14 km, reducing about 90% of survey work compared with those created by SLA or SLC. Nevertheless, the simplified survey line is challenging in detecting the deepest area. Fortunately, most lakes agree with the assumption that the deepest underwater area is close to the steepest lake shoreline, except for Kusai Lake and Zharinam Co Particularly in the case of Kusai Lake, the water depth estimated based on SSA has an underestimation bias of 28.33%.

After deciding the lake bottom elevation, the corresponding lake area was calculated based on the constructed E-A relationship. The lake-bottom areas were predicted based on the assumption that the E-A relationship within the water-fluctuating region could be extended to the permanently inundated area. It should be noted that the predicted lake area cannot be accepted if the value is less than zero. In this case, the expected bottom area was calculated using the lake surface area and lake-bottom ratio. As shown in **Table 2**, such an alternative solution was used in the case of Aksai Chin Lake, Tangra Yumco, Kusai Lake, and Taro Co.

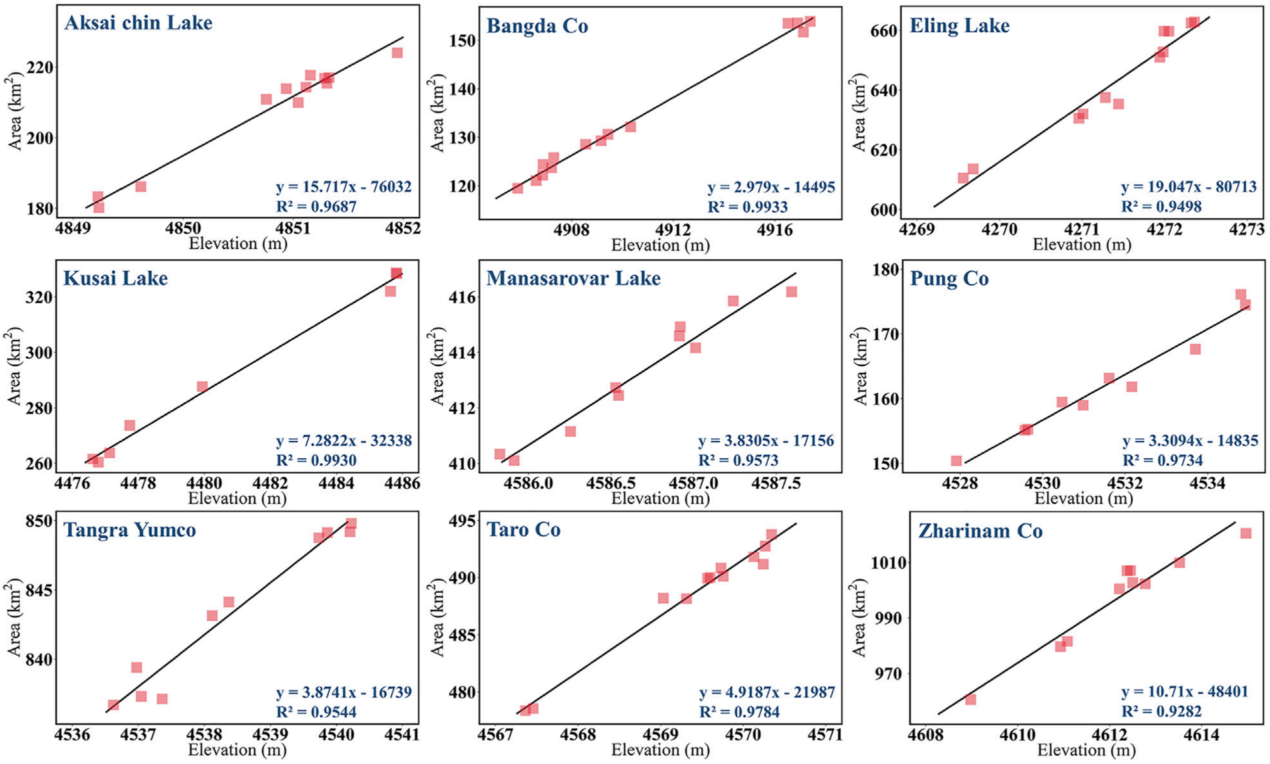

FIGURE 5 | E-A relationship of nine selected lakes.

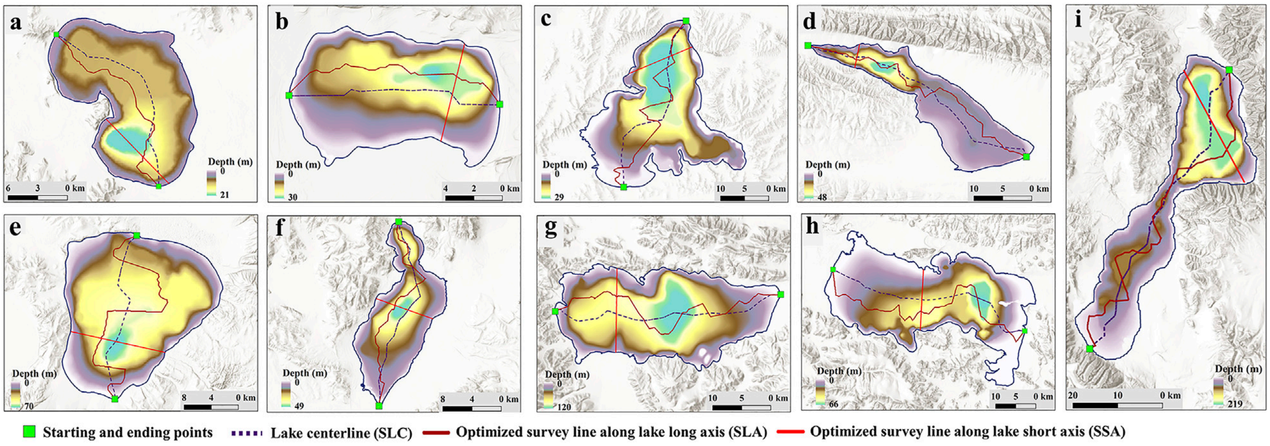

FIGURE 6 | The generated survey line using three different strategies. The lakes are in order as follows: Aksai Chin Lake, Bangda Co, Eling Lake, Kusai Lake, Manasarovar Lake, Pung Co, Taro Co, Zharinam Co, and Tangra Yumco.

4.2 Estimated Lake Volumes

In this study, we calculated the lake volume of each lake based on the circa-2000 lake map and the corresponding lake level. The comparison of the predicted volumes among three different survey strategies is listed in **Table 3**. The bias of lake volume between referenced data derived from the lake bathymetry and the estimated value by using the proposed method was used for accuracy assessment. Generally, the bias of the lake volume in most cases is less than 30%. The mean bias values of SLC, SLA, and SSA are 22.97, %, 23.83%, and 15.99%. Although the SSA is restricted in survey length, its performance accuracy is even higher than the other two survey strategies. SSA achieved the lowest bias in the case of Aksai Chin Lake, Bangda Co, Pung Co, Tangra Yumco, and Zharinam Co. This strategy balanced well

TABLE 2 | Measured lake depth and predicted lake bottom area under different survey strategies.

Lake name	Survey type	Measured depth (m)	Depth bias	Predicted bottom area using E-A relationship (km^2)	Predicted bottom area using elevation profile (km^2)	Length of survey line (km)
Aksai Chin Lake	SLC	19.42	6.55%	<0	11.46	21.55
	SLA	20.59	0.91%	<0	9.17	23.21
	SSA	20.76	0	<0	60.89	8.25
Bangda Co	SLC	24.81	16.84%	42.34	17.44	15.46
	SLA	29.82	0	27.38	5.45	17.17
	SSA	24.82	16.77%	42.29	43.6	7.06
Eling Lake	SLC	29.79	0	43.84	111.53	41.70
	SLA	29.79	0	43.84	130.11	55.67
	SSA	29.79	0	43.84	192.07	14.16
Kusai Lake	SLC	48.50	2.56%	<0	7.32	45.22
	SLA	49.77	0	<0	7.06	50.51
	SSA	35.67	28.33%	<0	52.29	4.14
Manasarovar Lake	SLC	70.35	0	138.62	40.51	26.58
	SLA	60.37	14.19%	176.83	24.80	47.37
	SSA	70.33	0.03%	138.70	45.57	14.25
Pung Co	SLC	45.76	9.25%	14.62	18.63	27.65
	SLA	47.03	2.27%	3.49	0.92	32.40
	SSA	47.70	0.94%	1.37	18.42	8.22
Tangra Yumco	SLC	208.78	6.97%	25.43	4.76	74.20
	SLA	200.72	8.73%	56.65	65.07	92.81
	SSA	219.36	0.25%	<0	70.91	28.35
Taro Co	SLC	119.85	0.22%	<0	41.94	41.54
	SLA	119.81	0.22%	<0	74.23	49.99
	SSA	96.85	19.33%	<0	48.69	14.40
Zharinam Co	SLC	60.39	8.38%	358.91	27.08	54.97
	SLA	58.05	11.94%	384.00	46.45	76.30
	SSA	46.16	29.97%	511.33	301.94	15.05

TABLE 3 | The predicted lake volumes (10^8 m^3) and the volume bias under different survey strategies.

Lake name	Lake level (m)	Survey line along long axis (SLA)	Survey line along short axis (SSA)	Survey line along lake centerline (SLC)
Aksai Chin Lake	4846.43	12.35	16.03	11.8
		−18.99%	5.14%	−22.62%
Bangda Co	4917.388	13.58	12.54	12.53
		7.85%	−0.45%	−0.49%
Eling Lake	4269.67	65.9	65.9	65.9
		−29.53%	−29.52%	−29.52%
Kusai Lake	4475.48	44.55	37.31	43.45
		39.65%	16.96%	36.22%
Manasarovar Lake	4585.32	118.77	129.42	129.43
		−19.59%	−12.38%	−12.37%
Pung Co	4530.77	25.34	25.68	23.53
		−10.23%	−9.01%	−16.65%
Tangra Yumco	4536.09	596.08	661.86	609.62
		−14.38%	−4.94%	−12.44%
Taro Co	4567.74	209.27	179.6	212.03
		−27.11%	−37.44%	−26.15%
Zharinam Co	4613.14	261.58	227.60	267.09
		47.17%	28.05%	50.27%

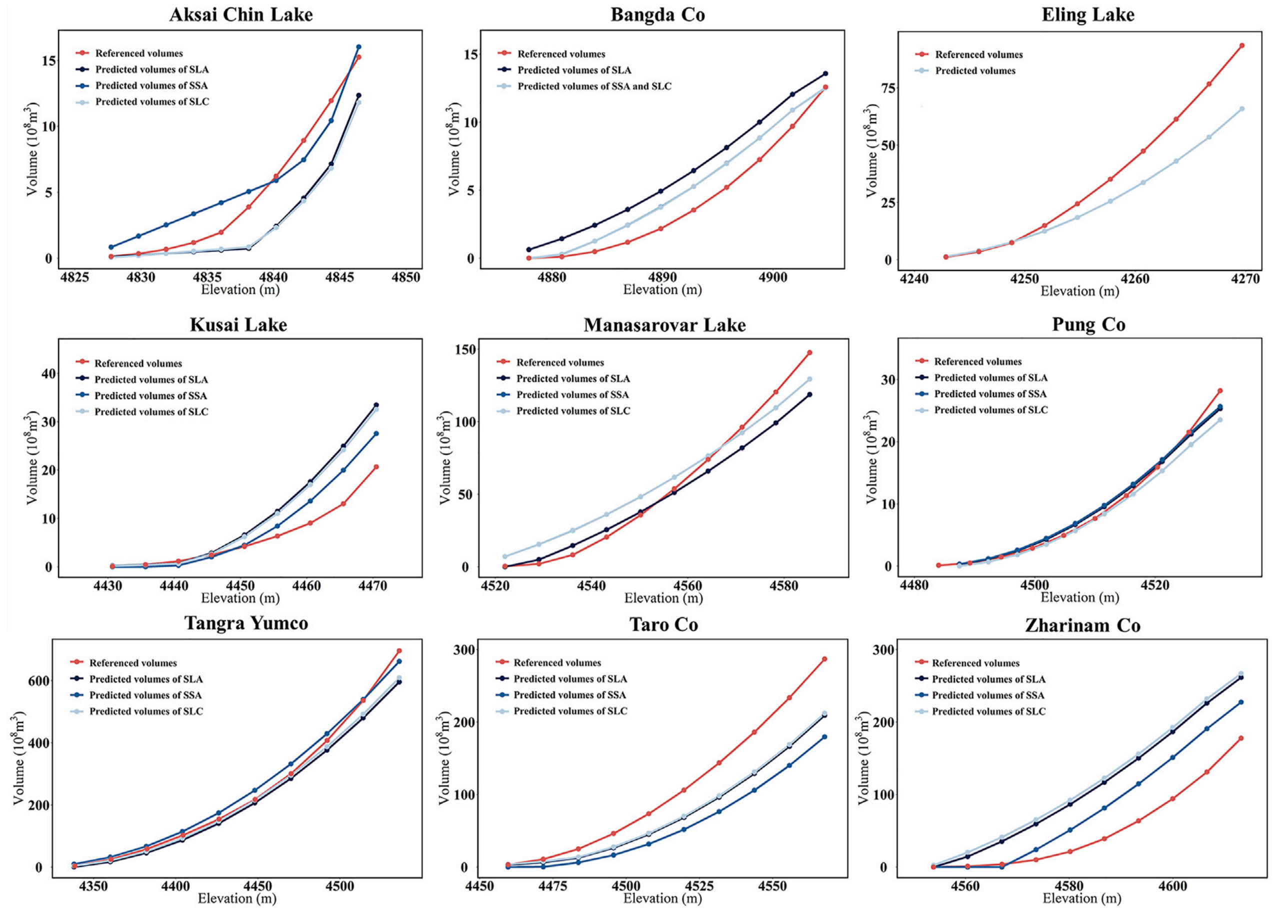

FIGURE 7 | Comparations of E-V relationships between the predicted results and the reference data.

between efficiency and accuracy and is strongly recommended for determining the lake-bottom elevation in the proposed method. It is worth noting the volume bias is negative for most of the lakes, suggesting that the proposed method trends to achieve an overall underestimation of lake volume. This phenomenon should not be entirely ascribed to the missing of the deepest zone. For example, all the three strategies of the water-depth survey line can search the deepest elevation of Eling Lake. However, its water volume estimate is still highly underestimated. It is inferred that the unconformity between the variation of lake geometry and the simplified processing may induce uncertainties in lake volume estimation. Besides estimating the lake volume in 2000, the elevation-volume (E-V) relationship was also constructed by using ten equal interval elevations from the lake bottom to lake level in 2000 (**Figure 7**). The constructed E-V relationship can estimate the lake volume when the lake level is below that of 2000.

This study does not attempt to extrapolate the E-V curve to the lake level above the benchmark value obtained in 2000. As the SRTM DEM can capture the newly exposed region, the gained lake volume since 2000 can be calculated directly. After adding the benchmark volume in 2000, we can estimate the lake volume in any period with a higher lake level. Beneficial from the available topography in the newly flooded region, the bias of the estimated volume is likely to decline when a higher lake level is adopted. For example, the estimated lake volume of Zharinam Co based on the SSA strategy was obviously overestimated in 2000, with a volume bias of 28.05%. After experiencing a dramatic lake expansion, the estimated volume increased from 22.76 Gt to 27.98 Gt. Meanwhile, the bias of the estimated volume dropped to 22.77%.

5 DISCUSSION

5.1 Uncertainties Analysis of the Proposed Method

To facilitate potential applications of our proposed method, we here discuss how the lake volume estimation could be influenced, including the buffer size in lakeside slope calculation and the simplification of lake morphology.

Buffer size determines the width of the exposed terrains around a lake used for calculating the shoreline gradient value. The variation of the estimated gradient value will further lead to different survey routes. This study suggests the default buffer size of 600 m based on previous studies (Liu and Song, 2022). We also

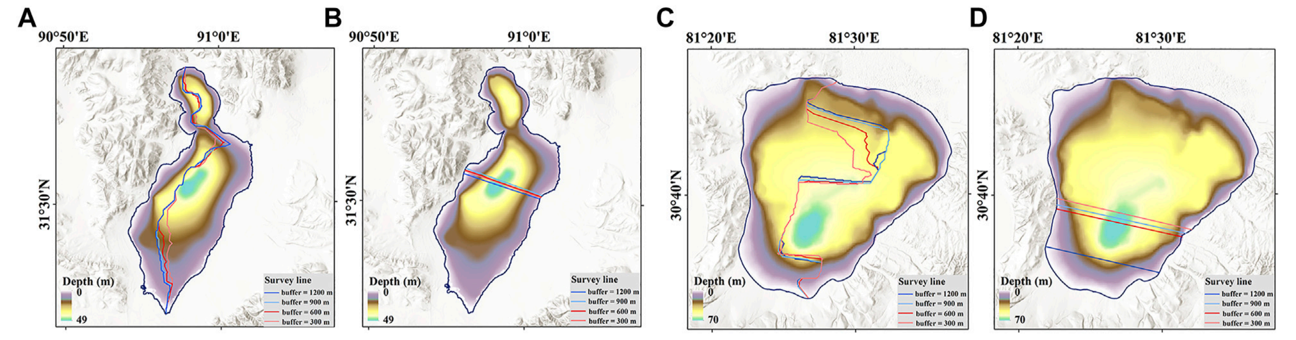

FIGURE 8 | The generated survey lines (in long and short axis) using four different buffer sizes **(A,B)** Pung Co and **(C,D)** Manasarovar Lake.

TABLE 4 | Comparation between the proposed hypsometric curve method and the results provided by Bathymetric method and HydroLAKES.

Lake name	Method	Survey length	Volume (10^8 m^3)	Bias
Aksai Chin Lake	Hypsometric curve	8.25	10.35	5.14%
	Bathymetric method	21.55	15.04	–1.38%
	HydroLAKES	-	15.89	4.20%
Bangda Co	Hypsometric curve	7.06	12.54	–0.45%
	Bathymetric method	15.46	12.89	2.41%
	HydroLAKES	-	9.1	–27.72%
Kusai Lake	Hypsometric curve	4.14	37.31	16.96%
	Bathymetric method	45.22	33.7	5.64%
	HydroLAKES	-	43.49	36.33%
Mapangyong Co	Hypsometric curve	14.25	129.42	–12.38%
	Bathymetric method	26.58	144.65	–2.07%
	HydroLAKES	-	185.37	25.50%
Pung Co	Hypsometric curve	8.22	25.68	–9.01%
	Bathymetric method	27.65	31.50	11.62%
	HydroLAKES	-	18.06	–36.00%
Taro Co	Hypsometric curve	14.40	179.6	–37.44%
	Bathymetric method	41.54	234.32	–18.38%
	HydroLAKES	-	161.52	–43.74%

investigate the influences of the buffer selection on the survey line generation. As shown in **Figure 8**, four buffer sizes ranging from 300 to 1200 m were used to generate the survey routes by taking Pung Co and Manasarovar Lake as examples. The generated SLA becomes more zigzag as the increase of buffer size. It can be explained by the potentially greater difference in topographic relief between two sides when a large buffer size was used. The varying buffer size could also lead to the change of detected SSA. It should be noted that only the deepest value along the survey routes was further used for lake volume calculation. In this case, the variation of survey routes has little impact on the final results, except for the generated SSA when the buffer size was set to 1200.

Another factor that may cause the uncertainty of the proposed method is the simplified processing of the lake's geometric shape. In this study, the underlying assumption of the E-A relationship application in estimating the lake-bottom area is that the lake was approximated as a cone. However, the spatial heterogeneity of the lake geometry between the water-fluctuating region zone and permanently standing water region may cause biased predictions of the lake-bottom area. We also noticed its potential influences as the negative lake area appeared in a few cases. Therefore, an alternative method was adopted by calculating the ratio of bottom area to lake surface area using the measured elevation profile. Such similar simplification may also bring uncertainties in lake total volume calculation. As the lake bathymetry mapping is not the target of this study, the water volume estimation in which a cone approximation provides the mathematics method. However, the reported studies indicated that the lake waterbody could be approximated by various geometric shapes such as box, triangular prism, ellipsoid, and the cone (Khazaei et al., 2022). The unified treatment of a cone shape has improved the efficiency, while the oversimplification restricted its performance for effective representation in some cases.

5.2 Comparison With the Existing Approaches

To better understand the characteristics of the proposed method, a comparison with the existing approaches was further conducted (**Table 4**). HydroLAKES provided the estimated lake volume globally by utilizing the geo-statistical model based on the connection between lake mean depth and lake surrounding terrains (Messager et al., 2016). In this study, Zharinam Co and Tangra Yumco were excluded from the comparison as their volumes were collected from literature records rather than the modeling estimates according to the data specification in HydroLAKES. In comparison, the predicted water volumes for the other seven lakes in HydroLAKES have larger errors than the proposed method. Without any constraint from underwater surveys, the HydroLAKES volume values of Kusai Lake, Pung Co, and Taro Co's are biased greater than 30%. For Longmu Lake, a case not involved in this study, the estimated volume (1.03 Gt) is even less than half of the referenced volume (2.52 Gt).

A comparison was also conducted between this study and the our pervious study, in which the lake bathymetry was constructed based on the machine-learning method and the limited underwater surveys along the lake centerline (Liu and Song, 2022). Generally, the performance of the lake volume based on the constructed bathymetry is better, with the volume bias less than 20% for all the selected lakes. Specifically, eight of the selected lakes achieved a higher volume bias based on the proposed method, except for Bangda Co. However, sufficient underwater surveys are not feasible for all the lakes on the TP due to the limitation of time cost and weather conditions. The advantage of the proposed method is its minimized cost of underwater surveys. The optimized survey line along the short axis is likely to achieve the deepest underwater elevation at a minimal cost. Hence, this method could effectively complement the large-scale lake investigation in the TP or similar harsh environments.

6 CONCLUSION

In order to overcome the challenges in lake volume estimation over the TP, this study aims to propose an efficient method by integrating the remote sensing data and limited underwater surveys. Lake bathymetry, the base data for a commonly-used method for lake volume estimation, is no longer a prerequisite in this method. Instead, this study estimates the lake volume by coupling the lake hypsometric curve and bottom elevation based on the minimal field survey of water depths. The key issue of this method is how to detect the lake-bottom zone without full-coverage measurements. Three survey route strategies were designed, including the lake centerline and the optimized survey lines along the lake's long axis and short axis. The performances of the proposed methods were demonstrated on nine typical lakes over the TP. Generally, the proposed method with three survey strategies can produce acceptable estimates of lake water volume. The mean value of the estimated bias is approximately 20% for the three strategies. An optimized survey line along the lake short axis is highly recommended because its survey work is much less than the other two strategies, with a good balance between efficiency and accuracy.

This study provides a practical approach for simplifying the lake volume estimation and has the potential to narrow the knowledge gap in quantifying the lake volume of the TP. Although the uncertainties of this approach in some specific lakes cannot be ignored, it is still a necessary supplement for the ongoing project of lake bathymetry measurement across the TP. In addition, this approach is promising to be applied in other remote and data-scarce areas for investigating the lake volume with limited filed work. A better representation of the lake physical characteristics will provide essential information for understanding hydrological fluxes and managing water resources.

DATA AVAILABILITY STATEMENT

Landsat-7 ETM+ and Landsat-8 OLI images are stored in Google Earth Engine cloud computing platform (https://earthengine.google.com/). MERIT DEM is available at http://hy-dro.iis.u-tokyo.ac.jp/yamadai/MERIT_DEM/. The time series of the water level are obtained from online databases (HYDROWEB: http://hydroweb.theia-land.fr/; DAHITI: http://dahiti.dgfi.tum.de/en/). Further inquiries can be directed to the corresponding author.

AUTHOR CONTRIBUTIONS

CS and KL designed the study. PZ and SL provided data. KL and CF analyzed the data. KL and CS led the writing of the manuscript. All authors contributed to the article and approved the submitted version.

FUNDING

This study was supported by the Second Tibetan Plateau Scientific Expedition and Research (STEP) (Grant No.2019QZKK0202), and the National Natural Science Foundation of China (Grant Nos. 42171421, 41971403, and 41930102).

ACKNOWLEDGMENTS

We are grateful to the satellite data providers: USGS for Landsat, NSIDC for ICESat/ICESat-2, LEGOS for Hydroweb, Yamazaki Lab for MERIT DEM. We also grateful to the scientific editor and the reviewers for their valuable comments on the manuscript.

REFERENCES

Abileah, R., and Vignudelli, S. (2011). “A Completely Remote Sensing Approach to Monitoring Reservoirs Water Volume,” in Fifteenth International Water Technology Conference, IWTC 15, Alexandria, Egypt, 29 May, 2011, 59–72.

Armon, M., Dente, E., Shmilovitz, Y., Mushkin, A., Cohen, T. J., Morin, E., et al. (2020). Determining Bathymetry of Shallow and Ephemeral Desert Lakes Using Satellite Imagery and Altimetry. *Geophys. Res. Lett.* 47, 1–9. doi:10.1029/2020GL087367

Bandini, F., Olesen, D., Jakobsen, J., Kittel, C. M. M., Wang, S., Garcia, M., et al. (2018). Technical Note: Bathymetry Observations of Inland Water Bodies Using a Tethered Single-Beam Sonar Controlled by an Unmanned Aerial Vehicle. *Hydrol. Earth Syst. Sci.* 22, 4165–4181. doi:10.5194/hess-22-4165-2018

Busker, T., de Roo, A., Gelati, E., Schwatke, C., Adamovic, M., Bisselink, B., et al. (2019). A Global Lake and Reservoir Volume Analysis Using a Surface Water Dataset and Satellite Altimetry. *Hydrol. Earth Syst. Sci.* 23, 669–690. doi:10.5194/hess-23-669-2019

Cael, B. B., Heathcote, A. J., and Seekell, D. A. (2017). The Volume and Mean Depth of Earth’s Lakes. *Geophys. Res. Lett.* 44, 209–218. doi:10.1002/2016GL071378

Chen, F., Zhang, J., Liu, J., Cao, X., Hou, J., Zhu, L., et al. (2020). Climate Change, Vegetation History, and Landscape Responses on the Tibetan Plateau during the Holocene: A Comprehensive Review. *Quat. Sci. Rev.* 243, 106444. doi:10.1016/j.quascirev.2020.106444

Cheng, J., Song, C., Liu, K., Fan, C., Ke, L., Chen, T., et al. (2022). Satellite and UAV-Based Remote Sensing for Assessing the Flooding Risk from Tibetan Lake Expansion and Optimizing the Village Relocation Site. *Sci. Total Environ.* 802, 149928. doi:10.1016/j.scitotenv.2021.149928

Coggins, L. X., and Ghadouani, A. (2019). High-Resolution Bathymetry Mapping of Water Bodies: Development and Implementation. *Front. Earth Sci.* 7, 1–11. doi:10.3389/feart.2019.00330

Crétaux, J.-F., Arsen, A., Calmant, S., Kouraev, A., Vuglinski, V., Bergé-Nguyen, M., et al. (2011). SOLS: A Lake Database to Monitor in the Near Real Time Water Level and Storage Variations from Remote Sensing Data. *Adv. Space Res.* 47, 1497–1507. doi:10.1016/j.asr.2011.01.004

Fassoni-Andrade, A. C., Paiva, R. C. D., and Fleischmann, A. S. (2020). Lake Topography and Active Storage from Satellite Observations of Flood Frequency. *Water Resour. Res.* 56, 1–18. doi:10.1029/2019WR026362

Getirana, A., Jung, H. C., and Tseng, K.-H. (2018). Deriving Three Dimensional Reservoir Bathymetry from Multi-Satellite Datasets. *Remote Sens. Environ.* 217, 366–374. doi:10.1016/j.rse.2018.08.030

Heathcote, A. J., del Giorgio, P. A., and Prairie, Y. T. (2015). Predicting Bathymetric Features of Lakes from the Topography of Their Surrounding Landscape. *Can. J. Fish. Aquat. Sci.* 72, 643–650. doi:10.1139/cjfas-2014-0392

Hollister, J. W., Milstead, W. B., and Urrutia, M. A. (2011). Predicting Maximum Lake Depth from Surrounding Topography. *PLoS One* 6, e25764–6. doi:10.1371/journal.pone.0025764

Immerzeel, W. W., and Bierkens, M. F. P. (2012). Asia’s Water Balance. *Nat. Geosci.* 5, 841–842. doi:10.1038/ngeo1643

Jia, W., and Liu, X. (2019). Decadal- to Centennial-Scale Climate Changes over the Last 2000 Yr Recorded from Varved Sediments of Lake Kusai, Northern Qinghai-Tibetan Plateau. *Quat. Res.* 92, 340–351. doi:10.1017/qua.2019.19

Khazaei, B., Read, L. K., Casali, M., Sampson, K. M., and Yates, D. N. (2022). GLOBathy, the Global Lakes Bathymetry Dataset. *Sci. Data* 9, 1–10. doi:10.1038/s41597-022-01132-9

Lei, Y., Yao, T., Bird, B. W., Yang, K., Zhai, J., and Sheng, Y. (2013). Coherent Lake Growth on the Central Tibetan Plateau since the 1970s: Characterization and Attribution. *J. Hydrology* 483, 61–67. doi:10.1016/j.jhydrol.2013.01.003

Li, X., Long, D., Huang, Q., Han, P., Zhao, F., and Wada, Y. (2019a). High-temporal-resolution Water Level and Storage Change Data Sets for Lakes on the Tibetan Plateau during 2000-2017 Using Multiple Altimetric Missions and Landsat-Derived Lake Shoreline Positions. *Earth Syst. Sci. Data* 11, 1603–1627. doi:10.5194/essd-11-1603-2019

Li, Y., Gao, H., Allen, G. H., and Zhang, Z. (2021). Constructing Reservoir Area-Volume-Elevation Curve from TanDEM-X DEM Data. *IEEE J. Sel. Top. Appl. Earth Obs. Remote Sens.* 14, 2249–2257. doi:10.1109/JSTARS.2021.3051103

Li, Y., Gao, H., Jasinski, M. F., Zhang, S., and Stoll, J. D. (2019b). Deriving High-Resolution Reservoir Bathymetry from ICESat-2 Prototype Photon-Counting Lidar and Landsat Imagery. *IEEE Trans. Geosci. Remote Sens.* 57, 7883–7893. doi:10.1109/tgrs.2019.2917012

Li, Y., Gao, H., Zhao, G., and Tseng, K.-H. (2020). A High-Resolution Bathymetry Dataset for Global Reservoirs Using Multi-Source Satellite Imagery and Altimetry. *Remote Sens. Environ.* 244, 111831. doi:10.1016/j.rse.2020.111831

Liu, C., Zhu, L., Wang, J., Ju, J., Ma, Q., Qiao, B., et al. (2021a). *In-situ* Water Quality Investigation of the Lakes on the Tibetan Plateau. *Sci. Bull.* 66, 1727–1730. doi:10.1016/j.scib.2021.04.024

Liu, K., Ke, L., Wang, J., Jiang, L., Richards, K. S., Sheng, Y., et al. (2021b). Ongoing Drainage Reorganization Driven by Rapid Lake Growths on the Tibetan Plateau. *Geophys. Res. Lett.* 48, 1–11. doi:10.1029/2021GL095795

Liu, K., Song, C., Ke, L., Jiang, L., Pan, Y., and Ma, R. (2019). Global Open-Access DEM Performances in Earth’s Most Rugged Region High Mountain Asia: A Multi-Level Assessment. *Geomorphology* 338, 16–26. doi:10.1016/j.geomorph.2019.04.012

Liu, K., and Song, C. (2022). Modeling Lake Bathymetry and Water Storage from DEM Data Constrained by Limited Underwater Surveys. *J. Hydrology* 604, 127260. doi:10.1016/j.jhydrol.2021.127260

Luo, S., Song, C., Zhan, P., Liu, K., Chen, T., Li, W., et al. (2021). Refined Estimation of Lake Water Level and Storage Changes on the Tibetan Plateau from ICESat/ICESat-2. *Catena* 200, 105177. doi:10.1016/j.catena.2021.105177

Ma, Q., Zhu, L., Lü, X., Guo, Y., Ju, J., Wang, J., et al. (2014). Pollen-inferred Holocene Vegetation and Climate Histories in Taro Co, Southwestern Tibetan Plateau. *Chin. Sci. Bull.* 59, 4101–4114. doi:10.1007/s11434-014-0505-1

Messager, M. L., Lehner, B., Grill, G., Nedeva, I., and Schmitt, O. (2016). Estimating the Volume and Age of Water Stored in Global Lakes Using a Geo-Statistical Approach. *Nat. Commun.* 7, 1–11. doi:10.1038/ncomms13603

Pekel, J.-F., Cottam, A., Gorelick, N., and Belward, A. S. (2016). High-resolution Mapping of Global Surface Water and its Long-Term Changes. *Nature* 540, 418–422. doi:10.1038/nature20584

Qiao, B., Zhu, L., Wang, J., Ju, J., Ma, Q., Huang, L., et al. (2019a). Estimation of Lake Water Storage and Changes Based on Bathymetric Data and Altimetry Data and the Association with Climate Change in the Central Tibetan Plateau. *J. Hydrology* 578, 124052. doi:10.1016/j.jhydrol.2019.124052

Qiao, B., Zhu, L., Wang, J., Ju, J., Ma, Q., and Liu, C. (2017). Estimation of Lakes Water Storage and Their Changes on the Northwestern Tibetan Plateau Based on Bathymetric and Landsat Data and Driving Force Analyses. *Quat. Int.* 454, 56–67. doi:10.1016/j.quaint.2017.08.005

Qiao, B., Zhu, L., and Yang, R. (2019b). Temporal-spatial Differences in Lake Water Storage Changes and Their Links to Climate Change throughout the Tibetan Plateau. *Remote Sens. Environ.* 222, 232–243. doi:10.1016/j.rse.2018.12.037

Saylam, K., Brown, R. A., and Hupp, J. R. (2017). Assessment of Depth and Turbidity with Airborne Lidar Bathymetry and Multiband Satellite Imagery in Shallow Water Bodies of the Alaskan North Slope. *Int. J. Appl. Earth Observation Geoinformation* 58, 191–200. doi:10.1016/j.jag.2017.02.012

Sheng, Y., Song, C., Wang, J., Lyons, E. A., Knox, B. R., Cox, J. S., et al. (2016). Representative Lake Water Extent Mapping at Continental Scales Using Multi-Temporal Landsat-8 Imagery. *Remote Sens. Environ.* 185, 129–141. doi:10.1016/j.rse.2015.12.041

Song, C., Huang, B., and Ke, L. (2013). Modeling and Analysis of Lake Water Storage Changes on the Tibetan Plateau Using Multi-Mission Satellite Data. *Remote Sens. Environ.* 135, 25–35. doi:10.1016/j.rse.2013.03.013

Song, C., Ke, L., Pan, H., Zhan, S., Liu, K., and Ma, R. (2018). Long-term Surface Water Changes and Driving Cause in Xiong’an, China: from Dense Landsat Time Series Images and Synthetic Analysis. *Sci. Bull.* 63, 708–716. doi:10.1016/j.scib.2018.05.002

Verpoorter, C., Kutser, T., Seekell, D. A., and Tranvik, L. J. (2014). A Global Inventory of Lakes Based on High-Resolution Satellite Imagery. *Geophys. Res. Lett.* 41, 6396–6402. doi:10.1002/2014GL060641

Wang, J., Peng, P., Ma, Q., and Zhu, L. (2010). Modem Limnological Features of Tangra Yumco and Zhari Namco, Tibetan Plateau. *J. Lake Sci.* 22 (4), 629–632. (In Chinese with English abstract)

Wang, J., Peng, P., Ma, Q., and Zhu, L. (2013). Investigation of Water Depth, Water Quality and Modern Sedimentation Rate in MapamYumco and La’ang Co, Tibet. *J. Lake Sci.* 25 (4), 609–616. (In Chinese with English abstract)

Woolway, R. I., Kraemer, B. M., Lenters, J. D., Merchant, C. J., O'Reilly, C. M., and Sharma, S. (2020). Global Lake Responses to Climate Change. *Nat. Rev. Earth Environ.* 1, 388–403. doi:10.1038/s43017-020-0067-5

Xu, N., Ma, Y., Yang, J., Wang, X. H., Wang, Y., and Xu, R. (2022). Deriving Tidal Flat Topography Using ICESat-2 Laser Altimetry and Sentinel-2 Imagery. *Geophys. Res. Lett.* 49, 1–10. doi:10.1029/2021gl096813

Yamazaki, D., Ikeshima, D., Tawatari, R., Yamaguchi, T., O'Loughlin, F., Neal, J. C., et al. (2017). A High-Accuracy Map of Global Terrain Elevations. *Geophys. Res. Lett.* 44, 5844–5853. doi:10.1002/2017GL072874

Yang, K., Lu, H., Yue, S., Zhang, G., Lei, Y., La, Z., et al. (2018). Quantifying Recent Precipitation Change and Predicting Lake Expansion in the Inner Tibetan Plateau. *Clim. Change* 147, 149–163. doi:10.1007/s10584-017-2127-5

Yao, F., Wang, J., Yang, K., Wang, C., Walter, B. A., and Crétaux, J.-F. (2018). Lake Storage Variation on the Endorheic Tibetan Plateau and its Attribution to Climate Change since the New Millennium. *Environ. Res. Lett.* 13, 064011. doi:10.1088/1748-9326/aab5d3

Yigzaw, W., Li, H. Y., Demissie, Y., Hejazi, M. I., Leung, L. R., Voisin, N., et al. (2018). A New Global Storage-Area-Depth Data Set for Modeling Reservoirs in Land Surface and Earth System Models. *Water Resour. Res.* 54 (10), 372–410. doi:10.1029/2017WR022040

Zhang, B., Wu, Y., Zhu, L., Wang, J., Li, J., and Chen, D. (2011). Estimation and Trend Detection of Water Storage at Nam Co Lake, Central Tibetan Plateau. *J. Hydrology* 405, 161–170. doi:10.1016/j.jhydrol.2011.05.018

Zhang, G., Ran, Y., Wan, W., Luo, W., Chen, W., Xu, F., et al. (2021a). 100 Years of Lake Evolution over the Qinghai-Tibet Plateau. *Earth Syst. Sci. Data* 13, 3951–3966. doi:10.5194/essd-13-3951-2021

Zhang, G., Yao, T., Xie, H., Yang, K., Zhu, L., Shum, C. K., et al. (2020). Response of Tibetan Plateau Lakes to Climate Change: Trends, Patterns, and Mechanisms. *Earth-Science Rev.* 208, 103269. doi:10.1016/j.earscirev.2020.103269

Zhang, R., Zhu, L., Ma, Q., Chen, H., Liu, C., and Zubaida, M. (2021b). The Consecutive Lake Group Water Storage Variations and Their Dynamic Response to Climate Change in the Central Tibetan Plateau. *J. Hydrology* 601, 126615. doi:10.1016/j.jhydrol.2021.126615

Conflict of Interest: The authors declare that the research was conducted in the absence of any commercial or financial relationships that could be construed as a potential conflict of interest.

frontiers | Frontiers in Environmental Science

TYPE Original Research
PUBLISHED 30 August 2022
DOI 10.3389/fenvs.2022.963921

Trends of terrestrial water storage and actual evapotranspiration in Chinese inland basins and their main affecting factors

Xuan Liu[1,2], Zhaofei Liu[1,2,3]* and Haoshan Wei[1,2]

[1]Institute of Geographic Sciences and Natural Resources Research, Chinese Academy of Sciences, Beijing, China, [2]College of Resources and Environment, University of Chinese Academy of Sciences, Beijing, China, [3]Key Laboratory of Carrying Capacity Assessment for Resource and Environment, Ministry of Natural Resources, Beijing, China

OPEN ACCESS

EDITED BY
Xiuping Li,
Institute of Tibetan Plateau Research (CAS), China

REVIEWED BY
Jie Wang,
Nanjing University of Information Science and Technology, China
Mohd Yawar Ali Khan,
King Abdulaziz University, Saudi Arabia

*CORRESPONDENCE
Zhaofei Liu,
zfliu@igsnrr.ac.cn

SPECIALTY SECTION
This article was submitted to Environmental Informatics and Remote Sensing,
a section of the journal
Frontiers in Environmental Science

RECEIVED 08 June 2022
ACCEPTED 20 July 2022
PUBLISHED 30 August 2022

CITATION
Liu X, Liu Z and Wei H (2022), Trends of terrestrial water storage and actual evapotranspiration in Chinese inland basins and their main affecting factors.
Front. Environ. Sci. 10:963921.
doi: 10.3389/fenvs.2022.963921

The Chinese inland basins (CIBs) are vulnerable to global warming and human activities due to low precipitation and high potential evaporation. Terrestrial water storage (TWS) is an important component of the hydrological cycle and essential for evaluating the water resource security of the CIBs. Although some studies have focused on water storage trends in sub-basins of the CIBs, only few studies have analyzed water storage trends in the CIBs as a whole. In this study, trends and magnitudes of precipitation, TWS, and actual evapotranspiration (AET) were detected by the rank-based non-parametric Mann–Kendall test and trend magnitude method. Based on the hydrological budget of the closed inland basin, the monthly series of AET were simulated and the main factors affecting TWS changes in the CIBs and each closed basin were identified. Results showed that both precipitation and AET significantly increased in the CIBs. Precipitation decreased from the northwest and southeast regions to the central region in the CIBs. Moreover, the annual TWS in the CIBs significantly decreased mainly due to the increased AET. Approximately 60% AET increase was attributed to increased irrigation diversions. At the basin scale, similar to the CIBs, changes in AET were the predominant factor influencing changes in TWS in the Tarim basin (TRB), Turpan basin (TPB), and Hexi Corridor basin (HCB). Qiangtang Plateau basin (QPB) Qaidam basin (QDB) the increase in precipitation contributed more than 60% increase in TWS glacier melting and irrigation diversion.

Abbreviations: CIBs, Chinese inland basins; GRACE, Gravity recovery and climate experiment; TWS, Terrestrial water storage; TWSA, Terrestrial water storage anomalies; AET, Actual evapotranspiration; TRB, Tarim basin; TPB, Turpan basin; HCB, Hexi Corridor basin; QDB, Qaidam basin; QPB, Qiangtang Plateau basin; NASA, National Aeronautics and Space Administration; CSR, Center for Space Research at the University of Texas; GFZ, Geo-Forschungs-Zentrum in Potsdam; JPL, Jet Propulsion Laboratory; Mascons, Mass concentration blocks; JPLM, JPL mascons; CSRM, CSR mascons.

KEYWORDS

hydrological budget, inland closed basin, water balance, continental river basin, terrestrial water storage

1 Introduction

Terrestrial water storage (TWS), which includes snow water storage, canopy water storage, surface water storage, soil moisture storage, and groundwater storage, comprehensively reflects regional precipitation, runoff, evapotranspiration, groundwater, and human activities (Scanlon et al., 2018). It is an important variable for global hydrological cycle observation (Liu et al., 2016; Deng and Chen, 2017). Although TWS accounts for only 3.5% water in the global hydrological cycle, it is an important component of the terrestrial and global water cycle that provides important control over water, energy, and biotic ecosystem processes (Hu et al., 2018; Chen et al., 2022), and thus plays an important role in the global climate system (Bierkens, 2015). TWS and their components control various hydrometeorological, ecological, and biogeochemical processes on different spatial and temporal scales (Koster et al., 2004; Seneviratne et al., 2010; Dong et al., 2022), and thus there is great spatial and temporal heterogeneity in the global scale (Güntner et al., 2007; Güntner, 2008).

In the past decades, extreme climatic events (such as droughts and floods) and human activities (such as groundwater extraction) have influenced TWS beyond normal thresholds on a global scale. For example, TWS has significant decreased due to groundwater over-exploitation in Illinois (Yeh et al., 2006), the Central Valley (Famiglietti et al., 2011; Scanlon et al., 2012; He et al., 2017), northern India (Xiang et al., 2016), the Middle East (Voss et al., 2013), and northern China (Feng et al., 2013). In addition, severe droughts in the southern U.S. High Plains (Scanlon et al., 2012), eastern Texas (Long et al., 2013), Brazil (Getirana, 2016), and southeastern and northern Africa (Ramillien et al., 2014; Rodell et al., 2018) have significantly decreased TWS, particularly groundwater storage. On the contrary, TWS has also increased at other regions, including the Qaidam basin (QDB) (Bibi et al., 2019; Meng et al., 2019) and Qiangtang Plateau basin (QPB) (Liu et al., 2019; Meng et al., 2019) in the Chinese inland basins (CIBs). However, only few studies have examined the attributes of the underlying factors driving these trends.

Remote sensing products, such as gravity recovery and climate experiment (GRACE) satellite data, are widely used to assess global hydrology. GRACE satellites have been likened to giant weighing scales in the sky that monitor monthly changes in mass as water storage increases or decreases due to climate variability and human impacts (Scanlon et al., 2018). GRACE satellites provide global total water storage anomaly (TWSA) data since their launch in 2002. These satellites provide a more direct estimate than global TWSA change models derived from monitoring the time variable gravity field (Wahr et al., 2004). The coarse spatial resolution of GRACE data (~100,000 km^2) may actually be beneficial when estimating changes in TWSA at continental to global scales.

Inland basins, also referred to as endorheic basins, are defined as regions where runoff in the basin has no direct hydraulic connection with the ocean (Liu, 2022). Thus, inland river basin runoff is isolated from the ocean and eventually enters inland lakes or is absorbed by evapotranspiration. These areas are among the most sensitive to climate change and human activities (Huang et al., 2016; Wang et al., 2018). The CIBs are located in the hinterland of Asia. Accurately monitoring the TWSA changes of a large area is difficult by traditional stations. GRACE satellite monitoring becomes a feasible solution in this case. Since the CIBs have temperate continental climate characterized by low precipitation and high evapotranspiration, the hydrology and ecosystem of CIBs are sensitive to changes in precipitation, actual evapotranspiration (AET), and TWSA. Therefore, analysis of terrestrial TWSA variability and attribution in the CIBs is important for water resource management, ecosystem health, and sustainable irrigated agriculture in China. However, few studies have focused on the variation and attribution of CIBs as a whole. In addition, there were some inconsistent conclusions on the TWSA trends in CIB sub-basins. Wang et al. (2020) reported that TWSA decreased during 2002–2016 in the Hexi Corridor basin (HCB) using one TWSA product. Cao et al. (2018) found that the basin TWSA significantly increased during 2002–2013 using another TWSA product. Thus, opposite results might be detected from different datasets. This study used multiple GRACE datasets to reduce the uncertainty caused by using only a single dataset. The hydrological budget (hydrologic gains and losses) is effective for analysis at the basin scale (Liu et al., 2014; Liu et al., 2016). Unlike outflow basins, which include AET and runoff in hydrologic losses, inland river basins include only AET. In other words, the hydrologic budget in inland river basins can only be expressed in terms of precipitation, AET, and TWSA. Therefore, this method is more suitable for analyzing the TWSA variability and its main attribution in inland river basins.

This study uses multi-source of data in the CIBs and each closed basin to simulate the monthly AET series of each inland basin using the hydrologic budget method, detect the spatiotemporal characteristics of annual and monthly precipitation, TWSA, and AET in each basin using a non-parametric test, and identify the main attributes of TWSA change in each closed basin using the water balance principle. The results obtained in this study could be useful to regional water resource management, ecosystem health, and sustainable agricultural irrigation in China.

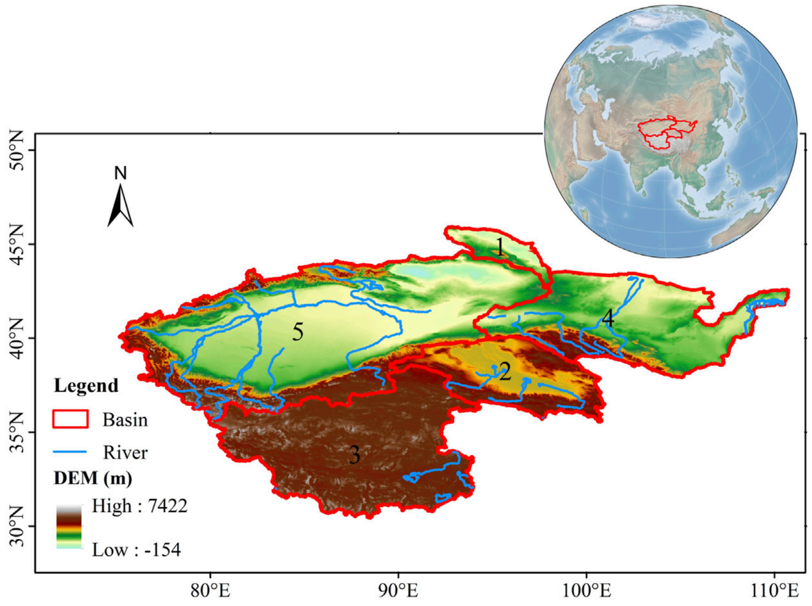

FIGURE 1
Location and distribution of each basin in the Chinese inland basins (CIBs). 1–5 represents the Turpan basin (TPB), Qaidam basin (QDB), Qiangtang Plateau basin (QPB), Hexi Corridor basin (HCB), and Tarim basin (TRB), respectively.

2 Study area

The CIBs are located in northwest China (Figure 1), covering 2.61×10^{11} km^2 area, accounting for 27% Chinese land area; however, it takes up only 5.5% total water resource of China. It is one of the most arid regions worldwide and includes five closed inland basins: the Turpan basin (TPB), QDB, QPB, HCB, and Tarim basin (TRB) (Figure 1). The terrain within the basin is complex. The landform is mainly plateau and inland basin. The CIBs are affected by the plateau monsoon and East Asian monsoon climate systems. The climate is complex and changeable. Except in Yili and Tacheng in northern CIBs, annual precipitation in most areas is less than 200 mm. The annual precipitation in the CIBs is 164.5 mm. The annual precipitation of TPB, QDB, QPB, HCB, and HCB are 86.2, 147.8, 264.8, 153.3, and 112.9 mm, respectively.

3 Materials and methods

3.1 Gravity recovery and climate experiment data

3.1.1 The RL06 spherical harmonics

The GRACE satellites, launched by National Aeronautics and Space Administration (NASA) and Deutsches Zentrum für Luft- und Raumfahrt in March 2002, allows us to measure large scale TWSA trends with monthly temporal resolution. Temporal variations in the gravity field over land are primarily due to TWSA, which is the vertically integrated measure of groundwater, soil moisture, snow, ice, and surface water.

This study uses data from March 2002 to February 2021 (39 months of data are missing). The gridded GRACE TWSA data were obtained from the Center for Space Research at the University of Texas (CSR), the Geo-Forschungs-Zentrum in Potsdam (GFZ), and the Jet Propulsion Laboratory (JPL).

The spatial resolution of all three datasets is 1°. More than 300 grid points covering the study area were chosen for estimating the values. To reduce uncertainty, the missing data were obtained *via* simple temporal interpolation using adjacent data (Andrew et al., 2017).

3.1.2 The global mascons

Mass concentration blocks (mascons) are another form of gravity field basis function. Compared to the standard spherical harmonic method of empirical post-processing filtering, "mascons" eases the implementation of geophysical constraints and are a more rigorous method (Watkins et al., 2015; Wiese et al., 2016). The JPL mascons (JPLM) and CSR mascons (CSRM) solutions are available at 0.5° and 0.25°. In this study, the GRACE TWSA solution was compared for the period from 2002 to 2020.

3.2 Meteorological data

This study estimated the precipitation trend in the CIBs from 2002 to 2020 using the China Monthly Surface

Precipitation 0.5°×0.5° Gridded Dataset V2.0 (http://data.cma.cn/), which is a gridded dataset released by the National Meteorological Information Center of the China Meteorological Administration. This dataset was derived by interpolating the observed precipitation data from 2,472 stations over China since 1961. Owing to the high quality of this dataset, it has been widely used in the CIBs (Zhu et al., 2015; Bueh et al., 2016; Zhang et al., 2017; Wang et al., 2019).

3.3 Methodology

3.3.1 Monthly actual evapotranspiration simulation

According to the hydrological budget in an inland basin, the difference between precipitation and AET corresponds to the variation in water storage in the basin; therefore, the monthly AET in the basin can be simulated as (Liu, 2022):

$$\mathbf{AET}_i = \mathbf{P}_i - \mathbf{\Delta S}_i \tag{1}$$

Where AET_i, P_i, and S_i are the monthly series (in mm) of AET, precipitation, and storage change, respectively. The average gridded precipitation and TWSA data series for each closed basin was calculated based on each grid area weight within the basin. The area weighting of the boundary grids was shown by the proportion of the area within the basin boundary.

The consistency of the time series for each variable should be considered while simulating monthly AET. Monthly AET and precipitation are averaged within a month, calculating between the beginning and end of the month. ΔS is the difference between the water storage at the end and beginning of the month. However, the TWSA data used in this study represent the average water storage within a month. ΔS was calculated as:

$$\boldsymbol{S}_i = \frac{\boldsymbol{TWS}_{i+1} - \boldsymbol{TWS}_{i-1}}{2} \tag{2}$$

where $TSWA_{i+1}$ and $TWSA_{i-1}$ represent water storage at the end and beginning of the simulated month, respectively. The accuracy of this calculation has been verified by Long et al. (2014).

3.3.2 Time series decomposition

The TWSA outputs reveal the monthly variations of total water storage; therefore, seasonality should be first removed from the original TWSA series to estimate TWSA trends (Andrew et al., 2017). Precipitation and evapotranspiration data should be processed similarly. The seasonal trend decomposition uses the local regression to decompose the time series was proposed by Cleveland and Cleveland (1990). In this study, local regression was used to decompose the TWSA monthly time series. Local regression smoothing is the key of the local regression method. It fits the smoothed series X_j to the input time series $X_j = X_{tj}$, where t_j is the discrete sampling time series. The smoothed value for each point j is given by the value of the polynomial at time t_j increased by j. The local regression consists of an outer and inner loop with a sequence of smoothing operators and generates three components from the time series:

$$\boldsymbol{S}_{total} = \boldsymbol{S}_{long-term} + \boldsymbol{S}_{seasonal} + \boldsymbol{S}_{residual} \tag{3}$$

where S_{total} indicates the original signal, $S_{\text{long-term}}$ is the trend signal, S_{seasonal} is the seasonal signal, and S_{residual} is indicated as the sub-seasonal signal and noise.

3.3.3 Trend detection and identification of its main attribution methods

The Mann–Kendall (M–K) test, one of the commonly used time series trend tests in meteorology and hydrology (Hirsch et al., 1982), applied for trend detection in this study. It also rejects a few outliers and the sample does not need to follow a certain distribution and is suitable for non-normally distributed data (Bibi et al., 2019).

Based on the hydrological budget in inland closed basins, the main factors causing AET and TWSA variations were identified. Based on the water source consumed by the AET, AET variation is attributed to alterations in precipitation and the consumption of other water supply sources. It can be calculated as follows (Liu, 2022):

$$\boldsymbol{\Delta AET} = \boldsymbol{\Delta P} + \boldsymbol{\Delta Others} \tag{4}$$

Where ΔAET, ΔP, and $\Delta Others$ indicate changes in AET, precipitation, and other water supply sources (such as irrigation from ground water and glacial melt water), respectively.

Based on the hydrological budget within a closed basin, changes in TWSA are mainly attributable to precipitation and AET, while changes in AET are mainly caused by precipitation and potential evaporation. Precipitation and potential evaporation positively and negatively contribute to AET, respectively. Furthermore, precipitation and AET positively and negatively affect TWSA, respectively. Increased precipitation will promote an increase in TWSA, whereas increased AET will exacerbate the decrease in TWSA, and vice versa. Thus, the contribution of precipitation and other factors to TWSA changes can be semi-quantified by analyzing the trend between AET and precipitation. The study roadmap for the entire study is shown in Figure 2.

4 Results

4.1 Trends and spatial distribution of terrestrial water storage anomalies in the Chinese inland basins

The TWSA time series in CIBs derived from five GRACE solutions are highly consistent according to Figure 3A. Overall, the TWSA decreased significantly. Specifically, the TWSA increased during 2002–2005, continuously declined from 2005 to 2010, slightly increased from 2010 to 2012, then decreased during

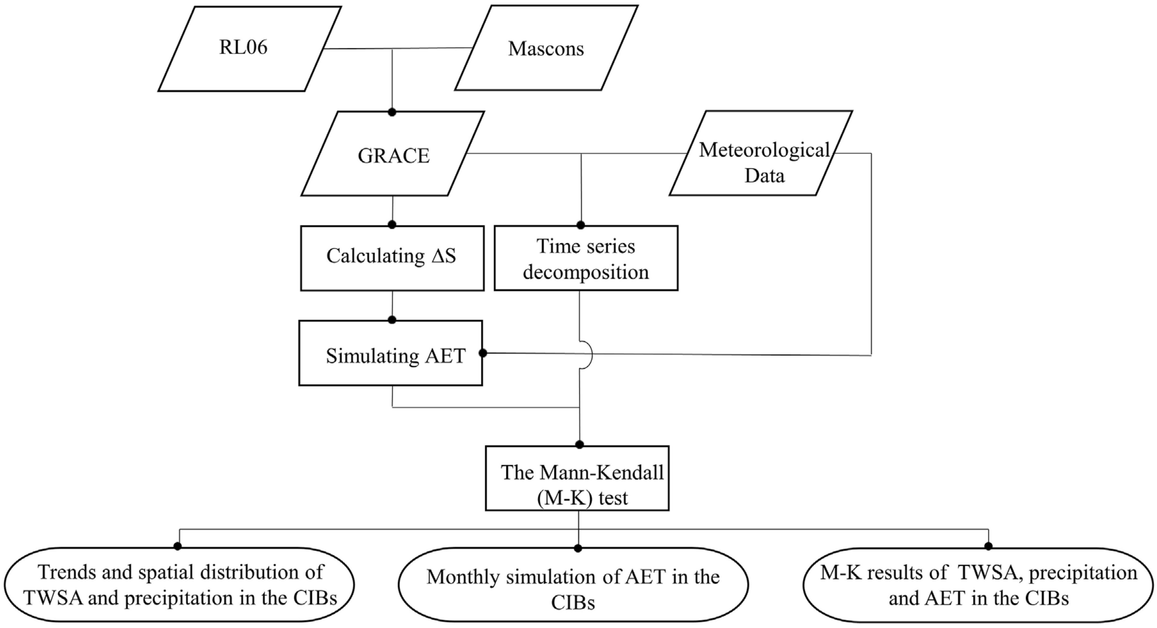

FIGURE 2
The study roadmap.

2012–2016, further rising in a fluctuation way. Across the entire time scale, the TWSA of CIBs decreased significantly by 26 km^3/yr.

Figures 3B–F shows the monthly series of TWSA in each sub-basin, obtained from different GRACE solutions. The TWSA significantly increased in the QDB and QPB, while it significantly decreased in other sub-basins. Specifically, the TWSA of the TPB decreased with 0.15 km^3/yr fluctuations throughout the time scale. The TWSA of the HCB briefly increased from 2002 to 2004, declined from 2004 to 2007, and then continuously fluctuated from 2007 to 2020. Overall, the TWSA of HCB decreased at 0.4 km^3/yr throughout the time scale. TWSA trend in the TRB is similar to that in the CIBs, with TWSA decreasing at 2.9 km^3/yr over the entire time scale. The TWSA trends for QPB and QDB significantly fluctuated from 2002 to 2020, with 1.2 and 1.5 km^3/yr growth rates, respectively.

Figure 4 shows the spatial distribution of TWSA trends derived from different GRACE solutions. The spatial distribution of the five solutions were highly consistent. It showed a significant loss of water storage at the northwestern and southwestern CIB regions during the study period. Water storage significantly increased in the central and southeastern CIB regions. According to the sub-basins, TWSA significantly increased in the northeastern QPB and the entire QDB, while it significantly decreased in the TPB and the HCB. Moreover, the JPLM solution-produced TWSA series deviated from the other four solution-produced TWSAs in the CIBs (Figure 4). This finding is also consistent with previous finding that decreasing and increasing TWSA trends of JPLM solution are larger than those of CSR, JPL, and GFZ globally (Scanlon et al., 2018).

Viewing the time change of the TWSA in the CIBs revealed that the similarity between the five GRACE solutions started to decrease from 2016 (Figure 3A). The periodic change of TWSA in sub-basins also indicated that TWSA fluctuation increased in the five basins in 2016 for the five solutions (Figures 3B–F). Therefore, the TWSA of GRACE were calculated according to the time for data variance and median changes (Figure 5). From 2002 to 2007, the median GRACE data continued to decline, while the variance increased and then decreased. The median GRACE data began to rise but did not rise above the original median from 2007 to 2011. The variance change did not change much from the previous time period. The median GRACE data began to fluctuate around the initial median line from 2012 to 2016; however, the overall variance was low. The median GRACE data suddenly increased and reached the maximum in 2017. Simultaneously, the variance reached the maximum. Then, the median data continuously decreased from 2018 to 2020. The median GRACE data was lower than the initial median value since 2019, and the variance decreased gradually.

4.2 Trends and spatial distribution of precipitation and actual evapotranspiration simulation in the Chinese inland basins

Figure 6 indicates the spatial distribution of precipitation trends in the CIBs from 2002 to 2020. Macroscopically, precipitation increased in the northeast, northwest and

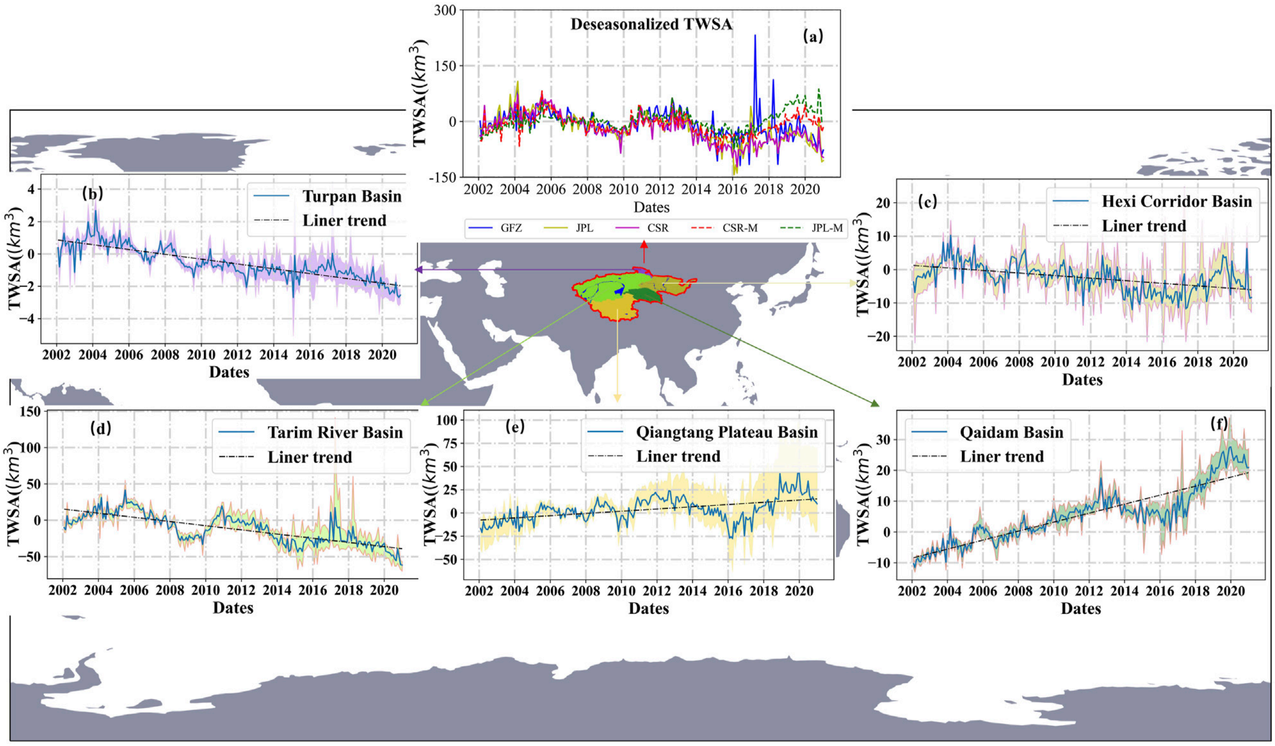

FIGURE 3
Total water storage anomaly (TWSA) trends and Gravity recovery and climate experiment (GRACE) product trend ranges in the Chinese inland basins (CIBs) and its sub-basins. **(A)** The comparison of deseasonalized TWSA in the CIBs; **(B–F)** the TWSA trend range in the Turpan Basin, Hexi Corridor Basin, Tarim Basin, Qiangtang Basin, and Qaidam Basin, respectively. The black dashed lines indicate their linear trends.

southeast edges of the CIBs, while it decreased in the inner regions of the basin.

Precipitation significantly increased in the northern part of the HCB, the eastern edge of the southwestern margin of the QDB, the central-eastern part of the QPB, the central-western and northwestern marginal regions of the TRB, and the southwestern part of the TPB; however, it significantly decreased in the central-eastern part of the HCB, the central and southwestern marginal regions of the QPB, the central and southeastern part of TRB, and the eastern marginal regions of the TPB. Furthermore, it did not change significantly in the remaining regions.

Overall, the annual precipitation significantly increased in the CIBs (11.1 mm/10a), as well as all sub-basins except the QPB (4.5 mm/10a). The increase was the highest in the HCB (9.7 mm/10a). The TRB, QDB, HCB, QPB, and TPB contributed approximately 40%, 30%, 20%, 8%, and 2% precipitation, respectively.

Monthly AETs were simulated using precipitation data and average monthly series of five GRACE products according to the methodology of the hydrological budget (Figure 7). Overall, the annual AET significantly increased in the CIBs (20.3 mm/10a), as well as all sub-basins except the QPB (3.6 mm/10a) and QDB (21 mm/10a). The increase was the highest in the HCB (29.5 mm/10a). Since the increase in precipitation is less than that in AET, combined with the principle of water balance, precipitation in the CIBs was insufficient to meet the demand from the AET during this period.

4.3 The main attribution of the terrestrial water storage anomalies and actual evapotranspiration trends in the Chinese inland basins

Figure 8 shows the TWSA, precipitation and AET M–K significance and trends for the whole CIBs and each closed basin. This study reports that the precipitation and TWSA of the whole CIBs significantly increased and decreased, respectively (9 and 11 mm/10a, respectively). Based on the water balance of the closed basin, quantifying the magnitude of the changes in precipitation and TWSA showed that the decreased TWSA of the whole CIBs was mainly due to AET increase. The main factors affecting changes in AET changes were analyzed based on the attribution identification method described in Section 3.3.3.

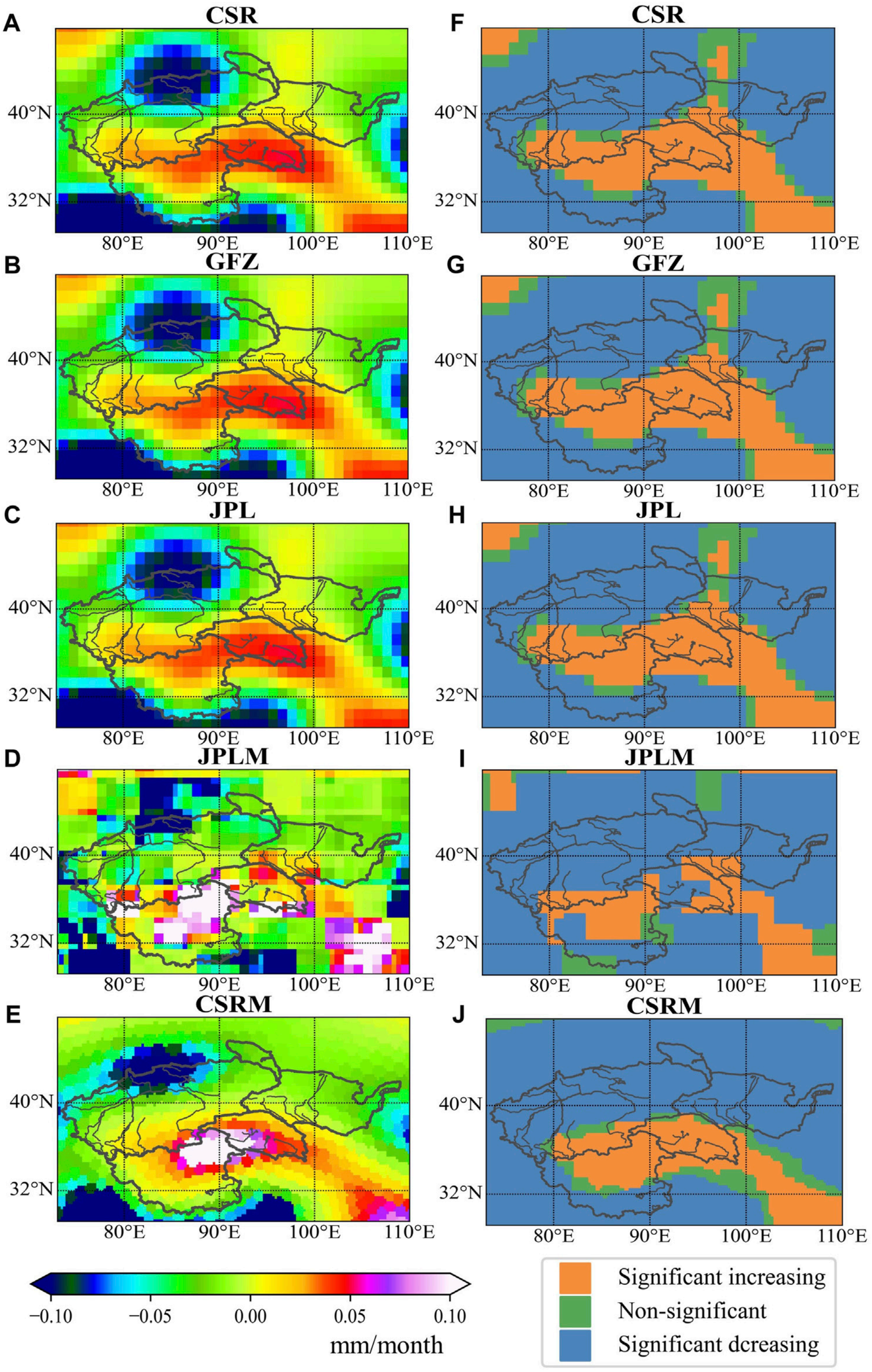

FIGURE 4
The spatial pattern of total water storage anomaly (TWSA) trends (left) and significant (right) derived from different Gravity recovery and climate experiment (GRACE) solution: TWSA trends and significant are calculated using M–K. **(A,F)** indicate the GRACE resolution of RL06 spherical harmonics from the Center for Space Research at the University of Texas (CSR). **(B,G)** indicate the GRACE resolution of RL06 spherical harmonics from the Geo-Forschungs-Zentrum in Potsdam (GFZ). **(C,H)** indicate the GRACE resolution of RL06 spherical harmonics from the Jet Propulsion Laboratory (JPL). **(D,I)** indicate the GRACE resolution of mass concentration blocks (mascons) from the JPL. **(E,J)** indicate the GRACE resolution of mass concentration blocks (mascons) from the CSR.

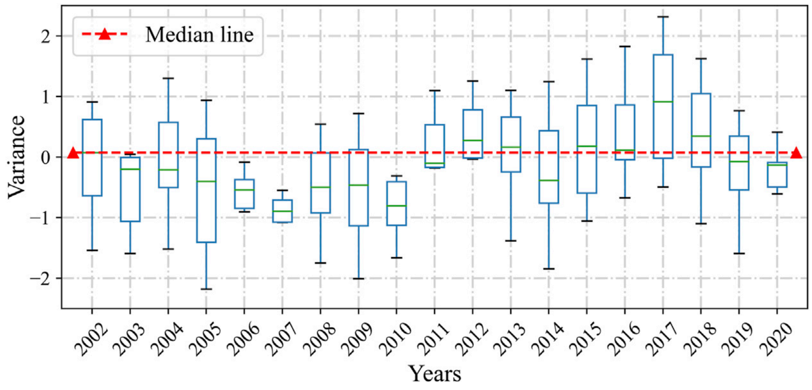

FIGURE 5
Trends of Gravity recovery and climate experiment (GRACE) total water storage anomaly (TWSA) data by time variance and median. Red line indicated median of initial month data.

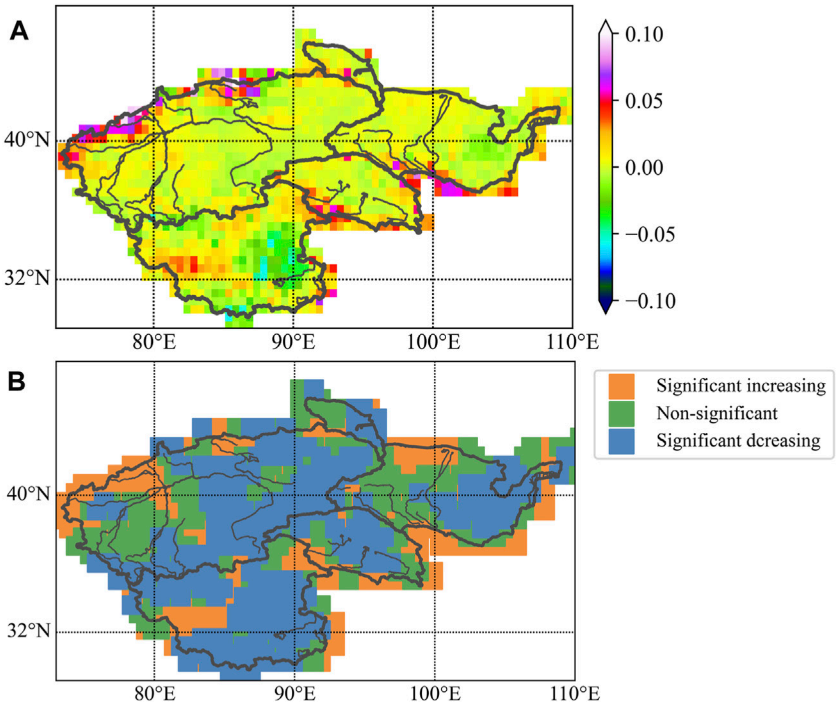

FIGURE 6
The spatial pattern of **(A)** M–K trends and precipitation significance **(B)** in the Chinese inland basins (CIBs).

Additionally, the contribution of precipitation and other water sources to changes in the AET were semi-quantified by comparing the trend magnitudes of AET and precipitation. The increase in precipitation in the CIB accounted for 40% AET, indicating that the increasing consumption of other water sources was the dominant factor for increasing the AET in the CIB. This increased consumption, which might be mainly due to irrigation diversion from ground water and glacial melt runoff, explained 60% AET increase. This increased consumption may be due to a combination of mechanisms including increased evaporation rates due to rising temperatures and increased irrigation diversion from ground water and glacial melt runoff, thus increasing AET. Interestingly, 60% AET increase was due to the increased precipitation and the

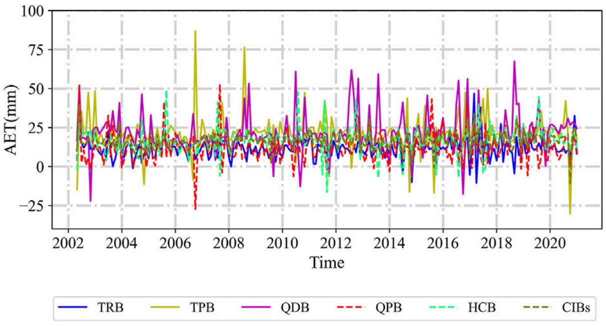

FIGURE 7
The deseasonalized series of actual evapotranspiration (AET) in the Chinese inland basins (CIBs) and each sub-basin. The results were calculated based on water balance combined with five Gravity recovery and climate experiment (GRACE) solutions and precipitation data. TRB, TPB, QDB, QPB, and HCB indicates Tarim Basin, Turpan Basin, Qaidam Basin, Qiangtang Basin, and Hexi Corridor Basin, respectively.

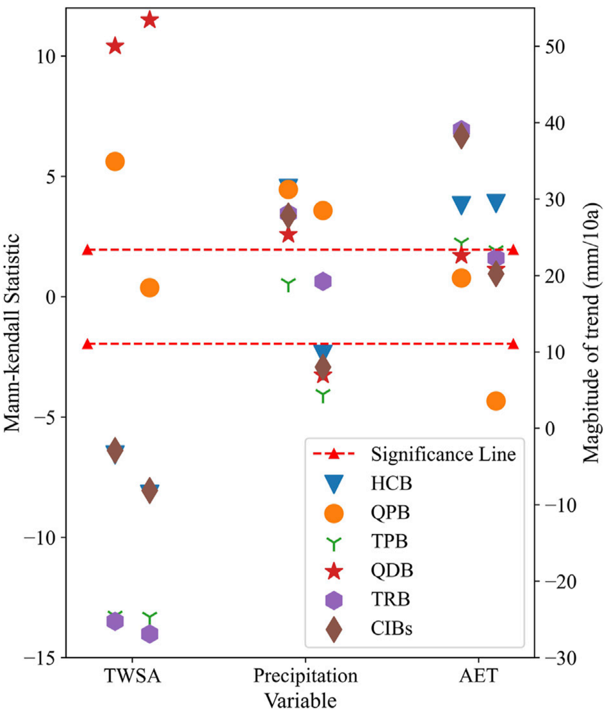

FIGURE 8
Significance (left) and trend (right) of total water storage anomaly (TWSA), precipitation and actual evapotranspiration (AET) M−K in the Chinese inland basins (CIBs) and each closed basin. The left side indicates the significance statistic obtained after M−K calculation, the right side indicates the magnitude of change obtained from M−K calculation. The red dashed line indicates the cut-off line of significance. TRB, TPB, QDB, QPB, and HCB indicates Tarim Basin, Turpan Basin, Qaidam Basin, Qiangtang Basin, and Hexi Corridor Basin, respectively.

rest might be influenced by the glacial melting and river irrigation in the basin.

The changes in AET primarily influenced the changes in TWSA in each closed basin, similar to that in the CIBs. Among them, the increased AET of the HCB, TRB, and TPB primarily decreases the TWSA in the basin. Precipitation remains the main reason for the increased AET in HCB (>60%). In the TRB and TPB, the proportion of precipitation increase contributing to AET increase was <20%. This indicates that increased precipitation had made a relatively small contribution to the AET increase. The glacier melting and irrigation diversion caused by enhanced evaporation rates played a dominant role in AET increase. In the QPB and QDB, AET reduction in the basins increased TWSA. More than 50% AET decrease in the QDB is caused by precipitation. This indicates that increased precipitation had made a relatively small contribution to the AET decrease. The decrease in the consumption of other water sources caused by weakened evaporation rates played a dominant role in AET decrease.

5 Discussion

5.1 Comparison with previous study results

Although few studies have focused on the whole CIBs, some studies have focused on the attribution of TWSA changes in the CIB sub-basins. These results were verified with those of this study.

The significantly increased TWSA in the QDB and QPB was verified with the results of previous studies (Bibi et al., 2019; Liu et al., 2019; Meng et al., 2019). However, the main reasons attributed to this trend differed from those identified in previous studies. Previous studies believed that the TWSA increased in QDB primarily due to the increase of precipitation, while the TWSA of QPB was dominated by decreased AET. In this study, TWSA increase in the QDB is mainly due to the decrease of AET, while the increase of TWS in the QPB is mainly due to the increase of AET. One of the reasons for the different results is that previous studies analyzed relatively short TWSA time series (5–8 years), while this study focused on the whole 19-year time series analysis.

The significantly decreased TWSA in the TRB has also been confirmed by previous studies (Wang et al., 2021; Zuo et al., 2021). Increased AET is also the main factor influencing changes in the TWSA. However, previous studies have considered that temperature is the main reason for the increase in AET, while the increase of AET in this study was mainly due to the increase of water consumption caused by human activities and glacier retreat. Human activities were considered in this study as an factor affecting AET.

5.2 Data uncertainty analyses

Due to the lack of actual measurement data for validation, determining the product more suitable for the CIBs is difficult; however, the correlation coefficient between the time series of the five data sets in the first 15 years is >0.87 (Figure 3A). Moreover, the five data sets are consistent according to the spatial distribution map (Figure 4). Interestingly, differences between the solutions were detected when processing the five GRACE solutions (Figure 4). There was large data fluctuation in different basins around 2017 (Figure 3). The following attempts were made to explain this phenomenon.

For the differences of the five solutions, the overall performance of the five solutions in the five basins was first analyzed, and the variance of the tertiary solutions processed by the first three institutions was statistically significantly smaller than that of the last two mascons. Considering that the spherical harmonic coefficient method removes some real geophysical signals when smoothing through the empirical smoothing function while processing the noise of the GRACE data signal, the entire amplitude and variance of the data will be smaller than that of the mascons method, which applies *a priori* knowledge (Zhang et al., 2019). This can be corresponded to the results in Figure 4, where the results of the first three products solved by the spherical harmonic coefficient method are similar. The range of trend of the last two products is significantly larger than that of the first three. Therefore, using these two GRACE solutions to integrate the analysis will not only increase the overall information, but also cause errors in the final analysis results.

The GRACE satellite started functioning in April 2002 (Figure 5). The median value of that year was used as the starting reference and data stability is increasing over time. From 2012 to 2016, the median data fluctuated in the initial median line, probably because the GRACE satellite data was more volatile than those of the previous years as the satellite service life increased. The satellite data quality fluctuation increased and reached the current maximum in 2017 because the satellite terminated the data in June 2017. Then, the GRACE-FO satellite took over the GRACE satellite mission and continued to transmit data from June 2018. The median data value in 2018 was slightly higher than the initial median value, but the median data value immediately dropped below the initial median value in the following 2 years, indicating that the quality of GRACE-FO satellite data has been improving except for the first year.

Although the average sequence of five TWSA was used in this study to reduce the uncertainty caused by a single solution, studies on water resources research should consider a depth study of the inversion of TWSA of GRACE. When simulating AET monthly series, ΔS indicates the change of monthly water storage, that is, the difference of water storage between the end and beginning of the month. However, the TWSA of GRACE is the intra-month water storage. In this study, the difference between the TWSA of the previous month and the next month is used to represent the monthly water storage variability within the basin, which increases the uncertainty of the experiment to some extent.

6 Conclusion

Trends of annual and monthly precipitation, TWSA, and AET were detected at each basin by the M–K test. The main attribution of TWSA variability for the CIBs and each of its closed basins was identified.

Annual precipitation in the CIBs increased from 2002 to 2020. It generally increased at the eastern, northwestern and southeastern regions of the CIBs, while decreasing in the central regions of the basin. It also increased in each sub-basin. The increase was significant in all sub-basins except the QPB. The magnitude of increase was highest in the HCB. The TRB received the most precipitation with a weight of 40%, while the TPB received the least.

The TWSA and AET showed significantly decreased and increased in the CIBs and most of its sub-basins, respectively. TWSA increased in the QPB and QDB. TWSA decreased in the CIBs primarily due to the increased AET. Precipitation caused more than 50% increased AET. Similar to that in the CIBs, AET change was the main factor driving TWSA change in each closed basin. In particular, the increased AET in the HCB, TRB, and TPB was the main factor for the decreased TWSA in these basins. The increased AET in the HCB was mainly due to precipitation. However, melting glaciers and irrigation diversion primarily caused the increased AET in the TRB and TPB. Interestingly, AET reduction in the QPB and QDB decreased TWSA. More than 50% AET reduction in the QDB was caused by precipitation, while more than 70% AET reduction in the QPB was caused by the decreased consumption of other water resources.

Data availability statement

Publicly available datasets were analyzed in this study. This data can be found here: https://grace.jpl.nasa.gov/data/get-data/monthly-mass-grids-land/, http://data.cma.cn/.

Author contributions

XL conceived and designed the concept, reviewed the literature, collected data, and wrote the manuscript. ZL conceived the concept, edited the article, and supervised the study. HW helped to receive technical support. All authors have read and agreed to the published version of the manuscript.

Funding

This study was supported and funded by the Second Tibetan Plateau Scientific Expedition and Research Program (2019QZKK1006), the National Natural Science Foundation of

China (42171029), and the Strategic Priority Research Program of the Chinese Academy of Sciences (XDA23090302).

Acknowledgments

We thank NASA for their contribution to GRACE data production and the China Meteorological Administration for their support of China's meteorological data. The GRACE data can be obtained from https://grace.jpl.nasa.gov/data/get-data/monthly-mass-grids-land/. The meteorological data can be obtained from http://data.cma.cn/.We appreciate reviewers and editors for their critical and constructive comments to improve the paper quality.

Conflict of interest

The authors declare that the research was conducted in the absence of any commercial or financial relationships that could be construed as a potential conflict of interest.

Publisher's note

References

Andrew, R., Guan, H., and Batelaan, O. (2017). Estimation of GRACE water storage components by temporal decomposition. *J. Hydrol. X.* 552, 341–350. doi:10.1016/j.jhydrol.2017.06.016

Bibi, S., Wang, L., Li, X., Zhang, X., and Chen, D. (2019). Response of groundwater storage and recharge in the Qaidam Basin (Tibetan Plateau) to climate variations from 2002 to 2016. *JGR. Atmos.* 124, 9918–9934. doi:10.1029/2019JD030411

Bierkens, M. F. P. (2015). Global hydrology 2015: state, trends, and directions. *Water Resour. Res.* 51, 4923–4947. doi:10.1002/2015WR017173

Bueh, C., Li, Y., Lin, D., and Lian, Y. (2016). Interannual variability of summer rainfall over the northern part of china and the related circulation features. *J. Meteorol. Res.* 30, 615–630. doi:10.1007/s13351-016-5111-5

Cao, Y., Nan, Z., Cheng, G., and Zhang, L. (2018). Hydrological variability in the arid region of northwest china from 2002 to 2013. *Adv. Meteorology* 2018, 1–13. doi:10.1155/2018/1502472

Chen, L., Hu, Z., Du, X., Khan, M. Y. A., Li, X., and Wen, J. (2022). An optimality based spatial explicit ecohydrological model at watershed scale: model description and test in a semiarid grassland ecosystem. *Front. Environ. Sci.* 10, 798336. doi:10.3389/fenvs.2022.798336

Cleveland, R. B., and Cleveland, W. S. (1990). Stl: a seasonal-trend decomposition procedure based on loess. *J. Official Statistics* 6, 3

Deng, H., and Chen, Y. (2017). Influences of recent climate change and human activities on water storage variations in Central Asia. *J. Hydrol. X.* 544, 46–57. doi:10.1016/j.jhydrol.2016.11.006

Dong, Z., Hu, H., Wei, Z., Liu, Y., Xu, H., Yan, H., et al. (2022). Estimating the actual evapotranspiration of different vegetation types based on root distribution functions. *Front. Earth Sci.* 10, 893388. doi:10.3389/feart.2022.893388

Famiglietti, J. S., Lo, M., Ho, S. L., Bethune, J., Anderson, K. J., Syed, T. H., et al. (2011). Satellites measure recent rates of groundwater depletion in california's central Valley. *Geophys. Res. Lett.* 38, 2010GL046442. doi:10.1029/2010GL046442

Feng, W., Zhong, M., Lemoine, J.-M., Biancale, R., Hsu, H.-T., and Xia, J. (2013). Evaluation of groundwater depletion in North China using the gravity recovery and climate experiment (GRACE) data and ground-based measurements. *Water Resour. Res.* 49, 2110–2118. doi:10.1002/wrcr.20192

Getirana, A. (2016). Extreme water deficit in Brazil detected from space. *J. Hydrometeorol.* 17, 591–599. doi:10.1175/JHM-D-15-0096.1

Güntner, A. (2008). Improvement of global hydrological models using GRACE data. *Surv. Geophys.* 29, 375–397. doi:10.1007/s10712-008-9038-y

Güntner, A., Stuck, J., Werth, S., Döll, P., Verzano, K., and Merz, B. (2007). A global analysis of temporal and spatial variations in continental water storage. *Water Resour. Res.* 43, 5207. doi:10.1029/2006WR005247

He, X., Wada, Y., Wanders, N., and Sheffield, J. (2017). Intensification of hydrological drought in california by human water management. *Geophys. Res. Lett.* 44, 1777–1785. doi:10.1002/2016GL071665

Hirsch, R. M., Slack, J. R., and Smith, R. A. (1982). Techniques of trend analysis for monthly water quality data. *Water Resour. Res.* 18, 107–121. doi:10.1029/WR018i001p00107

Hu, H., Chen, L., Liu, H., Ali Khan, M., Tie, Q., Zhang, X., et al. (2018). Comparison of the vegetation effect on ET partitioning based on eddy covariance method at five different sites of northern china. *Remote Sens.* 10, 1755. doi:10.3390/rs10111755

Huang, J., Yu, H., Guan, X., Wang, G., and Guo, R. (2016). Accelerated dryland expansion under climate change. *Nat. Clim. Chang.* 6, 166–171. doi:10.1038/nclimate2837

Koster, R. D., Dirmeyer, P. A., Guo, Z., Bonan, G., Chan, E., Cox, P., et al. (2004). Regions of strong coupling between soil moisture and precipitation. *Science* 305, 1138–1140. doi:10.1126/science.1100217

Liu, W., Wang, L., Zhou, J., Li, Y., Sun, F., Fu, G., et al. (2016). A worldwide evaluation of basin-scale evapotranspiration estimates against the water balance method. *J. Hydrol. X.* 538, 82–95. doi:10.1016/j.jhydrol.2016.04.006

Liu, Z. (2022). Causes of changes in actual evapotranspiration and terrestrial water storage over the eurasian inland basins. *Hydrol. Process.* 36, e14482. doi:10.1002/hyp.14482

Liu, Z., Yao, Z., Huang, H., Wu, S., and Liu, G. (2014). Land use and climate changes and their impacts on runoff in the yarlung zangbo river basin, china. *Land Degrad. Dev.* 25, 203–215. doi:10.1002/ldr.1159

Liu, Z., Yao, Z., and Wang, R. (2019). Automatic identification of the lake area at Qinghai–Tibetan Plateau using remote sensing images. *Quat. Int.* 503, 136–145. doi:10.1016/j.quaint.2018.10.023

Long, D., Longuevergne, L., and Scanlon, B. R. (2014). Uncertainty in evapotranspiration from land surface modeling, remote sensing, and GRACE satellites. *Water Resour. Res.* 50, 1131–1151. doi:10.1002/2013WR014581

Long, D., Scanlon, B. R., Longuevergne, L., Sun, A. Y., Fernando, D. N., and Save, H. (2013). GRACE satellite monitoring of large depletion in water storage in response to the 2011 drought in Texas. *Geophys. Res. Lett.* 40, 3395–3401. doi:10.1002/grl.50655

Meng, F., Su, F., Li, Y., and Tong, K. (2019). Changes in terrestrial water storage during 2003–2014 and possible causes in Tibetan Plateau. *J. Geophys. Res. Atmos.* 124, 2909–2931. doi:10.1029/2018JD029552

Ramillien, G., Frappart, F., and Seoane, L. (2014). Application of the regional water mass variations from GRACE satellite gravimetry to large-scale water management in Africa. *Remote Sens. (Basel).* 6, 7379–7405. doi:10.3390/rs6087379

Reager, J. T., Gardner, A. S., Famiglietti, J. S., Wiese, D. N., Eicker, A., Thonicke, K., et al. (2016). Enhanced seasonal CO_2 exchange caused by amplified plant productivity in northern ecosystems. *Science* 6, 696–699. doi:10.1126/science.aac4971

Rodell, M., Famiglietti, J. S., Wiese, D. N., Reager, J. T., Beaudoing, H. K., Landerer, F. W., et al. (2018). Emerging trends in global freshwater availability. *Nature* 557, 651–659. doi:10.1038/s41586-018-0123-1

Scanlon, B. R., Faunt, C. C., Longuevergne, L., Reedy, R. C., Alley, W. M., McGuire, V. L., et al. (2012). Groundwater depletion and sustainability of irrigation in the US high Plains and Central Valley. *Proc. Natl. Acad. Sci. U. S. A.* 109, 9320–9325. doi:10.1073/pnas.1200311109

Scanlon, B. R., Zhang, Z., Save, H., Sun, A. Y., Müller Schmied, H., van Beek, L. P. H., et al. (2018). Global models underestimate large decadal declining and rising water storage trends relative to GRACE satellite data. *Proc. Natl. Acad. Sci. U. S. A.* 115, E1080–E1089. doi:10.1073/pnas.1704665115

Seneviratne, S. I., Corti, T., Davin, E. L., Hirschi, M., Jaeger, E. B., Lehner, I., et al. (2010). Investigating soil moisture–climate interactions in a changing climate: a review. *Earth. Sci. Rev.* 99, 125–161. doi:10.1016/j.earscirev.2010.02.004

Voss, K. A., Famiglietti, J. S., Lo, M., de Linage, C., Rodell, M., and Swenson, S. C. (2013). Groundwater depletion in the middle east from GRACE with implications for transboundary water management in the Tigris-Euphrates-Western Iran region. *Water Resour. Res.* 49, 904–914. doi:10.1002/wrcr.20078

Wahr, J., Swenson, S., Zlotnicki, V., and Velicogna, I. (2004). Time-variable gravity from GRACE: first results. *Geophys. Res. Lett.* 31 (11). doi:10.1029/2004GL019779

Wang, F., Chen, Y., Li, Z., Fang, G., Li, Y., Wang, X., et al. (2021). Developing a long short-term memory (LSTM)-based model for reconstructing terrestrial water storage variations from 1982 to 2016 in the Tarim River Basin, Northwest China. *Remote Sens. (Basel).* 13, 889. doi:10.3390/rs13050889

Wang, J., Song, C., Reager, J. T., Yao, F., Famiglietti, J. S., Sheng, Y., et al. (2018). Recent global decline in endorheic basin water storages. *Nat. Geosci.* 11, 926–932. doi:10.1038/s41561-018-0265-7

Wang, T.-Y., Wang, P., Zhang, Y.-C., Yu, J.-J., Du, C.-Y., and Fang, Y.-H. (2019). Contrasting groundwater depletion patterns induced by anthropogenic and climate-driven factors on Alxa Plateau, northwestern China. *J. Hydrol. X.* 576, 262–272. doi:10.1016/j.jhydrol.2019.06.057

Wang, X., Chen, Y., Li, Z., Fang, G., Wang, F., and Liu, H. (2020). The impact of climate change and human activities on the aral sea basin over the past 50 years. *Atmos. Res.* 245, 105125. doi:10.1016/j.atmosres.2020.105125

Watkins, M. M., Wiese, D. N., Yuan, D.-N., Boening, C., and Landerer, F. W. (2015). Improved methods for observing Earth's time variable mass distribution with GRACE using spherical cap mascons: improved gravity observations from GRACE. *J. Geophys. Res. Solid Earth* 120, 2648–2671. doi:10.1002/2014JB011547

Wiese, D. N., Landerer, F. W., and Watkins, M. M. (2016). Quantifying and reducing leakage errors in the JPL RL05M GRACE mascon solution. *Water Resour. Res.* 46, 7490–7502. doi:10.1002/2016WR019344

Xiang, L., Wang, H., Steffen, H., Wu, P., Jia, L., Jiang, L., et al. (2016). Groundwater storage changes in the Tibetan Plateau and adjacent areas revealed from GRACE satellite gravity data. *Earth Planet. Sci. Lett.* 449, 228–239. doi:10.1016/j.epsl.2016.06.002

Yeh, P. J.-F., Swenson, S. C., Famiglietti, J. S., and Rodell, M. (2006). Remote sensing of groundwater storage changes in Illinois using the Gravity Recovery and Climate Experiment (GRACE): rapid communication. *Water Resour. Res.* 42. doi:10.1029/2006WR005374

Zhang, C., Tang, Q., and Chen, D. (2017). Recent changes in the moisture source of precipitation over the Tibetan Plateau. *J. Clim.* 30, 1807–1819. doi:10.1175/JCLI-D-15-0842.1

Zhang, L., Yi, S., Wang, Q., Chang, L., Tang, H., and Sun, W. (2019). Evaluation of GRACE mascon solutions for small spatial scales and localized mass sources. *Geophys. J. Int.* 218, 1307–1321. doi:10.1093/gji/ggz198

Zhu, X., Zhang, M., Wang, S., Qiang, F., Zeng, T., Ren, Z., et al. (2015). Comparison of monthly precipitation derived from high-resolution gridded datasets in arid Xinjiang, central Asia. *Quat. Int.* 358, 160–170. doi:10.1016/j.quaint.2014.12.027

Zuo, J., Xu, J., Chen, Y., and Li, W. (2021). Downscaling simulation of groundwater storage in the tarim river basin in northwest China based on GRACE data. *Phys. Chem. Earth Parts A/B/C* 123, 103042. doi:10.1016/j.pce.2021.103042

frontiers | Frontiers in Environmental Science

TYPE Original Research
PUBLISHED 28 September 2022
DOI 10.3389/fenvs.2022.1006399

Trend of snow cover under the influence of climate change using Google Earth Engine platform: A case study of Astore (Western Himalayas) and Shigar (Karakoram region)

Muhammad Farhan Ul Moazzam[1], Ghani Rahman[2], Byung Gul Lee[1] and Nadhir Al Ansari[3]*

[1]Department of Civil Engineering, College of Ocean Science, Jeju National University, Jeju, South Korea, [2]Department of Geography, University of Gujrat, Gujrat, Pakistan, [3]Department of Civil, Environmental and Natural Resources Engineering, Lulea University of Technology, Lulea, Sweden

OPEN ACCESS

EDITED BY
Xiuping Li,
Institute of Tibetan Plateau Research,
Chinese Academy of Sciences (CAS),
China

REVIEWED BY
Zhongfan Zhu,
Beijing Normal University, China
Muhammad Shahid,
National University of Sciences and
Technology (NUST), Pakistan

*CORRESPONDENCE
Nadhir Al Ansari,
nadhir.alansari@ltu.se

SPECIALTY SECTION
This article was submitted to
Environmental Informatics and
Remote Sensing,
a section of the journal
Frontiers in Environmental Science

RECEIVED 29 July 2022
ACCEPTED 08 September 2022
PUBLISHED 28 September 2022

CITATION
Moazzam MFU, Rahman G, Lee BG and Ansari NA (2022), Trend of snow cover under the influence of climate change using Google Earth Engine platform: A case study of Astore (Western Himalayas) and Shigar (Karakoram region).
Front. Environ. Sci. 10:1006399.
doi: 10.3389/fenvs.2022.1006399

Freshwater resources present in the Upper Indus Basin (UIB) supply water to Pakistan's irrigation. Half of the annual water discharge in the UIB is contributed from the glacier and snow-fed basins in the Hindu Kush, Karakoram, and Himalaya (HKH) region, and it is currently under the threat of climate change. Therefore, it is very necessary to study and monitor the spatiotemporal changes in the snow cover area (SCA) and its response to climate variables to efficiently manage water reservoirs. Thus, keeping this problem in mind, we conducted this study using the Google Earth Engine Application Programming Interface (GEE API) for Astore and Shigar. We used mean annual Landsat data between 1991 and 2021 to derive the SCA using the normalized difference snow index (NDSI). ASTER GDEM data was used to extract the elevation and analyze the distribution of SCA on different elevation zones. Eventually, we used the climate research unit (CRU) data (rainfall and temperature) to analyze them with SCA. The results revealed that SCA in Astore and Shigar has an increasing trend with a rate of 11.16 km^2/year and 4.27 km^2/year, respectively. Mean annual precipitation and temperature also confirmed the increasing trend of SCA because mean annual precipitation is increasing and temperature is decreasing in both regions. SCA and elevation analysis revealed that SCA is decreasing on foothills while increasing at the valley top. This is because temperature is increasing and precipitation is decreasing from zone 1 to zone 3 and vice versa for zone 4. It is found that Astore and Shigar in UIB have an increasing trend of SCA and are not affected by global warming. Therefore, it is necessary to conduct studies on large scale to efficiently evaluate the impact of climate change on SCA.

KEYWORDS

GEE API, Landsat, NDSI, CRU, topographic parameters

Introduction

Hindu Kush, Karakoram, and Himalaya (HKH) regions are the longest mountainous regions and are spread over various countries including Afghanistan, Bhutan, China, India, Myanmar, Nepal, and Pakistan. The HKH region stores a huge amount of freshwater resources outside the polar region; therefore, it is also known as the Third Pole or Water Tower of Asia (Kehrwald et al., 2008). Many largest rivers in these countries originate from the HKH region and are fed through snow and glacier meltwater (Banerjee et al., 2021). Therefore, this region supports the livelihood of people living downstream through water supply (Sharma et al., 2013, Sahu and Gupta, 2020) and fulfills their essential needs in terms of agriculture production, hydropower generation, drinking, and industrialization (Jain et al., 2009; Hori et al., 2017). However, due to climate change, glaciers and snow-covered areas are under serious threat and consistently change with time (Wester et al., 2019). Pakistan is an agro-economic country and largely dependent on water supply from the Indus River System (IRS) (SIHP, 1990), and the inflow of water in the Indus River is mostly contributed by glaciers and snow meltwater (Bookhagen and Burbank, 2010; Immerzeel et al., 2012). Snow-covered mountains are not directly influenced by the human population, but they are vulnerable to climate change, and subsequently, the rising trend of temperature, decreasing trend of snow cover duration, and changing pattern of snowfall result in early melting of snow cover and influence river runoff in the summer season (Krishnan et al., 2019; Notarnicola, 2020; Yi et al., 2021). Eventually, it will result in scarcity of water, landslide, drought, floods, and glacial lake outburst flood (GLOF) (Tahir et al., 2019). Snow cover research on this region usually revealed a decreasing trend of SCA; however, Tahir et al. (2016), Shafiq et al. (2019), and Azizi and Akhtar, 2021) reported an increasing trend of SCA due to an increasing trend of winter precipitation and decreasing trend of summer temperature. Another study also projected an increasing trend of precipitation in the HKH region during 1901–2099, while temperature indices show an inter-annual decreasing trend (Panday et al., 2015). Moazzam et al. (2022) recently studied the precipitation projection of Gilgit-Baltistan for the 21st century and revealed a significant increasing trend in the midcentury (2021–2060) under representative concentration pathway (RCP) 4.5 and RCP 8.5. Negi and Kanda, (2020) also reported an increasing trend of SCA in the Northwest Himalayan region due to the slowdown warming trend. Therefore, these climate variabilities imply differences in SCA. Hence, it is necessary to monitor the changing phenomena of snow cover. However, a large area is at risk in the HKH region, and knowledge of spatial variability of SCA is limited on a large scale.

In the past, it was very difficult to map the SCA because of high altitude and tough terrains (Aniya et al., 1996; Jacobsen and Theakstone, 1997), but, since the early 1960s, remote sensing sensors have been designed to easily map the SCA with various techniques and methodologies (Abid and Zia, 2019). Now researchers are using various indices and methods for SCA mapping, i.e., normalized difference snow index (NDSI), normalized difference snow thermal index (NDSTI), normalized difference water index (NDWI), normalized difference principal component index (NDPSCI), normalized difference debris index (NDDI), machine learning algorithms [support vector machine (SVM), artificial neural network (ANN), and random forest (RF)], and image classification techniques. In this study, we used NDSI, which is one of the widely used indices globally because of its satisfactory results in mountain shadows.

It is a very challenging task to study the large snow-covered area and manually filter the images with less amount of clouds, download, make composite, and stitch the image which consumes immense time. Therefore, we used a cloud computing (Google Earth Engine) platform, which makes it easy to perform all these tasks using JavaScript or Python APIs. This study aimed to investigate the snow cover area of Astore and Shigar using the normalized difference snow index (NDSI) between 1991 and 2021. The snow cover area was correlated with climate variables (temperature and precipitation) and topographic parameters (elevation). The significance of this study was to understand the SCA relationship with the temperature and rainfall which is useful for mountainous and low-lying glacier-dependent communities.

We chose Astore and Shigar in this study because previous studies have been conducted on the comparison of Astore with Hunza and Gilgit (Tahir et al., 2016); hence, there is a need for a comparative study between other sub-basins of UIB. Therefore, in this study, we evaluated Astore (West Himalayas; snow-fed) and Shigar (Karakoram; glacier-fed) based on meteorological and topographical indicators. Astore and Shigar have distinct geographical locations due to some basic features, i.e., both districts are influenced by the same climate (westerlies) but in a different way. Astore is largely dependent on winter rainfall at low elevation, while Shigar depends on westerly circulated solid precipitation. Shigar is located in the rain shadow of the Western Himalayan region; therefore, it receives a very small amount of monsoon precipitation (Ali et al., 2009), while Astore is located on a north-facing slope in lower latitude and mid-altitude. Therefore, we conducted this study based on these contrasting features.

Study area

The Upper Indus Basin is located between 72° 03′–77 ° 44′E and 34° 16′–37 ° 06′N. It splits the Karakoram from the Greater Himalayan region (Bishop et al., 2010). The Indus River starts from the Tibetan Plateau and flows toward the northern region of Pakistan and supplies inflow to the Tarbela Dam (Farhan et al.,

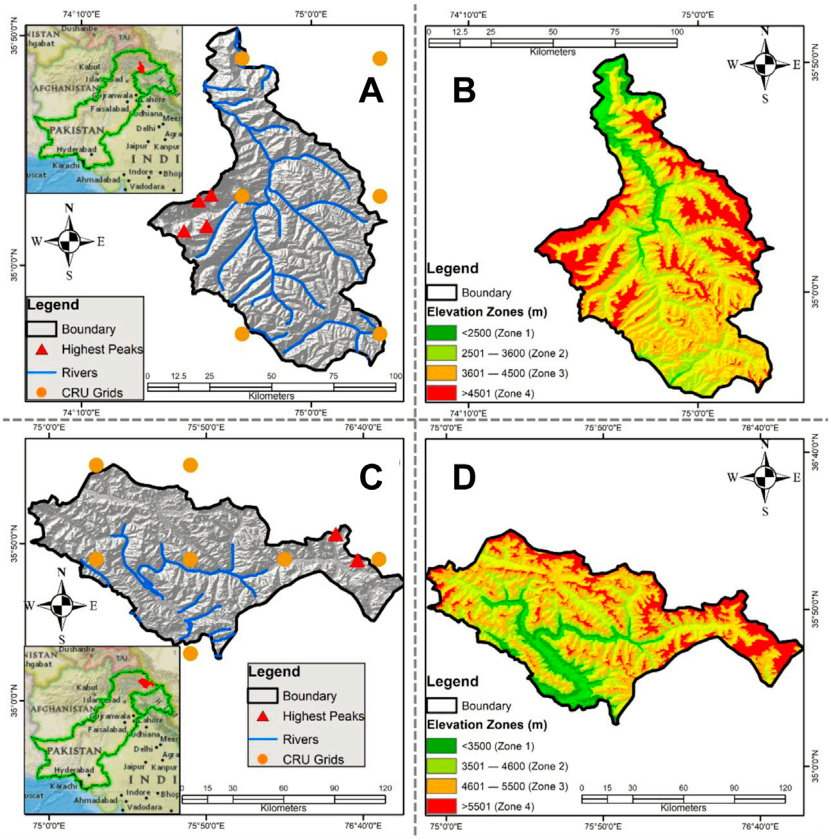

FIGURE 1
(A) Location map of Astore, **(B)** elevation zones of Astore, **(C)** location map of Shigar, and **(D)** elevation zones of Shigar.

2015; Farhan et al., 2020). For this study we have chosen two districts, namely, Astore and Shigar that lie in the Western Himalayas and Karakoram region, respectively.

Astore is located in the extreme Western Himalayan region of Northern Pakistan (Figure 1A). Astore covers an area of 5,233 km^2 with 4.8% area covered with glaciers from Randolph Glacier Inventory version 6.0 (RGI, 2017). The elevation of Astore ranges from the valley floor to the highest peaks, i.e., Nanga Parbat (1,150–8,056 m) (Figure 1B). The mean annual temperature of Astore ranges between −2.9 and 9.9, while precipitation ranges between 500–870 mm from higher to lower altitude met stations (Farhan et al., 2015). Almost 75% of the precipitation falls in winter and spring seasons due to westerly circulation, while 25% falls in summer and autumn seasons from monsoon and local jet streams (Farhan et al., 2020). The Astore River discharge is influenced by winter rainfall together with solid precipitation forced by westerlies (Tahir et al., 2015).

Shigar is located in the Karakoram region of Northern Pakistan (Figure 1C). Shigar covers an area of 8,913. The elevation of Shigar ranges between 1,967 and 8,611 m from valley to high mountains (Figure 1D). According to

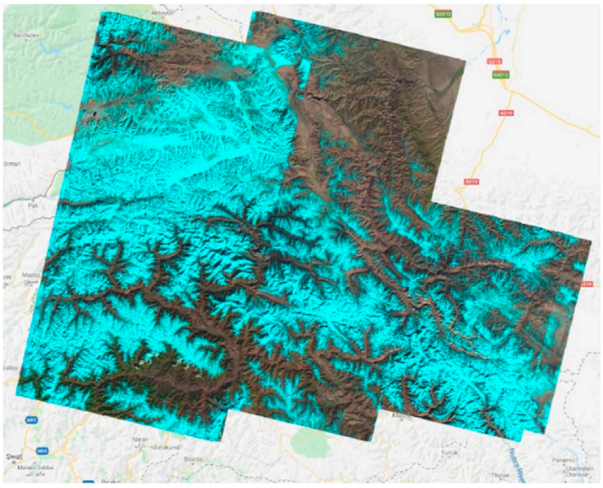

FIGURE 2
Mosaiced image with 10 scenes in Google Earth Engine (GEE) with false color composite and less than 10% cloud cover over the study area.

Koppen–Geiger's climate classification, Shigar falls under the cold desert region, and Shigar receives a little amount of precipitation. Large glacier mountains make a barrier for monsoon storms and enforce a modest impact of the storm on the region (Khan et al., 2014). A considerable amount of winter precipitation and temperature increased; however, the summer season revealed a cooling pattern for the Skardu region (Fowler and Archer, 2005; Hakeem et al., 2014). The Shigar River discharge is dependent on solid precipitation forced by westerlies that melts in the summer season and generates high discharge (ICIMOD, 2005; Fowler and Archer, 2006; Hakeem et al., 2014).

Materials and methods

In this section, we discussed the detailed methodology of the research. The methodological framework of this study was designed following the objective of the study. The study is based on a cloud computing platform (Google Earth Engine) because it provides easy access to global remote sensing datasets in a matter of no time using JavaScript or Python APIs (Gorelick et al., 2017). The Landsat images used in this study were atmospherically corrected, orthorectified, top of atmospheric reflectance (TOA) calibrated, and georeferenced scenes with an accuracy of 0.4 pixels (Zanter, 2016), available in the dataset catalog of GEE. We acquired the Landsat data using the Google Earth Engine (GEE) platform with JavaScript. A total of 5 paths/rows and around 10 scenes were required to cover the study area (Figure 2). We filtered the Landsat Tier-1 data by applying the multiple queries [e.g., date ("2021-01-01", "2021-12-31"), cloud cover (<10%), and region of interest (Astore, Shigar)] using the GEE image collection catalog.

The images selected in this study do not have a cloud above the region of interest (ROI). We selected the mean annual images to evaluate the yearly SCA variations. Next, we pulled the shapefile of Astore and Shigar which was used to mask the satellite images. Eventually, using the JavaScript code in GEE, we performed NDSI analysis on the masked images from 1991 to 2021, to extract the snow cover area for Astore and Shigar. To evaluate the spatiotemporal variation in SCA, snow and non-snow pixels were segregated using NDSI; usually, a threshold of 0.4 was used which is suitable for classifying the snow and non-snow pixels even in mountain-shadowed areas (Burns and Nolin, 2014). Then, we reclassified the satellite image into the snow and non-snow pixels, and eventually the year-wise SCA was calculated using snow pixels as follows:

$$NDSI = \frac{Green_{0.53} - SWIR_{1.65}}{Green_{0.53} + SWIR_{1.65}}.$$

We acquired the rainfall and temperature data from the climate research unit (CRU) for the study area with a spatial resolution of 0.5° for the period of 1991–2021. We correlated the SCA with rainfall and temperature on an annual basis to evaluate the impact of climate change on SCA.

We also utilized the Advanced Spaceborne Thermal Emission and Reflection Radiometer (ASTER) GDEM (30 m) to extract the topographic parameters, i.e., elevation in GEE. NDSI classified images, and the topographical parameter was exported for the region of interest (Astore and Shigar) for further analysis in ArcGIS software. In ArcGIS software, we reclassified the NDSI-classified images and calculated the area covered by snow for the study.

Afterward, the elevation was compared with NDSI-reclassified images of Astore and Shigar to calculate the area covered by snow on each elevation zone. Eventually, we prepared the tables, maps, and graphs. The detailed methodological framework of this study is presented in Figure 3.

Landsat data

In this study, Landsat data were acquired from 1991 to 2021 (mean annual images) for the study area because Landsat data are freely available (Patel et al., 2019). Landsat has the longest time series data with a multi-spectral and spatial resolution to evaluate the snow cover (Rastner et al., 2019). All Landsat satellites complete the circle around the Earth in 16 days; however, their characteristics vary (Table 1). In this study, we used Landsat 5 TM, Landsat 7 ETM, and Landsat 8 OLI data.

ASTER data

To evaluate the SCA with topographic parameters, it is necessary to use the digital elevation model (DEM) because elevation, slope, and aspect can be calculated from DEM. Therefore, we used ASTER GDEM v3 data to calculate the elevation and slope for further evaluation of SCA in this study. ASTER DEM has a 30-m spatial resolution. The version 3 data of ASTER has 1.8 million stereo pairs with improved horizontal and vertical accuracy in comparison with the previous version (Meetei et al., 2022). The elevation of Astore and Shigar was divided into four zones (Table 2) to calculate the elevation-wise SCA using the zonal statistics tool in the model builder of ArcGIS.

Climate research unit data (rainfall and temperature)

In this study, we also used climatic data (rainfall and temperature). Due to the scarcity of meteorological station data in this region, therefore, alternatively, we used the CRU v4.05 dataset which was released on 17th March 2021 (Harris et al., 2021) because the CRU dataset achieved better accuracy in

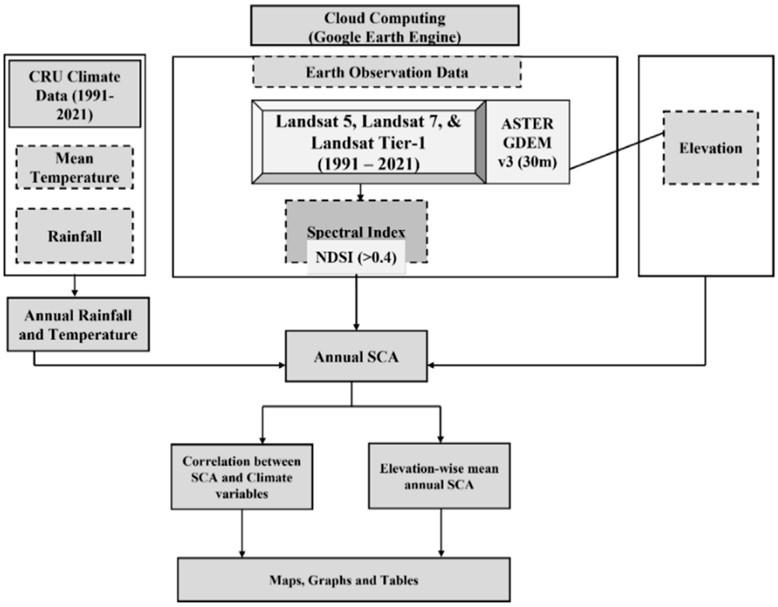

FIGURE 3
Research methodology.

TABLE 1 Details of satellite images.

Satellite mission	Sensor	Band	Resolution (m)	
Landsat 5	TM (1984–2013)	7	30/60	Optical/thermal
Landsat 7	ETM (1999–2016)	9	30/60	
Landsat 8	OLI TIRS (2013–Present)	11	30/100	

TABLE 2 Statistical details of topographic parameters for Astore and Shigar.

Astore			Shigar		
Elevation zone	Elevation (m)	Area [km^2 (%)]	Elevation zone	Elevation (m)	Area [km^2 (%)]
1	<2,500	410 (7.83%)	1	<3,500	1,105 (12.39%)
2	2,501–3,600	1,465 (28%)	2	3,501–4,600	2,611 (29.29%)
3	3,601–4,500	2,257 (43.13%)	3	4,601–5,500	3,663 (41.1%)
4	>4,501	1,102 (21.06%)	4	>5,501	1,535 (17.23%)
Total		5,233 (100%)			8,913 (100%)

the HKH region and it can accurately acquire the data in this region (Kanda et al., 2020). Another study also suggested that CRU and ERA-I datasets perform better, and both datasets precisely capture the spatial distribution of temperature and precipitation in the Greater Himalayas, Northwest Himalayas, and Karakoram region (Negi and Kanda, 2020). CRU data was developed by the climate research unit of the University of East Anglia at the NERC collaborative center using the angular distance weighting method at 0.5° resolution. In this study, we acquired the CRU data [(https://crudata.uea.ac.uk/cru/data/hrg/

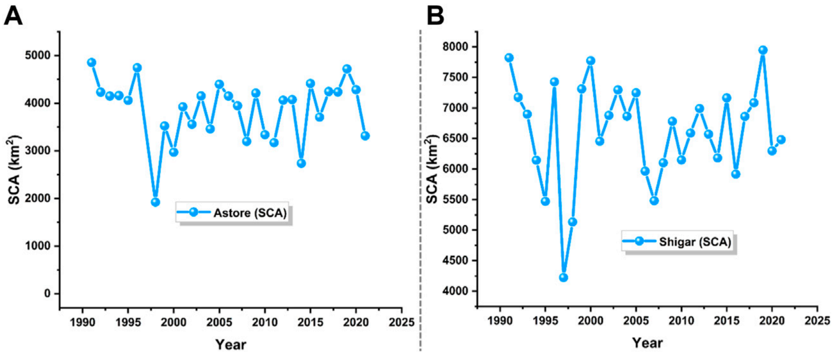

FIGURE 4
Inter-annual SCA variability for **(A)** Astore and **(B)** Shigar.

cru_ts_4.05/ge/) (accessed on 15 May 2022)] between 1991 and 2021 (Harris et al., 2020; Harris et al., 2021). The climatic data were used to estimate the influence of changing climate on SCA.

Results and discussion

Annual snow cover area

In this study, the SCA for Astore and Shigar was computed through Landsat data between 1991 and 2021 in GEE. The mean annual SCA was calculated for both regions as presented in Figures 4A,B. It was observed that SCA varies greatly in both regions due to high variability in precipitation and temperature (Khan et al., 2014; Tahir et al., 2015). Astore SCA varies between 36.7% (1998) and 92.7% (1991) (Supplementary Figures S1,S2), while in Shigar it varies between 47.4% (1997) and 89.18% (2019) (Supplementary Figures S3,S4). A huge variation of SCA can be reflected through the high discharge of Astore River and Shigar River basins. Hakeem et al. (2014) revealed that Shigar River basin runoff is mainly contributed by seasonal and annual SCA. It was observed that Astore and Shigar have an increasing trend of SCA with a rate of 11.16 km^2/year and 4.27 km^2/year, respectively. Tahir et al. (2015) and Tahir et al. (2016) also revealed an increasing/stable trend of SCA in the Western Himalayas and Central Karakoram region. River basins in the UIB are highly dependent on SCA and glaciers; therefore, this increasing trend of SCA can highly contribute to the Astore River and Shigar River in the future. The increasing trend of precipitation and decreasing trend of temperature feed the mountainous region and reduce the snow melt resulting in a stable/increasing trend of SCA. The results of this study are similar to Gilgit River and Hunza River basins.

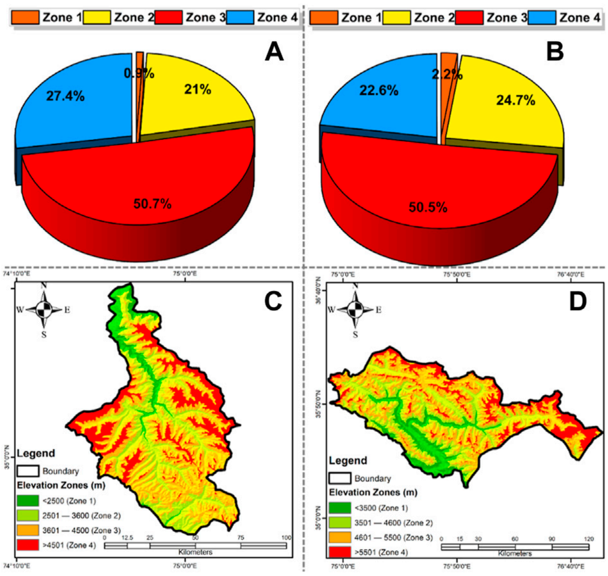

FIGURE 5
Elevation-zone wise mean SCA (1991–2021) of **(A)** Astore, **(B)** Shigar, **(C)** Astore elevation zones, **(D)** Shigar elevation zones.

It was also observed that the annual SCA was decreasing during 1991–2005 (−38.04 km^2/year) in Astore because the temperature was increasing and precipitation was decreasing, while, in the latter part of the study (2006–2021), the results revealed that SCA was increasing (25.76 km^2/year) because the temperature was decreasing and precipitation was increasing. It was observed in Shigar that in both periods annual SCA was increasing because the precipitation has an increasing trend and the temperature has a decreasing trend. A similar increasing trend in precipitation and decreasing trend in temperature was observed by Tahir et al. (2015) and Tahir et al. (2016).

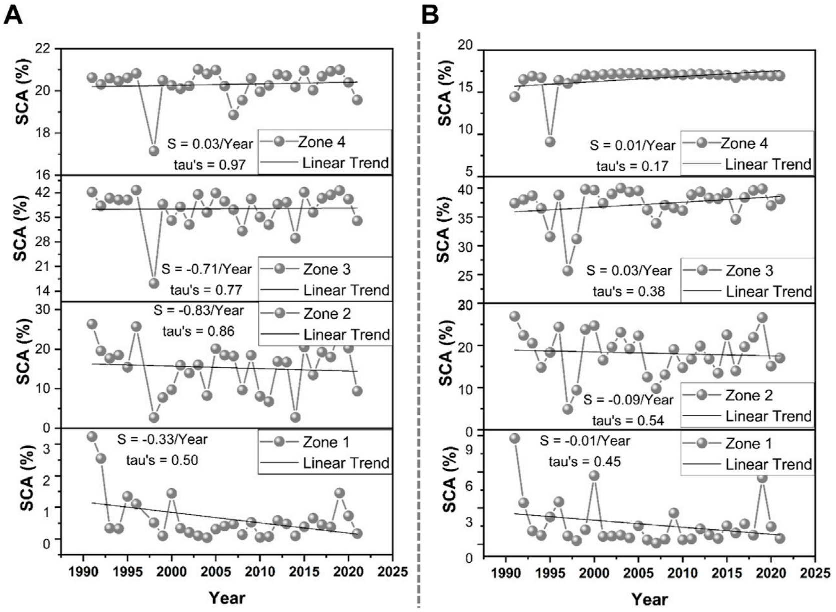

FIGURE 6
Mann–Kendall trend of annual SCA derived from Landsat data in four elevation zones of **(A)** Astore and **(B)** Shigar over a 31-year period (1991–2021). Kendall tau, "tau's"; Sen's slope, "S."

Topographic parameter and snow cover area

Topographic parameters, i.e., elevation, slope, and aspect play a significant role in snow cover changes (Li and Li, 2014; Bhambri et al., 2017) because the process of accumulation and melting can be controlled by topography and atmospheric conditions. The air and surface temperatures are increasing at higher altitudes which can significantly affect the SCA (Huang et al., 2017). Many researchers studied elevation-dependent warming and concluded that it will have a significant impact on hydrological cycles due to the huge and early snow melt process (Pepin et al., 2015; Thakuri et al., 2019). Therefore, in this study, we correlated elevation and SCA. It was observed that elevation zone 1 covers 7.83% of the total area of Astore, and usually, in this zone, the precipitation falls in the form of rainfall; hence, on average, this zone covers 0.9% of SCA. The temperature of this zone varies from −8.07 C in January to 12.50 C in August. The snow accumulation period of this zone is comparatively shorter; consequently, this zone occupies only a small portion of SCA (Figure 5A); on contrary, zone 4 of the elevation class covers 21.06% of the total area which is mainly covered with glaciers above the 5,000 mean sea level (m.s.l) (Figure 5C). The areal extent of permanent SCA is mostly situated at zone 4 because at higher altitudes the precipitation falls in the form of snowfall and the temperature of this zone varies from −10.70 C in January to 11.50 C in August. In this zone, the below-freezing temperature remains until April, and the snow melt period becomes shorter. Therefore, zone 4 has weaker snow cover variations (*S* = 0.03%/year, tau's = 0.97) (Figure 6A) (Tahir et al., 2015; Misra et al., 2020). Zone 4 of the elevation class covered 27.4% of SCA (Figure 5A). Zone 2 and zone 3 of the elevation class cover a large portion in Astore; similarly, they cover 21% and 50.7% of SCA, but we observed high year-to-year variation in these zones because these zones receive a large amount of precipitation in the form of snow during the accumulation season, but in the melt season the precipitation falls in the form of rain and heavy rainfall in the monsoon season (rain on snow), leading to rapid melting of snow cover. Another reason for the decreasing trend of SCA is that SCA is highly exposed to high temperatures (S = −0.83 and -0.71%/year; tau's = 0.86 and 0.77). Particularly, in this study, we observed that zone 2 and zone 3 have an increasing trend of temperature and decreasing trend of rainfall, which is the reason for decreasing trend of SCA (Supplementary Table S4). Annual SCA at mid-altitude zones decreases but insignificantly which is closely related to the elevation-dependent temperature change as compared to precipitation (Misra et al., 2020; Shen et al., 2021) (Supplementary Table S4).

Many previous research studies suggested that snow accumulation and snow melt were significantly based on the topography, latitude, and weather conditions of the area (Woo and Thorne, 2006; Jain et al., 2009; Kour et al., 2016). Therefore,

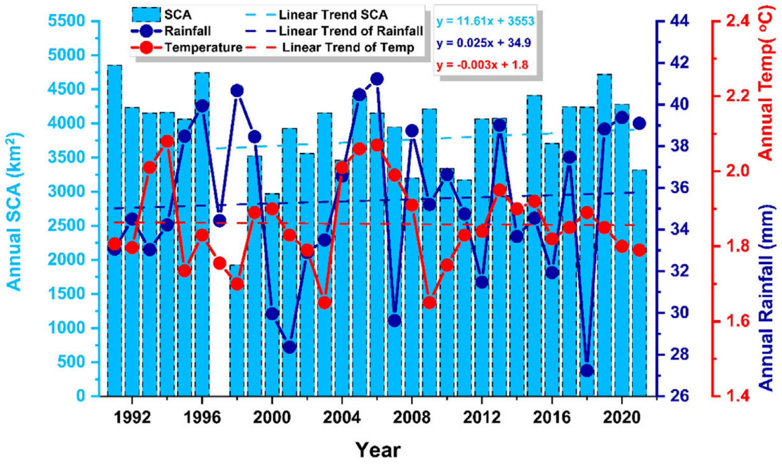

FIGURE 7
Annual SCA, rainfall, and temperature of Astore.

the elevation of Shigar was correlated with SCA in this research to examine its impact. The valley floor (zone 1) and high altitude (zone 4) of Shigar cover an area of 12.39% and 17.23%, respectively. At high altitudes, snow is the main form of precipitation and represents a glaciated area, while the valley floor receives precipitation in the form of rainfall. The temperature of zone 1 remains below the freezing point for 5 months in Shigar, while at high-altitude zone 4 the freezing temperature remains for 7 months, which represents the snow accumulation and snow melting period and variations of SCA in zone 1 and zone 4. At high altitudes, less temperature can be examined with a high amount of precipitation which can turn it into snow accumulation (Supplementary Table S4). Subsequently, elevation with climate variables greatly affects the snow cover distribution (Jain et al., 2009). The mid-altitude zones cover 70% of the total area and occupy 75.2% of SCA. This huge portion of SCA at mid-altitude is sensitive and exposed to high temperature in the melt season resulting in high discharge in the river and also presents high SCA variations (Hasson et al., 2014a; Hakeem et al., 2014) (S = −0.09 and 0.03%/year; tau's 0.54 and 0.38) (Figure 6B).

Trends in annual SCA were computed for a period of 31 years in four elevation zones of Astore and Shigar (Table 2; Figure 6). Low-altitude zones of both regions revealed a decreasing trend, but the trend was insignificant, while, at high-altitude zones of Astore and Shigar, the trend was insignificantly positive (Figure 6; Supplementary Tables S4,S5). The tau values at high elevation for Astore and Shigar were 0.97 and 0.17, while S-values were 0.03% and 0.01%/year, respectively (Figures 6A,B). On contrary, the tau values for mid-altitude zones of Astore were 0.86 and 0.77, while S-values were −0.83% and −0.71%/year (Figure 6A; Supplementary Table S4). Similarly, the tau values of Shigar at mid-altitude were 0.54 and 0.38, while S-values were −0.09% and 0.03%/year. (Figure 6B; Supplementary Table S5).

Climate variables and snow cover area

For a better interpretation of the snow cover area, we compared SCA with climate variables (temperature and precipitation) for the period of 1991–2021. The rainfall and temperature patterns were examined to see the response of SCA to the changing climate. The mean annual temperature and rainfall of Astore and Shigar were computed, and it was revealed that the mean annual temperature of Astore and Shigar was decreasing, while precipitation was increasing in both regions (Figures 7, 8). A linear trend value for Astore (Shigar) was 0.025 mm/year (0.028 mm/year) for precipitation and −0.003 °C/year (−0.017 °C/year) for temperature was found over the studied period (1991–2021) (Figures 7, 8). The increasing and decreasing trends of precipitation and temperature indicate the reason for the stable/increasing trend of SCA because the increasing trend of precipitation feeds the mountainous area and influences the SCA.

In this study, we analyzed the seasonal trend of temperature and precipitation to understand which climatic variable led to an increasing or stable trend of SCA in Astore and Shigar. Long-term (1991–2021) precipitation and temperature data were used to compute the trend. The results revealed that winter precipitation in Astore have an insignificant positive trend (tau's = 0.84; S = 0.04 mm/year); however, the summer season has an insignificant negative trend of precipitation (tau's = 0.61; −0.097 mm/year) (Table 3). While it was noticed that the summer season temperature has an insignificant decreasing

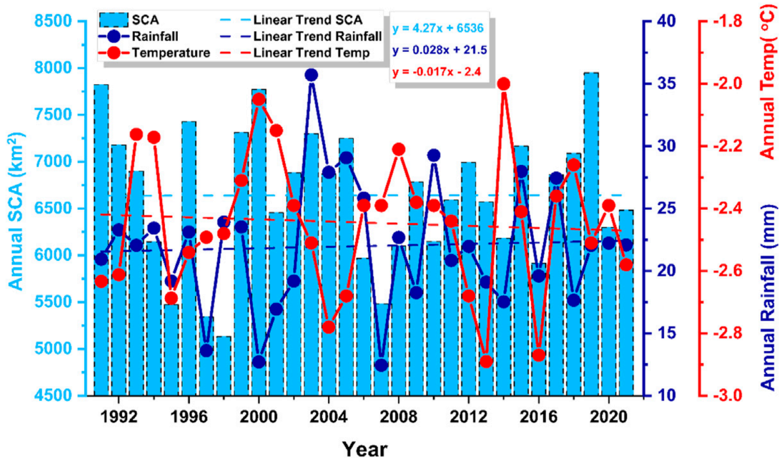

FIGURE 8
Annual SCA, rainfall, and temperature of Shigar.

TABLE 3 MK trend analysis of climate variables of Astore for summer and winter seasons for the period of 1991–2021.

Trend	Precipitation		Temperature	
	Winter (DJF)	Summer (JAS)	Winter (DJF)	Summer (JAS)
Linear regression	y = 0.04x + 38.3	y = −0.02x + 40.4	y = 0.034x–11.9	y = −0.007x + 7.6
Tau's	0.84 ($p > 0.05$)	0.61 ($p > 0.05$)	0.44 ($p > 0.05$)	0.79 ($p > 0.05$)
Sen's Slope	0.04 mm/year	−0.097 mm/year	0.009 (°C/year)	−0.033 (°C/year)

TABLE 4 MK trend analysis of climate variables of Shigar for summer and winter seasons for the period of 1991–2021.

Trend	Precipitation		Temperature	
	Winter (DJF)	Summer (JAS)	Winter (DJF)	Summer (JAS)
Linear regression	y = 0.03x + 27.4	y = 0.07x + 9.5	y = 0.015x–12.7	y = 0.03x + 7.6
Tau's	0.86 ($p > 0.05$)	0.66 ($p > 0.05$)	0.34 ($p > 0.05$)	0.81 ($p > 0.05$)
Sen's Slope	0.034 mm/year	0.019 mm/year	0.013 (°C/year)	0.037 (°C/year)

trend, the winter season temperature has an increasing trend. The increasing and decreasing trends of precipitation and temperature in both seasons can be a possible reason for the stable/increasing trend of SCA in Astore because winter precipitation is increasing which can bring more snowfall in the region and summer season temperature is decreasing which restricts snow melt (Archer and Fowler, 2004; Hewitt, 2007). The increasing trend of precipitation in Asia was also reported by Hartmann et al. (2013). Recently, Moazzam et al. (2022) also revealed that precipitation will increase in the northern region of Pakistan (Gilgit-Baltistan) under representative concentration pathway (RCP) 4.5 and RCP 8.5 (Moazzam et al., 2022).

In contrast, it was observed that, in Shigar, precipitation is increasing in winter (tau's = 0.86; S = 0.034 mm/year) and summer seasons (tau's = 0.66; S = 0.019 mm/year), while temperature is also increasing in both seasons (Table 4). The increasing trend of SCA in Shigar may be influenced by the increased winter precipitation due to the western disturbance (Ahmad et al., 2019). A recent book published by ICIMOD also reported an increasing trend in winter precipitation (Krishnan et al., 2019). The increasing probability of western disturbance-induced rainfall and snowfall in the winter season will impact an increase in SCA (Midhuna et al., 2020).

Discussion

In this study, we analyzed the snow cover changes of Astore and Shigar using Landsat data in the Google Earth Engine (GEE) platform for the period of 1991–2021. The normalized difference snow index (NDSI) was used in this study for the extraction of snow cover because in previous studies (Burns and Nolin, 2014; Shafique et al., 2018; Tong et al., 2020) NDSI revealed a better accuracy in shadowed and mountainous regions. In this study, it was found that the snow cover area is increasing in Astore and Shigar which is in line with some previous studies (Tahir et al., 2015; Tahir et al., 2016; Anjum et al., 2019; Shafiq et al., 2019). The increasing trend of SCA nourishes the glaciers and makes a positive contribution to the mass balance of glaciers in the Karakoram region which was reported previously (Scherler et al., 2011; Nüsser and Schmidt, 2021; Bhambri et al., 2022), not like other mountainous regions around the globe because the temperature is decreasing and precipitation is increasing in this region. Similarly, IPCC Fifth Assessment Report indicated an increase in SCA due to a positive trend of precipitation (Hartmann et al., 2013) which is also supported by another study that the frequency and occurrence of westerlies-induced precipitation will increase up to 2,100 (Ridley et al., 2013). Moazzam et al. (2022) also revealed an increasing trend of precipitation until mid of this century. The cooling phenomena of the summer season are also a reason for the increasing trend of SCA (Fowler and Archer, 2006). The increasing trend of SCA in the Astore region is unexpected because previous studies reported a decreasing trend of glacier mass balance in the Himalayan region (Ali et al., 2015; Bajracharya et al., 2015; Hayat et al., 2019). Astore is located in the extreme Western Himalayan region and has a different climate from the Eastern Himalayan region and receives westerlies-induced precipitation due to the vicinity of the southern Karakoram region; hence, the winter precipitation of Astore is somewhat similar to Shigar precipitation (Tables 3, 4). Therefore, the climate variability trend plays a significant role in the increasing or decreasing trend of SCA in the Central Karakoram and Western Himalayas region (Tahir et al., 2015). A seasonal analysis was performed for the winter and summer seasons' precipitation and temperature of Astore and Shigar (Figure 7). The precipitation and temperature (winter) of Astore have an increasing trend but not significantly, while in the summer season both temperature and precipitation have a decreasing trend. The results of this study support a study conducted by Archer and Fowler, (2004) who explained an insignificant decreasing trend in the summer season, while in Shigar it was noted that precipitation and temperature in winter and summer seasons have an insignificant increasing trend. The increasing trend of winter temperature still persists negatively in high-elevation zones (Tahir et al., 2016). Archer and Fowler, (2004) stated an increasing trend of summer and winter precipitation in the Upper Indus Basin. The increasing trend of SCA in Astore is clearer than that in Shigar (Tables 3, 4) because summer temperature in Astore has a decreasing trend [tau's = 0.79; S = −0.033 (°C/year)]. Fowler and Archer, (2006) stated that the summer season's temperature plays a key role in SCA and glacier melt; another study also stated that the pre-monsoon and monsoon temperature of the high mountain area is decreasing (Hussain et al., 2005). The elevation and SCA were also analyzed, and it was found that zone 1 of both regions has a decreasing trend (Qureshi et al., 2017; Ali et al., 2021), while zone 4 has a slightly increasing trend of SCA because the high-altitude region is less exposed to solar radiation as compared to foothills (Saydi and Ding, 2020). The higher altitude regions have consistently below-freezing temperatures throughout the year; therefore, increasing precipitation can possibly feed the high-altitude region, and hence SCA expands (Tahir et al., 2011; Hasson et al., 2014b). Worldwide glaciers are decreasing due to an ongoing climate change prognosis, whereas in some valleys of Karakoram and Himalayan regions its increase is a good sign which has been previously noted in a number of studies under the title of the Karakoram anomaly (Hewitt, 2005; Farinotti et al., 2020; Dimri, 2021). The glacier of the study region feeds the flow in the Indus River, which is a resource and sometimes becomes a hazard for 220 million people in low-lying areas. The increase in glacial mass has also increased river flow in Shigar and Astore rivers (Khalida et al., 2015) which is also a positive sign for the low-lying agricultural land.

Conclusion

Spatial and temporal SCA changes have been calculated using Landsat data with the GEE platform and analyzed with climate variables (rainfall and temperature) and elevation for the Astore and Shigar regions. The results of this study have been evaluated, and it is concluded that SCA in both regions has an increasing trend due to the increasing trend of precipitation and decreasing trend of temperature in the studied period. The results also indicated that the SCA was decreasing (−38.04 km^2/year) during 1991–2005 in the Astore region, while in the same period Shigar had an increasing trend. In the latter part of the study (2006–2021), the results revealed an increasing trend of SCA in both regions. The annual SCA varies greatly due to the influence of rainfall and temperature. The minimum annual SCA was observed in the years 1998 (36.7%) and 1997 (47.4%) in Astore and Shigar, while maximum SCA was observed in the years 1991

(92.7%) and 2019 (89.18%) in Astore and Shigar, respectively. A thorough investigation of SCA and elevation revealed that the lowest and highest altitudes have insignificant decreasing and increasing trends of SCA in both regions. SCA and climate variables indicated that precipitation is increasing and temperature is decreasing with time which is a possible reason for the increasing trend of SCA in both regions. The increasing SCA is a positive sign of water resources for the future and agricultural activities in the study region as well as the region relying on water resources from Astore and Shigar rivers. The increasing precipitation, especially decreasing temperature in the study region is in contrast to the current global climate warming, and this needs to be further investigated at the microlevel. This study can help improve the knowledge and understanding of water resource management.

Data availability statement

The original contributions presented in the study are included in the article/Supplementary Material; further inquiries can be directed to the corresponding author.

Author contributions

MM and BL: conceptualization; MM: acquired the data, data curation, formal analysis, and investigation; MM and GR: methodology, validation, visualization, and writing—original draft; BL: supervision, project administration, resources, and writing—review and editing; and NA: acquired funding and writing—review and editing.

Acknowledgments

The author thanks the United States Geological Survey (USGS) and the National Aeronautics and Space Administration (NASA) for providing the Landsat data. The authors are thankful to NASA and the Ministry of Economy, Trade, and Industry (METI) for providing ASTER DEM free of cost for this study.

Conflict of interest

The authors declare that the research was conducted in the absence of any commercial or financial relationships that could be construed as a potential conflict of interest.

Publisher's note

Supplementary material

The Supplementary Material for this article can be found online at: https://www.frontiersin.org/articles/10.3389/fenvs.2022.1006399/full#supplementary-material

References

Abid, Z., and Zia, S. (2019). Mapping and analysis of Baltoto glacier and Shigar river. *Pak. Geogr. Rev.* 74, 20–32.

Ahmad, M., Alam, K., Tariq, S., and Blaschke, T. (2019). Contrasting changes in snow cover and its sensitivity to aerosol optical properties in Hindukush-Karakoram-Himalaya region. *Sci. Total Environ.* 699, 134356. doi:10.1016/j.scitotenv.2019.134356

Ali, G., Hasson, S., and Khan, A. M. (2009). *Global change impact studies centre (GCISC)*. Islamabad, Pakistan.Climate change: Implications and adaptation of water resources in Pakistan

Ali, S., Khan, G., Hassan, W., Qureshi, J. A., and Bano, I. (2021). *Assessment of glacier status and its controlling parameters from 1990 to 2018 of Hunza basin, western karakorum*. Heidelberg: Environmental Science and Pollution Research, 1–13.

Ali, S., Li, D., Congbin, F., and Khan, F. (2015). Twenty first century climatic and hydrological changes over Upper Indus Basin of Himalayan region of Pakistan. *Environ. Res. Lett.* 10, 014007. doi:10.1088/1748-9326/10/1/014007

Aniya, M., Sato, H., Naruse, R., Skvarca, P., and Casassa, G. (1996). Patagonia lcefield, south America. *Photogrammetric Eng. Remote Sens.* 62, 1361–1369.

Anjum, M. N., Ding, Y., Shangguan, D., Liu, J., Ahmad, I., Ijaz, M. W., et al. (2019). Quantification of spatial temporal variability of snow cover and hydro-climatic variables based on multi-source remote sensing data in the Swat watershed, Hindukush Mountains, Pakistan. *Meteorol. Atmos. Phys.* 131, 467–486. doi:10.1007/s00703-018-0584-7

Archer, D. R., and Fowler, H. J. (2004). Spatial and temporal variations in precipitation in the Upper Indus Basin, global teleconnections and hydrological implications. *Hydrol. Earth Syst. Sci.* 8, 47–61. doi:10.5194/hess-8-47-2004

Azizi, A. H., and Akhtar, F. (2021). Analysis of spatiotemporal variation in the snow cover in Western Hindukush-Himalaya region. *Geocarto Int.*, 1–23. doi:10.1080/10106049.2021.1939442

Bajracharya, S. R., Maharjan, S. B., Shrestha, F., Guo, W., Liu, S., Immerzeel, W., et al. (2015). The glaciers of the Hindu Kush Himalayas: Current status and observed changes from the 1980s to 2010. *Int. J. Water Resour. Dev.* 31, 161–173. doi:10.1080/07900627.2015.1005731

Banerjee, A., Chen, R., Meadows, M. E., Sengupta, D., Pathak, S., Xia, Z., et al. (2021). Tracking 21st century climate dynamics of the Third Pole: An analysis of topo-climate impacts on snow cover in the central Himalaya using Google Earth Engine. *Int. J. Appl. Earth Observation Geoinformation* 103, 102490. doi:10.1016/j.jag.2021.102490

Bhambri, R., Bolch, T., Chaujar, R. K., and Kulshreshtha, S. C. (2017). Glacier changes in the Garhwal Himalaya, India, from 1968 to 2006 based on remote sensing. *J. Glaciol.* 57, 543–556. doi:10.3189/002214311796905604

Bhambri, R., Hewitt, K., Haritashya, U. K., Chand, P., Kumar, A., Verma, A., et al. (2022). Characteristics of surge-type tributary glaciers, Karakoram. *Geomorphology* 403, 108161. doi:10.1016/j.geomorph.2022.108161

Bishop, M. P., Bush, A. B., Copland, L., Kamp, U., Owen, L. A., Seong, Y. B., et al. (2010). Climate change and mountain topographic evolution in the central Karakoram, Pakistan. *Ann. Assoc. Am. Geogr.* 100, 772–793. doi:10.1080/00045608.2010.500521

Bookhagen, B., and Burbank, D. W. (2010). Toward a complete Himalayan hydrological budget: Spatiotemporal distribution of snowmelt and rainfall and their impact on river discharge. *J. Geophys. Res.* 115, F03019. doi:10.1029/2009jf001426

Burns, P., and Nolin, A. (2014). Using atmospherically-corrected Landsat imagery to measure glacier area change in the Cordillera Blanca, Peru from 1987 to 2010. *Remote Sens. Environ.* 140, 165–178. doi:10.1016/j.rse.2013.08.026

Dimri, A. (2021). Decoding the Karakoram anomaly. *Sci. Total Environ.* 788, 1–13. doi:10.1016/j.scitotenv.2021.147864

Farhan, S. B., Zhang, Y., Aziz, A., Gao, H., Ma, Y., Kazmi, J., et al. (2020). Assessing the impacts of climate change on the high altitude snow-and glacier-fed hydrological regimes of Astore and Hunza, the sub-catchments of Upper Indus Basin. *J. Water Clim. Change* 11, 479–490. doi:10.2166/wcc.2018.107

Farhan, S. B., Zhang, Y., Ma, Y., Guo, Y., and Ma, N. (2015). Hydrological regimes under the conjunction of westerly and monsoon climates: A case investigation in the Astore basin, northwestern Himalaya. *Clim. Dyn.* 44, 3015–3032. doi:10.1007/s00382-014-2409-9

Farinotti, D., Immerzeel, W. W., De Kok, R. J., Quincey, D. J., and Dehecq, A. (2020). Manifestations and mechanisms of the Karakoram glacier anomaly. *Nat. Geosci.* 13, 8–16. doi:10.1038/s41561-019-0513-5

Fowler, H., and Archer, D. (2006). Conflicting signals of climatic change in the upper Indus Basin. *J. Clim.* 19, 4276–4293. doi:10.1175/jcli3860.1

Fowler, H., and Archer, D. (2005). Hydro-climatological variability in the Upper Indus Basin and implications for water resources. *Regional Hydrological Impacts Clim. Change—Impact Assess. Decis. Mak.* 295, 131–138.

Gorelick, N., Hancher, M., Dixon, M., Ilyushchenko, S., Thau, D., and Moore, R. (2017). Google earth engine: Planetary-scale geospatial analysis for everyone. *Remote Sens. Environ.* 202, 18–27. doi:10.1016/j.rse.2017.06.031

Hakeem, S. A., Bilal, M., Pervez, A., and Tahir, A. A. (2014). Remote sensing data application to monitor snow cover variation and hydrological regime in a poorly gauged river catchment—northern Pakistan. *Int. J. Geosciences* 5, 27–37. doi:10.4236/ijg.2014.51005

Harris, I., Jones, P., and Osborn, T. (2021). in *Cru TS4.05: Climatic Research Unit (CRU) Time-Series (TS) version 4.05 of high-resolution gridded data of month-by-month variation in climate (Jan. 1901- Dec. 2020).* Editors N. E. C. F. E. D. ANALYSIS and C. R. U. CRU).

Harris, I., Osborn, T. J., Jones, P., and Lister, D. (2020). Version 4 of the CRU TS monthly high-resolution gridded multivariate climate dataset. *Sci. Data* 7, 109. doi:10.1038/s41597-020-0453-3

Hartmann, D. L., Tank, A. M. K., Rusticucci, M., Alexander, L. V., Brönnimann, S., Charabi, Y. A. R., et al. (2013). *Climate change 2013 the physical science basis: Working group I contribution to the fifth assessment report of the intergovernmental panel on climate change*. Cambridge University Press.Observations: Atmosphere and surface

Hasson, S., Lucarini, V., Khan, M. R., Petitta, M., Bolch, T., and Gioli, G. (2014a). Early 21st century snow cover state over the Western river basins of the Indus River system. *Hydrol. Earth Syst. Sci.* 18, 4077–4100. doi:10.5194/hess-18-4077-2014

Hasson, S., Lucarini, V., Pascale, S., and Böhner, J. (2014b). Seasonality of the hydrological cycle in major South and Southeast Asian river basins as simulated by PCMDI/CMIP3 experiments. *Earth Syst. Dyn.* 5, 67–87. doi:10.5194/esd-5-67-2014

Hayat, H., Akbar, T. A., Tahir, A. A., Hassan, Q. K., Dewan, A., and Irshad, M. (2019). Simulating current and future river-flows in the Karakoram and Himalayan regions of Pakistan using snowmelt-runoff model and RCP scenarios. *Water* 11, 761. doi:10.3390/w11040761

Hewitt, K. (2005). The Karakoram anomaly? Glacier expansion and the 'elevation effect, 'Karakoram Himalaya. *Mt. Res. Dev.* 25, 332–340. doi:10.1659/0276-4741(2005)025[0332:tkagea]2.0.co;2

Hewitt, K. (2007). Tributary glacier surges: An exceptional concentration at panmah glacier, Karakoram Himalaya. *J. Glaciol.* 53, 181–188. doi:10.3189/172756507782202829

Hori, M., Sugiura, K., Kobayashi, K., Aoki, T., Tanikawa, T., Kuchiki, K., et al. (2017). A 38-year (1978–2015) Northern Hemisphere daily snow cover extent product derived using consistent objective criteria from satellite-borne optical sensors. *Remote Sens. Environ.* 191, 402–418. doi:10.1016/j.rse.2017.01.023

Huang, X., Deng, J., Wang, W., Feng, Q., and Liang, T. (2017). Impact of climate and elevation on snow cover using integrated remote sensing snow products in Tibetan Plateau. *Remote Sens. Environ.* 190, 274–288. doi:10.1016/j.rse.2016.12.028

Hussain, S. S., Mudasser, M., Sheikh, M., and Manzoor, N. (2005). Climate change and variability in mountain regions of Pakistan implications for water and agriculture. *Pak. J. Meteorology* 2.

ICIMOD (2005). *Inventory of glaciers and glaciers lakes andIdentification of potential glacial LakeOutburst floods (GLOFs) affected by GlobalWarming in the mountains of HimalayanRegion Pakistan*.

Immerzeel, W. W., Van Beek, L., Konz, M., Shrestha, A., and Bierkens, M. (2012). Hydrological response to climate change in a glacierized catchment in the Himalayas. *Clim. change* 110, 721–736. doi:10.1007/s10584-011-0143-4

Jacobsen, F. M., and Theakstone, W. H. (1997). Monitoring glacier changes using a global positioning system in differential mode. *Ann. Glaciol.* 24, 314–319. doi:10.1017/s0260305500012374

Jain, S. K., Goswami, A., and Saraf, A. K. (2009). Role of elevation and aspect in snow distribution in western Himalaya. *Water Resour. manage.* 23, 71–83. doi:10.1007/s11269-008-9265-5

Kanda, N., Negi, H. S., Rishi, M. S., and Kumar, A. (2020). Performance of various gridded temperature and precipitation datasets over Northwest Himalayan Region. *Environ. Res. Commun.* 2, 085002. doi:10.1088/2515-7620/ab9991

Kehrwald, N. M., Thompson, L. G., Tandong, Y., Mosley-Thompson, E., Schotterer, U., Alfimov, V., et al. (2008). Mass loss on Himalayan glacier endangers water resources. *Geophys. Res. Lett.* 35, L22503. doi:10.1029/2008gl035556

Khalida, K., Muhammad, Y., Yasir, L., and Ghulam, N. (2015). Detection of river flow trends and variability analysis of Upper Indus Basin, Pakistan. *Sci. Int. (Lahore)* 27, 1261–1270.

Khan, S., Ashiq, M., and Gabriel, H. (2014). *Assessment of flows in a glaciated region-Shigar river basin, Pakistan*. Taxila: Technical Journal, University of Engineering and Technology Taxila, 19.

Kour, R., Patel, N., and Krishna, A. P. (2016). Effects of terrain attributes on snow-cover dynamics in parts of Chenab basin, Western Himalayas. *Hydrological Sci. J.* 61, 1859–1876. doi:10.1080/02626667.2015.1052815

Krishnan, R., Shrestha, A. B., Ren, G., Rajbhandari, R., Saeed, S., Sanjay, J., et al. (2019). "Unravelling climate change in the Hindu Kush Himalaya: Rapid warming in the mountains and increasing extremes," in *The Hindu Kush Himalaya assessment: Mountains, climate change, sustainability and people*. Editors P. WESTER, A. MISHRA, A. MUKHERJI, and A. B. SHRESTHA (Cham: Springer International Publishing).

Li, Y., and Li, Y. (2014). Topographic and geometric controls on glacier changes in the central Tien Shan, China, since the Little Ice Age. *Ann. Glaciol.* 55, 177–186. doi:10.3189/2014aog66a031

Meetei, P. N., Ahluwalia, R. S., Rai, S., Khobragade, S., Sarangi, S., Goel, M., et al. (2022). Spatio-temporal analysis of snow cover and effect of terrain attributes in the Upper Ganga River Basin, central Himalaya. *Geocarto Int.* 37, 1139–1159. doi:10.1080/10106049.2020.1762764

Midhuna, T. M., Kumar, P., and Dimri, A. P. (2020). A new Western Disturbance Index for the Indian winter monsoon. *J. Earth Syst. Sci.* 129, 59. doi:10.1007/s12040-019-1324-1

Misra, A., Kumar, A., Bhambri, R., Haritashya, U. K., Verma, A., Dobhal, D. P., et al. (2020). Topographic and climatic influence on seasonal snow cover: Implications for the hydrology of ungauged Himalayan basins, India. *J. Hydrology* 585, 124716. doi:10.1016/j.jhydrol.2020.124716

Moazzam, M. F. U., Rahman, G., Munawar, S., Tariq, A., Safdar, Q., and Lee, B.-G. (2022). Trends of rainfall variability and drought monitoring using standardized precipitation index in a scarcely gauged basin of northern Pakistan. *Water* 14, 1132. doi:10.3390/w14071132

Negi, H., and Kanda, N. (2020). *Climate change and the white world*. Springer.An appraisal of spatio-temporal characteristics of temperature and precipitation using gridded datasets over NW-Himalaya

Notarnicola, C. (2020). Hotspots of snow cover changes in global mountain regions over 2000–2018. *Remote Sens. Environ.* 243, 111781. doi:10.1016/j.rse.2020.111781

Nüsser, M., and Schmidt, S. (2021). Glacier changes on the Nanga Parbat 1856–2020: A multi-source retrospective analysis. *Sci. Total Environ.* 785, 147321. doi:10.1016/j.scitotenv.2021.147321

Panday, P. K., Thibeault, J., and Frey, K. E. (2015). Changing temperature and precipitation extremes in the Hindu Kush-Himalayan region: An analysis of CMIP3 and CMIP5 simulations and projections. *Int. J. Climatol.* 35, 3058–3077. doi:10.1002/joc.4192

Patel, A., Prajapati, R., Dharpure, J. K., Mani, S., and Chauhan, D. (2019). Mapping and monitoring of glacier areal changes using multispectral and elevation data: A case study over chhota-shigri glacier. *Earth Sci. Inf.* 12, 489–499. doi:10.1007/s12145-019-00388-x

Pepin, N., Bradley, R. S., Diaz, H., Baraër, M., Caceres, E., Forsythe, N., et al. (2015). Elevation-dependent warming in mountain regions of the world. *Nat. Clim. Chang.* 5, 424–430. doi:10.1038/nclimate2563

Qureshi, M. A., Yi, C., Xu, X., and Li, Y. (2017). Glacier status during the period 1973–2014 in the Hunza basin, western Karakoram. *Quat. Int.* 444, 125–136. doi:10.1016/j.quaint.2016.08.029

Rastner, P., Prinz, R., Notarnicola, C., Nicholson, L., Sailer, R., Schwaizer, G., et al. (2019). On the automated mapping of snow cover on glaciers and calculation of snow line altitudes from multi-temporal landsat data. *Remote Sens.* 11, 1410. doi:10.3390/rs11121410

RGI (2017). *A dataset of global glacier outlines: Version 6.0: Technical report, global land ice measurements from Space*. Colorado, USA.

Ridley, J., Wiltshire, A., and Mathison, C. (2013). More frequent occurrence of westerly disturbances in Karakoram up to 2100. *Sci. Total Environ.* 468, S31–S35. doi:10.1016/j.scitotenv.2013.03.074

Sahu, R., and Gupta, R. (2020). Snow cover area analysis and its relation with climate variability in Chandra basin, Western Himalaya, during 2001–2017 using MODIS and ERA5 data. *Environ. Monit. Assess.* 192, 1–26. doi:10.1007/s10661-020-08442-8

Saydi, M., and Ding, J.-L. (2020). Impacts of topographic factors on regional snow cover characteristics. *Water Sci. Eng.* 13, 171–180. doi:10.1016/j.wse.2020.09.002

Scherler, D., Bookhagen, B., and Strecker, M. R. (2011). Spatially variable response of Himalayan glaciers to climate change affected by debris cover. *Nat. Geosci.* 4, 156–159. doi:10.1038/ngeo1068

Shafiq, M. U., Ahmed, P., Islam, Z. U., Joshi, P. K., and Bhat, W. A. (2019). Snow cover area change and its relations with climatic variability in Kashmir Himalayas, India. *Geocarto Int.* 34, 688–702. doi:10.1080/10106049.2018.1469675

Shafique, M., Faiz, B., Bacha, A. S., and Ullah, S. (2018). Evaluating glacier dynamics using temporal remote sensing images: A case study of Hunza valley, northern Pakistan. *Environ. Earth Sci.* 77, 162–211. doi:10.1007/s12665-018-7365-y

Sharma, V., Mishra, V. D., and Joshi, P. K. (2013). Implications of climate change on streamflow of a snow-fed river system of the Northwest Himalaya. *J. Mt. Sci.* 10, 574–587. doi:10.1007/s11629-013-2667-8

Shen, L., Zhang, Y., Ullah, S., Pepin, N., and Ma, Q. (2021). Changes in snow depth under elevation-dependent warming over the Tibetan Plateau. *Atmos. Sci. Lett.* 22, e1041. doi:10.1002/asl.1041

SIHP (1990). *Snow and ice hydrology project, upper Indus river basin*. Lahore: WAPDA-IDRC-Wilfrid Laurier University.

Tahir, A. A., Adamowski, J. F., Chevallier, P., Haq, A. U., and Terzago, S. (2016). Comparative assessment of spatiotemporal snow cover changes and hydrological behavior of the Gilgit, Astore and Hunza River basins (Hindukush–Karakoram–Himalaya region, Pakistan). *Meteorol. Atmos. Phys.* 128, 793–811. doi:10.1007/s00703-016-0440-6

Tahir, A. A., Chevallier, P., Arnaud, Y., and Ahmad, B. (2011). Snow cover dynamics and hydrological regime of the Hunza river basin, Karakoram range, northern Pakistan. *Hydrol. Earth Syst. Sci.* 15, 2275–2290. doi:10.5194/hess-15-2275-2011

Tahir, A. A., Chevallier, P., Arnaud, Y., Ashraf, M., and Bhatti, M. T. (2015). Snow cover trend and hydrological characteristics of the Astore River basin (Western Himalayas) and its comparison to the Hunza basin (Karakoram region). *Sci. total Environ.* 505, 748–761. doi:10.1016/j.scitotenv.2014.10.065

Tahir, A. A., Hakeem, S. A., Hu, T., Hayat, H., and Yasir, M. (2019). Simulation of snowmelt-runoff under climate change scenarios in a data-scarce mountain environment. *Int. J. Digital Earth* 12, 910–930. doi:10.1080/17538947.2017.1371254

Thakuri, S., Dahal, S., Shrestha, D., Guyennon, N., Romano, E., Colombo, N., et al. (2019). Elevation-dependent warming of maximum air temperature in Nepal during 1976–2015. *Atmos. Res.* 228, 261–269. doi:10.1016/j.atmosres.2019.06.006

Tong, R., Parajka, J., Komma, J., and Blöschl, G. (2020). Mapping snow cover from daily Collection 6 MODIS products over Austria. *J. Hydrology* 590, 125548. doi:10.1016/j.jhydrol.2020.125548

Wester, P., Mishra, A., Mukherji, A., and Shrestha, A. (2019). *The Hindi Kush Himalaya assessment-mountians, climate change, sustainability and people*. Springer Nature Switzerland.

Woo, M. K., and Thorne, R. (2006). Snowmelt contribution to discharge from a large mountainous catchment in subarctic Canada. *Hydrol. Process.* 20, 2129–2139. doi:10.1002/hyp.6205

Yi, Y., Liu, S., Zhu, Y., Wu, K., Xie, F., and Saifullah, M. (2021). Spatiotemporal heterogeneity of snow cover in the central and Western Karakoram Mountains based on a refined MODIS product during 2002–2018. *Atmos. Res.* 250, 105402. doi:10.1016/j.atmosres.2020.105402

Zanter, K. (2016). Landsat 8 (L8) data users handbook. *Landsat Sci. Official Website* 33.

frontiers | Frontiers in Earth Science

TYPE Original Research
PUBLISHED 27 October 2022
DOI 10.3389/feart.2022.1004846

The interactive feedback mechanisms between terrestrial water storage and vegetation in the Tibetan Plateau

Haijun Deng[1,2,3], Yaning Chen[4], Xingwei Chen[1,2,3], Yang Li[5]*, Zhiguo Ren[6], Zhiwei Zhang[7], Zhouyao Zheng[1,2,3] and Sheng Hong[1,2,3]

[1]Institute of Geography, Fujian Normal University, Fuzhou, China, [2]Fujian Provincial Engineering Research Centre for Monitoring and Assessing Terrestrial Disasters, Fujian Normal University, Fuzhou, China, [3]Fujian Provincial Key Laboratory for Plant Eco-Physiology, Fujian Normal University, Fuzhou, China, [4]State Key Laboratory of Desert and Oasis Ecology, Xinjiang Institute of Ecology and Geography, Chinese Academy of Sciences, Urumqi, China, [5]Nuclear and Radiation Safety Center, Beijing, China, [6]Northwest Institute of Eco-Environment and Resources, Chinese Academy of Sciences, Lanzhou, China, [7]College of Resources and Environmental Sciences, Tibet Agriculture and Animal Husbandry University, Nyingchi, China

A component of terrestrial water storage, vegetation is also an influential driver of changes in terrestrial water storage. In the context of warming on the Tibetan Plateau, it is essential to explore the relationship between changes in terrestrial water storage and vegetation in this region to understand further the role of vegetation in the changes of water systems in alpine mountains. Our study combines terrestrial water storage anomalies data and vegetation indices to determine how their interact. The results indicate a warming rate of 0.44°C/decade ($p<0.01$) over the Tibetan Plateau from 1980–2020, while evapotranspiration trended upward (12.9 mm/decade, $p<0.01$), which is slower than precipitation (15 mm/decade, $p<0.01$). On the Tibetan Plateau, spatial-temporal differences in temperature, precipitation, and evapotranspiration dominate the variations in terrestrial water storage. The change in terrestrial water storage was relatively stable from 2003 to 2011, but decreased from 2012 to 2016. Terrestrial water storage increased in endorheic basins while decreasing in exorheic basins. Partial correlation analysis indicates a negative correlation between the terrestrial water storage anomaly and the temperature. It is found that terrestrial water storage and net precipitation are positively correlated in the Yangtze River Basin and the northeast of the endorheic basins. However, the Qaidam Basin and the north part of the Yellow River Basin are negatively correlated. Under the current climate change state (the increased rate of precipitation is faster than actual evapotranspiration), vegetation change has an insignificant impact on the changes in terrestrial water storage. In contrast, changes in terrestrial water storage (surplus/deficit) significantly affect vegetation changes (greening/browning) in parts of the Tibetan Plateau. The study contributes to a deeper understanding of the relationship between water system changes and vegetation on the Tibetan Plateau.

EDITED BY
Lei Wang,
Institute of Tibetan Plateau Research (CAS), China

REVIEWED BY
Baisha Weng,
China Institute of Water Resources and Hydropower Research, China
Xiangjiang Yu,
Jilin University, China

*CORRESPONDENCE
Yang Li,
ly_mly@126.com

SPECIALTY SECTION
This article was submitted to Cryospheric Sciences, a section of the journal Frontiers in Earth Science

RECEIVED 27 July 2022
ACCEPTED 30 September 2022
PUBLISHED 27 October 2022

CITATION
Deng H, Chen Y, Chen X, Li Y, Ren Z, Zhang Z, Zheng Z and Hong S (2022), The interactive feedback mechanisms between terrestrial water storage and vegetation in the Tibetan Plateau.
Front. Earth Sci. 10:1004846.
doi: 10.3389/feart.2022.1004846

KEYWORDS

climate change, terrestrial water storage, temperature and precipitation, vegetation change, Tibetan plateau

1 Introduction

The Tibetan Plateau is known as the " Asian Water Towers " because it has substantial both solid water resources (mainly glaciers and snow) and liquid water resources (mostly lake water). In the context of global warming, the Tibetan Plateau is undergoing a decrease in solid water storage and an increase in liquid water storage (Yao et al., 2022; Xiong et al., 2019). Essentially, glacier retreat, snow melt, and permafrost degradation are only transitions in water body states and do not affect the overall terrestrial water storage changes on the Tibetan Plateau. Temperature, evapotranspiration, and runoff have increased, resulting in glaciers and snow melt water loss. These factors contribute to an imbalance in water storage on the Tibetan plateau.

Terrestrial water storage (TWS) is a crucial indicator for quantitatively assessing the dynamics of the regional water balance, which consists of glaciers, snow, soil moisture, groundwater, surface water (rivers and lakes), and vegetation canopy water (Syed et al., 2008). Global warming has resulted in glacier retreat, snow melt, permafrost degradation, and lake expansion on the Tibetan Plateau, significantly affecting terrestrial water storage (Che et al., 2019; Wang et al., 2018). Assessing water balance changes on the Tibetan Plateau based on traditional hydrological methods has considerable uncertainty because of the region’s large gap in hydro-meteorological observations (Kang et al., 2020), especially in the endorheic basins. The development and advancement of remote sensing monitoring technologies in the last 2 decades, especially the Gravity Recovery and Climate Experiment (GRACE) gravity satellite launched in March 2002 and the GRACE second-generation satellite GRACE Follow On (GRACE-FO) in May 2018, have provided the opportunity to monitor terrestrial water storage changes (Sun et al., 2014; Pokhrel et al., 2021).

Since its launch, the GRACE gravity satellite has been widely used to study the terrestrial water storage changes on the Tibetan Plateau and surrounding areas (Matsuo and Heki, 2010; Long et al., 2014). There are apparent spatial differences in terrestrial water storage changes on the Tibetan Plateau (Li et al., 2022). The decrease in terrestrial water storage in the southern part of the Tibetan Plateau is caused by rising temperatures and decreasing precipitation (Jacob et al., 2012; Wang et al., 2020). Terrestrial water storage increased in the Sanjiangyuan area due to soil moisture rising (Meng et al., 2019), but surface water storage in the region is declining (Liu et al., 2020). The southeastern part of the Tibetan Plateau shows an overall decreasing trend in terrestrial water storage (-2.4 mm/a), especially the region’s most severe water storage deficit in the Salween River basin (Zhu et al., 2020). Terrestrial water storage in the inner Tibetan Plateau is on the rise, with the increase in lake water storage being the main contributor in terms of water storage components (Song et al., 2015; Zhang et al., 2019) and the increase in precipitation in terms of the water cycle (Deng et al., 2018; Meng et al., 2019).

The southeastern part of the Tibetan Plateau has high vegetation cover and is an area of forest distribution. In contrast, the central and northwestern parts have low vegetation cover and are areas of scrub or herbaceous distribution. The change in vegetation to either greening or browning in the context of warming of the Tibetan Plateau (Shen et al., 2013; Cai et al., 2015; Zhang et al., 2017) will have a significant impact on terrestrial water storage: firstly, vegetation canopy water is a component of terrestrial water storage; secondly, changes in vegetation transpiration will also affect evapotranspiration. Thus, it is necessary to clarify the interaction between changes in terrestrial water storage and changes in vegetation on the Tibetan Plateau due to global warming. It will contribute to a better understanding of the mechanisms underlying changes in terrestrial water storage on the Tibetan Plateau. However, this aspect has received little attention in the current research.

Therefore, based on the changes in temperature, precipitation, and evapotranspiration of the Tibetan Plateau, this study analyses the terrestrial water storage changes. Then explains the interrelationship between terrestrial water storage changes and vegetation. It answers whether there is an interactive feedback mechanism between terrestrial water storage changes and vegetation changes on the Tibetan Plateau. Section 2 describes the study area, data, and methods; Section 3 includes temperature, precipitation, evapotranspiration, and terrestrial water storage changes before examining the mechanisms explaining terrestrial water storage change and vegetation change. Section 4 provides detailed discussions, and Section 5 presents the conclusions.

2 Data and methods

2.1 Study area

The Tibetan Plateau covers an area of about 254 × 10^4 km^2 and is the highest plateau in the world, with an average altitude of more than 4,000 m (Figure 1A). The Tibetan Plateau has a wide distribution of solid water resources (mainly glaciers, snow, and permafrost) and large liquid water reserves (especially lake water). It is the source of many major rivers in Asia, including the Yellow, Yangtze, Lancang- Mekong, Ganges, and Indus rivers. As a result, it is known as the “Asian Water Towers.”

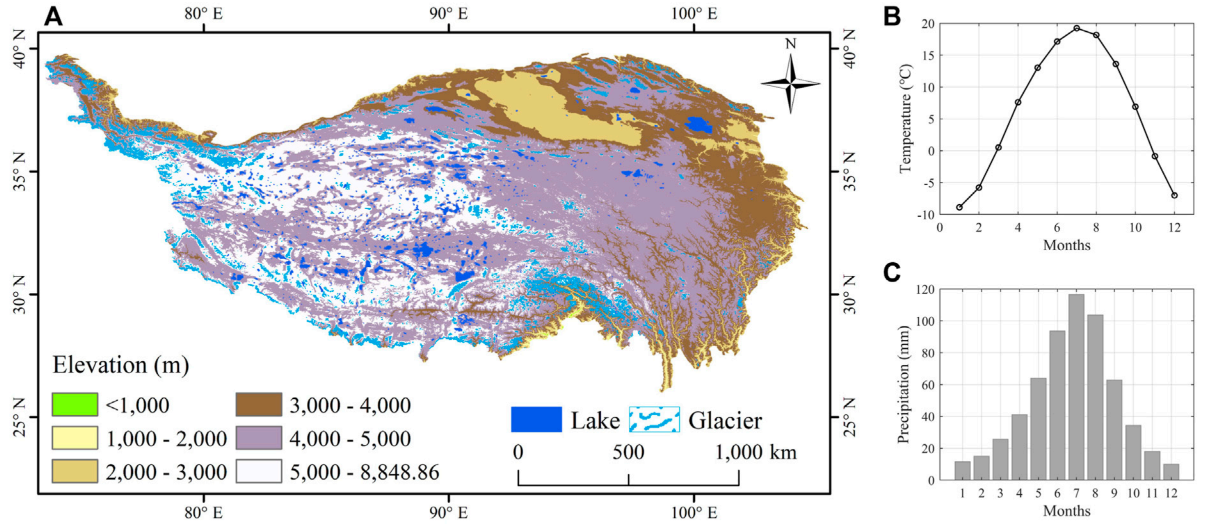

FIGURE 1
Study area **(A)**, boundary data for the Tibetan Plateau provided by the Global Change Science Research Data Publishing System (http://www.geodoi.ac.cn/WebCn/doi.aspx?Id=135), glacier vector data from the National Center for Glacial Permafrost Desert Science and Data (http://www.ncdc.ac.cn)[33], and lake data from Wan et al. (2016)[34]. **(B–C)** Mean monthly temperature and precipitation based on the CN05.

The average annual temperature of the Tibetan Plateau is about 6.1°C, with the average temperature in summer being above 15°C and the average temperature in winter below -5°C (Figure 1B). The average annual precipitation on the plateau is about 596 mm, with rainfall mainly occurring between May and September (Figure 1C).

2.2 Data sources

2.2.1 Climate data

Temperature and precipitation datasets were obtained from the China National Meteorological Information Center (CNMIC, https://data.cma.cn/). The period covered from January 1961 to December 2020, with a spatial resolution of 0.5° × 0.5° (CN05). The accuracy of the CN05 dataset was assessed using strict quality control, which included cross-validation and error analysis. We calculated the temperature and precipitation for winter (December; January and February the following year), spring (March-May), summer (June-August), and autumn (September-November). The seasonal division here refer to Cai's result (Cai et al., 2017).

Evapotranspiration (ET) and vegetation transpiration data were collected from the Global Land Evaporation Amsterdam Model (GLEAM v3.5; https://www.gleam.eu/), which is based on satellite and reanalysis data (ERA5 net radiation and air temperature) and has a temporal span of January 1980-December 2020, with a spatial resolution of 0.25°.

2.2.2 Vegetation index

The Normalized Difference Vegetation Index-third generation (NDVI) data using the Global Inventory Monitoring and Modeling System (GIMMS), GIMMS NDVI 3 g (https://ecocast.arc.nasa.gov/data/pub/gimms), with the time range of 1981–2015, spatial resolution 1/12° (roughly 8 km). In this study, NDVI data for 2002–2015 is used to reveal the vegetation index variation characteristics of the Tibetan Plateau. NDVI <0.3, represent low coverage; 0.3 ≤ NDVI <0.5, moderate coverage; 0.5 ≤ NDVI, high coverage.

2.2.3 GRACE data

In this study, the GRACE Level-2 data was released by the University of Texas Center for Space Studies (UTCSR, http://www2.csr.utexas.edu/grace/) for April 2002- June 2017 from the mass concentration blocks (Mascons) method, with a spatial resolution of 0.25°. The dataset comprised data from 183 months with 20 missing values (June-2002, July-2002, July-2003, January-2011, June-2011, May-2012, October-2012, March-2013, August-2013, September-2013, February-2014, July-2014, December-2014, June-2015, October-2015, November-2015, April-2016, September-2016, October-2016, and February-2017). The missing values of terrestrial water storage anomaly (TWSA) were filled using the multiyear mean of a missing month and the TWSA of its nearest month (Long et al., 2015).

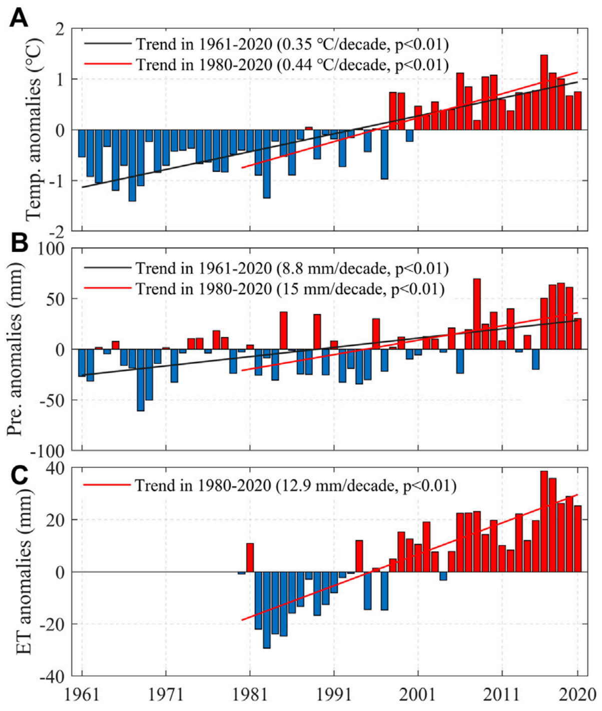

FIGURE 2
The anomalies of climate variables in the Tibetan Plateau from 1961 to 2020, **(A)** temperature anomalies, **(B)** precipitation anomalies, and **(C)** evapotranspiration (ET) anomalies (from 1980 to 2020). The base period of anomalies is 1981–2010.

2.3 Methodology

2.3.1 Terrestrial water storage calculations

The GRACE twin satellites, launched in March 2002, collaborate with the US space agencies (NASA) and the German aerospace center (DLR). The satellites use a precise microwave ranging system, based on the satellite-to-satellite tracking in the low-low model (SST-LL), to measure the distance between themselves due to gravitational acceleration. Onboard GPS instruments determine the exact position of the satellites over the Earth. The GRACE measures changes in Earth's gravity field, which after deducting tidal effects (including sea tides, solid tides, and polar tides generated by the Earth's rotation), as well as non-tidal atmospheric and oceanic effects, the signal changes largely reflect changes in total water storage on the seasonal scale (Rodell and Famiglietti, 1999).

In this study, the monthly TWS anomaly (TWSA) data of GRACE RL06 Mascon solutions (version 02) from the Center for Space Research (CSR RL06 v02). The solutions with all the appropriate corrections applied (ellipsoidal correction, C20, degree 1, GIA, etc.) in 0.25° grids. The ellipsoidal correction of CSR RL06 v02 for mass anomaly grid representation has been applied as described by Ditmar (2018). The C20 (degree two order 0) coefficients are replaced with the C20 solutions from satellite laser ranging (SLR) (Loomis et al., 2019) for consistency with all the other solutions. The degree-1 coefficients (Geocenter) corrections are applied using the estimates in TN-13a (available at https://podaac-tools.jpl.nasa.gov/drive/files/allData/grace/docs/TN-13_GEOC_CSR_RL06.txt). A glacial isostatic adjustment (GIA) correction has been applied based on the model ICE6G-D (Peltier et al., 2018). On this basis, the TWSA in the endorheic of the Tibetan Plateau during March 2002-June 2017 (the basis period of anomaly is January 2004-December 2009, and the observation series of this period without missing value) is obtained, and then to analyze the seasonal and interannual variations of TWSA.

2.3.2 Net precipitation calculation

Net precipitation is a key hydrological variable directly related to water resources. The net precipitation (net pre) is equal to the precipitation (P) minus the evapotranspiration (ET) (Equation 1). As precipitation data for the CN05 are spatially resolved at 0.5°, evapotranspiration data are spatially resolved at 0.25°, so we resample the evapotranspiration data to 0.5° here. Resampling is performed here using Matlab's griddata function.

$$net\ pre = P - ET \tag{1}$$

Where net pre represents net precipitation (mm), P is precipitation (mm), and ET is evapotranspiration (mm).

2.3.3 Trend rate estimate

In this study, we applied the Mann-Kendal (M–K) nonparametric method to detect trends of temperature, precipitation, evapotranspiration, transpiration, and NDVI in the Tibetan Plateau. Furthermore, the trend rate was estimated using Sen's (1968) nonparametric trend estimator.

3 Results

3.1 Recent climate change in Tibetan Plateau

In this study, we first analyze the climate change (including temperature, precipitation, and evapotranspiration) in the Tibetan Plateau during 1961–2020 due to climate warming being the main driving force for changes in TWSA on the Tibetan Plateau. Figure 2A shows that the warming rate of temperature was 0.35°C/decade ($p<0.01$) during 1961–2020, while it reached 0.44°C/decade ($p<0.01$) during 1981–2020, which was nearly 0.1°C/decade faster. The results of the Tibetan Plateau temperature anomalies (the basis period of anomaly is 1981–2010) during the past 60 years indicate that the anomalies were negative before 1990 and positive after 2000

TABLE 1 The average values and trend rates (per decade) of temperature (°C), precipitation (mm), and actual evapotranspiration (mm) in different periods of the Tibetan Plateau.

	Temperature		Precipitation		Evapotranspiration	
	Average	Trend	Average	Trend	Average	Trend
1961–1990	-2.49	0.17**	365.1	3.0	-	-
1971–2000	-2.15	0.23**	369.0	-3.5	-	-
1981–2010	-1.75	0.59***	374.9	13.4**	277.5	16.5***
1991–2020	-1.30	0.44***	387.4	26.9***	290.1	11.4***

Note: Temperature and precipitation data are collected from 1961 to 2020, and actual evapotranspiration data is collected from 1980 to 2020. "***" indicate that the results pass the significance test at the 0.01 confidence level ($p < 0.01$), and "**" denotes that the results pass the significance test at the 0.05 confidence level ($p < 0.05$). "-" represent no data record.

(Figure 2A). The anomaly in the 1960s was about -1°C while it reached 1°C in the 2010 s, indicating that the average temperature of the Tibetan Plateau has increased by 2°C in recent 60 years.

Precipitation has also increased on the Tibetan Plateau over the past 60 years. The precipitation anomaly was mainly negative before 1990 and positive after 1990 (Figure 2B). The increased rate of precipitation is 15.0 mm/decade ($p<0.01$) from 1980 to 2020 was nearly twice as fast as that from 1961 to 2020 (8.8 mm/decade, $p<0.01$). The increased water vapor content caused by temperature rise is essential for the annual average precipitation increase over the Tibetan Plateau. At the same time, it has also been pointed out that there are significant spatial differences in precipitation on the Tibetan Plateau (Yao et al., 2022), with a decrease in precipitation in the monsoon-controlled southern and southeastern exorheic river basin and an increase in precipitation in the westerly-controlled northwestern endorheic basin (Zhu et al., 2019). Meanwhile, the evapotranspiration on the Tibetan Plateau shows an increasing trend (12.9 mm/decade, $p<0.01$) during the period 1980–2020 (Figure 2C), which is slower than the rate of increase in precipitation during the same period.

The trend rates of temperature, precipitation, and evapotranspiration for different climatic periods are shown in Table 1. The results showed that the temperature warming rate was 0.17°C/decade ($p<0.05$) in 1961–1990 and 0.23°C/decade ($p<0.05$) in 1971–2000, respectively, while the precipitation increased or decreased is insignificant. During the period 1981–2010, the temperature warming rate reached 0.59°C/decade ($p<0.01$), and the precipitation increase rate was 13.4 mm/decade ($p<0.05$). The rapid increase in temperature during this period accelerated the increase in evapotranspiration to 16.5 mm/decade ($p<0.01$), which exceeded the increase in precipitation. During the period 1991–2020, the warming rate of temperature was 0.44°C/decade ($p<0.01$), the rate of increase in precipitation reached 26.9 mm/decade ($p<0.01$), and the rate of increase in evapotranspiration slowed down (11.4 mm/decade, $p<0.01$). The rapid increase in precipitation during this period slowed the rate of warming during this period, which in turn affected the changes in evapotranspiration.

The average temperature of the Tibetan Plateau increased steadily in all seasons, but the warming rates of different seasons differed in different periods (Figures 3A,B). During 1961–1990, the warming rates of winter and autumn were higher than in spring and winter. The warming rates of summer and autumn were faster than winter and spring from 1971 to 2000. During 1981–2010, the warming rate exceeded 0.4°C/decade, more than other periods, especially in winter, nearly to 0.8°C/decade. During 1991–2020, the warming rate in winter and autumn exceeded 0.6°C/decade faster than in spring and summer (<0.4°C/decade).

The mean summer precipitation on the Tibetan Plateau has steadily risen over the four climatic periods, while the other season's precipitation has remained relatively stable (Figure 3C). During 1961–1990, except for a slight decrease in summer precipitation, the other seasons showed an upward trend (Figure 3D). Precipitation increased in winter and autumn from 1971–2000 but declined in spring and summer. Meanwhile, precipitation increased in spring and summer but decreased in winter and autumn from 1981 to 2010. From 1991 to 2020, except for winter, which showed a slightly declining trend, all other seasons showed an upward trend, especially summer, nearly 15 mm/decade. Therefore, precipitation increased on the Tibetan Plateau in summer but decreased in winter.

In the context of increasing temperature and precipitation, the actual evapotranspiration on the Tibetan Plateau also tends to rise (Figure 3E). The actual evapotranspiration for all seasons on the Tibetan Plateau in 1991–2020 is higher than in 1981–2010 (Figure 3F). However, the increasing trend of evapotranspiration in 1991–2020 is slower than in 1981–2010, except for winter, which is faster than in 1981–2010.

There are apparent seasonal differences in the changes in precipitation and actual evapotranspiration under the ongoing warming of the Tibetan Plateau. The increasing trend of precipitation in spring and summer is greater than the rising rate of actual evapotranspiration, while it is the opposite in autumn and winter. Therefore, it will aggravate the water storage deficit in the winter half-year on the Tibetan Plateau.

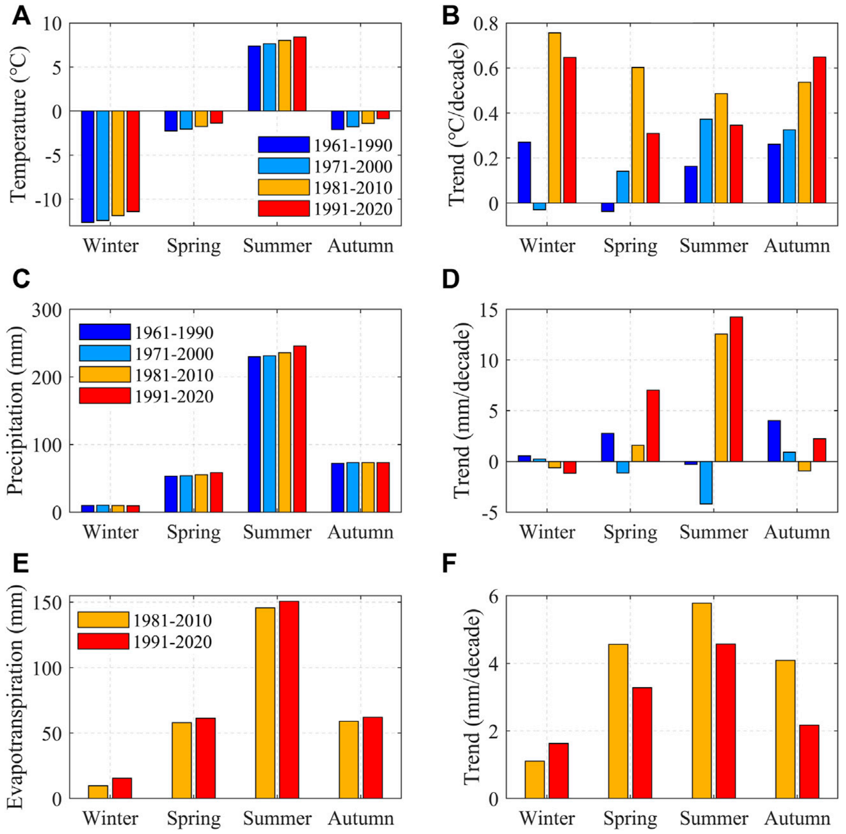

FIGURE 3
Seasonal changes of climate variables in the Tibetan Plateau. From left to right: results for averaged value and trend. From top to bottom: results for temperature **(A–B)**, precipitation **(C–D)**, and evapotranspiration **(E–F)**.

3.2 TWSA changes in Tibetan Plateau

The changes in TWSA on the Tibetan Plateau have noticeable stage differences (Figure 4A). From 2003 to 2012, the changes in TWSA were relatively stable, with positive anomalies in summer and autumn and negative anomalies in winter and spring; from 2012 to 2016, annual and seasonal variations of TWSA showed a downward trend. The results in Figure 4B show that the seasonal TWSA has a corresponding good relationship with net precipitation. The net precipitation in June-September is positive, and the connected water storage is positive. In contrast, the net precipitation from October to the following January is negative, but the TWSA in these 4 months is also positive due to the summer's surplus effect of summer positive TWSA. From February to April, the net precipitation was negative, the corresponding TWSA was negative, and the net precipitation in May was favorable. The TWSA was negative, mainly affected by the winter's deficit effect in winter negative TWSA. Therefore, in general, the response of terrestrial water storage changes to net precipitation is leg 1–3 months over the Tibetan Plateau.

Figure 5A shows that the TWSA negative anomalies occurred in the southern and eastern parts of the Tibetan Plateau and the southern part of the endorheic basin. The most significant negative anomalies in TWSA at the Yarlung Zangbo River bend. The northern part of Inner TP and Qaidam basin are positive anomalies in TWSA. According to the results of Figure 4A, the whole study period can be divided into two stages: 2003–2011 and 2012–2016. From 2003 to 2011, the spatial range of positive and negative anomalies in TWSA was similar (Figure 5B). However, from 2012 to 2016, the spatial range of positive anomalies in TWSA was narrowed to the endorheic basin, while most region of the Tibetan Plateau was a negative anomaly, especially at the Yarlung Zangbo River bend, which reached -500 mm (Figure 5C). Similarly, seasonal TWSA also shows the same spatial pattern (Supplementary Figure S1). This indicates that the extent and scope of the TWSA deficit are increasing on the Tibetan Plateau, reflecting the increasingly profound impact of climate warming on the water system on the Tibetan Plateau.

The spatial pattern of the annual (Figure 6A1) and seasonal (Figures 6B1–E1) TWSA variation is consistent,

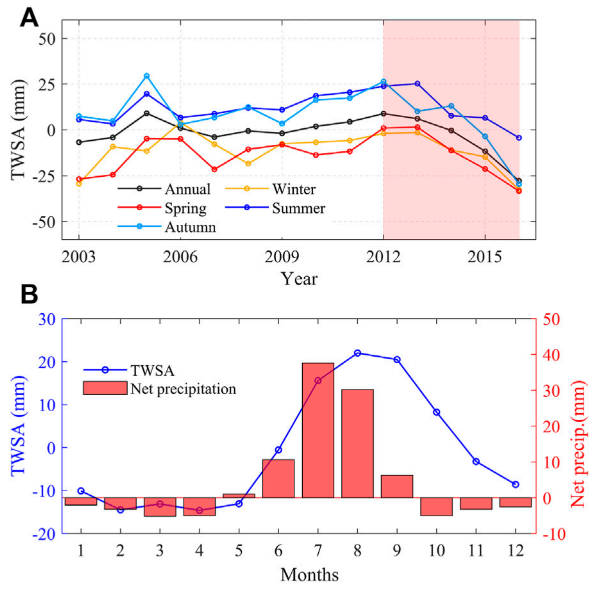

FIGURE 4
The TWSA in the Tibetan Plateau from 2003 to 2016. **(A)** is annual and seasonal TWSA, and **(B)** is monthly TWSA and net precipitation (precipitation minus actual evapotranspiration). The anomalies base period of TWSA and net precipitation is between January 2004 and December 2009.

both showing an increase in the endorheic basins and a decrease in the exorheic basins. We calculate the TWSA relationship with temperature and net precipitation using partial correlation analysis. In addition, we resample TWSA data to 0.5° since temperature and net precipitation have a 0.5° spatial resolution. The partial correlation analysis result shows that the negative correlation between annual TWSA and temperature in the Tibetan Plateau, except for the endorheic basin (Figure 6A2). Figure 6A3 indicated that the positive correlation between annual TWSA and net precipitation in the Yangtze River basin and the northeastern part of the endorheic basins. In contrast, a negative correlation is found between the Qaidam Basin and the north part of the Yellow River basin (Figure 6A3). In winter, the TWSA positively correlates with temperature (Figure 6B2) and net precipitation (Figure 6B3) in the exorheic basins. In contrast, those in the endorheic basins and the Qaidam Basin negatively correlate with net precipitation. In spring, the change of TWSA is negatively correlated with temperature in most regions of the Tibetan Plateau (Figure 6C2), except for the northeastern endorheic basins and the western part of the Qaidam Basin. In summer, the variation of TWSA in the endorheic zone is positively correlated with temperature (Figure 6D2), while it is positively correlated with net precipitation in the exorheic basins (Figure 6D3). In autumn, the decreasing TWSA region has a significant negative correlation with temperature (Figure 6E2), and the increasing TWSA region positively correlates with temperature and net precipitation (Figure 6E3). Overall, temperature determines the spatial pattern of TWSA variations, as plateau warming accelerates the retreat of the cryosphere, changes in precipitation types, and vegetation changes, which in turn drive changes in TWSA.

The warming rate over most regions of the Tibetan Plateau exceeded 0.04°C/yr from 2000 to 2019 and even exceeded 0.06°C/yr (Figure 7A). During this period, increasing precipitation in most regions (Figure 7B), including the Yangtze River basin, Yellow River basin, Qilian Mountains, and the western and northern parts of the endorheic basins, while decreasing precipitation was observed in the southeastern part of the endorheic basins, Yarlung Zangbo River Basin, and the Hengduan Mountains. The evapotranspiration in most areas of the Tibetan Plateau shows an increasing trend. In contrast, the endorheic zone, the Yellow River, and the Yangtze River Basin show a decreasing trend (Figure 7C). Net precipitation (precipitation minus actual evapotranspiration) increases mainly in the Yellow River and Yangtze River basins and the western part of the endorheic basins (Figure 7D) due to the increase in precipitation and decrease in evapotranspiration.

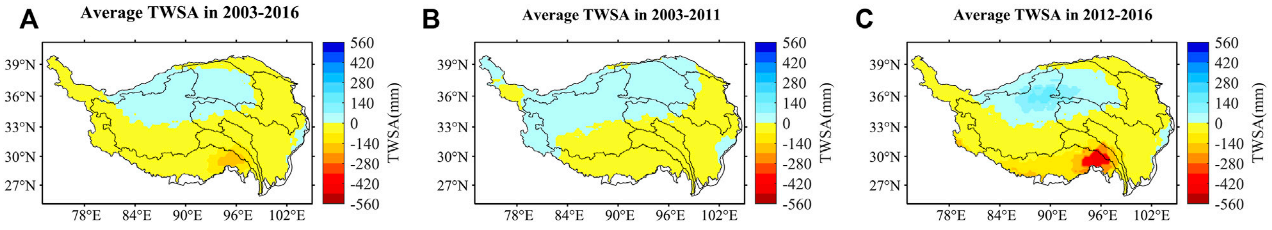

FIGURE 5
The spatial pattern of average annual TWSA in the Tibetan Plateau. **(A)** is averaged TWSA in 2003–2016, **(B)** is averaged TWSA in 2003–2011, and **(C)** is averaged TWSA in 2012–2016.

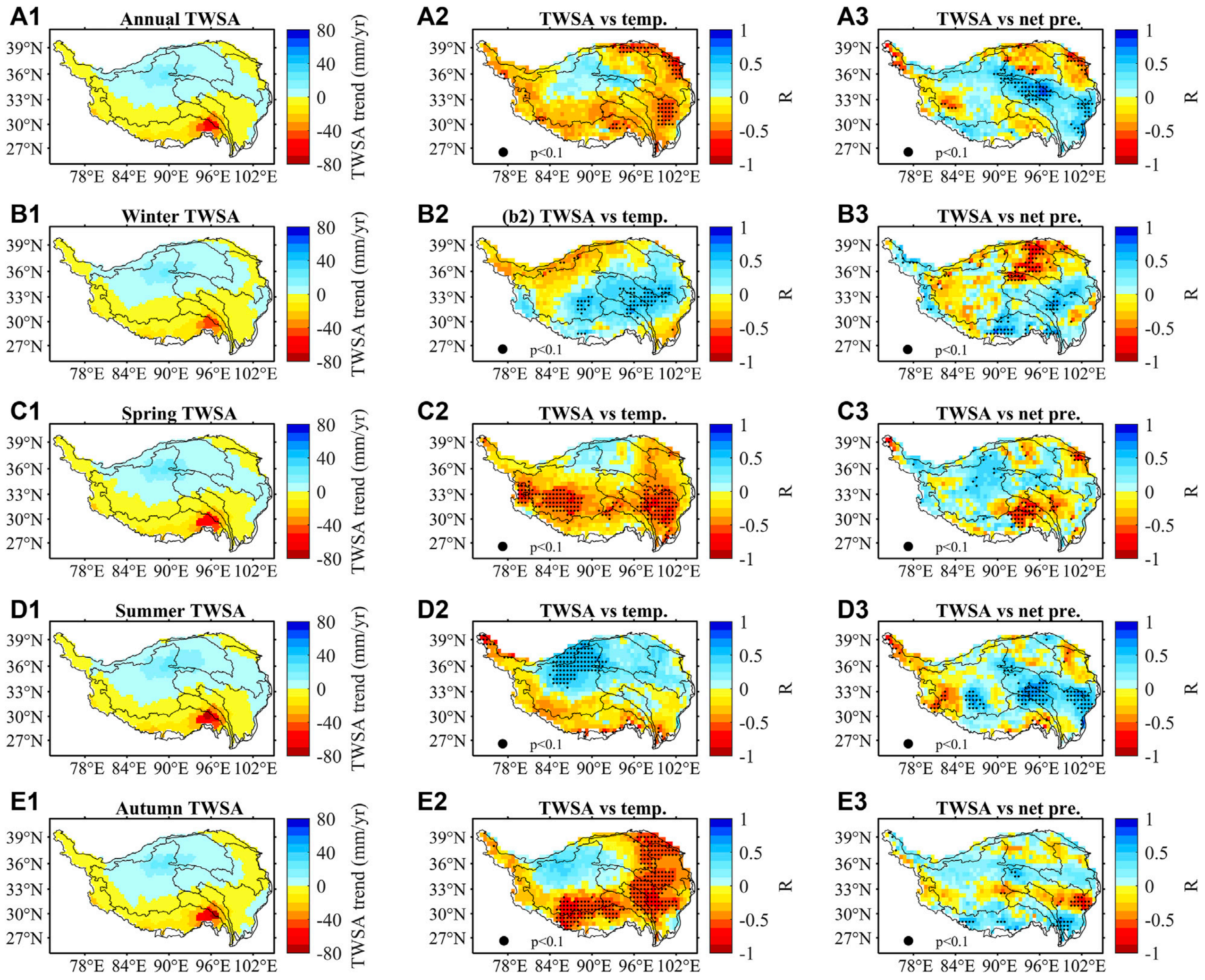

FIGURE 6
The spatial pattern of TWSA changes across the Tibetan Plateau from 2003 to 2016. From left to right: results for TWSA changes, the partial correlation between TWSA and temperature, and partial correlation between TWSA and net precipitation. From top to bottom: results for Annual, winter, spring, summer, and autumn. The black dots represent significance at the 0.1 confidence level ($p < 0.1$).

The reduction in net precipitation in the southern part of the Tibetan Plateau, the Hengduan Mountains, the Yarlung Zangbo River Basin, and the eastern part of the endorheic basins is mainly due to the decrease in precipitation. The reduction in net precipitation in the Qaidam Basin and the northeastern part of the endorheic basins is due to the increase in evapotranspiration that exceeds the increase in precipitation.

The empirical orthogonal function (EOF) analysis the mode of TWSA shows in the Figure 8. The first mode of TWSA represents the characteristics of TWSA changes in the Tibetan Plateau (Figure 8A), i.e., a surplus in the endorheic basins and a deficit in the exorheic basins. The second mode of TWSA represents the TWSA deficit in the northern part of the Tibetan Plateau after 2012 (Figure 8B). The third mode means the TWSA deficit in the western part of the endorheic basins (Figure 8C). Figure 8D show that the cumulative variance contribution of the first, second, and third modes reached 87%. On this basis, the correlation analysis results in Table 2 showed that the first mode of TWSA was mainly influenced by air temperature, while the second mode of TWSA was significantly negatively correlated with NDVI (r=-0.68, p<0.05). It indicates that air temperature determined the spatial pattern of the spatial variation of TWSA on the Tibetan Plateau, and vegetation change may also be an essential factor.

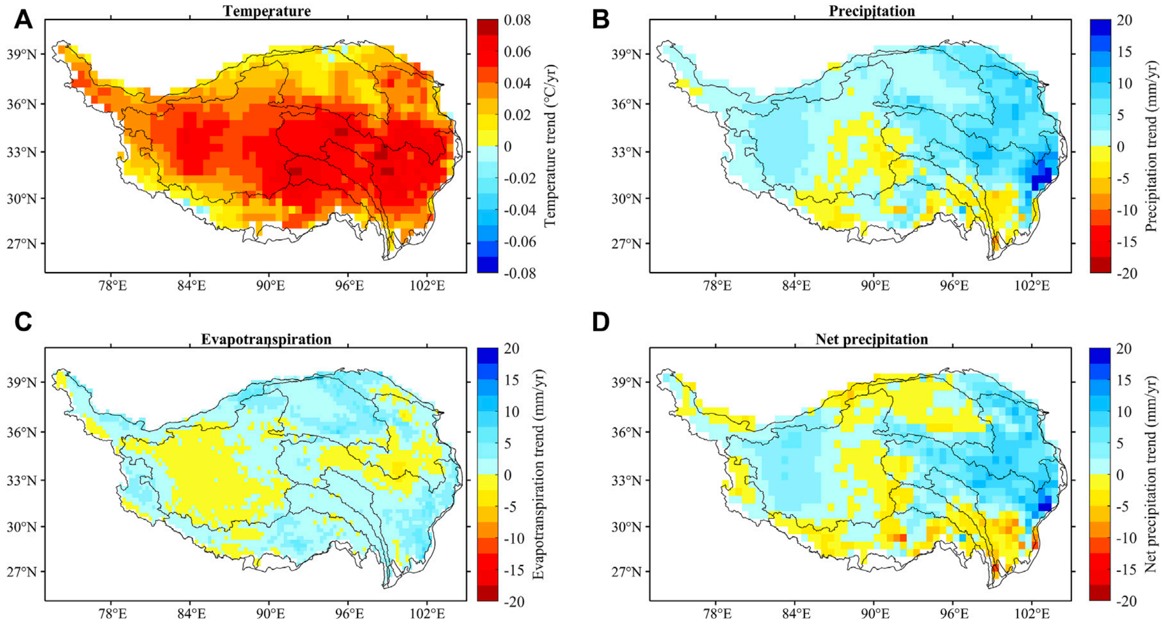

FIGURE 7
The spatial changes of temperature **(A)**, precipitation **(B)**, actual evapotranspiration **(C)**, and net precipitation **(D)** across the Tibetan Plateau during 2000–2019.

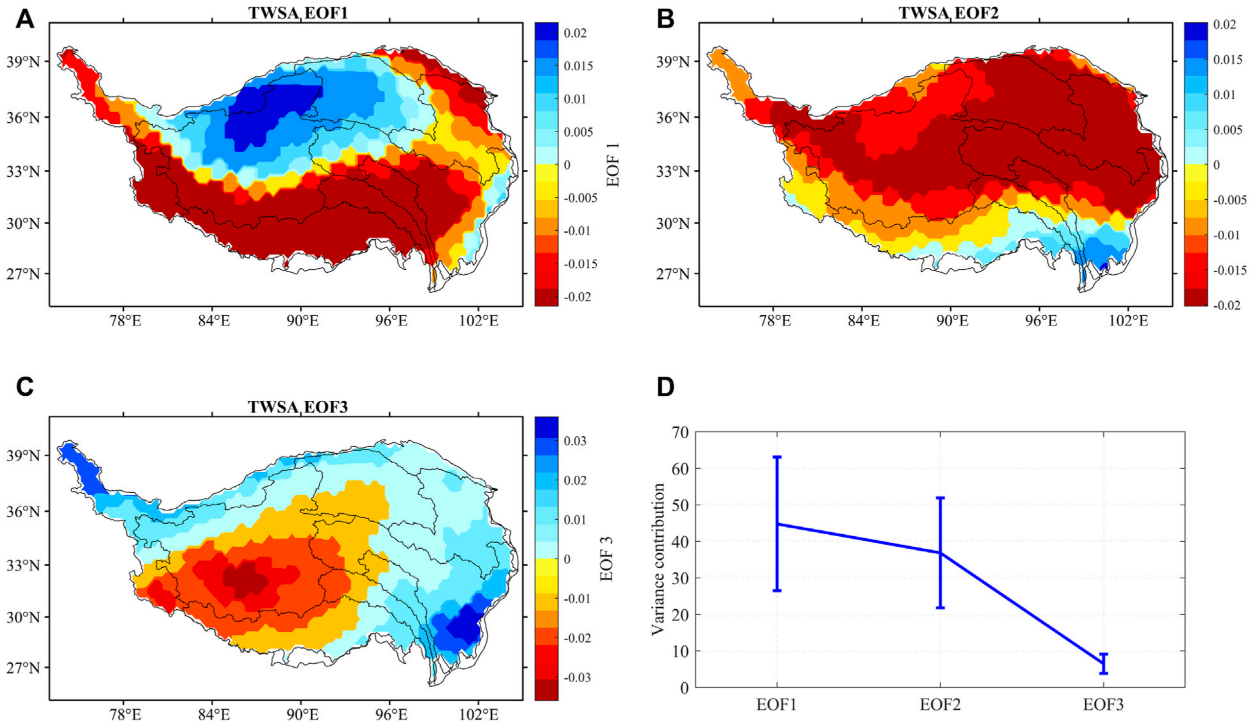

FIGURE 8
The spatial modes of TWSA in the Tibetan Plateau, **(A)** is EOF1, **(B)** is EOF2, **(C)** is EOF3, and **(D)** is variance contribution rate and error bar using the North test.

TABLE 2 The correlation between the time coefficient of EOF modes and climate factor.

	EOF1	EOF2	EOF3
Temperature	0.49*	0.29	-0.045
Net precipitation	-0.11	-0.03	-0.14
NDVI	0.33	-0.68**	0.30

Note: * $p<0.1$; ** $p<0.05$.

3.3 The relationship between TWSA changes and vegetation

Transpiration is an essential component of actual evapotranspiration and is directly related to vegetation. Figure 9A shows that the vegetation index (*NDVI* value) is higher in the eastern and southeastern parts of the Tibetan Plateau (*NDVI* > 0.5) and lower in other regions (*NDVI* < 0.3). Meanwhile, using 2004–2009 as a base period of anomaly (which is consistent with the TWSA), the results showed that the anomaly of *NDVI* in most regions of the Tibetan Plateau was between -0.025 and 0.025 *NDVI* (Figure 9B), but reached -0.1 *NDVI* at the Yarlung Zangbo River bend in the southern part of the Tibetan Plateau. The vegetation index changes in most areas of the Tibetan Plateau are not noticeable (-0.005 - 0.005 *NDVI*/yr) (Figure 9C) but significantly increased in the northeastern part of the Tibetan Plateau, the northeast part of the endorheic basins. The vegetation index decreased in the southern part of the Tibetan Plateau (-0.1 *NDVI*/yr), which is closely related to the TWS deficit. The transpiration change is directly related to the vegetation cover under warming in the Tibetan Plateau. In the higher vegetation cover area (*NDVI*>0.5, Figure 9C), when vegetation indexes decline, vegetation transpiration may be reduced (i.e., Yellow River Basin and Yangtze River Basin) or increased (southern Tibetan Plateau) (Figure 9D). However, in the lower vegetation cover area (*NDVI*<0.3), when the vegetation index decreases (i.e., the endorheic zone and the Qaidam Basin), vegetation transpiration will decrease (Figures 9C,D); when the vegetation index increases (i.e., northeastern endorheic basins, western Yarlung Tsangpo River Basin, and Indus Basin), vegetation transpiration will increase (Figures 9C,D).

In the Tibetan Plateau, the low proportion of vegetation canopy water to TWS means vegetation mainly influences TWSA through transpiration. Therefore, we analyzed the pattern of relationship between TWSA and transpiration on the Tibetan Plateau based on the singular value decomposition (SVD) method. The SVD decomposition results showed that the variance contribution of the first mode of TWSA reached 60.27% (Supplementary Figure S2). The spatial pattern of the first mode of TWSA was positively correlated in the endorheic basins and negative in the exorheic basin. Meanwhile, the

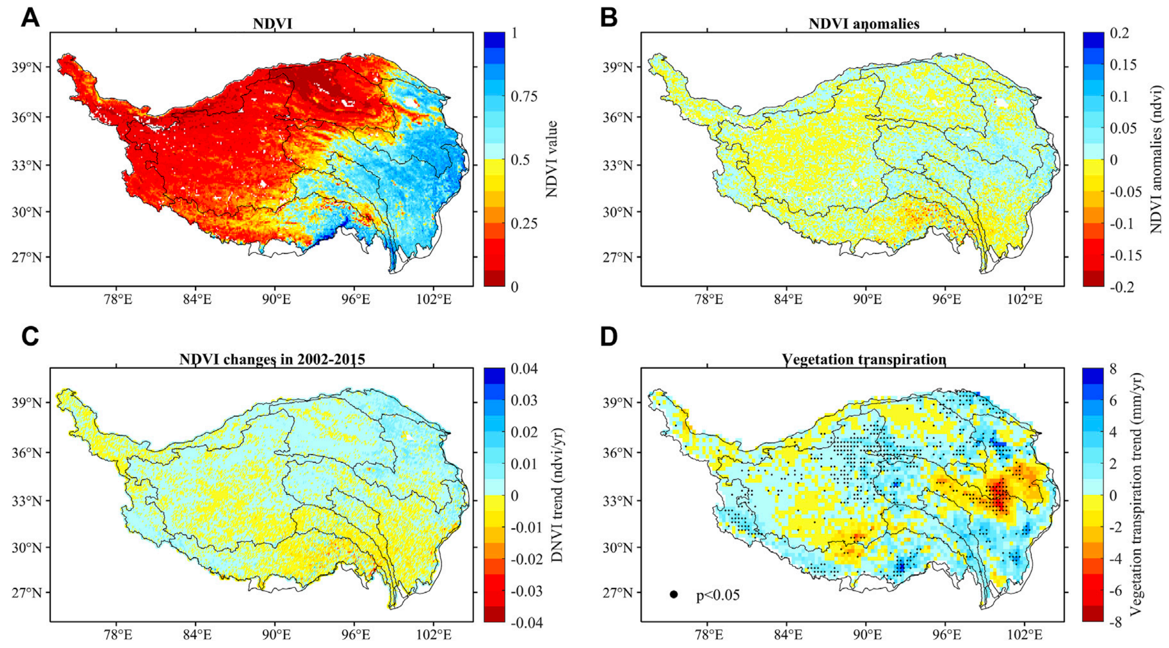

FIGURE 9
The changes in vegetation index and vegetation transpiration on the Tibetan Plateau between 2002 and 2015. **(A)** an annual average of NDVI; **(B)** an annual average of anomalies of NDVI are based on 2004–2009, with a similar base period for TWSA anomalies; **(C)** NDVI changes during 2002–2015; and **(D)** vegetation transpiration trends from 2002 to 2015.

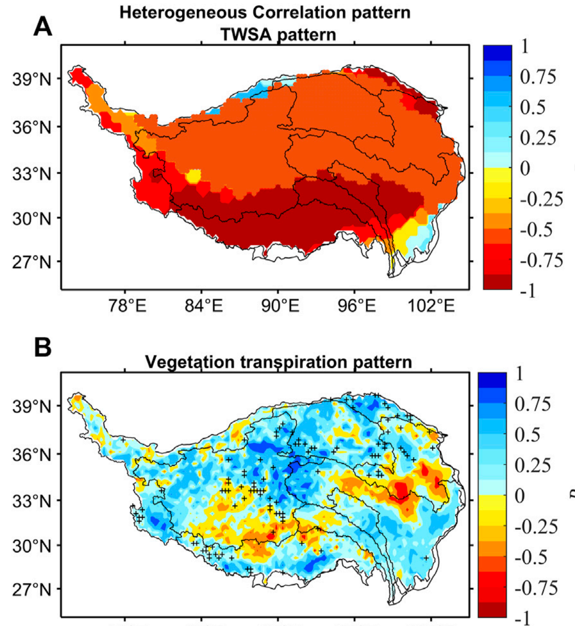

FIGURE 10
Heterogeneous correlation maps between the first mode of TWSA **(A)** and vegetation transpiration **(B)**. The black plus represents significance at 95%.

spatial pattern of the first mode of transpiration was positive in the endorheic basin and negatively correlated in the exorheic basin. The heterogeneous correlation results show that the correlation coefficients of the right field (transpiration) to the left field (TWSA) are all negatively related (Figure 10A), which indicates that the increase in transpiration is causing terrestrial water storage loss. However, the correlation is insignificance (p>0.05). It suggests that the transpiration increase will not contribute to the TWSA deficit under the current precipitation conditions (precipitation is more significant than actual evapotranspiration). The heterogeneous correlation coefficient of the left field (TWSA) to the right field (transpiration) (Figure 10B) shows a positive correlation in the northeastern part of the endorheic basins, while the exorheic basins and the western part of the endorheic basins show a negative correlation. It indicates that transpiration tends to increase in the TWSA surplus region while transpiration tends to decrease in the TWSA deficit region.

Therefore, there is a close relationship between TWSA and vegetation on the Tibetan Plateau. Under the current climatic conditions (the rate of increase in precipitation is faster than the increase in evapotranspiration), the effect of transpiration change on the TWSA is negative but insignificant. However, the impact of TWSA changes on vegetation transpiration is positively correlated, mainly occurring in the endorheic basin. The TWSA surplus in the northeastern endorheic zone is causing greening vegetation and increasing transpiration. In contrast, the TWSA deficit in the southern part of the endorheic basin is an important reason for the browning of vegetation and the decrease of transpiration.

4 Discussion

Increasing temperatures and precipitation on the Tibetan Plateau in the context of global warming have exacerbated uncertainties in the hydrological cycle processes in the region (Yao et al., 2019a). Since the mid-20th century, temperature and precipitation have increased on the Tibetan Plateau. The warming rate in the northern part of the Tibetan Plateau is faster than in other regions (Guo and Wang, 2012). The annual mean temperature warming rate on the Tibetan Plateau is faster than the global warming rate over the same period (Deng et al., 2017; Pepin et al., 2019). At the same time, the warming rate on the Tibetan Plateau increases with altitude, i.e., there is elevation-dependent warming (Yan et al., 2016; Pepin et al., 2019; You et al., 2020a), especially for below 5,000 m regions (Gao et al., 2018). This elevation-dependent warming will continue in the future (Guo et al., 2016; You et al., 2019). Precipitation increased at a rate of 1.4 mm/yr on the Tibetan Plateau during 1960–2014 (Deng et al., 2017). Meanwhile, snowfall increased in the Karakorum region and decreased in the Himalayas (Kapnick et al., 2014; You et al., 2020b).

In the context of global warming, the water storage of the Tibetan Plateau is undergoing dramatic imbalance, such as glacier retreat, snowpack reduction, permafrost degradation, lake expansion, and runoff increase (Chen et al., 2015; Yao et al., 2019b), which have received widespread attention from the scientific community. Glacier changes are sensitive to the response to plateau warming (Zhao et al., 2019). Spatially, glacier retreat rates are decreasing from the southeastern part to the inner Tibetan Pleau (Wang et al., 2019). In the last 50 years, glaciers on the Tibetan Plateau have been in negative mass equilibrium (Yao et al., 2019a), especially since the 1990s. From 2003 to 2009, the glacier's mass retreated across the Tibetan Plateau to -15.6 ± 10.1 Gt/yr (Neckel et al., 2014).

Spatial differences in temperature and precipitation variations on the Tibetan Plateau trigger spatial differences in glacier retreat, snowmelt, and terrestrial water storage, leading to regional differences in river runoff changes. Changes in TWSA on the Tibetan Plateau are closely related to precipitation; for example, increased water storage in the Yangtze River Basin and Yellow River Basin is associated with an increase in precipitation (Meng et al., 2019; Yang et al., 2019), while decreased TWSA is closely associated with decreased precipitation in the Yarlung Tsangpo River Basin (Deng et al., 2018). The TWSA (Figure 6A1) and net precipitation (Figure 7D) increased in the Yangtze River Basin headwaters and northeast of the endorheic basin. Thus, Figure 6A3 shows a positive correlation between TWSA and net precipitation. TWSA increased in the Qaidam Basin and the northern Yellow River Basin (the Datong River) due to glaciers and snow melting from surrounding mountains. Therefore, TWSA and net precipitation negatively correlate in the Qaidam Basin and the northern Yellow River Basin (Figure 6A3). Runoff increased in the Yangtze and Lancang River source areas due to rising temperatures (Li et al., 2013), while the Yellow River source area runoff decreased due to evapotranspiration and precipitation increased (Cuo et al., 2013). The runoff changes in the Yarlung Tsangpo River were determined by temperature and precipitation, but temperature played a more significant role than precipitation (Liu et al., 2018).

Vegetation is a vital medium for coupling the atmosphere-pedosphere- hydrosphere, and changing will impact the hydrological system. On the Tibetan Plateau, vegetation changes are strongly influenced by the Asian monsoon, particularly seasonal variations (Zhong et al., 2010). Thus, vegetation's spatial distribution is consistent with precipitation distribution, i.e., the vegetation index decreases from southeast to northwest (Figure 9A). Meanwhile, vegetation changes in response to precipitation with a 1-month lag (Zhong et al., 2010). On the Tibetan Plateau, the vegetation greening season advanced at a rate of 1.04 days/yr from 1982 to 2011 due to climate change (Zhang et al., 2013; Zhang et al., 2012). Different vegetation types will respond differently to climate change: alpine meadows and desert vegetation will shrink while shrubs and forests will expand (Zhao et al., 2011). During the growing season, the Tibetan Plateau may experience a slower rate of warming due to increased transpiration (Shen et al., 2015).

In the Tibetan Plateau, the low proportion of vegetation canopy water to TWS means vegetation mainly influences TWSA through transpiration (Deng et al., 2022). There, there is a complex correlation between changes in TWSA and the vegetation on the Tibetan Plateau. The impacts of vegetation changes on the TWSA is negative and insignificant under current climate change condition (precipitation increased rate faster than actual evapotranspiration increased). However, the effects of TWSA on vegetation changes were significant in the northeastern part of the endorheic basins. Thus, in the context of current climate change, the impact of vegetation change on TWSA on the Tibetan Plateau is relatively small compared to other climate factors.

5 Conclusion

There was an increase in annual temperatures, precipitation, and evapotranspiration on the Tibetan Plateau. Over the period 1961–2020, temperatures and precipitation increased at rates of 0.35°C/decade and 8.8 mm/decade, respectively. Over the decades 1980–2020, the Tibetan Plateau warmed by 0.44°C/decade, precipitation increased by 15.0 mm/decade, and evapotranspiration rose by 12.9 mm/decade. In spring and summer, precipitation increases faster than evapotranspiration. In contrast, precipitation increases slower than evapotranspiration in winter and autumn. It will exacerbate the TWSA deficit in the Tibetan Plateau throughout the winter half-year.

There are evident stages and spatial variability in TWSA on the Tibetan Plateau. TWSA changes were relatively stable from 2003 to 2011 but decreased from 2012 to 2016. Tibetan Plateau TWSA changes are laggards to net precipitation by approximately 1–3 months. Positive anomalies of TWSA occur in the northeastern endorheic basins, while negative anomalies occur at the Yarlung Zangbo River bend (less than -500 mm). TWSA changes on the Tibetan Plateau are negatively related to temperature because temperature rise accelerates the melting of solid water bodies. TWSA positively correlates with net precipitation in the Yangtze River basin and the northeastern endorheic basins while negatively correlates in the Qaidam and Yellow River basins. Overall, the Tibetan Plateau's TWSA spatial pattern is determined by temperature variation.

In areas with low vegetation cover (NDVI <0.3), transpiration decreases as the vegetation index decreases (i.e., in the western and southern portions of the endorheic basins and the Qaidam Basin), while transpiration increases as the vegetation index increases (i.e., in the northeastern part of the endorheic basins and on the Tibetan Plateau). SVD analysis indicates that the heterogeneous correlation coefficient of the right field (transpiration) to the left field (TWSA) indicates a negative correlation (but it is insignificant), indicating that even though increased transpiration does not result in a deficit of TWSA under the current climate change conditions (the increase in precipitation is faster than the increase in evapotranspiration). The heterogeneous correlation coefficient of the left field (TWSA) to the right field (transpiration) shows a positive correlation ($p<0.05$) in the northeastern part of the endorheic basins, while the western part of the endorheic basins and the exorheic basins show a negative correlation. It indicates that transpiration tends to increase in areas with TWSA surpluses and decrease in areas with TWSA deficits.

Data availability statement

The original contributions presented in the study are included in the article/Supplementary Materials, further inquiries can be directed to the corresponding author.

Author contributions

HD finished the analysis and writing of the paper. YC provides data and paper corrections. YL provides thesis data and editing. LW and XC edit papers. ZR and ZiZ offered suggestions for revision. ZoZ and SH corrected the paper.

Funding

This research was supported by the National Natural Science Foundation of China (41807159 and 41877167), and Public Welfare Scientific Institutions of Fujian Province (2022R1002005).

Acknowledgments

The authors are grateful to the Chinese Meteorology Administration (http://data.cma.cn/) for providing precipitation and temperature data.

Conflict of interest

The authors declare that the research was conducted in the absence of any commercial or financial relationships that could be construed as a potential conflict of interest.

Publisher's note

Supplementary material

The Supplementary Material for this article can be found online at: https://www.frontiersin.org/articles/10.3389/feart.2022.1004846/full#supplementary-material

References

Cai, D., Fraedrich, K., Sielmann, F., Zhang, L., Zhu, X., Guo, S., et al. (2015). Vegetation dynamics on the Tibetan plateau (1982–2006): An attribution by ecohydrological diagnostics. *J. Clim.* 28 (11), 4576–4584. doi:10.1175/jcli-d-14-00692.1

Cai, D., You, Q., Fraedrich, K., and Guan, Y. (2017). Spatiotemporal temperature variability over the Tibetan plateau: Altitudinal dependence associated with the global warming hiatus. *J. Clim.* 30 (3), 969–984. doi:10.1175/jcli-d-16-0343.1

Che, T., Hao, X., Dai, L., Li, H., Huang, X., and Xiao, L. (2019). Snow cover variation and its impacts over the qinghai-tibet plateau. *Bull. Chin. Acad. Sci.* 34 (11), 1247–1253. doi:10.16418/j.issn.1000-3045.2019.11.007

Chen, D. L., Xu, B. Q., Yao, T. D., Guo, Z. T., Cui, P., Chen, F. H., et al. (2015). Assessment of past, present and future environmental changes on the Tibetan Plateau (in Chinese). *Chin. Sci. Bull.* 60, 3025–3035. doi:10.1360/N972014-01370

Cuo, L., Zhang, Y., Gao, Y., Hao, Z., and Cairang, L. (2013). The impacts of climate change and land cover/use transition on the hydrology in the upper Yellow River Basin, China. *J. Hydrology* 502, 37–52. doi:10.1016/j.jhydrol.2013.08.003

Deng, H., Chen, Y., and Chen, X. (2022). Driving factors and changes in components of terrestrial water storage in the endorheic Tibetan Plateau. *J. Hydrology.* 612, 128225. doi:10.1016/j.jhydrol.2022.128225

Deng, H., Pepin, N., and Chen, Y. (2017). Changes of snowfall under warming in the Tibetan Plateau. *J. Geophys. Res. Atmos.* 122 (14), 7323–7341. doi:10.1002/2017jd026524

Deng, H., Pepin, N., Liu, Q., and Chen, Y. (2018). Understanding the spatial differences in terrestrial water storage variations in the Tibetan Plateau from 2002 to 2016. *Clim. Change* 151 (3), 379–393. doi:10.1007/s10584-018-2325-9

Ditmar, P. (2018). Conversion of time-varying Stokes coefficients into mass anomalies at the Earth's surface considering the Earth's oblateness. *J. Geod.* 92, 1401–1412. doi:10.1007/s00190-018-1128-0

Gao, Y., Chen, F., Lettenmaier, D. P., Xu, J., Xiao, L., and Li, X. (2018). Does elevation-dependent warming hold true above 5000 m elevation? Lessons from the Tibetan plateau. *npj Clim. Atmos. Sci.* 1, 19. doi:10.1038/s41612-018-0030-z

Guo, D., and Wang, H. (2012). The significant climate warming in the northern Tibetan Plateau and its possible causes. *Int. J. Climatol.* 32 (12), 1775–1781. doi:10.1002/joc.2388

Guo, J., Mu, D., Liu, X., Yan, H., Sun, Z., and Guo, B. (2016). Water storage changes over the Tibetan plateau revealed by GRACE mission. *Acta Geophys.* 64 (2), 463–476. doi:10.1515/acgeo-2016-0003

Jacob, T., Wahr, J., Pfeffer, W., and Swenson, S. (2012). Recent contributions of glaciers and ice caps to sea level rise. *Nature* 482 (7386), 514–518. doi:10.1038/nature10847

Kang, S., Guo, W., Wu, T., Zhong, Y. Y., Chen, R. S., Xu, M., et al. (2020). Cryospheric changes and their impacts on water resources in the belt and road regions. *Adv. Earth Sci. (in Chinese)* 35 (1), 1–17. doi:10.11867/j.issn.1001-8166.2020.002

Kapnick, S. B., Delworth, T. L., Ashfaq, M., Malyshev, S., and Milly, P. C. D. (2014). Snowfall less sensitive to warming in Karakoram than in Himalayas due to a unique seasonal cycle. *Nat. Geosci.* 7 (11), 834–840. doi:10.1038/ngeo2269

Li, L., Shen, H., Dai, S., Li, H., and Xiao, J. (2013). Response of water resources to climate change and its future trend in the source region of the Yangtze River. *J. Geogr. Sci.* 23, 208–218. doi:10.1007/s11442-013-1004-z

Li, X., Long, D., Scanlon, B. R., Mann, M. E., Li, X. D., and Tian, F. Q. (2022). Climate change threatens terrestrial water storage over the Tibetan Plateau. *Nat. Clim. Chang.* 12, 801–807. doi:10.1038/s41558-022-01443-0

Liu, C., Xu, C., Liu, Y., and Xie, X. W. (2020). Terrestrial water storage changes in three-River source region as detected based on GRACE RL06 data (in Chinese). *Journal of Geodesy and Geodynamics* 40 (10), 1092–1096. doi:10.14075/j.jgg.2020.10.019

Liu, J., Zhang, W., Liu, T., and Li, Q. (2018). Runoff dynamics and associated multi-scale responses to climate changes in the middle reach of the Yarlung Zangbo River Basin, China. *Water* 10, 295. doi:10.3390/w10030295

Long, D., Longuevergne, L., and Scanlon, B. R. (2015). Global analysis of approaches for deriving total water storage changes from GRACE satellites. *Water Resour. Res.* 51 (4), 2574–2594. doi:10.1002/2014WR016853

Long, D., Shen, Y., Sun, A., Hong, Y., Longuevergne, L., Yang, Y., et al. (2014). Drought and flood monitoring for a large karst plateau in Southwest China using extended GRACE data. *Remote Sensing of Environment* 155, 145–160. doi:10.1016/j.rse.2014.08.006

Loomis, B. D., Rachlin, K. E., and Luthcke, S. B. (2019). Improved Earth oblateness rate reveals increased ice sheet losses and mass-driven sea level rise. *Geophys. Res. Lett.* 46, 6910–6917. doi:10.1029/2019gl082929

Matsuo, K., and Heki, K. (2010). Time-variable ice loss in Asian high mountains from satellite gravimetry. *Earth and Planetary Science Letters* 290 (1-2), 30–36. doi:10.1016/j.epsl.2009.11.053

Meng, F., Su, F., Li, Y., and Tong, K. (2019). Changes in terrestrial water storage during 2003-2014 and possible causes in Tibetan Plateau. *J. Geophys. Res. Atmos.* 124, 2909–2931. doi:10.1029/2018jd029552

Neckel, N., Kropáček, J., Bolch, T., and Hochschild, V. (2014). Glacier mass changes on the Tibetan Plateau 2003–2009 derived from ICESat laser altimetry measurements. *Environ. Res. Lett.* 9, 014009. doi:10.1088/1748-9326/9/1/014009

Peltier, W. R., Argus, D. F., and Drummond, R. (2018). Comment on "An Assessment of the ICE-6G_C (VM5a) Glacial Isostatic Adjustment Model" by Purcell et al. *J. Geophys. Res. Solid Earth* 123, 2019–2028. doi:10.1002/2016jb013844

Pepin, N., Deng, H., Zhang, H., Zhang, F., Kang, S., and Yao, T. (2019). An examination of temperature trends at high elevations across the Tibetan plateau: The use of MODIS LST to understand patterns of elevation-dependent warming. *J. Geophys. Res. Atmos.* 124 (11), 5738–5756. doi:10.1029/2018jd029798

Pokhrel, Y., Felfelani, F., Satoh, Y., Boulange, J., Burek, P., Gadeke, A., et al. (2021). Global terrestrial water storage and drought severity under climate change. *Nat. Clim. Chang.* 11, 226–233. doi:10.1038/s41558-020-00972-w

Rodell, M., and Famiglietti, J. (1999). Detectability of variations in continental water storage from satellite observations of the time dependent gravity field. *Water Resour. Res.* 35 (9), 2705–2723. doi:10.1029/1999wr900141

Sen, P. K. (1968). Estimates of the regression coefficient based on kendall's tau. *Journal of the American Statistical Association* 63 (324), 1379–1389. doi:10.1080/01621459.1968.10480934

Shen, M., Piao, S., Jeong, S. J., Zhou, L., Zeng, Z., Ciais, P., et al. (2015). Evaporative cooling over the Tibetan Plateau induced by vegetation growth. *Proc. Natl. Acad. Sci. U. S. A.* 12 (30), 9299–9304. doi:10.1073/pnas.1504418112

Shen, M., Sun, Z., Wang, S., Zhang, G., Kong, W., Chen, A., et al. (2013). No evidence of continuously advanced green-up dates in the Tibetan Plateau over the last decade. *Proc. Natl. Acad. Sci. U. S. A.* 110 (26), E2329. doi:10.1073/pnas.1304625110

Song, C., Ke, L., Huang, B., and Richards, K. S. (2015). Can mountain glacier melting explains the GRACE-observed mass loss in the southeast Tibetan Plateau: From a climate perspective? *Global and Planetary Change* 124, 1–9. doi:10.1016/j.gloplacha.2014.11.001

Sun, Z., Long, D., Yang, W., Li, X., and Pan, Y. (2014). Reconstruction of GRACE data on changes in total water storage over the global land surface and sixty basins. *Water Resources Research* 56, e2019WR026250. doi:10.1029/2019WR026250

Syed, T. H., Famiglietti, J. S., Rodell, M., Chen, J., and Wilson, C. R. (2008). Analysis of terrestrial water storage changes from GRACE and GLDAS. *Water Resour. Res.* 44, W02433. doi:10.1029/2006wr005779

Wan, W., Long, D., Hong, Y., Ma, Y., Yuan, Y., Xiao, P., et al. (2016). A lake data set for the Tibetan Plateau from the 1960s, 2005, and 2014. *Sci. Data* 3, 160039. doi:10.1038/sdata.2016.39

Wang, J., Chen, X., Hu, Q., and Liu, J. (2020). Responses of terrestrial water storage to climate variation in the Tibetan Plateau. *Journal of Hydrology* 584, 124652. doi:10.1016/j.jhydrol.2020.124652

Wang, J., Song, C., Reager, J., Yao, F., Famiglietti, J. S., Sheng, Y., et al. (2018). Recent global decline in endorheic basin water storages. *Nat. Geosci.* 11 (12), 926–932. doi:10.1038/s41561-018-0265-7

Wang, N., Yao, T., Xu, B., Chen, A., and Wang, W. (2019). Spatiotemporal pattern, trend, and influence of glacier change in Tibetan Plateau and surroundings under global warming. *Bulletin of Chinese Academy of Sciences* 34 (11), 1220–1232. doi:10.16418/j.issn.1000-3045.2019.11.005

Xiong, C., Yao, R. Z., Shi, J. C., Lei, Y. H., and Pan, J. M. (2019). Change of snow and ice melting time in High Mountain Asia (in Chinese). *Chin Sci Bull* 64, 2885–2893. doi:10.1360/TB-2019-0085

Yan, L., Liu, Z., Chen, G., Kutzbach, J. E., and Liu, X. (2016). Mechanisms of elevation-dependent warming over the Tibetan Plateau in quadrupled CO2 experiments. *Climatic Change* 135 (3-4), 509–519. doi:10.1007/s10584-016-1599-z

Yang, K., Lu, H., Yue, S., Zhang, G., Lei, Y., La, Z., et al. (2019). Quantifying recent precipitation change and predicting lake expansion in the Inner Tibetan Plateau. *Climatic Change* 147, 149–163. doi:10.1007/s10584-017-2127-5

Yao, T., Xue, Y., Chen, D., Chen, F., Thompson, L., Cui, P., et al. (2019a). Recent Third Pole's rapid warming accompanies cryospheric melt and water cycle intensification and interactions between monsoon and environment: Multidisciplinary approach with observations, modeling, and analysis. *Bulletin of the American Meteorological Society* 100, 423–444. doi:10.1175/bams-d-17-0057.1

Yao, T., Bolch, T., Chen, D., Gao, J., Immerzeel, W., Piao, S., et al. (2022). The imbalance of the Asian water tower. *Nat. Rev. Earth Environ.* 3, 618–632. doi:10.1038/s43017-022-00299-4

Yao, T., Wu, G., Xu, B., Wang, W., Gao, J., and An, B. (2019b). Asian water tower change and its impacts. *Bulletin of Chinese Academy of Sciences* 34 (11), 1203–1209. doi:10.16418/j.issn.1000-3045.2019.11.003

You, Q. L., Zhang, Y. Q., Xie, X. Y., and Wu, F. Y. (2019). Robust elevation dependency warming over the Tibetan Plateau under global warming of 1.5°C and 2°C. *Climate Dynamics* 53, 2047–2060. doi:10.1007/s00382-019-04775-4

You, Q., Chen, D., Wu, F., Pepin, N., Cai, Z., Ahrens, B., et al. (2020a). Elevation dependent warming over the Tibetan plateau: Patterns, mechanisms and perspectives. *Earth-Science Reviews* 210, 103349. doi:10.1016/j.earscirev.2020.103349

You, Q., Wu, T., Shen, L., Pepin, N., Zhang, L., Jiang, Z., et al. (2020b). Review of snow cover variation over the Tibetan Plateau and its influence on the broad climate system. *Earth-Science Reviews* 201, 103043. doi:10.1016/j.earscirev.2019.103043

Zhang, G., Yao, T., Chen, W., Zheng, G., Shum, C., Yang, K., et al. (2019). Regional differences of lake evolution across China during 1960s-2015 and its natural and anthropogenic causes. *Remote Sensing of Environment* 221, 386–404. doi:10.1016/j.rse.2018.11.038

Zhang, G., Yao, T., Piao, S., Bolch, T., Xie, H., Chen, D., et al. (2017). Extensive and drastically different alpine lake changes on Asia's high plateaus during the past four decades. *Geophysical Research Letters* 44, 252–260. doi:10.1002/2016gl072033

Zhang, G., Zhang, Y., Dong, J., and Xiao, X. (2013). Green-up dates in the Tibetan Plateau have continuously advanced from 1982 to 2011. *Proc. Natl. Acad. Sci. U. S. A.* 110 (11), 4309–4314. doi:10.1073/pnas.1210423110

Zhang, T., Yang, X., Gu, W., Shu, X., and Jiang, M. (2012). Histological features of the gastric mucosa in children with primary bile reflux gastritis. *World J. Surg. Oncol.* 32 (1), 27–38. doi:10.1186/1477-7819-10-27

Zhao, D., Wu, S., Yin, Y., and Yin, Z. (2011). Vegetation distribution on Tibetan Plateau under climate change scenario. *Reg. Environ. Change* 11, 905–915. doi:10.1007/s10113-011-0228-7

Zhao, L., Hu, G., Zou, D., Wu, X., Ma, L., Sun, Z., et al. (2019). Permafrost changes and its effects on hydrological processes on qinghai-tibet plateau. *Bulletin of Chinese Academy of Sciences* 34 (11), 1233–1246. doi:10.16418/j.issn.1000-3045.2019.11.006

Zhong, L., Ma, Y., Salama, M. S., and Su, Z. B. (2010). Assessment of vegetation dynamics and their response to variations in precipitation and temperature in the Tibetan Plateau. *Climatic Change* 103, 519–535. doi:10.1007/s10584-009-9787-8

Zhu, L. P., Ju, J. T., Qiao, B. J., Yang, R. M., Liu, C., Han, B. P. (2019). Recent lake changes of the Asia Water Tower and their climate response: Progress, problems and prospects (in Chinese). *Chin Sci Bull* 64, 2796–2806. doi:10.1360/TB-2019-0185

Zhu, Y., Liu, S., Yi, Y., Li, W. Q., and Zhang, S. D. (2020). Spatiotemporal changes of terrestrial water storage in three parallel River basins and its response to ENSO (in Chinese). *Mountain Research* 2, 165–179. doi:10.16089/j.cnki.1008-2786.000499

frontiers | Frontiers in Earth Science

TYPE Original Research
PUBLISHED 31 October 2022
DOI 10.3389/feart.2022.1037668

Contribution of water rejuvenation induced by climate warming to evapotranspiration in a Siberian boreal forest

Hotaek Park[1,2]*, Tetsuya Hiyama[2] and Kazuyoshi Suzuki[3]

[1]Institute of Arctic Climate and Environment Research, JAMSTEC, Yokosuka, Japan, [2]Institute for Space—Earth Environmental Research, Nagoya University, Nagoya, Japan, [3]Institute of Arctic Climate and Environment Research, JAMSTEC, Yokohama, Japan

Check for updates

OPEN ACCESS

EDITED BY
Chunqiao Song,
Nanjing Institute of Geography and Limnology (CAS), China

REVIEWED BY
Haohao Wu,
Nanjing Institute of Geography and Limnology (CAS), China
Ning Ma,
Institute of Geographic Sciences and Natural Resources Research(CAS), China

*CORRESPONDENCE
Hotaek Park,
park@jamstec.go.jp

SPECIALTY SECTION
This article was submitted to Hydrosphere, a section of the journal Frontiers in Earth Science

RECEIVED 06 September 2022
ACCEPTED 13 October 2022
PUBLISHED 31 October 2022

CITATION
Park H, Hiyama T and Suzuki K (2022), Contribution of water rejuvenation induced by climate warming to evapotranspiration in a Siberian boreal forest.
Front. Earth Sci. 10:1037668.
doi: 10.3389/feart.2022.1037668

Water age is a useful metric to evaluate the influence of anthropogenic and natural forcings on the terrestrial water cycle. Current climate warming is enhancing the warming of permafrost soil in the Arctic. Although permafrost is a crucial component of the Arctic terrestrial water cycle, its influence on processes regulating the fluxes and ages of Arctic terrestrial water, particularly soil storage and evapotranspiration, is not well understood. In this study, a water age calculation scheme was implemented into the coupled hydrological and biogeochemical model (CHANGE) to assess the mechanisms through which climate warming affects the soil water storage–evapotranspiration–water age feedback cycle in a boreal forest. Continuous air temperature increase from 1980 to 2016 caused earlier snowmelt and soil thawing, inducing decreasing age trends in snow- and rain-sourced water. The younger water contributed to higher spring evapotranspiration. In summer, the higher evapotranspiration dried the surface soil layer. In turn, the drier surface layer increased the loss of fresh rainwater. Autumn precipitation, preserved in the frozen winter soil until the following spring, became an additional source of water and enhanced plant transpiration in the following summer. This increase accounted for 4.2% of the annual total transpiration. These results suggest that permafrost warming, characterized by earlier soil thawing and later freezing, induced higher evapotranspiration, thereby shortening the residence time of precipitation-sourced water in the active layer and further rejuvenating water in soil layers and in evapotranspiration. Under future climate warming conditions, this effect is expected to intensify and the water cycle will accelerate.

KEYWORDS

evapotranspiration, permafrost, water age, tracer module, climate warming

1 Introduction

Water age is defined as the time interval between the moment a water molecule enters the hydrological system and the moment it flows out (Sprenger et al., 2019). It is a useful metric to assess changes in water storages–fluxes interactions within the hydrological system (Pfister et al., 2017; Sprenger et al., 2018). In the Arctic terrestrial system, the hydrological processes regulating water storages and fluxes are completely different in winter, when soil freezes, and in summer, when soil thaws. Thus, the hydrological system, dormant during winter, experiences considerable phase changes in warmer seasons. These seasonal changes are driven primarily by air temperature. Meteorological observation data have revealed an increasing temperature trend in the Arctic over the past several decades, with particularly marked warming during spring (Bekryaev et al., 2010). Warmer air temperatures affect snowmelt (Kim et al., 2015; Zhang and Ma, 2018), soil thawing (Park et al., 2016a), and vegetation phenological and physiological activity (Ohta et al., 2014). In turn, such changes enhance water flux variations, increasing water loss *via* evapotranspiration and runoff (Holmes et al., 2015; Wang et al., 2021; Zhang et al., 2021). Water cycle alterations are reflected in water age variations (Hrachowitz et al., 2016).

Previous studies have estimated the non-stationary age of stream water by directly measuring inputs and outputs of isotopic tracers at catchments (Tetzlaff et al., 2014; Birkel and Soulsby, 2015; Rinaldo et al., 2015). Several process-based numerical models have also been developed, in which the incorporation of isotopic tracers effectively allowed scientists to estimate water ages in the absence of direct *in situ* measurements, and to better understand the physical processes for runoff generation in global catchments under different climates (Maneta and Silverman, 2013; Stadnyk et al., 2013; van Huijgevoort et al., 2016; Ala-aho et al., 2017, 2018; Piovano et al., 2019). Water loss by evapotranspiration to the atmosphere is a crucial process affecting terrestrial water storages and fluxes and, ultimately, water ages. Few water age studies have focused on evapotranspiration rather than on stream water. However, evapotranspiration measurements have shown an isotopic connection to groundwater sources (Good et al., 2015), while water ages have been estimated from evapotranspiration with process-based, coupled ecohydrological models incorporating isotopic tracers to calculate the energy balance in the atmosphere–vegetation–soil system (Sprenger et al., 2015; Kuppel et al., 2018). Other modeling studies have evaluated the influence of cold-region processes on evapotranspiration and source water ages (Smith et al., 2019). Unfortunately, quantitative information on the influence of permafrost on water flux ages in northern cold regions, using observations or tracer-based models, remains limited.

Permafrost is an important component of the hydrological system in the terrestrial Arctic. It has been increasingly affected by climate-change-induced warming and thawing (Biskaborn et al., 2019). Permafrost warming during summer caused an increase in the active layer thickness (ALT), defined as the maximum soil thawing depth (Li et al., 2022), thereby increasing water storage capacity in the active layer and, possibly, enhancing evapotranspiration (Suzuki et al., 2021). Observations also showed the sensitivity of evapotranspiration to higher soil moisture in the active layer of a Siberian boreal forest (Ohta et al., 2014; Kotani et al., 2019). Active-layer soil moisture depends primarily on inputs from snow meltwater in spring and precipitation in summer (Ma and Zhang, 2022), and on outputs from evapotranspiration. In addition, the water content of the active layer before soil thaws in spring is representative of moisture conditions from the preceding autumn (Park et al., 2021). Similarly, active-layer soil moisture conditions reflect climatic and ecohydrological events. This suggests that calculating the water age of evapotranspiration generated by this moisture might provide valuable information on the influence of permafrost warming on the soil freezing/thawing process, thus on evapotranspiration and soil moisture variations.

We have developed a water age calculation module, which uses five water isotopic tracers as modeling targets, and coupled it to our process-based land surface model (Park et al., 2021). The main objective of this study was to quantify, using the modified land surface model, the influence of climate-driven permafrost variations on model-simulated water storages, fluxes, and ages, particularly evapotranspiration water ages, of a boreal forest in 1980–2016. Using the model-simulated water ages, this study specifically investigated an important property of permafrost: the delay it induced on the response of soil water from precipitation to hydrometeorological forcings.

2 Materials and methods

2.1 General model description

This study used the process-based, coupled hydrological and biogeochemical land surface model (CHANGE: Park et al., 2011). CHANGE incorporates principles of hydrology, biology, ecology, geochemistry, and physiology to calculate momentum, heat, water and carbon quantities and partitioning, and tracer fluxes in the atmosphere–vegetation–snow–soil system, including all interactions between components and processes within the system (Park et al., 2011, 2018). The energy budget is calculated for the canopy, snow, and soil surface separately. The resulting available energy is used to derive evapotranspiration, snowmelt, and ground heat flux, as well as canopy, snow, and soil temperature. The mass conservation principle is also applied to solve the water budget for the surface layer. During snowmelt or precipitation events, the water input in the surface soil layer is divided into infiltration and surface runoff. The infiltrated water becomes a source of soil moisture and plant transpiration and generates a subsurface flow evacuated either in the permafrost table or at the bottom boundary layer. CHANGE explicitly represents water dynamics and heat fluxes in a soil column with a depth of 70 m and accounts for the freezing/thawing phase changes and the effects of organic carbon on the soil hydrothermal properties. The simulated ice content in frozen soil

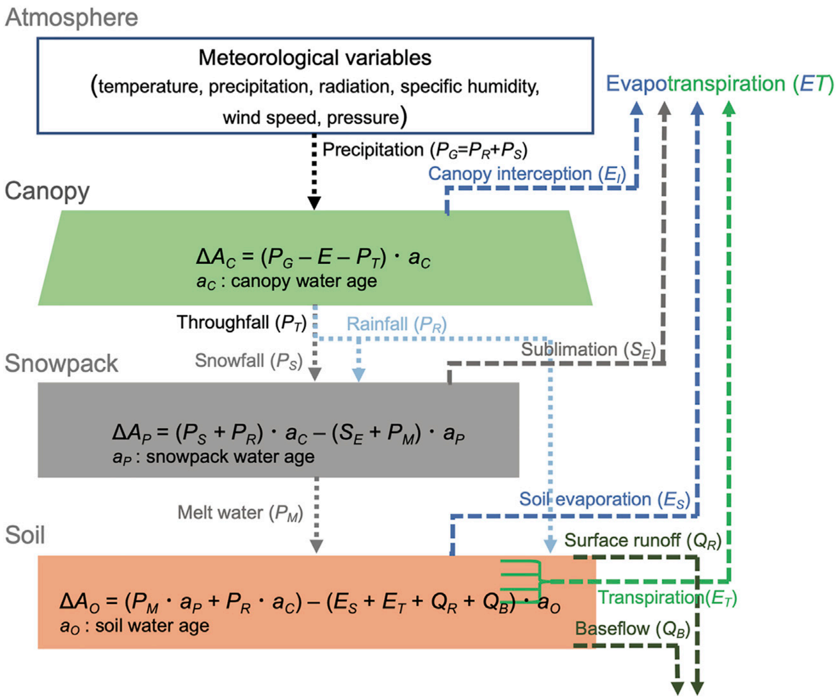

FIGURE 1
Schematic diagram of the water age calculation scheme for a one-dimensional water flow. Downward arrows represent water fluxes from upper to lower water storage pools, initiated in the atmosphere; upward arrows show water losses by evapotranspiration in individual storage pools.

layers increases their impedance to water flows. The layer impedance is parameterized as the soil moisture stress conditions associated with drying or freezing. Then, it is coupled to stomatal conductance and to the maximum carboxylation rate, which controls plant productivity and phenology. CHANGE also includes a coupled dynamic vegetation module that mechanistically simulates biogeochemical processes, including the carbon and nitrogen cycles in vegetation, litter, and soil, across multiple biomes.

Moreover, CHANGE includes a water isotope tracer module designed to characterize the spatiotemporal variability of isotopes and water sources, originating from precipitation and ground ice, in the hydrological system (Park et al., 2021). With this module, it is possible to quantify the contribution of ground ice meltwater induced by permafrost thawing to soil water storages and to the subsequent subsurface flow and evapotranspiration, especially the water footprint of permafrost degradation caused by climate warming.

2.2 Water age module

In a hydrological system, water input/output variations directly affect the water fluxes, thereby influencing the water age. In the new CHANGE module, water ages in storages (i.e., canopy, snowpack, and soil) are estimated along the one-dimensional water flow direction, with a scheme (Figure 1) similar to that used for tracer flux calculation (Park et al., 2021). The volumetric water age (A_i) variation in the lower storage (i), following an input of water (W_i) from the upper storage (i–1) at time step (t), is expressed as:

$$A_i^t = A_{i-1}^{t-1} - a_{i-1} F_{w,i} \Delta t \tag{1}$$

$$W_i^t = W_{i-1}^{t-1} - F_{w,i} \Delta t \tag{2}$$

$$a_{i-1} = A_{i-1} / W_{i-1} + \Delta t \tag{3}$$

where a_{i-1} is the water age in the upper storage, $F_{w,i}$ is the water flux from the upper storage, $\triangle t$ is the time step, and t–1 represents the previous time step. Conversely, the water age variation in the upper storage, induced by an upward water flux from the lower storage, is calculated with Eq. 4 and 5 of Park et al. (2021).

The simplifying assumption is that the water flux between storages is fully mixed, because the model essentially considers bulk tracer content values in fully mixed storages. The water mixing assumption is also applied to water age. In the water age calculation, the precipitation input age is set to zero. For example, the age of water intercepted by a dry canopy is zero, and thus the drip and evaporation rates are also zero. However, the age of water remaining on the canopy increases after each time step, so that new precipitation results in a younger canopy water age. Soil evaporation and plant transpiration remove water from a storage. The volumetric water age for evaporation (AE_i) from a storage (i) to the atmosphere at time step (t) is expressed as:

$$AE_i^t = AE_{i-1}^{t-1} + a_i E_{w,i} \Delta t \tag{4}$$

where $E_{w,i}$ represents the evaporative flux from the lower storage. Eq. 4 is also used to calculate water age variations from plant transpiration, derived using a partitioning function, and runoff. The age of water extracted by plant roots in each soil layer depends on the model-simulated plant transpiration and on soil water age. Therefore, the water age for plant transpiration is obtained by integrating over the individual layers. Additionally, dew formation is treated as an additional water input, resulting in younger water ages in the storages. For the snowpack, however, sublimation from the snow surface limits the production of snow meltwater, thus the snow age decreases. The snowpack age is also influenced by snowmelt and snowfall events.

The water flow between components of the hydrological system (i.e., canopy, snow, and soil) in the land surface scheme occurs sequentially downward, from the canopy to the snow then to the soil (Figure 1). Water ages for individual components are updated at each time step depending on the water fluxes. In permafrost, there is no water flux, thus the water age continuously increases. The water age scheme also assumes that the seasonal freezing/thawing phase change in the active layer does not affect soil water age. However, when the active layer thickens, the water age of the new active layer is expectedly younger, because of mixing with water from the upper layers or soil water loss by subsurface outflow. In our simulations, the water age of each soil layer was initialized to zero, because age observation data for frozen water or permafrost ice were not available. Therefore, simulated water ages for the permafrost layers below the active layer were nearly identical.

2.3 Study site and observations

The study site is located in eastern Siberia (62.2°N, 128.5°E), approximately 20 km north of Yakutsk. Climatological records at the study site from 1998 to 2010 indicate an annual mean air temperature (T_a) of −10.4°C and an annual mean precipitation (P_G) of 260 mm. Annual mean snowfall during winter (October–March) represents 40% of the annual mean precipitation, yielding a maximum snow depth of approximately 60 cm. Observations of the hydrometeorological variables at the study site were described by Kotani et al. (2019) and Hiyama et al. (2021). The study site is representative of a typical boreal forest landscape. A species of larch (*Larix cajanderi*) dominates the overstory, with a mean tree height of 18 m. The forest floor is covered by dense cowberry (*Vaccinium vitis-idaea*) and underlain by continuous, ice-rich permafrost. The study site has coarse humidified permafrost soils on heterogeneous sandy–loamy carbonate ground, textured by sand (74%), clay (15%), and loam (11%) with soil organic carbon content of 20 kg m^{-3}.

Meteorological records at the study site cover a limited time period and include dates without observations. These issues limit the model applicability for long-term simulations. To complement the observation records, the meteorological data were combined with ERA-Interim reanalysis data from the European Centre for Medium-Range Weather Forecasts (Dee et al., 2011). Continuous daily data from ERA-Interim were selected to reflect the local climatic conditions and to construct the primary forcing data for CHANGE by assimilating the observations acquired at the study site. Generation of the daily forcing data was described by Miyazaki et al. (2015).

2.4 Model simulations

A static land cover type, the boreal deciduous needleleaf forest, was set up for the CHANGE simulations. Vegetation phenology and physiology were prognostically estimated from the model output for carbon and nitrogen contents. Vertical profiles of thermal and hydraulic soil parameters were explicitly estimated on the basis of the measured soil texture fractions, which were then updated at each time step to account for the simulated soil organic carbon variations. The spin-up CHANGE simulation was conducted over 1,200 years with the detrended forcing data of the first 20 years and a CO_2 atmospheric concentration of 350 ppm. Dynamic equilibrium of the carbon and nitrogen contents for the total ecosystem was reached during the spin-up period. In this study, the hydrogen and oxygen isotopic ratios (δ^2H and $\delta^{18}O$) were excluded from the modeling variables, because dedicated CHANGE simulation results for δ^2H and $\delta^{18}O$ have previously been analyzed and validated (Park et al., 2021). Water ages were initialized to zero in all soil layers then updated by water exchanges caused by precipitation and evapotranspiration events during the spin-up period, to minimize the influence of initialization values on the simulation results, at least in the active layer.

The warming of the Arctic climate, particularly significant in the cold seasons (Bekryaev et al., 2010), is a major forcing factor affecting terrestrial hydrological processes. The Arctic terrestrial air temperature has increased by approximately 1.5–2.0°C during the past 4 decades (Bekryaev et al., 2010; Park et al., 2017). The study site has also recorded extreme increases in summer precipitation of 30–70 mm during 2004–2008 relative to the average of 150 mm during 1979–2013 (Iijima et al., 2016). These rates of change were adopted as thresholds for investigating the model sensitivity to extreme climatic events as well as plant responses to such changes. To investigate the sensitivity of water age to climate

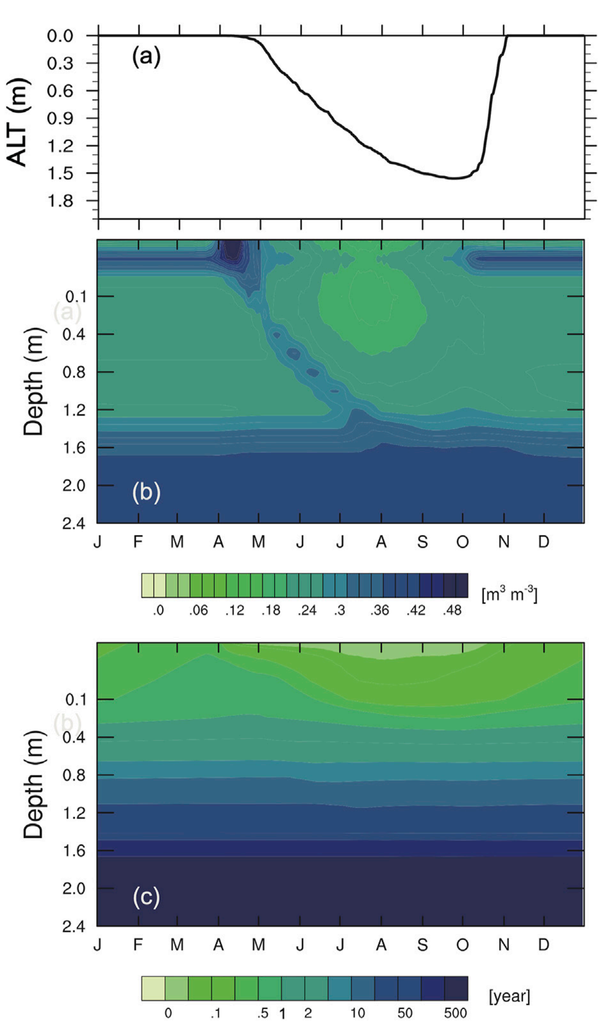

FIGURE 2
Seasonal variability, for the reference simulation, of climatological (1980–2016) daily averages for **(A)** the active layer thickness, and for the vertical profiles of **(B)** soil moisture and **(C)** water age. The vertical scale for the 0–0.4 m soil layer in Panels **(B)**–**(C)** is logarithmic.

warming, four simulations were conducted for the period 1980–2016, with the settings of the original simulation but with perturbed values of the air temperature and precipitation: a constant increase of the daily mean T_a by 2°C and 4°C (simulations EX_{T2} and EX_{T4}, respectively), a combined increase of T_a by 2°C and P_G by 30% (simulation EX_{T2C_P30}), and a simulation based on EX_{T2} but with a root depth increased to 1.06 m from the original depth of 0.58 m (EX_{T2_RT}). We also conducted an additional simulation to investigate the influence of autumn precipitation on evapotranspiration in the following year, also based on EX_{T2} but with P_G values reduced by 30% in August–September. The simulation results were then compared with the reference simulation.

3 Results

3.1 Soil moisture and water age

Climatological daily averages (averages for the same day over the whole study period) were calculated from the simulation results from 1980 to 2016, for the ALT and for vertical profiles of the soil moisture and of the water age. Their seasonal variations are presented in Figure 2. The ALT results showed typical seasonality, with soil thawing starting in mid-April and reaching its maximum in early October (Figure 2A). In April, snow began to melt at the study site. Snow meltwater infiltrated the soil and saturated the surface layer down to a depth of approximately 0.1 m (Figure 2B). Surface layer water was displaced downward by incoming precipitation in the growing season, when the active layer develops. The maximum daily mean ALT remained within 1.4–1.9 m from 1980 to 2016. In summer, the soil depth of approximately 0.6 m was comparatively drier than the deeper layers, because of soil water loss caused by higher plant transpiration and soil evaporation (Park et al., 2021). In autumn, when evapotranspiration was quite low, the surface soil layer of 0.1 m depth was wetted again. Water remained in the surface layer as frozen water until the following spring (Figure 2B).

The vertical profile of the simulated soil water age exhibited a clear monotonous distribution in all seasons, with younger ages in the surface layer and increasingly older ages with increasing depth (Figure 2C). At the study site, plant roots were primarily distributed within the 0–0.6 m surface soil column (Park et al., 2021). At these depths, water uptake by plant roots (Figure 2B) enhanced mixing of the existing water with fresh rainwater in summer, yielding younger water ages with a clear seasonal variability. Evaporation from the soil surface also increased water mixing and rejuvenation. The estimated water age in the surface soil column indicated full replacement of surface soil water by precipitation water within 1 year. Higher evapotranspiration also reduced infiltration of precipitation water into deeper soil layers. Thus, infiltration was effectively limited to depths of 0.8 m or less in summer (Figure 2B). The resulting limited mixing in deeper soil layers prevented rejuvenation and the stored water aged continuously. For example, the soil water age at a depth of 1.0 m was older than 10 years (Figure 2C). In permafrost, at depths of 1.9 m and below, water flow rarely occurred. The simulated water ages increased constantly, up to the length of the spin-up period (1,200 years).

3.2 Evapotranspiration and water age

Seasonal variations of the simulated climatological daily mean snow water equivalents (SWE), evapotranspiration subcomponents (plant transpiration, canopy interception and soil evaporation) separated according to the water sources (snow

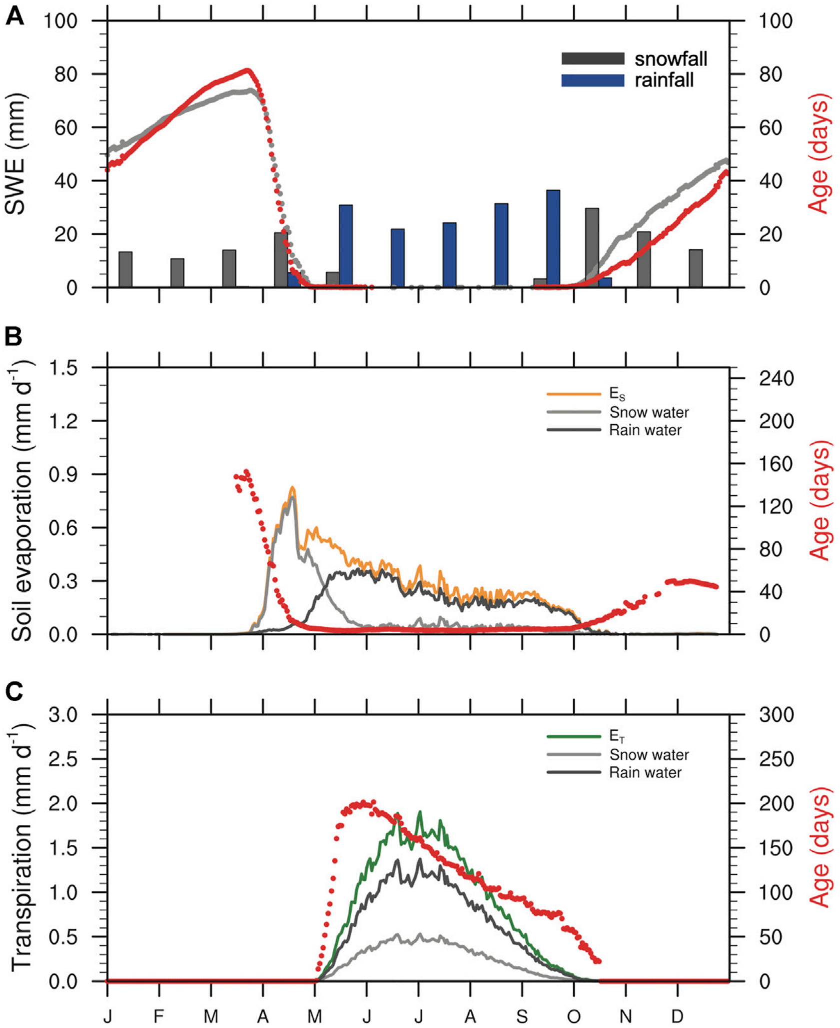

FIGURE 3
Seasonal variability, for the reference simulation, of climatological (1980–2016) daily averages for **(A)** the snow water equivalents (gray curve), and for the contributions of snowfall and rainfall to **(B)** soil evaporation and **(C)** plant transpiration. Daily mean water ages are indicated by red dots. Panel **(A)** also shows the climatological monthly average snowfall and rainfall amounts.

and rain), and the corresponding simulated water ages are displayed in Figure 3. The SWE showed typical seasonality, with accumulation starting in early autumn and reaching its maximum in March, concurrently with the maximum snow water age (80 days, Figure 3A). Snow began to melt at the end of March (Figure 3A), thus initiating soil evaporation (E_S, Figure 3B) when the E_S water was oldest (160 days), which reflected the water age of the surface soil layer. In April, the water age for soil evaporation sharply decreased to less than 20 days despite few rainfall events (Figure 3A), but a notable amount of water evaporated from the soil surface, explaining a surface soil layer age younger than in March (Figure 2C). From late April, the fraction of rain-sourced water evaporating from the surface markedly increased, while water ages decreased to less than 10 days in summer, indicating frequent precipitation events. Lower evapotranspiration and intermittent soil-freezing in October resulted in slightly older winter water ages for soil evaporation (Figure 3B). Annual mean water ages for interception by the vegetation canopy were considerably younger than those calculated for soil evaporation (Table 1).

Plnt roots extracted a large fraction of rain-sourced water from soil layers, accounting for 72% of the annual plant transpiration value (E_T). The E_T variations showed typical seasonality, peaking in June–July then decreasing, consistently with both the snow-sourced and rain-sourced transpiration values. In May, when the transpiration-induced water flux started, the corresponding water age increased rapidly. The deepening of the active layer in May allowed plant roots to reach deeper layers and extract older soil water. Subsequently, transpiration-induced water ages decreased continuously

TABLE 1 Climatological (1980–2016) annual average water flux (mm yr^{-1}) and age (days) for transpiration (E_T), interception (E_I), and soil evaporation (E_S) in the reference and sensitivity simulations. Here, the averaged ages represent the daily flux-weighted annual median water ages for each evapotranspiration subcomponent.

Simulation	E_T		E_I		E_S	
	flux	age	flux	age	flux	age
CNTR	128.4	148.0	39.1	0.18	62.3	11.0
EX_{T2}	144.7	131.5	39.7	0.17	62.5	10.8
EX_{T4}	158.6	117.3	39.8	0.16	62.0	9.9
EX_{T2_P30}	146.5	127.3	45.6	0.19	73.5	8.3
EX_{T2_RT}	144.8	181.3	39.7	0.17	62.1	10.9

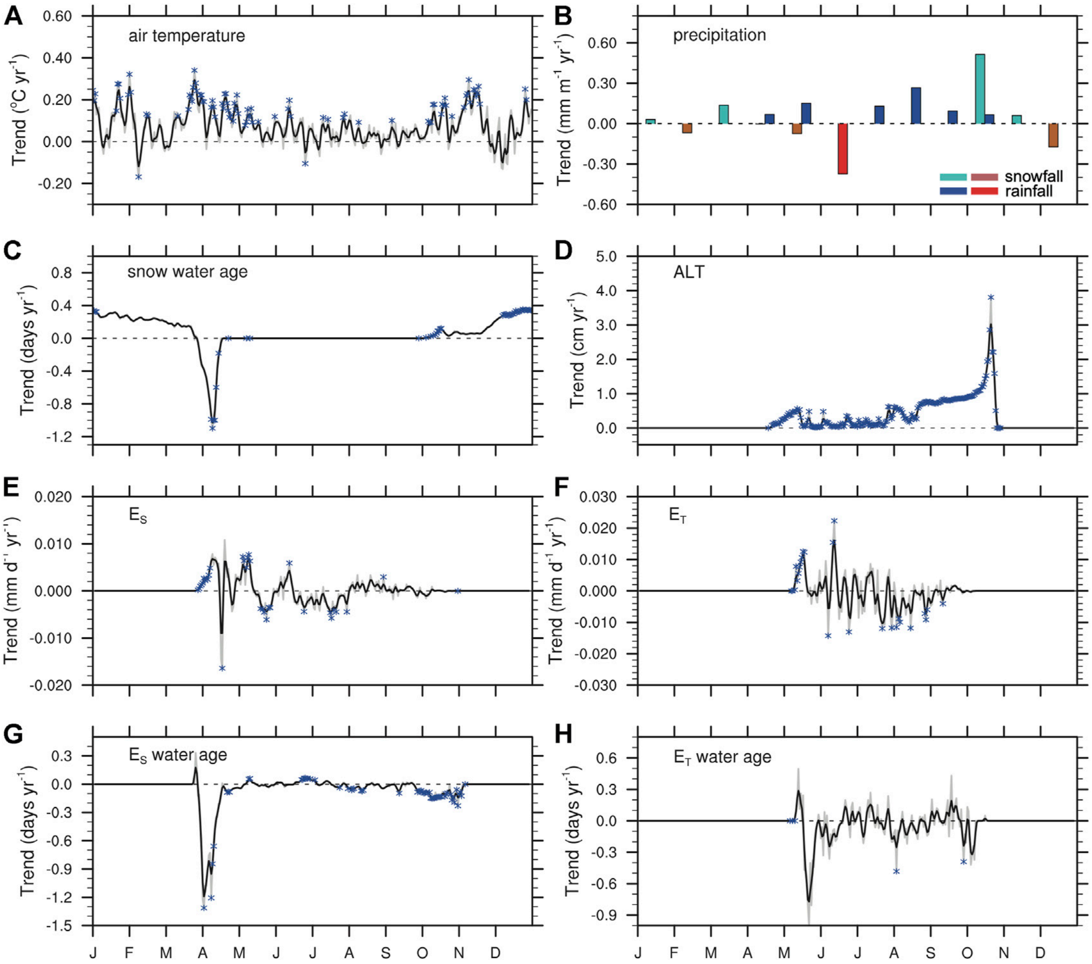

FIGURE 4
Seasonal variability, for the reference simulation, of climatological (1980–2016) daily average trends in **(A)** air temperature, **(C)** snow-sourced water age, **(D)** active layer thickness, **(E)** soil evaporation, **(F)** plant transpiration, **(G)** water age for soil evaporation, and **(H)** water age for plant transpiration. Panel **(B)** shows the climatological monthly average trends in snowfall and rainfall. The thin gray and thick black curves represent the original data and the 3-day average, respectively. Blue asterisks indicate statistically significant data ($p < 0.1$).

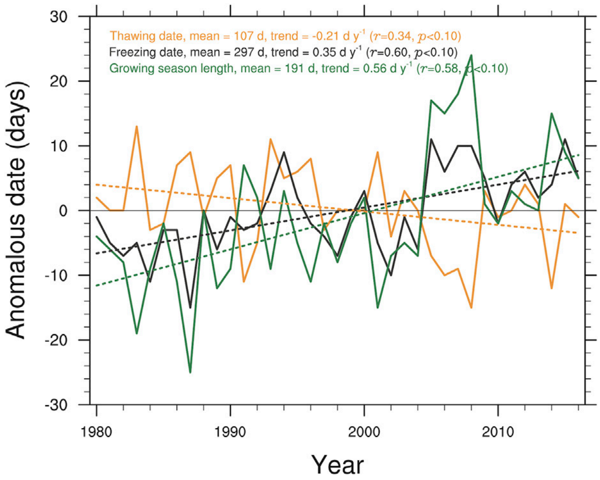

FIGURE 5
Interannual variability (1980–2016) of the simulated freezing and thawing anomalous dates and of the growing season length (yearly number of non-freezing days), and corresponding temporal trends (dashed lines) in the reference simulation.

during the growing season. In turn, summer precipitation wetted the soil previously dried by higher plant transpiration. The alternating drying and wetting phases rejuvenated soil water in summer, explaining the relatively younger transpiration water age. Soil freezing in the cold season caused the younger soil water to age, capturing it until the following spring (Figure 2C). Daily flux-weighted annual median water ages, for transpiration and soil evaporation in the reference simulation, were 148 days and 11 days, respectively (Table 1). For comparison, previous model simulations yielded transpiration water ages of 200 ± 10 days and 150–360 days in northern Sweden (Smith et al., 2019) and in the Scottish Highlands (Kuppel et al., 2020), respectively.

3.3 Trends

In this study, trends were calculated with the Mann–Kendall test for the water age module variables shown in Figure 4 (blue symbols represent statistically significant values, $p < 0.1$). Air temperature is an important driver of Arctic hydrological processes. Statistically significant warming trends were identified in the climatological daily mean T_a values in spring, autumn, and winter (Figure 4A). The warmer T_a caused stronger sublimation and earlier snowmelt in spring, explaining the decreasing trend in the snow water age (Figure 4C). Snow meltwater saturated the surface soil layer (Figure 2B). Snow-sourced water contributed to soil evaporation in spring (Figure 4E) and to the decreasing trend of the corresponding water age in April (Figure 4G). There was no perceptible transpiration water age trend (values within ±0.1 day yr^{-1}) in summer (Figure 4G). In October, when E_S was lowest (Figure 3B), the soil evaporation water age showed a persistent, statistically significant negative trend (Figure 4G), indicating that water age was directly influenced by the increasing rainfall (Figure 4B).

Once the snow cover had completely melted, the frozen soil began to thaw. The warmer T_a hastened soil thawing and induced a significant thickening trend in the active layer in summer, with a maximum ALT increase of 4 cm yr^{-1} in mid-October when the active layer extended to its maximum depth (Figure 4D). In spring, the active layer also thickened under the influence of the warming climate, which enhanced the ice–liquid water phase change. Under climate warming conditions, the phenological and physiological vegetation activity also increased, with plant roots extracting markedly more moisture from the soil (Parazoo et al., 2018). Plant transpiration exhibited a significant increasing trend in early May (Figure 4F), explained by the earlier start of plant transpiration and a deficit of snow meltwater (Figure 4B) under warmer T_a conditions, resulting in older E_T water ages. In late May, the E_T water age became rapidly younger (Figure 4H), because the increasing rainfall (Figure 4B) enhanced the mixing of young rain water with older soil moisture. Summer climatological trends of daily mean E_T and of E_T water age (Figures 4F,H, respectively) were alternately positive and negative, reflecting the influence of precipitation events.

Warming air temperatures also modified the soil freezing and thawing dates at the study site. In this study, freezing and thawing dates in the 0–5 cm topmost soil column were determined with the method of Park et al. (2016b). The simulated spring thawing date showed an overall negative trend of −0.21 days yr^{-1} ($p < 0.04$) over the 1980–2016 study period (Figure 5), indicating earlier soil thawing in response to increasing T_a (Figure 4A). The T_a warming trend also delayed soil freezing significantly (0.35 days yr^{-1}, $p < 0.01$). As a consequence of earlier soil thawing and later soil freezing, the growing season length (defined as the number of non-freezing days in 1 year) showed a statistically significant ($p < 0.01$) increasing trend over the study period (Figure 5), which resultantly contributed to the annual evapotranspiration (sum of E_S and E_T) increasing trends ($r = 0.19$, $p < 0.28$; Ma et al., 2022).

3.4 Sensitivity simulations

Four sensitivity simulations, characterized by specific perturbations of T_a and P_G and described in Section 2.4, were conducted to investigate the influence of climate warming on evapotranspiration and water age within the hydrological system. Figure 6 shows the seasonal variability of the anomalies, defined as the differences between the sensitivity simulation results and the reference simulation. Warmer air temperatures (+2°C and +4°C for T_a in

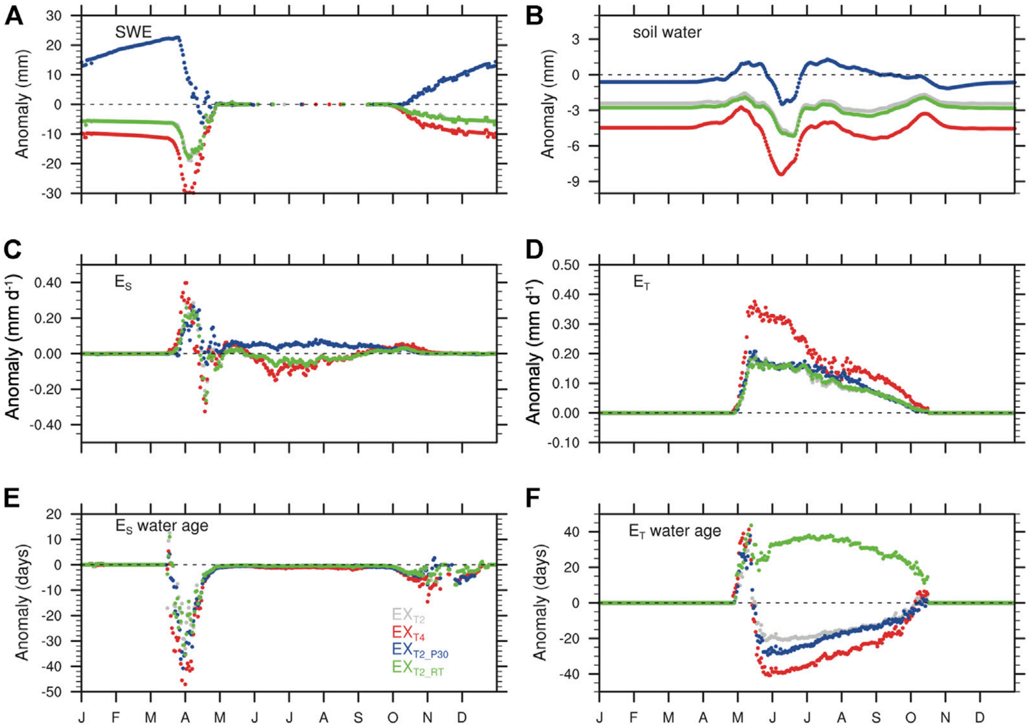

FIGURE 6
Seasonal variability (1980–2016) of daily average anomalies (differences between the sensitivity simulation results and the reference simulation) for **(A)** the snow water equivalents, **(B)** the 0–1 m soil column water content, **(C)** soil evaporation, **(D)** plant transpiration, **(E)** water age for soil evaporation, and **(F)** water age for plant transpiration.

simulations EX_{T2} and EX_{T4}, respectively) enhanced sublimation from the snowpack while reducing the contribution of snowfall to P_G, explaining lower SWE during the cold season (October–March) and earlier spring snowmelt than in the reference simulation (Figure 6A). As expected, a precipitation increase (+30% for P_G, simulation EX_{T2_P30}) compensated the influence of warmer T_a on the snowpack, resulting in positive SWE anomalies (Figure 6A). Modifications of the snow-related processes relatively to the reference simulation yielded consistently larger E_S values and earlier start dates in spring (Figure 6C), and younger E_S water ages (Figure 6E). Warmer T_a also induced an E_T increase caused by earlier vegetation activity (Figure 6D). Conversely, this enhanced activity dried the surface soil layer (Figure 6B), explaining the negative E_S anomalies in summer (Figure 6C). Soil dryness (magnitude of the negative anomaly) was directly related to the T_a increase, as illustrated by the larger negative anomalies for simulation EX_{T4} (Figure 6B), combined with higher losses by canopy interception (E_I in Table 1). Similarly to its influence on the snowpack, a P_G increase (EX_{T2_P30}) could compensate the summer soil drying induced by higher T_a values (Figure 6B). Furthermore, under climate warming conditions, plants largely used rain-sourced soil water for transpiration, yielding larger E_T anomalies for larger temperature increases, as shown in Figure 3C.

Earlier vegetation phenological activity caused by warmer T_a was also closely implicated to earlier and deeper soil thawing in spring. The resulting increase in plant water extraction from the active layer explained the anomalously older E_T water age in early spring (Figure 6F). This higher E_T quickly dried the soil (Figure 6B), which was then wetted again by increased precipitation. Therefore, under warming conditions, E_T was associated with anomalously younger water ages (Figure 6F). Climate warming possibly causes the root biomass and the rooting depth to increase. To investigate the influence of root depth on water ages, a fourth simulation was conducted on the basis of EX_{T2}, but with a root depth extended to 1.06 m (EX_{T2_RT}). This resulted in anomalously older E_T water ages (Figure 6F), because a downward water flux generally requires longer transit time to reach deeper soil layers.

4 Discussion

In this study, the CHANGE model was coupled with a water tracer module to assess the influence of climate warming on evapotranspiration regimes and the subsequent soil water budget variations in a boreal forest. The tracer module, originally designed to isolate the contributions of each water source to hydrological processes, was modified to incorporate water age dynamics. Dedicated model simulations were conducted to quantify the influence of climate warming on water fluxes–storages–ages interactions in the evapotranspiration process.

4.1 Influence of climate warming on evapotranspiration and water age

At the study site, the climate-induced evapotranspiration increase was larger in spring than in autumn, despite consistent T_a increases in both seasons (Figure 4A), possibly because solar radiation levels are higher in spring than in autumn (nearly reaching the yearly maximum) and because vegetation transitions from winter dormancy to the onset of the active growing season. The earlier start of the growing season, induced by warmer air temperatures, relaxes the low-temperature constraints on photosynthesis and on gas and water exchanges on the canopy, and enhances plant growth (Parazoo et al., 2018). Earlier vegetation activity and soil thawing allow plant roots to access soil water earlier in spring, yielding larger E_T values (Figure 6D). These findings are generally consistent with a previous study that demonstrated high correlation between the spring thawing date and the evapotranspiration intensity, using freezing/thawing records derived from satellite-based microwave remote sensing observations in the Northern Hemisphere high latitudes (Zhang et al., 2011). The positive influence of the earlier growing season onset on evapotranspiration was reinforced by the increase in snow meltwater availability, which limited plant moisture stress. The inflow of snow-sourced water into the surface soil layer showed a rejuvenating trend, explained by a shorter snowpack period and increased sublimation. The shorter freezing period (Figure 5) and the larger spring rainfall (Figure 4B) both contributed to surface soil water rejuvenation. Consequently, water ages for the spring evapotranspiration showed a decreasing trend over the study period (Figures 4G,H).

Conversely, this earlier and larger evapotranspiration in spring enhanced soil water loss, thus soil drying, in early summer (Figure 6B). The warming-driven leaf growth enhancement resulted in a larger quantity of canopy leaves that increased water losses by interception, thereby decreasing precipitation throughfall and causing the soil to dry. The low-soil-moisture constraint on evapotranspiration generally induced daily negative trends in summer (Figures 4E,F). However, rainwater from precipitation events, after reaching the dried soil, mixed with the older soil water. In turn, the mixed water was used for evapotranspiration (Tetzlaff et al., 2021), which explains the younger water ages calculated for soil evaporation and plant transpiration. This feedback cycle was enhanced under warming conditions, as confirmed by the sensitivity simulations in which warmer T_a induced considerable E_S and E_T increases (Figures 6C,D). Soil dryness is projected to increase further under future climate warming conditions (Andresen et al., 2020). Thus, more precipitation water will be consumed by plant transpiration, resulting in younger E_T water ages (Figure 6F). In autumn, plants enter the dormancy or senescence stage. In this case, the influence of warmer air temperatures or larger precipitation on photosynthesis and plant transpiration is mitigated by the seasonally lower solar radiation and shorter photoperiod. Warmer autumn air temperature delayed snow accumulation and soil freezing (Figure 5). This delay also contributed to the decreasing age trends calculated for soil water and plant transpiration in the following spring. Our

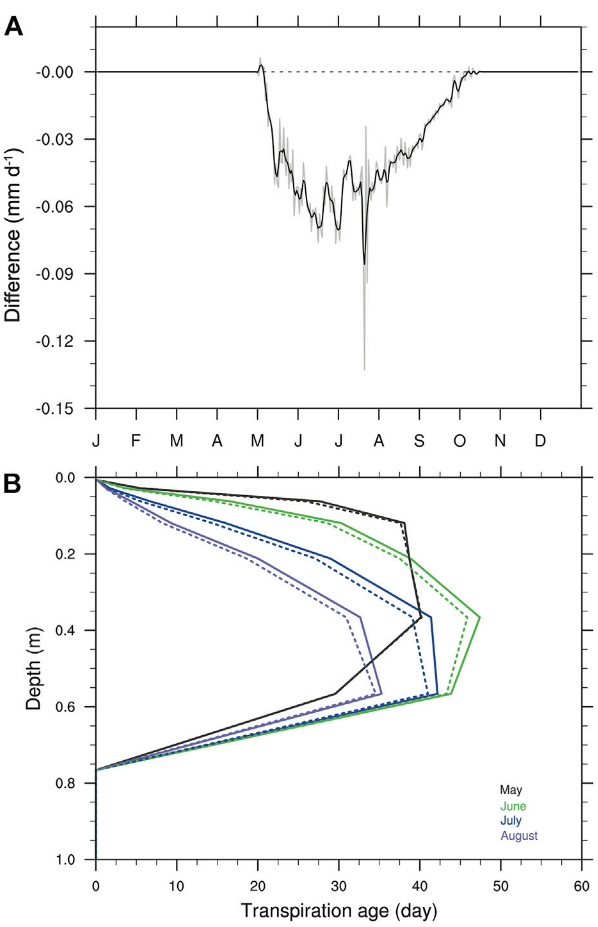

FIGURE 7
Comparison between the reference simulation and a simulation with a 30% reduction in August–September precipitation for **(A)** the seasonal variability (1980–2016) of daily average plant transpiration anomalies and **(B)** monthly average vertical profiles of plant transpiration water ages.

results suggest that subarctic climate warming has accelerated the terrestrial water cycle by increasing same-season use of precipitation-sourced young water for evapotranspiration.

4.2 Influence of permafrost warming on evapotranspiration and water age

Soil freezing in winter increased soil water ages (Figure 2B). This was reflected in the early spring E_S variations when mixing of the frozen, older soil water with younger snow meltwater and rain water induced a rapid decrease of the water ages for the surface soil layer (Figure 2B) and the E_S (Figure 3B). Conversely, seasonal variability of the E_T water ages was completely different, particularly at the onset of plant transpiration in May, with E_T values reaching their maximum within 1 month (Figure 3C). In CHANGE, the soil moisture stress associated with drying or freezing is represented by a normalized parameter (values within 0–1) and coupled to the plant photosynthetic and physiological processes. The E_T water age variations in the early growing season reflected the reduction of soil freezing stress after the active layer developed (Figure 3C). This was inconsistent with the E_T water age variation pattern identified in a non-permafrost Scottish Highlands site, characterized by winter soil frost and snow cover (Smith et al., 2019). On the contrary, the pattern identified by Smith et al. (2019) showed similar seasonality with our E_S water age estimates. The maximum E_T water age (approximately 200 days, Figure 3C), reached at the start of the growing season at the study site, clearly showed a connection between plant roots and the water accumulated during the preceding autumn. The E_T water ages then continuously decreased over the growing season, indicating the ecohydrological transition to a rainfall-driven phase during which the surface soil layer water storage was recharged by summer rainfall. Rain-sourced water accounted for a large fraction of the E_T water (Figure 3C). Analyzing the seasonal variability of E_T water ages has provided valuable insights into water dynamics associated with the active layer freezing/thawing process. It has also contributed to uncertainty reduction and better characterization of the relative contributions of model-estimated water sources to the E_T water. These contributions had not been validated with observational data prior to this study.

Winter freezing preserves the soil water conditions, established in the preceding autumn, until the following spring. This preserved water status represents the initial conditions for the growing season and strongly influences the related ecohydrological processes. An additional simulation was conducted to investigate the influence of autumn precipitation on evapotranspiration in the following year, with P_G values reduced by 30% in August–September based on EX_{T2}. Differences with the reference simulation were consistently negative during the growing season (Figure 7A). The lower P_G values reduced the E_T by 4.2% relatively to the reference values, demonstrating the influence of autumn precipitation on the E_T water ages. Monthly mean E_T ages differences (Figure 7B) between the reference (solid curves) and the additional simulation (dashed curves) were mostly found in soil layers below the surface but not deeper than 0.8 m (Figure 7B). In summer, E_T and E_S often caused the surface soil layer to dry. The remaining surface soil moisture was nearly fully displaced by the frequent precipitation inflow. This consistently occurs in the reference and additional simulations, regardless of the soil moisture level in early spring, consequently low E_T water age differences. In the additional simulation, the drier soil probably enhanced mixing of soil water with younger precipitation water infiltrated from the upper layers (Park et al., 2021). Water mixing and mobilization produced younger soil water in soil layers below the surface layer (Figure 7B). The presence of younger E_T water under a dried soil layer was broadly verified by the temperature-only sensitivity simulations EX_{T2} and EX_{T4} (Figure 6F). These results suggest that autumn precipitation water trapped in the soil by winter freezing causes deviations of the evapotranspiration and water ages from the hydrometeorological forcings in the following growing season. Sugimoto et al. (2003) established, in a larch forest of eastern Siberia, that the autumn soil water stored in the 0–1.2 m active layer column contributed to E_T in the following summer. A 1-year delayed correlation between soil water and evapotranspiration was also identified at the Kolyma watershed in eastern Siberia, underlain by continuous permafrost (Zhang et al., 2019; Suzuki et al., 2021). However, the warmer temperature increases permafrost thawing, leading to wetted surface layers and thus greater evapotranspiration. The increased evapotranspiration ultimately causes a drier surface, which is in turn fed back as a limitation on evapotranspiration. This feedback might become strengthened under the influence of future climate change. Climate models have projected long-term drying of the surface soil in permafrost regions (Andresen et al., 2020).

4.3 Model limitations and scope of the study

Previous observational studies investigated the climate-induced winter snow increase at the same study site and the influence of the resulting soil wetness on vegetation activity and on evapotranspiration (Ohta et al., 2014; Kotani et al., 2019). In

CHANGE, ecohydrological interactions are reproduced by a numerical model that includes a water tracer module to analyze the dynamics of precipitation-sourced water storages in the surface–subsurface system. The model calculated high contributions of summer rainwater to the increased evapotranspiration at the study site and characterized the evaporation-induced water isotopic enrichment, validated by observational data (Park et al., 2021). However, in this study, although a lack of observational data for water flux age calculations prevented us from validating the simulated evapotranspiration water ages, the coupling of the new water age calculation module with CHANGE produced encouraging results. The seasonal variability of evapotranspiration water ages was clearly associated with the active layer freezing/thawing process.

Simulated soil water ages were older in the deeper layers, because of the low water exchange at these depths (Figure 2). There was no indication of water movement by capillary rise from the deeper soil layers toward the upper layers under current climate conditions, because moisture conditions within the upper layers remained beyond the wilting point in summer (Figure 2B). This result was also verified for future climate warming scenarios. In the EX_{T4} simulation, for example, anomalous E_T water ages were younger than in the reference simulation (Figure 6F), indicating a larger dependence of E_T on summer precipitation than on water upwelling from deep soil layers. Moreover, when considering a plant root depth larger by 50 cm than that of the reference simulation (simulation EX_{T2_RT}), anomalous E_T water ages remained approximately 20 days older than the reference throughout the growing season (Figure 6F) as a result of increased extraction by the plant roots of older water from deeper soil layers. Evidence of the root depth influence was also identified by comparing the EX_{T2} and EX_{T2_RT} simulations. The comparison showed E_T water age differences of approximately 40 days despite an identical T_a increase of 2°C in both simulations (Figure 6F). Under future climate warming scenarios, root depth extension, larger spatial heterogeneities, and ALT increase are nearly certain. In such conditions, increased connection between plant transpiration and permafrost-sourced water is expected. Therefore, the root profile, as currently configured, is a likely source of uncertainties in simulations of ecohydrological processes associated with the model-simulated water sources and ages. Furthermore, the T_a and P_G perturbation defined in our simulations are not sufficient to characterize future climate warming conditions, which also depend on complex variations of meteorological variables such as humidity, surface solar radiation, or wind speed (Carvalho et al., 2022). In that sense, the sensitivity simulations presented in this study are not sufficiently realistic for accurate projections of evapotranspiration and water ages under future climate warming scenarios. Nevertheless, the main objective of this study was not the evaluation of future projections for evapotranspiration and water ages, but the analysis of evapotranspiration and water age responses to current climate warming conditions. Therefore, uncertainties on the forcing data should not preclude meaningful analyses with the newly implemented water age calculation scheme.

5 Conclusion

We incorporated a new water age calculation scheme into the tracer module of the process-based land surface model CHANGE and examined the influence of hydrological process modifications induced by permafrost warming on evapotranspiration and water ages. Climate warming caused earlier snowmelt and soil thawing, thereby enhancing soil evaporation and plant transpiration that, in turn, consumed increasingly younger water in spring. The progressively younger water ages for evapotranspiration in summer and autumn illustrated the dependence of the evapotranspiration on precipitation, because of the drying soil. These findings were consistent with our sensitivity model simulations. We also established that winter soil freezing contributed to summer plant transpiration by storing older soil water from the preceding autumn. However, climate warming shortened the freezing period. Thus, the early spring flux water ages became gradually younger. Our results demonstrated that climate warming strengthened the connection between evapotranspiration and precipitation-sourced freshwater in the soil system. Future climate-induced temperature increases will enhance permafrost warming and increase the contribution of summer rainfall to precipitation, also resulting in larger evapotranspiration. Therefore, we expect that future evapotranspiration increases will further accelerate the water cycle in boreal forests, with increasingly larger loss of younger precipitation water, a phenomenon that we identified under current climate conditions.

Data availability statement

The raw data supporting the conclusion of this article will be made available by the authors, without undue reservation.

Author contributions

HP developed the ideas, wrote most of this paper and drew most of the figures. All authors participated in data processing and preliminary analysis; HP coordinated the model experiments and analyzed the simulation results, KS and TH contributed the result analysis and manuscript writing and discussion.

Funding

This study was partly supported by the Japan Society for the Promotion of Science Grants-in-Aid for Scientific Research (KAKENHI) funding program, Grant Numbers 19H05668, 21H04934, and 22H03758. It was also supported by the Belmont Forum of the Japan Science and Technology Agency, Grant Number JPMJBF2003, and the Arctic Challenge for Sustainability II project funded by the Ministry of Education, Culture, Sports, Science and Technology, Japan, Grant Number JPMXD1420318865.

Acknowledgments

We thank Eric Dupuy, from Edanz (https://jp.edanz.com/ac) for editing a draft of this manuscript.

Conflict of interest

The authors declare that the research was conducted in the absence of any commercial or financial relationships that could be construed as a potential conflict of interest.

The reviewer NM declared a past co-authorship with the author HP to the handling editor.

Publisher's note

References

Ala-aho, P., Tetzlaff, D., McNamara, J. P., Laudon, H., Kormos, P., and Soulsby, C. (2018). Modeling the isotopic evolution of snowpack and snowmelt: Testing a spatially distributed parsimonious approach. *Water Resour. Res.* 53, 5813–5830. doi:10.1002/2017WR020650

Ala-aho, P., Tetzlaff, D., McNamara, J. P., Laudon, H., and Soulsby, C. (2017). Using isotopes to constrain water flux and age estimates in snow-influenced catchments using the STARR (Spatially distributed Tracer-Aided Rainfall–Runoff) model. *Hydrol. Earth Syst. Sci.BSyst. Sci.* 21, 5089–5110. doi:10.5194/hess-21-5089-2017

Andresen, C. G., Lawrence, D. M., Wilson, C. J., McGuire, A. D., Koven, C., Schaefer, K., et al. (2020). Soil moisture and hydrology projections of the permafrost region – A model intercomparison. *Cryosphere* 14, 445–459. doi:10.5194/tc-14-445-2020

Bekryaev, R. V., Polyakov, I. V., and Alexeev, V. A. (2010). Role of polar amplification in long-term surface air temperature variations and modern Arctic warming. *J. Clim.* 23, 3888–3906. doi:10.1175/2010jcli3297.1

Birkel, C., and Soulsby, C. (2015). Advancing tracer-aided rainfall-runoff modelling: A review of progress, problems and unrealised potential. *Hydrol. Process.* 29, 5227–5240. doi:10.1002/hyp.10594

Biskaborn, B. K., Smith, S. L., Noetzli, J., Matthes, H., Vieira, G., Streletskiy, D. A., et al. (2019). Permafrost is warming at a global scale. *Nat. Commun.* 10, 264. doi:10.1038/s41467-018-08240-4

Carvalho, D., Rafael, S., Monteiro, A., Rodrigues, V., Lopes, M., and Rocha, A. (2022). How well have CMIP3, CMIP5 and CMIP6 future climate projections portrayed the recently observed warming. *Sci. Rep.* 12, 11983. doi:10.1038/s41598-022-16264-6

Dee, D. P., Uppala, S. M., Simmons, A. J., Berrisford, P., Poli, P., Kobayashi, S., et al. (2011). The ERA-Interim reanalysis; configuration and performance of the data assimilation system. *Q. J. R. Meteorol. Soc.* 137, 553–597. doi:10.1002/qj.828

Good, S. P., Noone, D., and Bowen, G. J. (2015). Hydrologic connectivity constrains partitioning of global terrestrial water fluxes. *Science* 349, 175–177. doi:10.1126/science.aaa5931

Hiyama, T., Ueyama, M., Kotani, A., Iwata, H., Nakai, T., Okamura, M., et al. (2021). Lessons learned from more than a decade of greenhouse gas flux measurements at boreal forests in eastern Siberia and interior Alaska. *Polar Sci.* 27, 100607. doi:10.1016/j.polar.2020.100607

Holmes, R. M., Shiklomanov, A. I., Tank, S. E., McClelland, J. W., and Tretiakov, M. (2015). River discharge. *Arct. Rep. Card.* 2015, 60–65.

Hrachowitz, M., Benettin, P., van Breukelen, B. M., Fovet, O., Howden, N. J. K., Ruiz, L., et al. (2016). Transit times – The link between hydrology and water quality at the catchment scale. *WIREs. Water* 3, 629–657. doi:10.1002/wat2.1155

Iijima, Y., Nakamura, T., Park, H., Tachibana, Y., and Fedorov, A. (2016). Enhancement of Arctic storm activity in relation to permafrost degradation in eastern Siberia. *Int. J. Climatol.* 36, 4265–4275. doi:10.1002/joc.4629

Kim, Y., Kimball, J. S., Robinson, D. A., and Derksen, C. (2015). New satellite climate data records indicate strong coupling between recent frozen season changes and snow cover over high northern latitudes. *Environ. Res. Lett.* 10, 084004. doi:10.1088/1748-9326/10/8/084004

Kotani, A., Saito, A., Kononov, A. V., Petrov, R. E., Maximov, T. C., Iijima, Y., et al. (2019). Impact of unusually wet permafrost soil on understory vegetation and CO2 exchange in a larch forest in eastern Siberia. *Agric. For. Meteorol.* 265, 295–309. doi:10.1016/j.agrformet.2018.11.025

Kuppel, S., Tetzlaff, D., Maneta, M. P., and Soulsby, C. (2020). Critical zone storage controls on the water ages of ecohydrological outputs. *Geophys. Res. Lett.* 47, e2020GL088897. doi:10.1029/2020GL088897

Kuppel, S., Tetzlaff, D., Maneta, M. P., and Soulsby, C. (2018). EcH&lt;sub&gt;2&lt;/sub&gt;O-iso 1.0: Water isotopes and age tracking in a process-based, distributed ecohydrological model. *Geosci. Model Dev.* 11, 3045–3069. doi:10.5194/gmd-11-3045-2018

Li, C., Wei, Y., Liu, Y., Li, L., Peng, L., Chen, J., et al. (2022). Active layer thickness in the northern Hemisphere: Changes from 2000 to 2018 and future simulations. *J. Geophys. Res.-Atmosphere* 127, e2022JD036785. doi:10.1029/2022JD036785

Ma, N., Szilagyi, J., and Zhang, Y. (2022). Calibration-free complementary relationship estimates terrestrial evapotranspiration globally. *Water Resour. Res.* 57, e2021WR029691. doi:10.1029/2021WR029691

Ma, N., and Zhang, Y. (2022). Increasing Tibetan Plateau terrestrial evapotranspiration primarily driven by precipitation. *Agric. For. Meteorol.* 317, 108887. doi:10.1016/j.agrformet.2022.108887

Maneta, M. P., and Silverman, N. L. (2013). A spatially distributed model to simulate water, energy, and vegetation dynamics using information from regional climate models. *Earth Interact.* 17, 1–44. doi:10.1175/2012ei000472.1

Miyazaki, S., Saito, K., Mori, J., Yamazaki, T., Ise, T., Arakida, H., et al. (2015). The GRENE-TEA model intercomparison project (GTMIP): Overview and experiment protocol for stage 1. *Geosci. Model Dev.* 8, 2841–2856. doi:10.5194/gmd-8-2841-2015

Ohta, T., Kotani, A., Iijima, Y., Maximov, T. C., Ito, S., Hanamura, M., et al. (2014). Effects of waterlogging on water and carbon dioxide fluxes and environmental variables in a Siberian larch forest, 1998–2011. *Agric. For. Meteorol.* 188, 64–75. doi:10.1016/j.agrformet.2013.12.012

Parazoo, N. C., Arneth, A., Pugh, T. A. M., Smith, B., Steiner, N., Luus, K., et al. (2018). Spring photosynthetic onset and net CO2 uptake in Alaska triggered by landscape thawing. *Glob. Chang. Biol.* 24, 3416–3435. doi:10.1111/gcb.14283

Park, H., Iijima, Y., Yabuki, H., Ohta, T., Walsh, J., Kodama, Y., et al. (2011). The application of a coupled hydrological and biogeochemical model (CHANGE) for modeling of energy, water, and CO2 exchanges over a larch forest in eastern Siberia. *J. Geophys. Res.* 116, D15102. doi:10.1029/2010JD015386

Park, H., Kim, Y., and Kimball, J. S. (2016a). Widespread permafrost vulnerability and soil active layer increases over the high northern latitudes inferred from satellite remote sensing and process model assessments. *Remote Sens. Environ.* 175, 349–358. doi:10.1016/j.rse.2015.12.046

Park, H., Launiainen, S., Konstantinov, P. Y., Iijima, Y., and Fedorov, A. N. (2018). Modeling the effect of moss cover on soil temperature and carbon fluxes at a tundra site in Northeastern Siberia. *J. Geophys. Res.-Biogeosciences* 123, 3028–3044. doi:10.1029/2018JG004491

Park, H., Tanoue, M., Sugimoto, A., Ichiyanagi, K., Iwahana, G., and Hiyama, T. (2021). Quantitative separation of precipitation and permafrost waters used for evapotranspiration in a boreal forest: A numerical study using tracer model. *JGR. Biogeosciences* 126, e2021JG006645. doi:10.1029/2021JG006645

Park, H., Yoshikawa, Y., Oshima, K., Kim, Y., Ngo-Duc, T., Kimball, J. S., et al. (2016b). Quantification of warming climate-induced changes in terrestrial Arctic river ice thickness and phenology. *J. Clim.* 29, 1733–1754. doi:10.1175/JCLI-D-15-0569.1

Park, H., Yoshikawa, Y., Yang, D., and Oshima, K. (2017). Warming water in Arctic terrestrial rivers under climate change. *J. Hydrometeorol.* 18, 1983–1995. doi:10.1175/JHM-D-16-0260.1

Pfister, L., Martínez-Carreras, N., Hissler, C., Klaus, J., Carrer, G. E., Stewart, M. K., et al. (2017). Bedrock geology controls on catchment storage, mixing and release: A comparative analysis of 16 nested catchments. *Hydrol. Process.* 31, 1828–1845. doi:10.1002/hyp.11134

Piovano, T. I., Tetzlaff, D., Carey, S. K., Shatilla, N. J., Smith, A., and Soulsby, C. (2019). Spatially distributed tracer-aided runoff modelling and dynamics of storage and water ages in a permafrost-influenced catchment. *Hydrol. Earth Syst. Sci.* 23, 2507–2523. doi:10.5194/hess-23-2507-2019

Rinaldo, A., Benettin, P., Harman, C. J., Hrachowitz, M., McGuire, K. J., van der Velde, Y., et al. (2015). Storage selection functions: A coherent framework for quantifying how catchments store and release water and solutes. *Water Resour. Res.* 51, 4840–4847. doi:10.1002/2015WR017273

Smith, A., Tetzlaff, D., Laudon, H., Maneta, M., and Soulsby, C. (2019). Assessing the influence of soil freeze–thaw cycles on catchment water storage–flux–age interactions using a tracer-aided ecohydrological model. *Hydrol. Earth Syst. Sci.* 23, 3319–3334. doi:10.5194/hess-23-3319-2019

Sprenger, M., Herbstritt, B., and Weiler, M. (2015). Established methods and new opportunities for pore water stable isotope analysis. *Hydrol. Process.* 29, 5174–5192. doi:10.1002/hyp.10643

Sprenger, M., Stumpp, C., Weiler, M., Aeschbach, W., Allen, S. T., Benettin, P., et al. (2019). The demographics of water: A review of water ages in the critical zone. *Rev. Geophys.* 57, 800–834. doi:10.1029/2018RG000633

Sprenger, M., Tetzlaff, D., Buttle, Z., Laudon, H., and Soulsby, C. (2018). Water ages in the critical zone of long-term experimental sites in northern latitudes. *Hydrol. Earth Syst. Sci.* 22, 3965–3981. doi:10.5194/hess-22-3965-2018

Stadnyk, T., Delavau, C., Kouwen, N., and Edwards, T. W. D. (2013). Towards hydrological model calibration and validation: Simulation of stable water isotopes using the isoWATFLOOD model. *Hydrol. Process.* 27, 3791–3810. doi:10.1002/hyp.9695

Sugimoto, A., Naito, D., Yanagisawa, N., Ichiyanagi, K., Kurita, N., Kubota, J., et al. (2003). Characteristics of soil moisture in permafrost observed in East Siberian taiga with stable isotopes of water. *Hydrol. Process.* 17, 1073–1092. doi:10.1002/hyp.1180

Suzuki, K., Park, H., Makarieva, O., Kanamori, H., Hori, M., Matsuo, K., et al. (2021). Effect of permafrost thawing on discharge of the Kolyma river, northeastern Siberia. *Remote Sens. (Basel).* 13, 4389. doi:10.3390/rs13214389

Tetzlaff, D., Birkel, C., Dick, J., Geris, J., and Soulsby, C. (2014). Storage dynamics in hydropedological units control hillslope connectivity, runoff generation and the evolution of catchment transit time distributions. *Water Resour. Res.* 50, 969–985. doi:10.1002/2013WR014147

Tetzlaff, D., Buttle, J., Carey, S. K., Kohn, M. J., Laudon, H., McNamara, J. P., et al. (2021). A preliminary assessment of water partitioning and ecohydrological coupling in northern headwaters using stable isotopes and conceptual runoff models. *Hydrol. Process.* 35, 5153–5173. doi:10.1002/hyp.10515

van Huijgevoort, M. H. J., Tetzlaff, D., Sutanudjaja, E. H., and Soulsby, C. (2016). Using high resolution tracer data to constrain water storage, flux and age estimates in a spatially distributed rainfall-runoff model. *Hydrol. Process.* 30, 4761–4778. doi:10.1002/hyp.10902

Wang, P., Huang, Q., Pozdniakov, S. P., Liu, S., Ma, N., Wang, T., et al. (2021). Potential role of permafrost thaw on increasing Siberian river discharge. *Environ. Res. Lett.* 16, 034046. doi:10.1088/1748-9326/abe326

Zhang, K., Kimball, J. S., Kim, Y., and McDonald, K. C. (2011). Changing freeze-thaw seasons in northern high latitudes and associated influences on evapotranspiration. *Hydrol. Process.* 30, 4142–4151. doi:10.1002/hyp.8350

Zhang, Y., He, B. I. N., Guo, L., and Liu, D. (2019). Differences in response of terrestrial water storage components to precipitation over 168 global river basins. *J. Hydrometeorol.* 20, 1981–1999. doi:10.1175/jhm-d-18-0253.1

Zhang, Y., Ma, N., Park, H., Walsh, J. E., and Zhang, K. (2021). “Evaporation processes and changes over the northern regions,” in *Arctic hydrology, permafrost and ecosystems*. Editors D. Yang and D. L. Kane (Springer Nature Switzerland), 101–131. doi:10.1007/978-3-030-50930-9_4

Zhang, Y., and Ma, N. (2018). Spatiotemporal variability of snow cover and snow water equivalent in the last three decades over Eurasia. *J. Hydrol. X.* 559, 238–251. doi:10.1016/j.jhydrol.2018.02.031

frontiers | Frontiers in Earth Science

TYPE Original Research
PUBLISHED 05 January 2023
DOI 10.3389/feart.2022.1075988

OPEN ACCESS

EDITED BY
Chunqiao Song,
Nanjing Institute of Geography and Limnology (CAS), China

REVIEWED BY
Pengfeng Xiao,
Nanjing University, China
Xiaodong Huang,
Lanzhou University, China

*CORRESPONDENCE
Yang Gao,
✉ yanggao@itpcas.ac.cn

†These authors share first authorship

SPECIALTY SECTION
This article was submitted to Hydrosphere,
a section of the journal Frontiers in Earth Science

RECEIVED 21 October 2022
ACCEPTED 22 November 2022
PUBLISHED 05 January 2023

CITATION
Gao Y, Dong H, Dai Y, Mou N and Wei W (2023), Contrasting changes of snow cover between different regions of the Tibetan Plateau during the latest 21 years.
Front. Earth Sci. 10:1075988.
doi: 10.3389/feart.2022.1075988

Contrasting changes of snow cover between different regions of the Tibetan Plateau during the latest 21years

Yang Gao[1]*†, Huaiwei Dong[1,2]†, Yufeng Dai[1], Naixia Mou[2] and Wenfan Wei[1]

[1]State Key Laboratory of Tibetan Plateau Earth System, Environment and Resources (TPESER), Institute of Tibetan Plateau Research, Chinese Academy of Sciences, Beijing, China, [2]College of Geodesy and Geomatics, Shandong University of Science and Technology, Qingdao, China

The spatial and temporal resolutions of snow remote sensing data have been increasing, but the unique snow characteristics such as thin snow depth and high frequency of change on the Tibetan Plateau have limited their applicability in this region. In this study, five commonly used snow remote sensing data were evaluated based on snow observations at 139 stations during the latest 20 years, and the advantages of each data were integrated to develop a multi-source data fusion snow cover dataset for the Tibetan Plateau. Based on these data, we conducted snow zonation and comparative snow variability analysis on the Tibetan Plateau. The results indicated that the snow cover days on the Tibetan Plateau are not only influenced by the longest snow cover duration (SCD) but also controlled by the short-term snow cycles. More than 70% of the annual snow cover days come from short-term snow cycles, except the Amu Darya and Indus. From 2000 to 2021, 23.0% of the plateau has experienced a significant decrease in snow cover days (mainly in the southeast) and 4.9% has experienced a significant increase (mainly in the northwest). As the altitude increases, the area and magnitude of the decreased and increased snow cover increases, and at high altitude the areas with increased snow are greater than that with decreased. The significant reduction in the snow cover days over large areas of the plateau stems from the superimposed effect of the simultaneous reductions in the longest SCD and the short-term snow cycles, but the reduction in the Amu Darya and Indus comes mainly from the reduction in the short-term snow cycle. The significant increase in the snow cover days in the Amu Darya, Indus, Tarim, and Hexi mainly comes from the increase in the longest SCD, while that in the Yellow River and Qaidam mainly comes from the increase in the short-term snow cycles. This contrasting change in the snowpack on the Tibetan Plateau, which decreases in the southeast and increases in the northwest, with a large decrease at lower elevations and an increase at higher elevations, will bring new challenges to water resource management in the region.

KEYWORDS

multi-source data fusion, contrasting snow change, snow cycle, the longest snow cover duration, Tibetan Plateau

1 Introduction

Snow cover is a special form of land cover caused by low-temperature snowfall, snow transport, and accumulation in the process of melting (Che Z et al., 2008). It is an important part of the cryosphere, which is mainly distributed in the high-latitude and -altitude regions (Henderson et al., 2018). Snow cover has a large-scale cooling effect on the global climate system (Flanner et al., 2011), and its high reflectivity affects land–air energy exchange. Meanwhile, the changes in its status also affect water circulation processes. With an average altitude over 4,000 m, the Tibetan Plateau is the highest plateau in the world, which is covered by a large amount of seasonal and perennial snow. Rivers originating from the plateau provide domestic and production water for dozens of neighboring countries and regions, and snowmelt water is one of the important supplies for these rivers (Immerzeel et al., 2009; Smith et al., 2017; Hill et al., 2020). Climate warming causes rapid changes in snow cover on the Tibetan Plateau, which affects the annual distribution of runoff, local ecosystem, and disaster prevention. Therefore, comprehensive observation of snow cover and accurate acquisition of its dynamic changes are of great practical significant for water resource management.

Ground snow observation is usually carried out manually or automatically using a snow ruler or ultrasound for snow depth and a snow core tube or snow pillow for snow water equivalent. Studies based on ground-observed snow depth data show that snow on the Tibetan Plateau has different trends during different periods. Observation at 60 stations indicates a general increasing trend of snow on the Tibetan Plateau from 1957 to 1990 (Ke et al., 1997). Observation at 94 stations shows a significant decrease of snow cover days on the Tibetan Plateau from 1981 to 2010. Observation at 115 stations shows that a decreasing–increasing–decreasing trend in the eastern part of the plateau for three phases 1972–1987, 1987–1998, and 1998–2016. Although snow observations on the plateau are increasing and more and more stations are being used for snow studies (Chen et al., 2022), the majority of stations are located in the eastern part of the plateau, which does not allow for a comprehensive and accurate understanding of the snow over the whole plateau.

Remote sensing data have the characteristics of less restriction by the ground environment, wide coverage, and abundant information (Merz et al., 2013). The remote sensing data widely applying in snow studies can be divided into three categories according to spatial resolution. High-resolution snow cover data, including VIIRS/NPP Snow Cover Daily L3 Global 375 m SIN Grid (375 m, 2012–present) (Riggs and Hall, 2020), MODIS/Terra Snow Cover Daily L3 Global 500 m SIN Grid (MOD10A1) (500 m, 2000–present), MODIS/Aqua Snow Cover Daily L3 Global 500 m SIN Grid (MYD10A1) (500 m, 2002–present) (Chelamallu et al., 2013; Mishra et al., 2016) and related de-clouded data (Muhammad and Thapa, 2021; Gyawali and Bárdossy, 2022; Mattar et al., 2022), and IMS Daily Northern Hemisphere Snow and Ice Analysis data (IMS) (1km, 2014–present) (Chiu et al., 2020), can be used for basin-scale snow studies. Medium-resolution snow data, including IMS (4 km, 2004–present), daily 5-km Gap-free AVHRR snow cover extent product over China (AVHRR) (5 km, 1981–present) based on the advanced very-high-resolution radiometer (AVHRR), can be used for regional-scale snow studies. Low-resolution snow data, including weekly snow cover data developed by NOAA based on AVHRR (160 km, 1966–present) (Brown et al., 2014), daily snow cover data based on the Special Sensor Microwave/Image (SSM/I) (25 km, 1995–present), long-term series of daily snow depth dataset in China (CSD) (25 km, 1979–2021) (Che Z et al., 2008), and IMS (24 km, 1997–present) (Ramsay, 1998), can be used for global or continental scale snow studies. The more widely used data in the study of the Tibetan Plateau include high-resolution MODIS, IMS data, medium-resolution AVHRR data, and low-resolution CSD data. The evaluation results of MOD10A1/MYD10A1 on the Tibetan Plateau from 2002 to 2014 show that the total accuracy under clear sky can reach 85.0%, while more than 52.3% is covered by cloud (Yu et al., 2017). The total accuracy of 4 km and 1 km IMS snow and ice data on the plateau from 2010 to 2019 can reach 80.1% and 83.0%, respectively (Chu et al., 2021). The total accuracy of AVHRR snow cover data from 1985 to 2013 on the plateau can reach 87.4% (Li et al., 2022). The total accuracy of 25 km CSD from 2003 to 2014 on the plateau is 66.7% (Dai et al., 2017).

At present, a large number of remote sensing data have been applied to the monitoring of snow cover on the Tibetan Plateau. MODIS eight-day combined snow cover data MOD10A2 shows a significant decreasing trend of snow cover in the southeast and northwest of the plateau (Yang et al., 2017). The MODIS and IMS fusion data indicate that from 2002 to 2012, the areas with significantly earlier and later snow cover onset account for 18.1% and 8.5%, and the areas with earlier and later snow cover end account for 23.2% and 6.9%, respectively. The cloud-free MODIS snow data developed by the triple spline interpolation show that from 2000 to 2020, the snow cover onset of 14.4% region is delayed 2.3 days per year (d/y), and end of 15.5% is advanced 1.7 d/y (Tang et al., 2013). Previous studies focus more on the snow cover days, the start and end dates of snow cover (Dietz et al., 2013; Notarnicola, 2020), while little is known about the short-period snow cover on the Tibetan Plateau. Moreover, the reliability of snow monitoring is directly related to the used remote sensing data. High-resolution data can capture snow accurately, but most of them are obtained from optical sensors and affected by cloud. Multi-source data fusion is an effective method to integrate the respective advantages of different snow data. Targeted fusion strategies based on regional snow characteristics can significantly increase the adaptability of new products in the region.

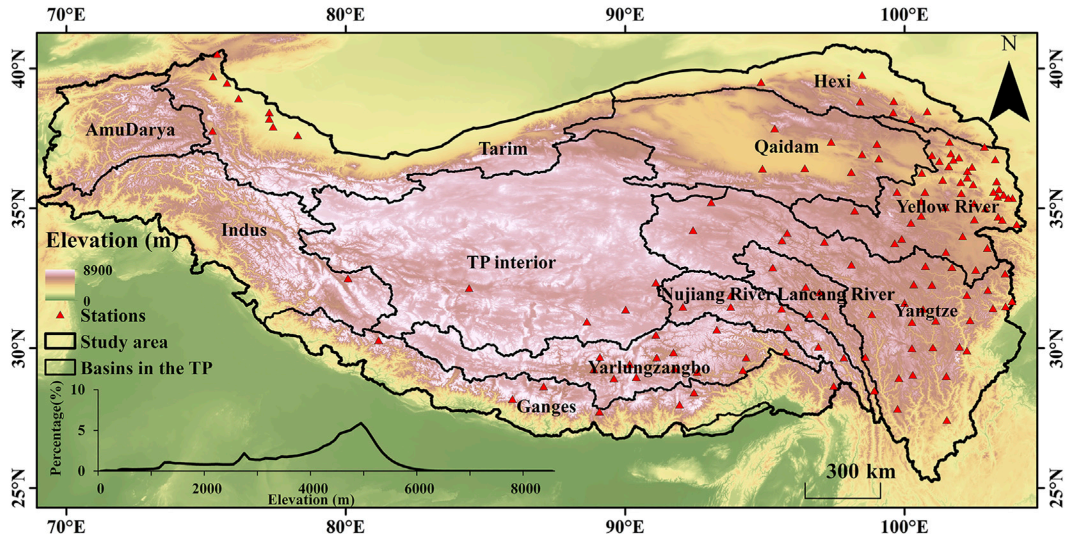

FIGURE 1
Study area and locations of 139 snow observation sites.

This study plans to evaluate and comparatively analyze the five commonly used snow cover data based on unified data and indexes, to generate the Tibetan Plateau MODIS dataset using the suitable NDSI snow recognition threshold based on the snow characteristics of this region, to formulate multi-source data fusion strategies based on the performance of each data on the Tibetan Plateau, and to develop a multi-source data fusion snow dataset with high spatial resolution at the day scale. Based on this, the snow cover days and their changes on the Tibetan Plateau has been analyzed, and the longest snow cover duration (SCD) and the number of snow cycles have been comprehensively considered to understand the snow and its dynamic changes. The second part of this paper introduces the study area and data. The third part introduces the evaluation index, fusion strategy, snow cover parameters, and variation analysis methods. The fourth part analyzes the data fusion effect, spatial difference, and contrasting changes of snow cover on the Tibetan Plateau. The fifth part is the conclusion.

2 Study area and data

2.1 Study area

The Tibetan Plateau is the largest snow-covered area on the Earth except for the poles, which is the birthplace of dozens of large rivers and is known as the "Asia water tower." The plateau is mainly influenced by the Indian monsoon and westerlies, with cold regions in the northwest and warm regions in the south and central parts. The precipitation over the plateau shows a decreasing trend from southeast to northwest. The Tibet Plateau is dominated by natural geomorphology, taking into account the elevation, mountain integrity, and river geomorphology, and is divided into 12 major basins: Indus, Amu Darya, Tarim, Hexi, Qaidam, Yellow River, TP interior, Yangtze, Lancang River, Nujiang River, Yarlungzangbo, and Ganges (Figure 1), and the proportion of each elevation area is 6.4% (<1500 m), 4.3% (1,500–2000m), 4.1% (2000–2500 m), 7.8% (2500–3000 m), 8.2% (3000–3500 m), 10.3% (3500–4000 m), 17.4% (4000–4500 m), 26.4% (4500–5000 m), and 15.1% (>5,000 m), respectively.

2.2 Data

2.2.1 Remote sensing data

Remote sensing data used in this study include MOD10A1/MYD10A1 snow cover data, IMS snow and ice data, AVHRR snow area data, and CSD (Figure 2). All data have been pre-processed for format conversion and numerical unification.

MODIS data version 6 before 31 August 2021, including MOD10A1 and MYD10A1, has been downloaded from the National Snow and Ice Data Center (NSIDC, https://nsidc.org). Different form version 5, which only provides "snow" and "no snow" binary maps, version 6 snow dataset provides normalized difference snow index (NDSI) and data quality parameters (Hall et al., 2002). According to the snow characteristics of different regions, users can define the recognition threshold suitable for the region to obtain more accurate snow data. The data have been acquired between 10: 30 a.m. and 1:30 p.m., respectively. The consistency of these two

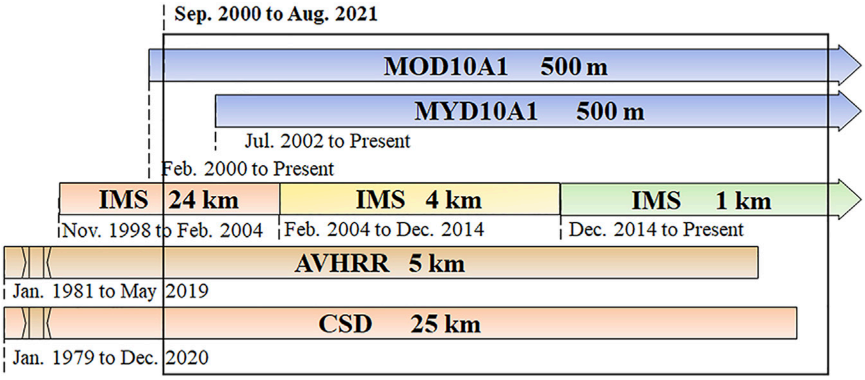

FIGURE 2
Remote sensing data used in this study.

data is stronger in winter and the weakest in summer (Painter et al., 2009).

The IMS snow/ice data are a multi-source fusion dataset of snow and sea ice for the Northern Hemisphere, distributed by the NSIDC. The source datasets include data from NOAA's very low orbit, Geostationary Operational Environmental Satellites, Geostationary Meteorological Satellite, United States Department of Defense Polar Satellites Orbiters, Multi-Function Transport Satellites, and European Meteorological Satellites. Also, the data of various radar sources from European countries, Japan, China, South Korea, Canada, and the United States and snow observations in many countries were combined (Ramsay, 1998; Helfrich et al., 2007). This study used data from 1 September 2000 to 31 August 2021.

The AVHRR snow data are obtained by quality control, cloud detection, snow identification by multi-layer decision tree, and gap filling. Based on normalized vegetation index (NDVI), NDSI, and DEM, the snow has been identified based on different thresholds for different surface conditions (Hao et al., 2021). The data within 16–56°N and 72–142°E can be obtained from the National Tibetan Plateau Data Center (TPDC, http://www.tpdc.ac.cn/en/). Data from 1 September 2000 to 31 May 2019 were used in this study.

The CSD is a snow depth dataset developed based on the snow characteristics in China (Che T et al., 2008; Dai et al., 2015; Dai et al., 2017), which can be downloaded from TPDC. The source data are passive microwave data SMMR (1979–1987), SSM/I (1987–2007), and SSMI/S (2008–2020). To ensure the consistency of the data in time, the data from different sensors are first cross-calibrated. Then, Chang's snow depth algorithm is fitted and revised based on the snow depth observations in China, and a snow depth inversion algorithm suitable for China is developed. According to different surfaces such as sand, permafrost, and cold desert, different snow recognition algorithms are developed. Data from 1 September 2000 to 31 August 2021 were used in this study.

2.2.2 Auxiliary data

The snow depth records from 1 September 2000 to 31 August 2020 at 139 stations, operated by China National Meteorological Administration, have been viewed as true values (Figure 1). Daily snow depth is measured by professionals using a ruler at 8 a.m. When the snow depth is greater than 1 cm, the snow depth is recorded as the integer centimeter. In this study, the samples with a snow depth of 1 cm or more have been defined as "snow," and samples with snow depth less than 1 cm have been defined as "no snow." The elevation of these stations range from 1,220 to 5,285 m; 82.0% of these stations are located between 2,000 and 4,500 m, accounting for 47.8% of the Tibetan Plateau. Nine stations are located at altitudes greater than 4,500 m, accounting for 21.6%. Therefore, these measured snow depth data can well represent the snow cover in the study area. Meanwhile, SRTM DEM (the Shuttle Radar Topography Mission, https://srtm.csi.cgiar.org) with spatial resolution of 90 m is used for hypsometry of each basin.

3 Methods

3.1 Evaluation metrics of remote sensing data

Three metrics, overall accuracy (OA), snow accuracy (SA), and snow omission error (SOE), have been used to evaluate the accuracy of the source data and the performance of the data fusion (Painter et al., 2009; Rittger et al., 2013). The overall accuracy is defined as the ratio of the number of correctly classified samples to the total number of samples, and thus represents the overall accuracy for recognition in the data corresponding to "snow" and "no snow." The snow accuracy is defined as the ratio between the number of correctly recognized "snow" samples and the number of "snow" samples identified by the remote sensing data, representing the correct snow recognition. The omission error is the ratio of the number of samples that misjudged “snow” as “no snow” based on remote sensing retrieval *vs.* the number of snow samples verified by ground observations, thus giving a measure of the snow missed by remote sensing observation.

3.2 MODIS snow recognition and multi-source data fusion

The “step-by-step iterative test” has been used to define a suitable MODIS NDSI threshold for snow recognition. The NDSI threshold was based on carrying out 99 iterations between 0 and 1 in the steps of 0.01. The snow recognitions under each threshold were evaluated based on the ground observations by three metrics, i.e., the OA, SA, and SOE. The optimal threshold of MODIS NDSI has been determined by comparing and analyzing these parameters. In this study, the Tibetan Plateau has been classified into 96 types, according to the month and altitude interval, and the corresponding NDSI threshold has been determined for each type (Supplementary Table S1). When the NDSI value is greater than or equal to the threshold, it is identified as “snow,” and when it is less than the threshold, it is identified as “no snow."

Multi-source data fusion is an important method to remove cloud masking of optical data and to combine the advantages of different types of data (Gafurov and Bardossy, 2009; Gao et al., 2010; Dietz et al., 2013). For the three spatial resolutions of the IMS, we have divided the five data into three periods: 1 September 2000–23 April 2004 (period 1), 24 April 2004–2 December 2014 (period 2), and 3 December 2014–31 August 2020 (period 3). The accuracies of these five data have been comprehensively evaluated and compared. According to the evaluation results of each data in these three periods, the corresponding fusion strategy has been formulated and adopted. According to different strategies, multi-source data fusion has been carried out and the new snow cover dataset has been generated. The specific fusion strategies are defined in Section 4.1.

3.3 Snow parameters definition and snow cover zoning

To provide a comprehensive understanding of the snowpack status, three parameters including the annual snow cover days, the longest snow cover duration (SCD), and the number of snow cycles have been used. The annual snow cover days is the sum of the number of snow days within a snow year (from September 1 in this year to August 31 in the next year). The process of “no snow–snow–no snow” in an area is defined as a snow cycle. SCD means the duration of a snow cycle. The number of snow cycles, i.e., how many such cycles are within a snow year, includes not only the long-term snow processes (more than 30 days) but also all the short-term snow processes (less than 30 days) (Zhang and Zhong, 2014). The longest SCD is the duration of the longest snow cover cycle.

Based on the annual snow cover days and the longest SCD, the Tibetan Plateau can be divided into four types: persistent, stable, unstable, and ephemeral snow covers (Li et al., 2022). The regions meeting any of the conditions of more than 180 days of annual snow cover days or more than 60 days of the longest SCD are defined as persistent snow cover. Outside the persistent snow cover, the regions meeting any of the conditions of annual snow cover days more than 60 days and the longest SCD more than 30 days are defined as the stable snow cover. Outside the aforementioned two types, regions with annual snow cover days or the longest SCD more than 10 days are defined as the unstable snow cover. Areas outside the aforementioned three types are defined as the ephemeral snow cover.

3.4 Trend analysis of snow cover changes

The trend of snow cover changes has been analyzed using the Mann–Kendall trend test algorithm (M–K algorithm). This method is a non-parametric test method. It does not require samples to follow a certain distribution and can overcome the interference of a few outliers, so it is widely used in climate trend testing and prediction. First, for the stationary and independent series, X_t (t = 1, 2, 3, . . . , n; n is the sequence length) defines the statistic S (1).

$$S = \sum_{i=1}^{n-1} \sum_{j=i+1}^{n} Sgn(x_i - x_j), \tag{1}$$

where Sgn (x_i-x_j) for

$$Sgn(x_i - x_j) = \begin{cases} 1 & (x_i - x_j > 0) \\ 0 & (x_i - x_j = 0) \\ -1 & (x_i - x_j < 0) \end{cases}.$$

For n≥10, the variance of the statistic S (approximately normally distributed) is Var(S) (2) and the standardized test statistic is Z (3).

$$Var(S) = \frac{n(n-1)(2n+5)}{18}, \tag{2}$$

$$Z = \begin{cases} \frac{S-1}{\sqrt{Var(S)}} & (S > 0) \\ 0 & (S = 0) \\ \frac{S+1}{\sqrt{Var(S)}} & (S < 0). \end{cases} \tag{3}$$

Here, Z represents the upward or downward trend of the series, where Z>0 indicates an upward trend and Z<0 indicates a

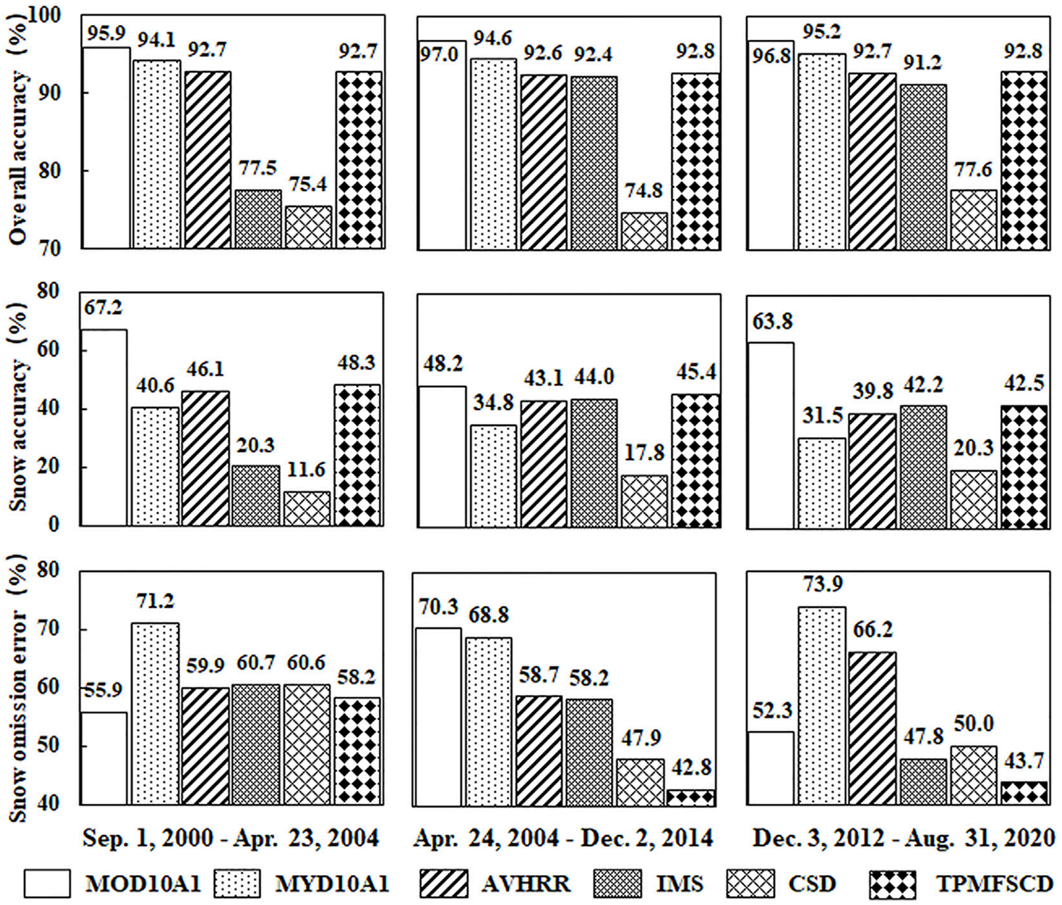

FIGURE 3
Accuracy evaluation of original and multi-source fusion snow cover data. **(A)** Overall accuracy. **(B)** Snow accuracy. **(C)** Snow omission error.

downward trend. For a given significance level α, if $|Z| \geq Z_{1-\alpha/2}$, it means that at the level of significance test α, Xt has an obvious upward or downward trend; 1.96 and 1.28 correspond to the critical values at significance levels (P) of 0.05 and 0.20, respectively. The calculation process is as follows: $\alpha = 0.05$ as an example, $Z_{1-\alpha/2}=Z_{0.975}$, the query standard normal distribution table $Z_{0.975}=1.96$, so when $|Z| \geq 1.65$, the sequence passes the 95% significance test. In this study, $p \leq 0.05$ and $0.05 < p \leq 0.2$ were defined as significant and weakly significant change, respectively. Only significant and weakly significant change has been analyzed in the following sections.

4 Results and discussion

4.1 Snow data evaluation and fusion results

The accuracy of the original and multi-source fusion snow cover data have been evaluated based on snow observations at 139 stations from 2000 to 2020 (Figure 3). Among the five original data, the overall accuracies of MOD10A1, MYD10A1, and AVHRR are above 90%. Snow accuracies are the highest for MOD10A1 with 48.2–67.2%, AVHRR with 39.8–46.1%, and MYD10A1 with 31.5–40.6%. The snow omission error rates are MOD10A1, AVHRR, and MYD10A1 in order from low to high, above 50%, 60%, and 70%, respectively. It can be seen that the applicability of these three data on the Tibetan Plateau is MOD10A1, AVHRR, and MYD10A1 in a descending order, but the spatial resolution of MOD10A1 and MYD10A1 is much higher than that of AVHRR. The overall accuracy of IMS data is only 77.5% in period 1, but above 90% in periods 2 and 3. Similarly, its snow accuracy is only 20.3% in period 1, but more than 40% in periods 2 and 3. In the latter two periods, the snow accuracies of IMS data are higher than that of AVHRR data, but the accuracy of IMS no snow part is lower than AVHRR. Compared with other data, the CSD data have lower overall accuracy (74.8–77.6%) and lower snow accuracy (11.6–20.3%), although its snow omission error is lower.

Considering the aforementioned analysis and spatial resolution of the data, two multi-source data fusion strategies have been determined to develop the Tibetan Plateau multi-source data fusion snow cover dataset (TPMFSCD). The specific fusion process is shown in Supplementary Figure S1. In the fusion process, the MODIS data are used as the benchmark to calculate the center coordinates of each pixel, and then the pixel values from other data in the corresponding positions under the same coordinate system (WGS84) are obtained to participate in data fusion. Before 24 April 2004, i.e., period 1, the fusion has been performed in the order of MOD10A1 cloud-free part, MYD10A1 cloud-free part, AVHRR identified part, IMS, and CSD. In periods 2 and 3, the fusion has been performed in the order of MOD10A1 cloud-free part, MYD10A1 cloud-free part, IMS snow part, AVHRR identified part, IMS no snow part, and CSD. The validation of the fusion results shows that the overall accuracy of the newly developed data is higher than 92%, and the snow accuracies range from 42.5% to 48.3%. Although the snow accuracy of the new data is lower than MOD10A1, it is higher than other data. At the same time, the snow omission error of the new data is effectively reduced, especially in the two periods after 2004. Compared to the existing cloud-free data AVHRR and IMS, the snow omission error of the new data is reduced by 4.1–15.9% and 15.4–22.5%, respectively. It can be seen that the newly developed TPMFSCD not only integrates the high snow accuracy of MODIS data in cloud-free condition but also improves the snow omission error. The TPMFSCD is completely cloud-free data with high spatial and temporal resolutions, which can reflect all the snow cover conditions on the Tibetan Plateau.

4.2 Spatial differences in snow cover on the Tibetan Plateau

The snow distribution on the Tibetan Plateau has obvious spatial heterogeneity (Figure 4). Percentage of the longest SCD is the ratio of the longest SCD to snow cover days, which is used to reflect the contribution of the longest snow cover period to the annual snow. The Amu Darya and Indus in the western part of the plateau have the longest average snow cover days, reaching 186 and 160 days, respectively. The longest SCD in these two basins last 5–9 months, with the average of 130 and 99 days, respectively, accounting for more than 60% of the snow cover days. The average snow cover days in the Tarim, Lancang River, Nujiang River, Yarlungzangbo, and Ganges are 89, 83, 106, 78, and 72 days, respectively. The longest SCD in most areas range from 25 to 35 days, and more than 70% of the snow cover comes from short-term snow cycles less than 5 days. Other basins, including the Hexi, Qaidam, TP interior, Yellow River, and Yangtze, have annual snow cover days of less than 2 months, 53, 47, 52, 58, and 56 days, respectively. The longest SCD is also short, at around 2 weeks, and more than 80% of the snow cover comes from the short-term snow cycles lasting less than 3 days. The snow cycles is ~5 times in areas below 2,000 m at the edge of the plateau, and ~20 times in areas above 2,000 m, except for the south of the TP interior and the upper reaches of the Yarlungzangbo. The snow cycle is more than 35 times at high altitude of the Tarim, Lancang River, Nujiang River, and Ganges. All of these indicate that the contribution of the longest SCD to the snow cover is limited, and the short-term snow cycles and their variation should be considered simultaneously when understanding the snow cover on the Tibetan Plateau.

As the altitude increases, the annual snow cover days and the longest SCD increase, while the number of snow cycles first increases and then decreases (Figure 5, Supplementary Figure S2). The snow cover in high-altitude areas is relatively stable, since the low temperature conditions here are more conducive to preserving the snow cover, even in summer. According to the annual snow cover days and the longest SCD, the plateau has been divided into persistent, stable, unstable, and ephemeral snow covers (Figure 6). The persistent snow cover is 5.84×10^5 km^2 (16.2%), mainly distributed in the Indus (5.5%,>2900 m), Amu Darya (3.6%, >3300 m), Tarim (1.6%,>5100 m), Ganges (1.7%,>5100 m), and Yarlungzangbo (1.1%, >5500 m). The three northern regions have the annual snow cover days of 253–316 days, the longest SCD of 176–218 days, and the snow cycle of 15 times, all of which in the two southern regions is ~300 days, ~140 days, and 22 times. The stable snow cover is 9.45×10^5 km^2 (26.2%), mainly distributed in the TP interior (4.7%, 5,300–5800 m), Yangtze (4.6%, 4,200–5500 m), Yellow River (3.3%, 3,600–4900 m), and Tarim (2.6%, 3,300–5100 m). The annual snow cover days is ~100 days, with the longest SCD of ~30 days, and snow cycle of 23–27 times. The unstable snow cover is 1.64×10^6 km^2 (45.5%), mainly distributed in the TP interior (12.7%, <5300 m), Yangtze (6.9%, 2500–4200 m), Yellow River (6.1%, <3600 m), and Tarim (4.5%, 3300 m), with the annual snow cover days of 25–43 days. The longest SCD lasts ~10 days, and the snow cycle is 8–17 times. The ephemeral snow cover is 4.36×10^5 km^2 (12.1%), mainly distributed in the area below 2,000 m of the Ganges and Yangtze and in the Qaidam. Compared with previous studies (Li and Li, 1983; Zhang and Zhong, 2014; Li et al., 2022), this study has fully considered the spatial and temporal continuities of snow cover and clarified the snow classification in different basins and their altitude dependences.

In terms of basins, the Amu Darya and Indus are dominated by persistent snow cover. The Lancang River and Nujiang River are dominated by stable snow cover, and other basins are dominated by unstable snow areas, followed by stable snow areas. Controlled by geographical location and climatic background, the altitude of each basin to reach the persistent and stable snow cover are different. The Amu Darya and Indus in the northwestern direction of the plateau are at high latitude and directly controlled by the westerly, reaching the persistent snow cover at ~3,000 m. Other areas of the plateau do not have the

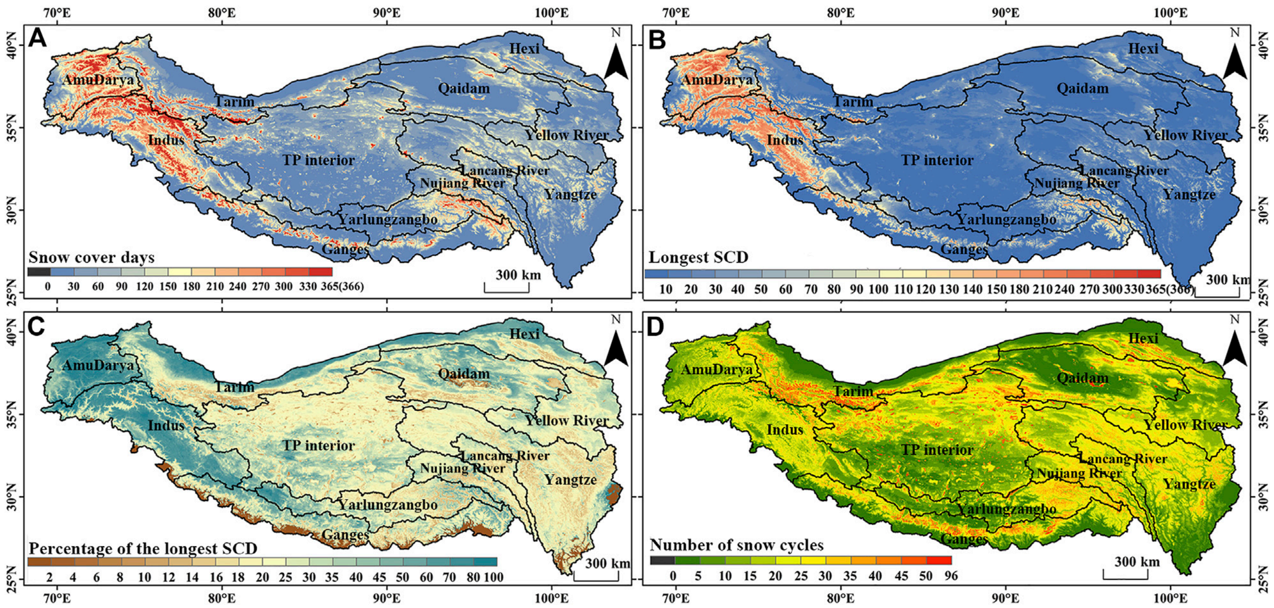

FIGURE 4
TPMFSCD observed snow characteristics on the Tibetan Plateau. **(A)** Snow cover days, **(B)** longest snow cover duration (SCD), **(C)** percentage of the longest SCD, and **(D)** number of snow cycles.

persistent snow cover until at least 5,000 m. In the TP interior and the upper reaches of the Yarlungzangbo, the persistent snow cover will not appear until at least 6,000 m. Similarly, the Amu Darya and Indus can have the stable snow cover at ~2,000 m, and the Ganges, controlled by the Indian monsoon, has the stable snow cover at 3,000 m. The Tarim, Hexi, and the Yellow River with higher latitude have the stable snow cover at ~3,500 m. The Qaidam, Yangtze, Lancang River, Nujiang River, and the middle and lower reaches of the Yarlungzangbo, which are inland or at lower latitudes, have the stable snow cover at ~4,200 m, and the stable snow cover does not occur until even above 5,300 m on the TP interior.

4.3 Contrasting changes of snow cover on the Tibetan Plateau

During the period from 2000 to 2021, we estimate a significant decrease in in the snow cover days for the large region on the Tibetan Plateau (23.0%), and significant increasing accounting 4.9%, with a trend of −1.5 and 2.1 d/y(Figure 7A). The areas with snow decreasing are mainly in the Yangtze, Lancang River, Nujiang River, Yarlungzangbo, and Ganges, located in the southeastern and south part of the plateau. The gradual rise of the snowline height in these areas from 1995 to 2016 (Liu et al., 2021) also confirms the decreasing trend of snow cover. Areas of increasing and decreasing snow coexist in the Amu Darya, Indus, Tarim in the northwestern part of the plateau, and in the Qaidam and Yellow Rivers in the northeast. The area of snow reduction increases with elevation, from 4.4% (<2,500 m) to 8.4% (2,500–4,000 m) to 10.3% (>4,000 m), and that of increased snow also increases from 0.2% (<2,500 m) to 1.0% (2,500–4,000 m) to 3.6% (>4,000 m) (Supplementary Figure S3A). The corresponding snow reductions range from −0.7 to −1.3 to −1.9 d/y, and the increases range from 0.4 to 2.0 to 2.2 d/y (Figure 7B). It can be seen that the change of snow cover is more pronounced, and the magnitude is greater at higher altitude. The reduction of snow cover at high elevation may aggravate the warming of the TP interior (Zhang et al., 2022).

During the same period, the longest SCD decreases in 17.4% and increases in 5.8% of the Tibetan Plateau (Supplementary Figure S3D), with the rate of −0.4 and 2.5 d/y (Figures 7C,D). The areas with large reduction in the longest SCD are located in the Yangtze, Lancang River, Nujiang River, and Brahmaputra rivers, and that of the increase are located in the Amu Darya and Indus. Number of snow cycle decreases in 27.6% and increases in 3.7% of the plateau (Supplementary Figure S3F), with the rate of −0.2 and 0.1 time per year (n/y) (Figure 7E). The number of snow cycle is significantly reduced in most snow-covered areas of the Tibetan Plateau, except for the central part of the Yellow River and the upper reaches of the Yarlungzangbo. Similarly, the area and magnitude of changes in the longest SCD and number of snow cycles increases with elevation (Figure 7F, Supplementary Figure S3).

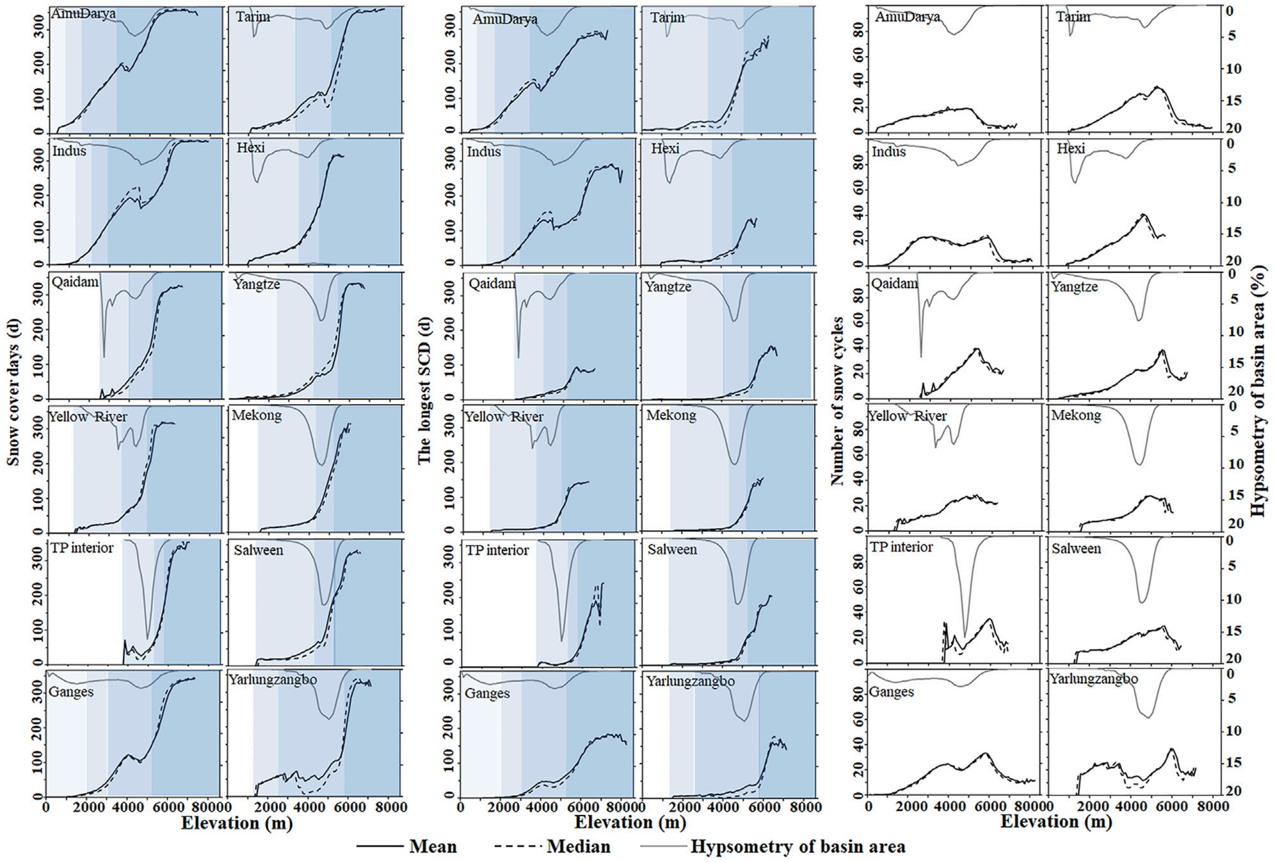

FIGURE 5
Snow cover days, the longest SCD, and number of snow cycles in each basin of the Tibetan Plateau.

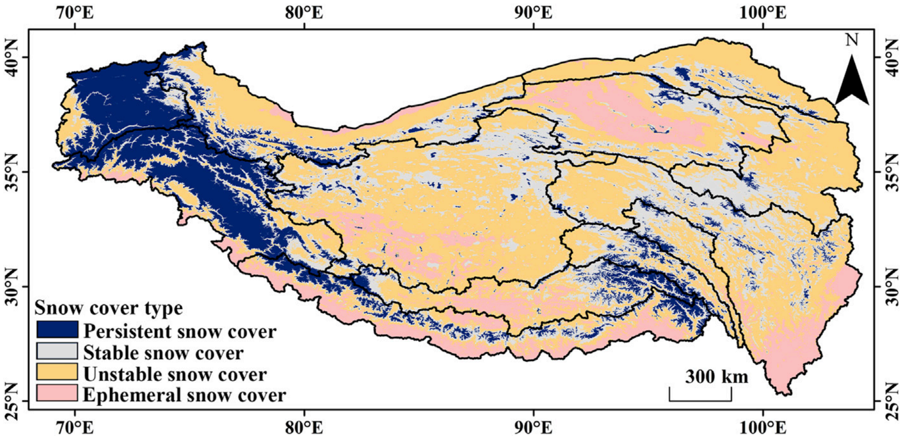

FIGURE 6
Snow cover zoning of the Tibetan Plateau.

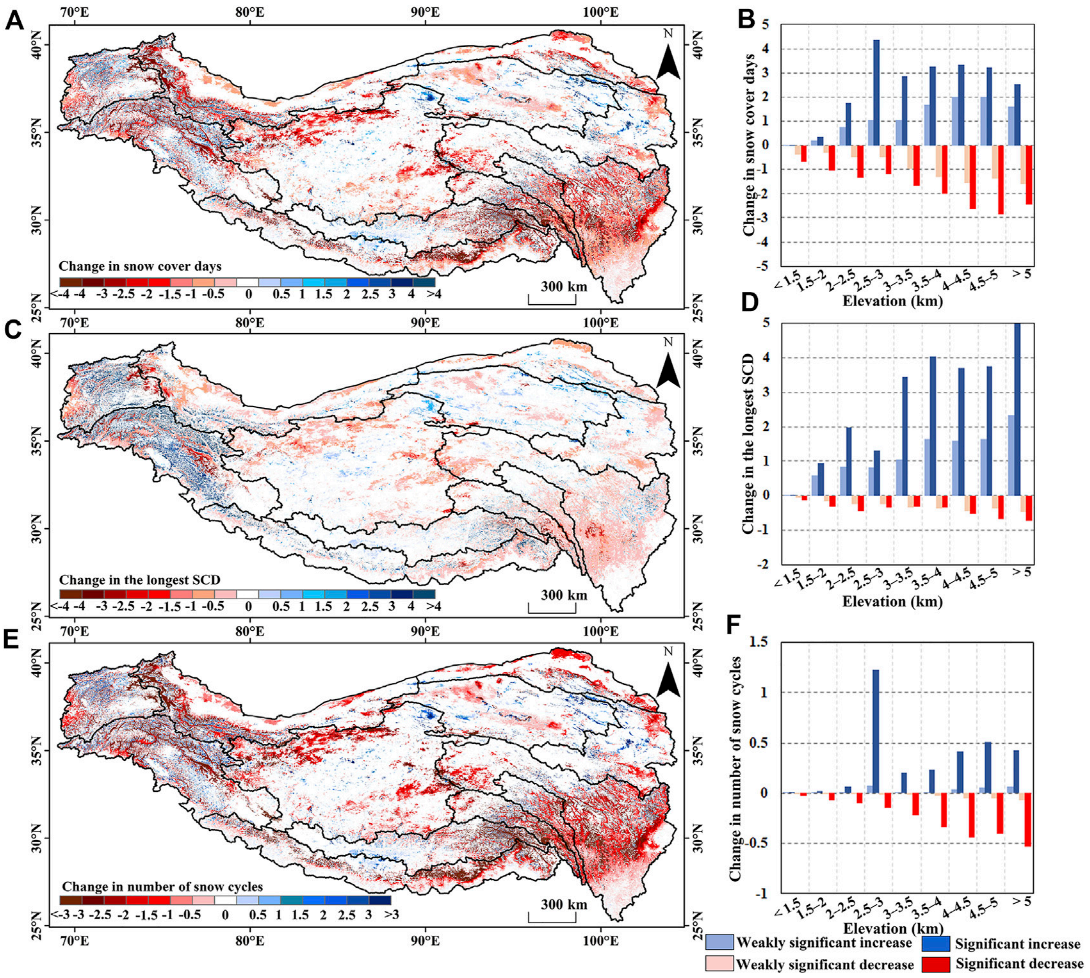

FIGURE 7
Changes in snow cover days **(A)**, longest SCD **(C)**, number of snow cycles, **(E)** and corresponding values in different elevation zones **(B,D,F)**.

Figures 8, 9 illustrate the percentage of increase and decrease area and trends in snow cover of each basin. In the latest 21 years, the snow cover days in all the basins dominated by the significant reductions, and the area with significant decrease is much larger than the area with significant increase. Compared to other basins, the basins with the largest proportion of snow increase are the Amu Darya and Indus. The snow cover days decrease in 21.2% of the basins and increase in 10.4%, with the rate of -1.9 and 1.8 d/y, respectively. Almost all the increasing areas are located above 3,000 m. As the altitude increases, the area of increasing snow cover days increase, and the area of increased snow cover days above 4,500 m is more than decreased. It is noteworthy that in both basins above 3,000 m, the areas and magnitude of the increased longest SCD are more than that of the decreased (14.4%, 4.0 d/y vs 6.4%, and −2.3 d/y). In the area less than 3,000 m, the longest SCD is dominated by a decrease of −0.9 d/y. For the snow cycle, 27.0% of the area decreases and 6.0% increases. The snow cycle increases by less than 1.3% at all elevation intervals. Therefore, the decrease of snow cover days on the Amu Darya and Indus are mainly due to the reduction of short-term snow cycles. Meanwhile, the increase of snow cover days over 3,000 m is mainly due to the increase of the longest SCD, while the short-term snow cycles also decreases. From the period of 2001–2005 to 2016–2021, the longest SCD on the Amu Darya increases from 128 to 138 days, and on the Indus from 84 to 109 days. The number of snow cycles on the Amu Darya decreases from 18 to 15, while that on the Indus decreases from 19 to 17. In addition, there is an increase in the longest SCD in some areas of these two basins, along with a decrease in the short-term snow cycles, which leaves the snow cover days unchanged.

In Tarim and Hexi, the areas and magnitudes of decreased and increased snow cover days are 23.0%, −1.4 d/y and 3.8%, 2.5 d/y, respectively. The areas and magnitudes of decrease and increase in the longest SCD are 18.4%, −0.3 d/y and 4.4%, 2.5 d/y,

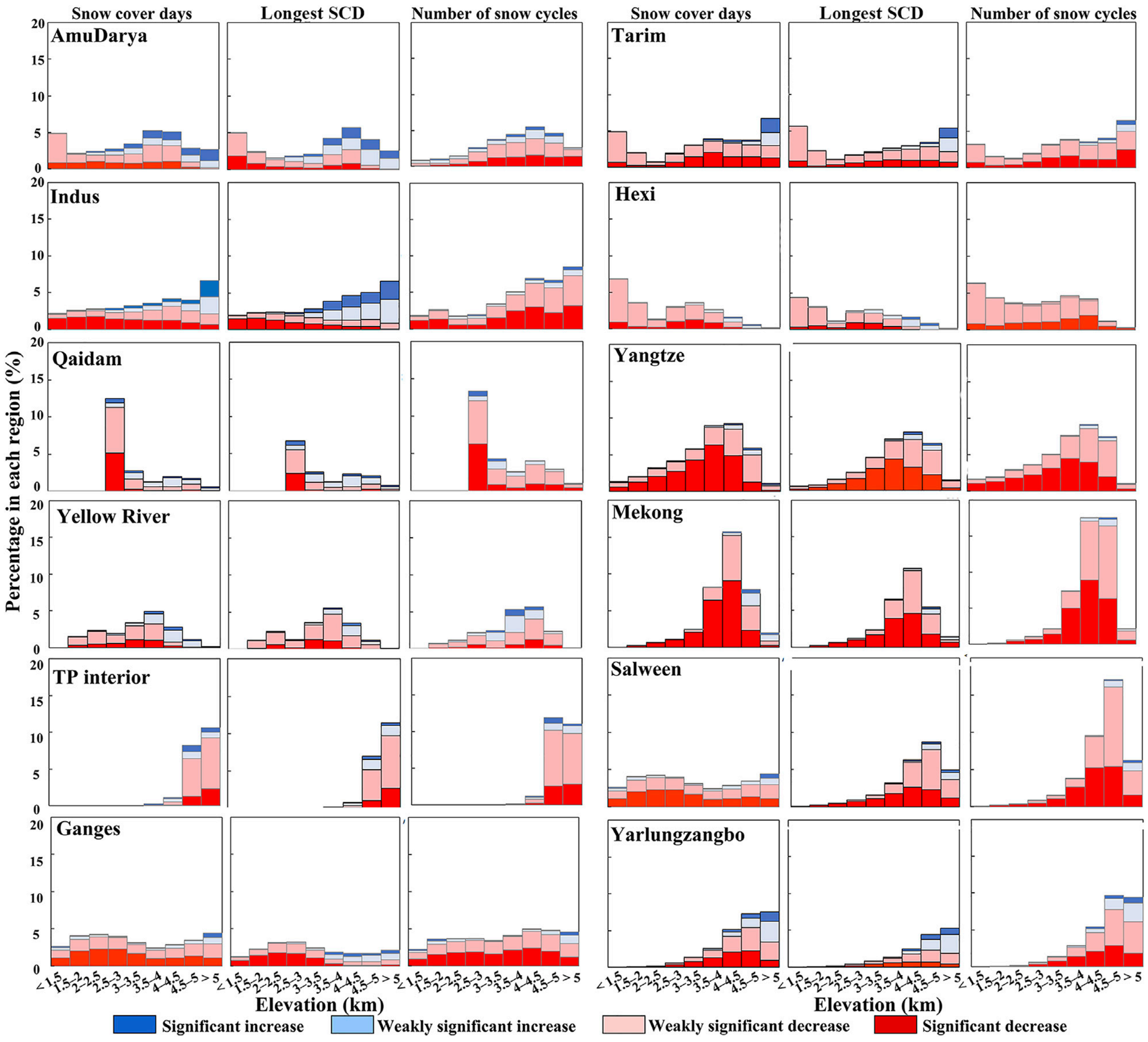

FIGURE 8
Percentage of snow cover increase and decrease areas in each basin.

respectively, while that of the snow cycles are 28.2%, −0.2 n/y and 2.0%, 0.2 n/y, respectively. The decrease in snow cover days, mainly located below 4,500 m, is not only related to the decrease of the longest SCD but also the decrease in the short-term snow cycles brings a greater impact. The area of increased snow cover days are located above 4,500 m, and there are more areas of increase than decrease, mainly influenced by the increase in the longest SCD, but the short-term snow cycles still decrease, which is identical to that of the Indus and Amu Darya.

In Qaidam, the Yellow River and TP interior, the snow cover days decrease and increase by 14.4% and 4.4% (-0.5 vs 2.2 d/y), respectively. The areas of increased snow cover days occur above 4,000 m. The longest SCD decrease and increase by 12.7% and 4.3% (- 0.1 vs 0.8 d/y), respectively, and the number of snow cycles decreases and increases by 18.9% and 4.5% (- 0.1 vs 0.2 n/y), respectively. The decrease in snow cover days in these regions is related to both the decrease in the longest SCD and the short-term snow cycles, and the increase in snow cover days is also the superposed effect of the increase in the longest SCD and short-term snow cycles. But the increase of the snow cover days in the Yellow River mainly comes from the increase of short-term snow cycles.

The most significant reduction of snow cover days is observed in the Yangtze, Lancang River, and Nujiang River.

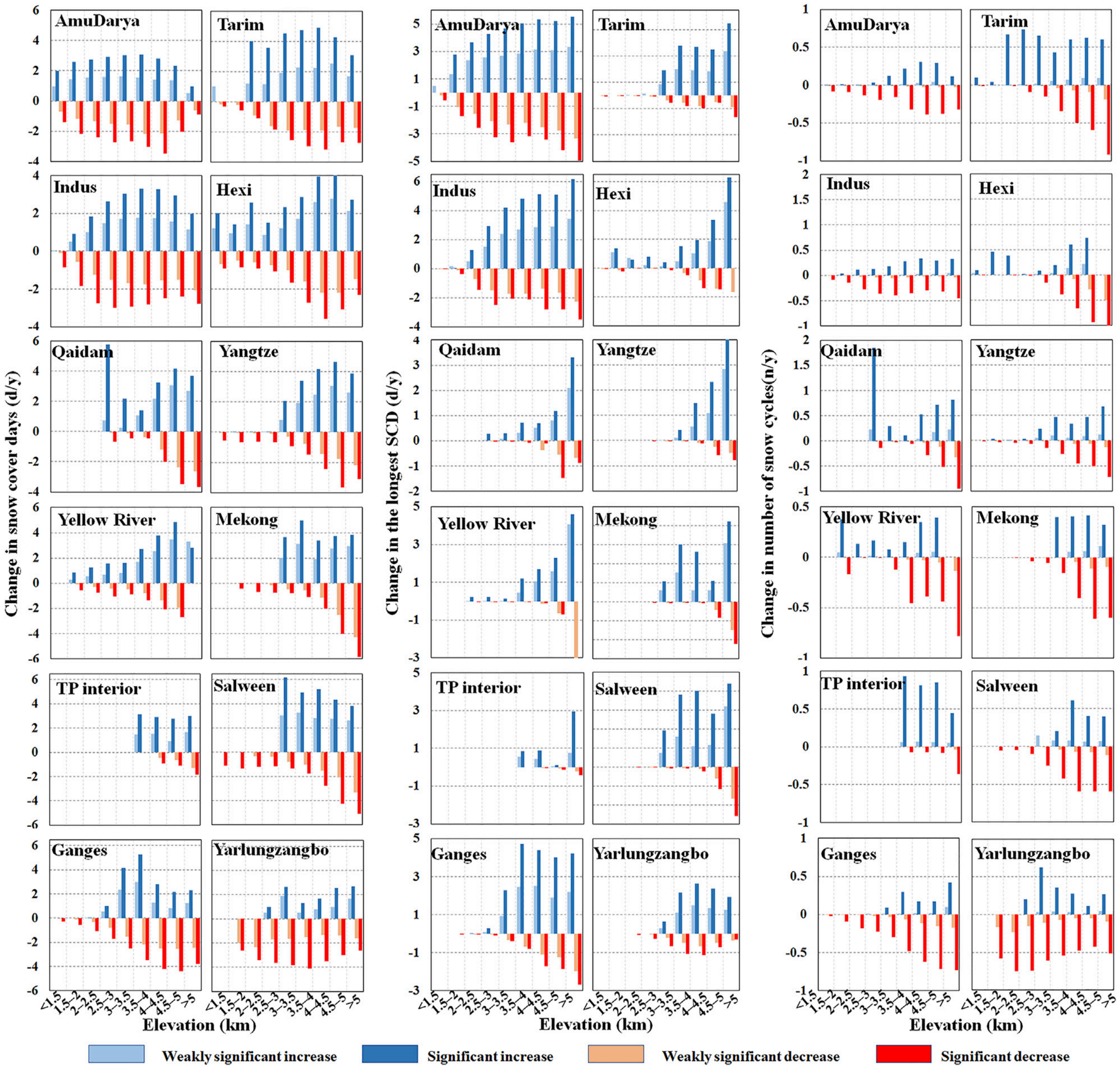

FIGURE 9
Trends in snow cover of each basin.

The snow cover days decreased in 35.0% (-1.8 d/y) of these regions and increased in only 3.3% (3.0 d/y). Most of the increased areas are located above 4,000 m, but the increased areas are much smaller than the decreased. The areas with decreased and increased longest SCD are 26.6% and 2.4% (-0.3 vs 1.8 d/y), respectively, while that snow cycles are 40.7% and 2.0% (-0.2 vs. 0.1n/y), respectively. The combination of the reductions in the longest SCD and the decreases of snow cycles over the large areas, has resulted in the reduction of the snow cover days.

The snow cover days in the Yarlungzangbo and Ganges also predominantly decreased, with 22.0% of the area decreasing and only 5.8% increasing in snow cover days, and the magnitude is -2.1 and 1.5 d/y, respectively. Unlike other basins where the increased and decreased snow cover are located in the same mountains, the increased snow in this region is mainly located in the middle and upper reaches of the Yarlungzangbo, mainly related to the increase in short-term snow cycles. The decreasing areas are mainly located in the Himalayas and Tanggula Mountains of this region. The areas of the decreased and increased longest SCDs are

11.4% and 5.6% (-0.5 vs 2.1 d/y), respectively and that of snow cycles are 26.7% and 5.4% (-0.2 vs 0.1n/y). The reduction of the snow cover days in these two regions is related to the decrease of the longest SCD, while the reduction in short-term snow cycles also plays a more important role.

5 Conclusion

The snowpack on the Tibetan Plateau not only provides an important freshwater resource for the surrounding region but its high albedo also governs the energy exchange of the ground–air system and thus influence climate change in Asia and globally. In recent years, the spatial and temporal resolutions of snow remote sensing data have been increasing, but the unique snow characteristics such as thin snow depth and high frequency of change on the Tibetan Plateau, as well as the complex and rugged land surfaces have limited their applicability in this region. This study comprehensively evaluated the applicability of five commonly used snow data, namely, MOD10A1, MYD10A1, IMS, AVHRR, and CSD on the Tibetan Plateau based on snow observations at 139 stations from 2000 to 2020. According to the evaluation of each snow data at different periods, two fusion strategies were developed and adopted to generate the Tibetan Plateau multi-source data fusion snow cover dataset from 2000 to 2021. The dataset with high spatial and temporal resolutions is completely cloud-free and have an overall accuracy of 92.7%.

The new data show that the annual snow cover days on the Tibetan Plateau is not only influenced by the largest SCD but is also controlled by the short-term snow cycles. The number of snow cycles is ~20 times per year in most areas of the plateau, and over 35 times at higher elevations. The Amu Darya and Indus in the western part of the plateau have the longest average annual snow cover days, greater than 160 days, and the longest SCD accounts for more than 60% of the snow cover days. The Tarim, Lancang River, Nujiang River, Yarlungzangbo, and Ganges have more than 70 days of snow cover days, but more than 70% comes from short-term snow cycles lasting less than 5 days. Other areas including Hexi, Qaidam, TP inland areas, Yellow River, and Yangtze have short snow cover days of 60 days, and more than 80% comes from short-term snow cycles lasting less than 3 days. The areas of persistent, stable, unstable, and ephemeral snow covers on the Tibetan Plateau are 16.2%, 26.2%, 45.5% and 12.1%, respectively. The persistent snow cover is mainly distributed in the Indus and Amu Darya. Under the direct effect of the westerly, the persistent snow cover occur above 3,000 m in these two basins. In contrast, the other areas do not have persistent snow cover until at least 5,000 m or more. Stable snow cover is mainly distributed above 3,500 m in the Tarim and Yellow River, above 4,200 m of Yangtze, and above 5,300 m in the TP interior.

Over the last two decades, 23.0%, 17.4%, and 27.6% of the Tibetan Plateau have experienced a significant decrease in the snow cover days, the longest SCD, and the number of snow cycles, with the rate of −1.5 d/y, −0.4 d/y, and −0.2 n/y, respectively. In contrast, 4.9%, 5.8%, and 3.7% of the regions have a significant increase in the snow cover days, the longest SCD and the number of snow cycles, with the rate of 2.1 d/y, 2.5 d/y, and 0.1 n/y. All basins have a predominantly significant reduction in snow cover days, and the areas with the decrease are much greater than the increase. Compared to other basins, the Amu Darya and Indus in the northwest have the largest proportion of snow increase, while the Yangtze, Lancang River, and Nujiang River in the southeast have the largest proportion of decrease. As the altitude increases, both the area and magnitude of increasing and decreasing snowpacks increase. The significant reduction in the snow cover days on the Tibetan Plateau stems from the superimposed effect of the simultaneous reduction in the largest SCD and the short-term snow cycles, while the reductions in the Amu Darya and Indus mainly comes from the reduction in the short-term snow cycles. The significant increase of snow cover days in the Amu Darya, Indus, Tarim, and Hexi mainly comes from the increase of the longest SCD, and that in the Yellow River and Qaidam mainly comes from the increase in the short-term snow cycles. The significant increase is mainly distributed at the high-altitude area, and the area with increased snow is greater than that with decreased above 4,500 in the Amu Darya, Indus, Tarim, and Hexi or above 4,000 m in the Yellow River and Qaidam. This contrasting change in the snowpack on the Tibetan Plateau, which decreases in the southeast and increases in the northwest, with a large decrease at lower elevations and an increase at higher elevations, will bring new challenges to water resource management in the region.

Data availability statement

The raw data supporting the conclusion of this article will be made available by the authors, without undue reservation.

Author contributions

YG: conceptualization, methodology, data curation, software, visualization, formal analysis, writing—original draft, writing—review and editing, and funding acquisition. HD: data processing, software, visualization, and formal analysis. YD: data curation, methodology, and formal analysis. NM: conceptualization and supervision. WW: writing—original draft and editing.

Funding

This work was supported by the Second Tibetan Plateau Scientific Expedition and Research (STEP) program (grant number 2019QZKK0201), the Natural Science Foundation of China (grant number 42171136), and the Basic Science Center for Tibetan Plateau Earth System (BSCTPES, NSFC grant number 41988101—03).

Acknowledgments

The authors would like to thank the Chinese Meteorological Administration (CMA) for providing snow observation information and data.

Conflict of interest

The authors declare that the research was conducted in the absence of any commercial or financial relationships that could be construed as a potential conflict of interest.

Publisher's note

Supplementary material

The Supplementary Material for this article can be found online at: https://www.frontiersin.org/articles/10.3389/feart.2022.1075988/full#supplementary-material

References

Brown, L. C., Howell, S. E. L., Mortin, J., and Derksen, C. (2014). Evaluation of the interactive multisensor snow and ice mapping system (IMS) for monitoring sea ice phenology. *Remote Sens. Environ.* 147, 65–78. doi:10.1016/j.rse.2014.02.012

Che, T., Li, X., Jin, R., Armstrong, R., and Zhang, T. (2008). Snow depth derived from passive microwave remote-sensing data in China. *Ann. Glaciol.* 49, 145–154. doi:10.3189/172756408787814690

Che, Z, Z., Jin, M., Zhang, X., Zhang, H., Niu, Y., and Dong, X. (2008). Effect of vegetation type on the ablation of snow cover in the qilian mountains. *J. Glaciol. Geocryol.* 30 (3), 392–397.

Chelamallu, H. P., Venkataraman, G., and Murti, M. V. R. (2013). Accuracy assessment of MODIS/Terra snow cover product for parts of Indian Himalayas. *Geocarto Int.* 29 (6), 592–608. doi:10.1080/10106049.2013.819041

Chen, L., Zhang, W., and Gao, H. (2022). Spatiotemporal dynamic characteristics of snow cover from 1980 to 2019 in the Three-River Source region and its response to climate change. *J. Glaciol. Geocryol.* 44 (1), 133–146.

Chiu, J., Paredes-Mesa, S., Lakhankar, T., Romanov, P., Krakauer, N., Khanbilvardi, R., et al. (2020). Intercomparison and validation of MIRS, MSPPS, and IMS snow cover products. *Adv. Meteorology* 2020, 1–10. doi:10.1155/2020/4532478

Chu, D., ZhaXi, D. Z., and CiDan, Y. Z. (2021). Analysis on applicability of NOAA IMS snow and ice products in snow cover monitoring over the Tibetan Plateau. *J. Glaciol. Geocryol.* 43 (6).

Dai, L., Che, T., Ding, Y., and Hao, X. (2017). Evaluation of snow cover and snow depth on the Qinghai–Tibetan Plateau derived from passive microwave remote sensing. *Cryosphere* 11 (4), 1933–1948. doi:10.5194/tc-11-1933-2017

Dai, L., Che, T., and Ding, Y. (2015). Inter-calibrating SMMR, SSM/I and SSMI/S data to improve the consistency of snow-depth products in China. *Remote Sens.* 7 (6), 7212–7230. doi:10.3390/rs70607212

Dietz, A. J., Kuenzer, C., and Conrad, C. (2013). Snow-cover variability in central Asia between 2000 and 2011 derived from improved MODIS daily snow-cover products. *Int. J. Remote Sens.* 34 (11), 3879–3902. doi:10.1080/01431161.2013.767480

Flanner, M. G., Shell, K. M., Barlage, M., Perovich, D. K., and Tschudi, M. A. (2011). Radiative forcing and albedo feedback from the Northern Hemisphere cryosphere between 1979 and 2008. *Nat. Geosci.* 4 (3), 151–155. doi:10.1038/ngeo1062

Gafurov, A., and Bardossy, A. (2009). Cloud removal methodology from MODIS snow cover product. *Hydrol. Earth Syst. Sci.* 13 (7), 1361–1373. doi:10.5194/hess-13-1361-2009

Gao, Y., Xie, H., Lu, N., Yao, T., and Liang, T. (2010). Toward advanced daily cloud-free snow cover and snow water equivalent products from Terra–Aqua MODIS and Aqua AMSR-E measurements. *J. Hydrology* 385 (1-4), 23–35. doi:10.1016/j.jhydrol.2010.01.022

Gyawali, D. R., and Bárdossy, A. (2022). Development and parameter estimation of snowmelt models using spatial snow-cover observations from MODIS. *Hydrol. Earth Syst. Sci.* 26 (12), 3055–3077. doi:10.5194/hess-26-3055-2022

Hall, D. K., Riggs, G. A., Salomonson, V. V., DiGirolamo, N. E., and Bayr, K. J. (2002). MODIS snow-cover products. *Remote Sens. Environ.* 83, 181–194. doi:10.1016/s0034-4257(02)00095-0

Hao, X., Huang, G., Che, T., Ji, W., Sun, X., Zhao, Q., et al. (2021). The NIEER AVHRR snow cover extent product over China – A long-term daily snow record for regional climate research. *Earth Syst. Sci. Data* 13 (10), 4711–4726. doi:10.5194/essd-13-4711-2021

Helfrich, S. R., McNamara, D., Ramsay, B. H., Baldwin, T., and Kasheta, T. (2007). Enhancements to, and forthcoming developments in the interactive multisensor snow and ice mapping system (IMS). *Hydrol. Process.* 21 (12), 1576–1586. doi:10.1002/hyp.6720

Henderson, G. R., Peings, Y., Furtado, J. C., and Kushner, P. J. (2018). Snow–atmosphere coupling in the northern Hemisphere. *Nat. Clim. Chang.* 8 (11), 954–963. doi:10.1038/s41558-018-0295-6

Hill, A. F., Rittger, K., Dendup, T., Tshering, D., and Painter, T. H. (2020). How important is meltwater to the chamkhar chhu headwaters of the Brahmaputra river? *Front. Earth Sci. (Lausanne).* 8. doi:10.3389/feart.2020.00081

Immerzeel, W. W., Droogers, P., de Jong, S. M., and Bierkens, M. F. P. (2009). Large-scale monitoring of snow cover and runoff simulation in Himalayan river basins using remote sensing. *Remote Sens. Environ.* 113 (1), 40–49. doi:10.1016/j.rse.2008.08.010

Ke, C., Li, P., and Wang, C. (1997). Variation trends of snow cover over the Tibetan plateau and their relations to temperature and precipitation. *J. Glaciol. Geocryol.* 19, 289–294.

Li, H., Zhong, X., Zheng, L., Hao, X., Wang, J., and Zhang, J. (2022). Classification of snow cover persistence across China. *Water* 14 (6), 933. doi:10.3390/w14060933

Li, P., and Li, D. (1983). Distribution of snow cover in China. *J. Glaciol. Geocryol.* 5 (4), 10–18.

Liu, C., Li, Z., Zhang, P., Tian, B., Zhou, J., and Chen, Q. (2021). Variability of the snowline altitude in the eastern Tibetan Plateau from 1995 to 2016 using google Earth engine. *J. Appl. Remote Sens.* 15 (4), 048505. doi:10.1117/1.jrs.15.048505

Mattar, C., Fuster, R., and Perez, T. (2022). Application of a cloud removal algorithm for snow-covered areas from daily MODIS imagery over andes mountains. *Atmosphere* 13 (3), 392. doi:10.3390/atmos13030392

Merz, B., Vorogushyn, S., Kriegel, D., and Gafurov, A. (2013). Evaluation of remotely sensed snow cover product in Central Asia. *Hydrology Res.* 44 (3), 506–522. doi:10.2166/nh.2012.094

Mishra, P., Zaphu, V. V., Monica, N., Bhadra, A., and Bandyopadhyay, A. (2016). Accuracy assessment of MODIS fractional snow cover product for eastern himalayan catchment. *J. Indian Soc. Remote Sens.* 44 (6), 977–985. doi:10.1007/s12524-016-0548-7

Muhammad, S., and Thapa, A. (2021). Daily terra–aqua MODIS cloud-free snow and randolph glacier inventory 6.0 combined product (M*D10A1GL06) for high-mountain Asia between 2002 and 2019. *Earth Syst. Sci. Data* 13 (2), 767–776. doi:10.5194/essd-13-767-2021

Notarnicola, C. (2020). Hotspots of snow cover changes in global mountain regions over 2000–2018. *Remote Sens. Environ.* 243, 111781. doi:10.1016/j.rse.2020.111781

Painter, T. H., Rittger, K., McKenzie, C., Slaughter, P., Davis, R. E., and Dozier, J. (2009). Retrieval of subpixel snow covered area, grain size, and albedo from MODIS. *Remote Sens. Environ.* 113 (4), 868–879. doi:10.1016/j.rse.2009.01.001

Ramsay, B. H. (1998). The interactive multisensor snow and ice mapping system. *Hydrol. Process.* 12 (10-11), 1537–1546. doi:10.1002/(sici)1099-1085(199808/09)12:10/11<1537::aid-hyp679>3.0.co;2-a

Riggs, G., and Hall, D. (2020). Continuity of MODIS and VIIRS snow cover extent data products for development of an Earth science data record. *Remote Sens.* 12 (22), 3781. doi:10.3390/rs12223781

Rittger, K., Painter, T. H., and Dozier, J. (2013). Assessment of methods for mapping snow cover from MODIS. *Adv. Water Resour.* 51, 367–380. doi:10.1016/j.advwatres.2012.03.002

Smith, T., Bookhagen, B., and Rheinwalt, A. (2017). Spatiotemporal patterns of High Mountain Asia's snowmelt season identified with an automated snowmelt detection algorithm. *Cryosphere* 11 (5), 2329–2343. doi:10.5194/tc-11-2329-2017

Tang, Z., Wang, J., Li, H., and Yan, L. (2013). Spatiotemporal changes of snow cover over the Tibetan plateau based on cloud-removed moderate resolution imaging spectroradiometer fractional snow cover product from 2001 to 2011. *J. Appl. Remote Sens.* 7 (1), 073582. doi:10.1117/1.jrs.7.073582

Yang, Z., Da, W., and Chu, D. (2017). Spatiotemporal variations of snow cover on the Tibetan plateau over the last 15 years. *Remote Sens. Technol. Appl.* 32 (1), 27–36.

Yu, X. Q., Qiu, Y. B., Ruan, Y. J., Shi, L. J., and Laba, Z. M. (2017). Validation and comparison of binary cloudless snow products in high Asia. *Remote Sens. Technol. Appl.* 32, 37–48.

Zhang, H., Immerzeel, W. W., Zhang, F., de Kok, R. J., Chen, D., and Yan, W. (2022). Snow cover persistence reverses the altitudinal patterns of warming above and below 5000 m on the Tibetan Plateau. *Sci. Total Environ.* 803, 149889. doi:10.1016/j.scitotenv.2021.149889

Zhang, T., and Zhong, X. (2014). Classification and regionalization of seasonal snow cover across the Eurasian Continent. *J. Glaciol. Geocryol.* 36 (3), 481–490.

frontiers | Frontiers in Earth Science

TYPE Original Research
PUBLISHED 05 January 2023
DOI 10.3389/feart.2022.998603

The total mass and spatial–temporal variability of aerial cryosphere over the Tibetan Plateau from 2003 to 2020

Yifan Yang[1], Tingfeng Dou[1]*, Gaojie Xu[1] and Cunde Xiao[2]

[1]College of Resources and Environment, University of Chinese Academy of Sciences, Beijing, China, [2]State Key Laboratory of Earth Surface Processes and Resource Ecology, Beijing Normal University, Beijing, China

OPEN ACCESS

EDITED BY
Lei Wang,
Institute of Tibetan Plateau Research,
Chinese Academy of Sciences (CAS),
China

REVIEWED BY
Changyong Cao,
National Oceanic and Atmospheric
Administration (NOAA), United States
Baojin Qiao,
Zhengzhou University, China
Zhihua He,
University of Saskatchewan, Canada

*CORRESPONDENCE
Tingfeng Dou,
doutf@ucas.ac.cn

SPECIALTY SECTION
This article was submitted to
Cryospheric Sciences,
a section of the journal
Frontiers in Earth Science

RECEIVED 20 July 2022
ACCEPTED 29 August 2022
PUBLISHED 05 January 2023

CITATION
Yang Y, Dou T, Xu G and Xiao C (2023),
The total mass and spatial–temporal
variability of aerial cryosphere over the
Tibetan Plateau from 2003 to 2020.
Front. Earth Sci. 10:998603.
doi: 10.3389/feart.2022.998603

Changes in snow, ice, and ecological system over the Tibetan Plateau (TP) are extremely sensitive to local precipitation and radiation budget, which are largely modulated by the atmospheric ice. However, how much ice is there in the atmosphere over the TP and how it is distributed are still unclear. The total mass, spatial distributions, and long-term trends of atmospheric ice over the TP were evaluated by using four sets of satellite retrieval data (Aqua, Terra, the Suomi National Polar-orbiting Partnership (Suomi NPP), and NOAA-20) and ERA5 reanalysis data from 2003 to 2020. Based on the estimations using multiple satellite datasets, we concluded that the total mass of atmospheric ice could be up to 0.26±0.03 Gt over the TP from 2013 to 2020. The spatial distributions of atmospheric ice derived from various datasets were highly consistent. In general, the southwest and northeast areas of the TP were the low-concentration areas (0.05 kg/m^2 in average), while the southeast area was the high-concentration area (0.09 kg/m^2 in average), and this spatial pattern was most evident in summer. The high values around (0.15 kg/m^2) were centered over Linzhi and its surrounding areas. The plentiful water vapor transported by southwest summer monsoon and steep topography jointly led to rapid growth of atmospheric ice in Southeast Tibet, which was the dominant reason for the higher ice concentration in this area.

KEYWORDS

aerial cryosphere, spatial–temporal variability, ice water path, multi-source data, Tibetan Plateau

1 Introduction

As a sensitive area of climate change, the air temperature of the TP had increased much faster than that of the other areas at the same latitude (Liu and Chen, 2000), and the mass and energy balance of ice and snow in this area are greatly influenced by radiation and precipitation associated with the aerial cryosphere. The aerial cryosphere is composed of all ice bodies in the atmosphere, including those in clouds (ice clouds and ice crystals) and those under clouds

TABLE 1 Acronyms and abbreviations used in this study.

Acronyms and abbreviations	Full name
ANN	Artificial neural network
CERES	Clouds and the Earth's Radiant Energy System
CWP	Cloud water path
ECMWF	European Centre for Medium-Range Weather Forecasts
FM	Flight model
GEBCO	General Bathymetric Chart of the Oceans
IWC	Ice water content
IWP	Ice water path
LWP	Liquid water path
MODIS	Moderate Resolution Imaging Spectroradiometer
Suomi NPP	Suomi National Polar-orbiting Partnership
TP	Tibetan Plateau
TPDC	National Tibetan Plateau Scientific Data Center
VIIRS	Visible Infrared Imaging Radiometer Suite

(snowflake and hail) (Qin et al., 2018). It is an element with the largest coverage in the cryosphere, which has an important impact on the radiation budget and water cycle in the climate system (Dou et al., 2020). Previous studies have indicated that the atmospheric ice dominated the distribution and lifetime of ice clouds and mixed-phase clouds over the TP (Long, 2016; Li et al., 2018; Zhao et al., 2021), thus profoundly affecting the surface radiation budget. Therefore, it is of great significance to investigate the spatial–temporal variability of the atmospheric ice over the TP.

With the rapid progress of satellite remote sensing technology and the improvement of data assimilation, the remote sensing data and reanalysis data were increasingly used to explore the pattern of different phases of water in the atmosphere in the past few decades (Liljegren et al., 2001; Horváth and Davies, 2007; O'Dell et al., 2008; Lebsock and Su, 2014; Khanal et al., 2020; Qi et al., 2022). Some studies suggested that the cloud water path (CWP) increased in most regions of the TP from the 1980s to the beginning of this century (Li et al., 2008; Yue et al., 2016). The annual average of the ice water path (IWP) had been relatively stable from 2000 to 2015 without any obvious trend (Li et al., 2018). In contrast, on the seasonal scale, the IWP in the premonsoon season (March to May) and winter showed a significant upward trend in the western TP, while in monsoon season (June to September), a significant downward trend in the western TP was observed (Zhao et al., 2021).

Earlier studies estimated the total mass (Dou et al., 2020; Xu et al., 2022) and investigated the spatial–temporal distribution of atmospheric ice on a global scale using multiple sets of satellite remote sensing data and high-quality reanalysis data (Duncan and Eriksson, 2018; Dou et al., 2020; Xu et al., 2022). However, the total mass and spatial–temporal distribution of atmospheric ice over the TP are poorly understood, and there is also a lack of uncertainty analysis based on the multi-source data. Here, we used four sets of satellite retrieval products, namely, Aqua, Terra, the Suomi NPP, and NOAA-20 in CERES_SSF_1deg-Month L3 data and ERA5 reanalysis to carry out a quantitative study of atmospheric ice over the TP and reveal the main controlling factors of its spatial pattern. Note that acronyms and abbreviations used in this study are given in Table 1.

2 Data and methods

2.1 Data

2.1.1 Boundary data

The boundary data on the TP in this study were downloaded from the National Tibetan Plateau Scientific Data Center (TPDC). The TP is about 3,360 km from east to west and 1,560 km from south to north, ranging from 25°59′30″N to

TABLE 2 The multi-year mean mass of aerial cryosphere over the TP derived from three satellite products and ERA reanalysis from 2013 to 2020 (Unit: Gt).

	Spring (MAM)	Summer (JJA)	Autumn (SON)	Winter (DJF)	Average
Aqua	0.28	0.34	0.26	0.23	0.28
ERA5	0.27	0.30	0.19	0.20	0.24
Terra	0.24	0.26	0.22	0.21	0.23
S-N-N	0.29	0.36	0.27	0.23	0.29

40°1′0″N and 67°40′37″E to 104°40′57″E, with a total area of 3.08 million km^2 (Zhang et al., 2002; Zhang et al., 2021a; Zhang et al., 2021b).

2.1.2 Topography data

The topography data we used were produced by The General Bathymetric Chart of the Oceans (GEBCO), which showed a global terrain model for the ocean and land, providing elevation data in meters, on a 15 arc-second interval grid (Group, 2019).

2.1.3 Remote sensing retrieval data

The remote sensing products were retrieved by the Terra, Aqua, Suomi NPP, and NOAA-20 satellites from the CERES_SSF_1deg-Month L3 data. Clouds and the Earth's Radiant Energy System (CERES) was a NASA project that looked into the role of cloud and radiation feedback in the climate system (Wielicki et al., 1996). When coupled with the global climate model, these data contributed to a better understanding of how clouds and radiation interacted with atmospheric thermodynamics. There were currently five satellites carrying CERES instruments, and four satellites being employed in this study were sun-synchronous. The Terra satellite crosses the equator from south to north, and because it does so, at about 10:30 a.m., it is also known as the "Morning Satellite." It has two CERES instruments, Flight Model 1 (FM1) and Flight Model 2 (FM2), as well as a Moderate Resolution Imaging Spectroradiometer (MODIS). A MODIS has 36 bands with a wavelength range of 0.412–14.45 µm and a spatial resolution of 250–1,000 m, allowing it to cover the entire globe in 2 days (Barnes et al., 2003). The Aqua satellite crosses the equator from north to south at about 1:30 p.m., and so it is known as the "Afternoon Satellite." It has two CERES instruments, FM3 and FM4, and a MODIS. The "Afternoon Satellite" Suomi NPP is also equipped with the CERES instrument FM5 and the Visible Infrared Imaging Radiometer Suite (VIIRS). The VIIRS contains 22 imaging and radiation bands with a wavelength range from 0.41 to 12.5 µm and a spatial resolution of 370–750 m (Cao et al., 2014). NOAA-20, the successor of the Suomi NPP, which is also an "Afternoon Satellite," is equipped with the FM6 CERES instrument and VIIRS (Cao et al., 2018). The four satellites mentioned previously were equipped with advanced spectral imagers so as to provide 24-h day-time and night-time IWP monthly average data CERES_SSF_1deg-Month L3 data, with a spatial resolution of 1°×1°. These products had the advantages of long time series, wide application range, and high space coverage. We chose 24-h day-time and night-time IWP data because it better represented the whole IWP in the research area even though the retrieval algorithms used during the day-time and night-time were different. Meanwhile, because the time series of the Suomi NPP and NOAA-20 satellite products were short, the payloads carried by them were the same, and their orbits were similar, so they were merged into one new product with the time series from 2013 to 2020.

2.1.4 Reanalysis data

The reanalysis data used here were ERA5, which was the fifth-generation reanalysis data product made by the European Centre for Medium-Range Weather Forecasts (ECMWF). A new data assimilation system, known as the ECMWF Integrated Forecasting System "Cy47r3" 4D-var, was applied for ERA5 by ECMWF. It was based on numerical calculation of the model and assimilation of a large amount of observation data. Due to these advantages, ERA5 contain detailed records of the global atmosphere, surface, and ocean waves since 1950. It had a significant improvement in the spatial resolution and numerical accuracy of variables when compared to the previous reanalysis data product ERA-Interim (Hersbach et al., 2020). We selected the monthly averaged ERA5 on single levels from 1979 to the present as the research data and employed the combination of two variables, total column cloud ice water and total column snow water, as the IWP to characterize the total ice content.

2.2 Methodology

IWP (g/m^2) is a primary indicator for calculating the atmospheric ice concentration. It was defined as the vertical integral of the ice water content (IWC) (g/m^3) in the atmospheric column (Holl et al., 2014).

The CERES_SSF_1deg-Month L3 data assumed that the atmosphere was plane parallel, and the whole cloud column was composed entirely of ice. Hence, the IWP value was the product of the effective size and optical thickness of ice crystals. The specific algorithm was as follows:

$$\boldsymbol{IWP = 2\rho R_e \tau / 3Q}, \tag{1}$$

where ρ is the density of ice (~0.9 g cm^{-3}), R$_e$ is the effective radius, τ is the optical depth, and Q is the extinction efficiency, which depends on R$_e$ and ranges from 2.01 to 2.11 (Tian et al., 2018).

3 Results

3.1 Total mass

The three satellite retrieval products (Aqua, Terra, and the Suomi NPP-NOAA-20) during 2013 and 2020 were used to estimate the total mass of atmospheric ice over the TP by considering the area weight because the Suomi NPP and

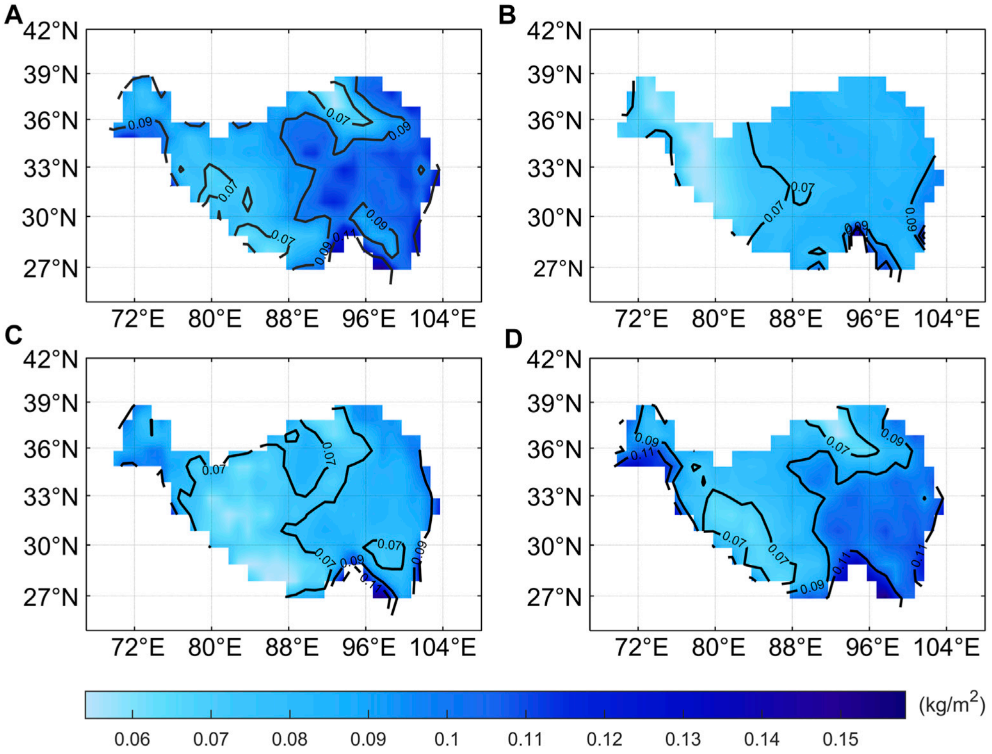

FIGURE 1
Spatial distributions of atmospheric ice over the TP retrieved by **(A)** Aqua, **(B)** ERA5, **(C)** Terra and **(D)** Suomi NPP NOAA-20 from 2013 to 2020.

NOAA-20 products were only produced since 2013 (Table 2). The total mass of atmospheric ice calculated based on Aqua and Suomi NPP-NOAA-20 was very close (~0.28 Gt) during this period, which is larger than that from Terra (0.23 Gt). The reason for this condition might be the difference in their orbits. The Aqua and Suomi-NPP were both A-train satellites. Combined with the estimation results of all satellite datasets, we concluded that the multi-year average total mass of atmospheric ice was 0.26 ± 0.03 Gt (~2.6 $\times 10^8$ tons) over the TP, which accounted for approximately 5‰ of the global aerial cryosphere. The total mass of atmospheric ice had a significant seasonal variation, with a maximum of 0.32 ± 0.05 Gt in summer and a minimum of 0.22 ± 0.01 Gt in winter. In general, the result of ERA5 (total mass 0.24 Gt) was comparable with that of Terra and smaller than those of Aqua and Suomi NPP-NOAA-20. This is also applied on a global scale, and the mass of atmospheric ice given by the reanalysis data was also on the low side. The main reason was that the current atmospheric models did not perform well enough in describing the ice formation mechanism, ignoring the secondary ice formation mechanism and underestimating the number concentration of ice condensation nuclei (ECMWF, 2021).

3.2 Spatial distribution and seasonal variability

The ice concentration ranged from 0.05 to 0.15 kg/m^2 over the TP, with an average of 0.08 kg/m^2. As shown in Figure 1, the spatial variability of atmospheric ice over the TP was obvious. Three sets of satellite retrieval products consistently revealed the spatial pattern of high ice concentration in the eastern TP and low ice concentration in the western TP (Figures 1A,C,D). ERA5 generally underestimated the spatial heterogeneity of atmospheric ice content, and there are only a few high-value areas in the southeast edge of the TP (Figure 1B). All the four datasets observed the high-value center of the ice concentration around Linzhi City in southeast Tibet, where the value was up to 0.15 kg/m^2. Additionally, the IWP over the southern slope of the TP was relatively higher than those of other areas. Overall, the spatial distributions derived from various satellite datasets were consistent, particularly between Aqua (Figure 1A) and Suomi NPP-NOAA-20 (Figure 1D).

In order to clarify the reasons for the spatial difference of atmospheric ice over the TP, the vertical profile of wind field, relative humidity at 95°E, 30°N, and the IWP of corresponding grids were analyzed from 2003 to 2020 combined with the topography (Figure 2). A large amount of water vapor was

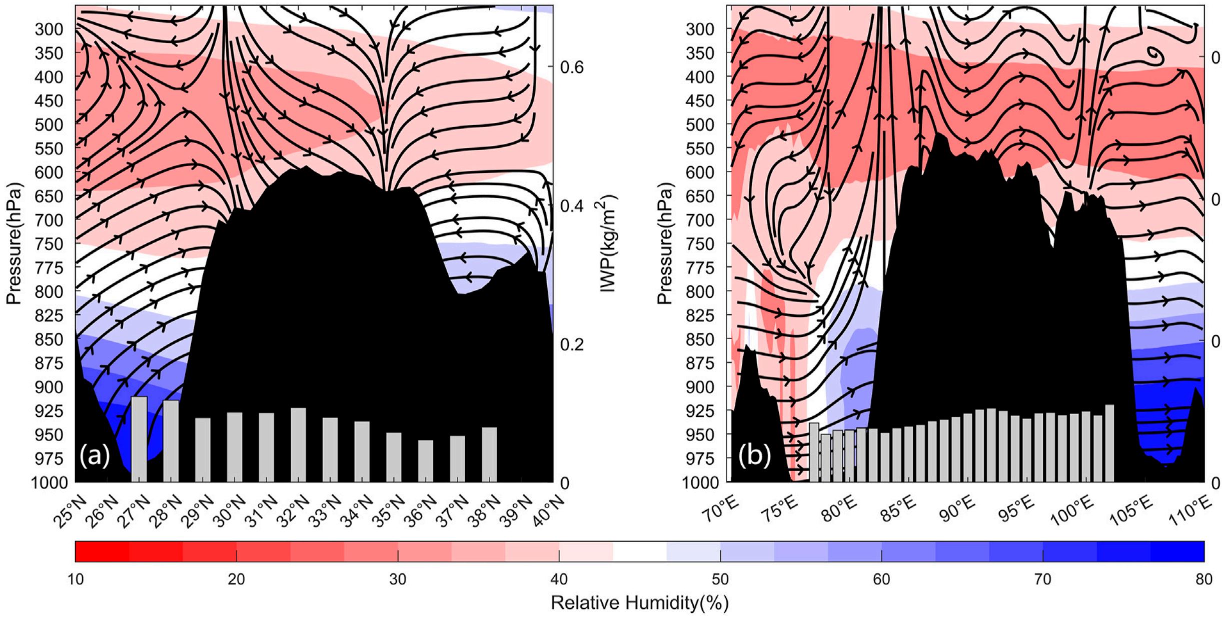

FIGURE 2
Vertical profile of wind field (stream lines), relative humidity (shaded areas), and topography (black waves) at the domain of 25°N–40°N and 70°E–110°E from 2003 to 2020. **(A)** Cross section of 95°E; **(B)** cross section of 30°N. The vertical velocity *w* was enlarged by 100 times because it is 2–3 orders of magnitude smaller than the horizontal velocity. The gray bars denote the IWP values at different latitudes and longitudes.

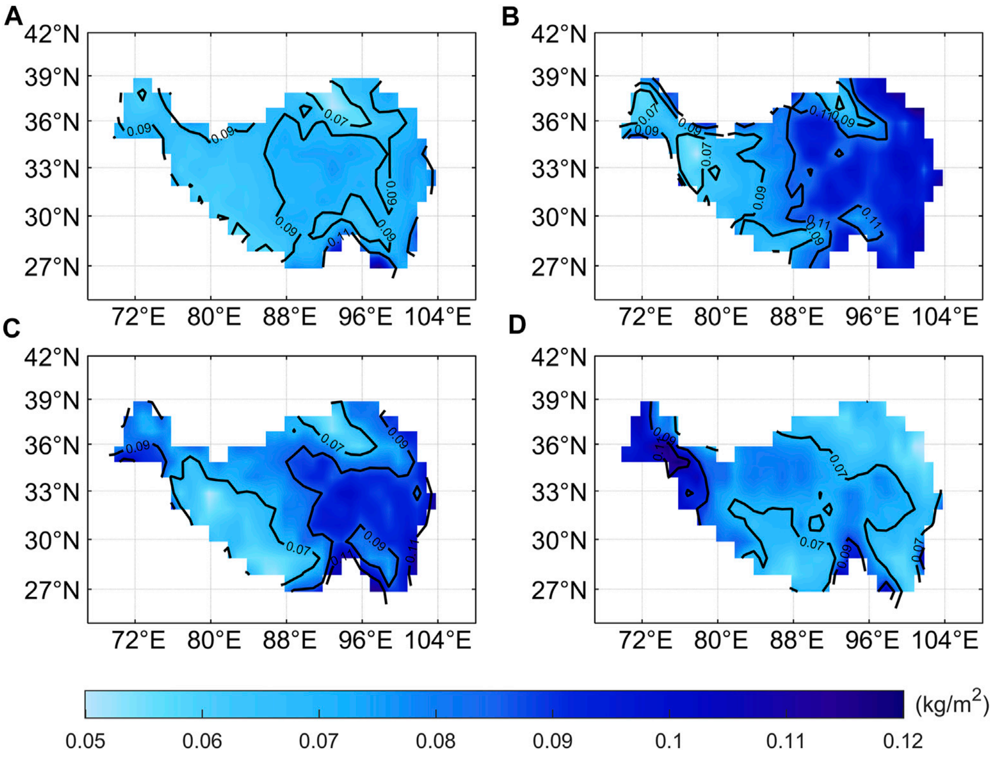

FIGURE 3
Spatial distributions of atmospheric ice over the TP in different seasons retrieved by the Aqua satellite from 2003 to 2020. **(A)** Spring (MAM), **(B)** summer (JJA), **(C)** autumn (SON), and **(D)** winter (DJF).

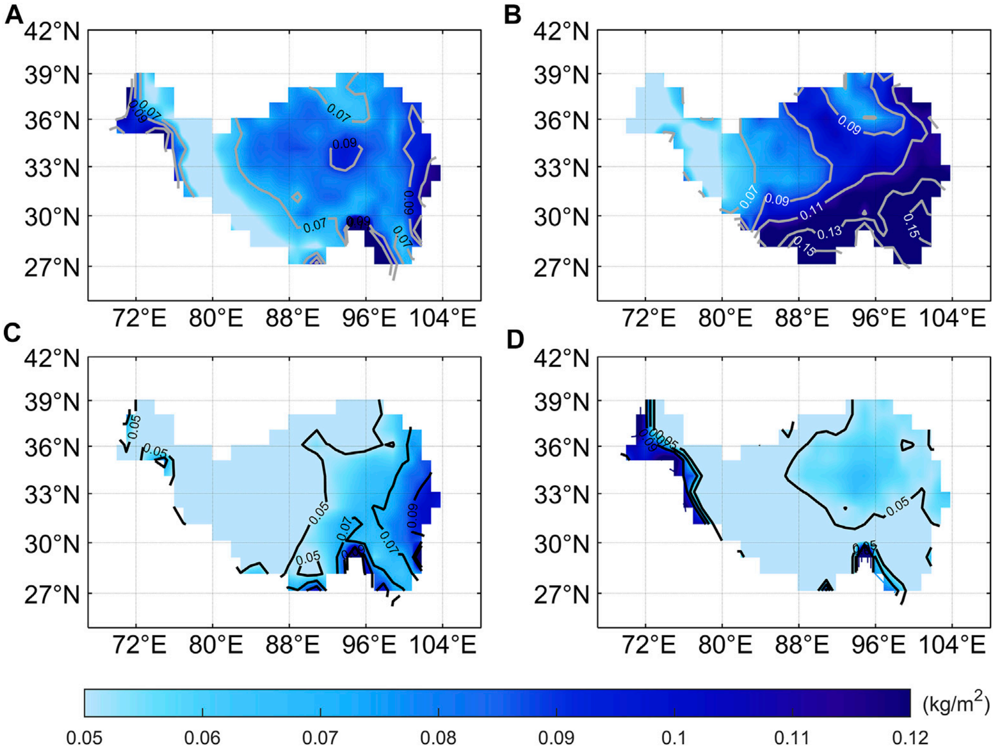

FIGURE 4
Spatial distributions of atmospheric ice over the TP in the different seasons given by ERA5 from 2003 to 2020. **(A)** Spring (MAM), **(B)** summer (JJA), **(C)** autumn (SON), and **(D)** winter (DJF).

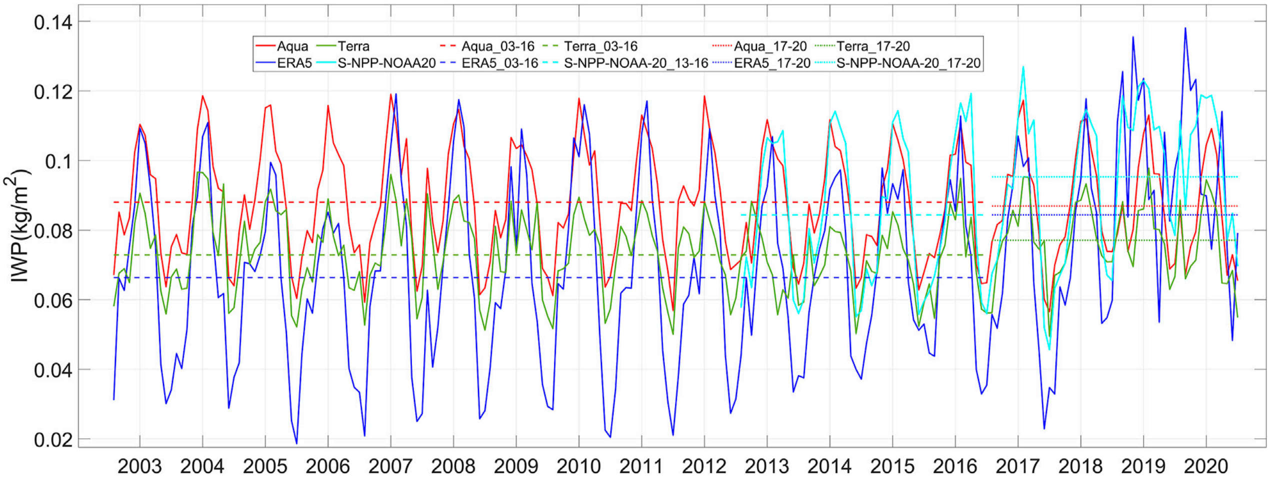

FIGURE 5
Time series of the atmospheric ice mass over the TP from 2003 to 2020. (dash line is the average value line).

transported to the southeast of the TP (around 27°N) through the Bay of Bengal channel, with the relative humidity exceeding to 65% at 850 hPa in this area, which provided a sufficient water vapor condition for the formation of atmospheric ice. In addition, strong updraft carried abundant water vapor to high altitudes, producing lots of atmospheric ice through condensing. The previous two

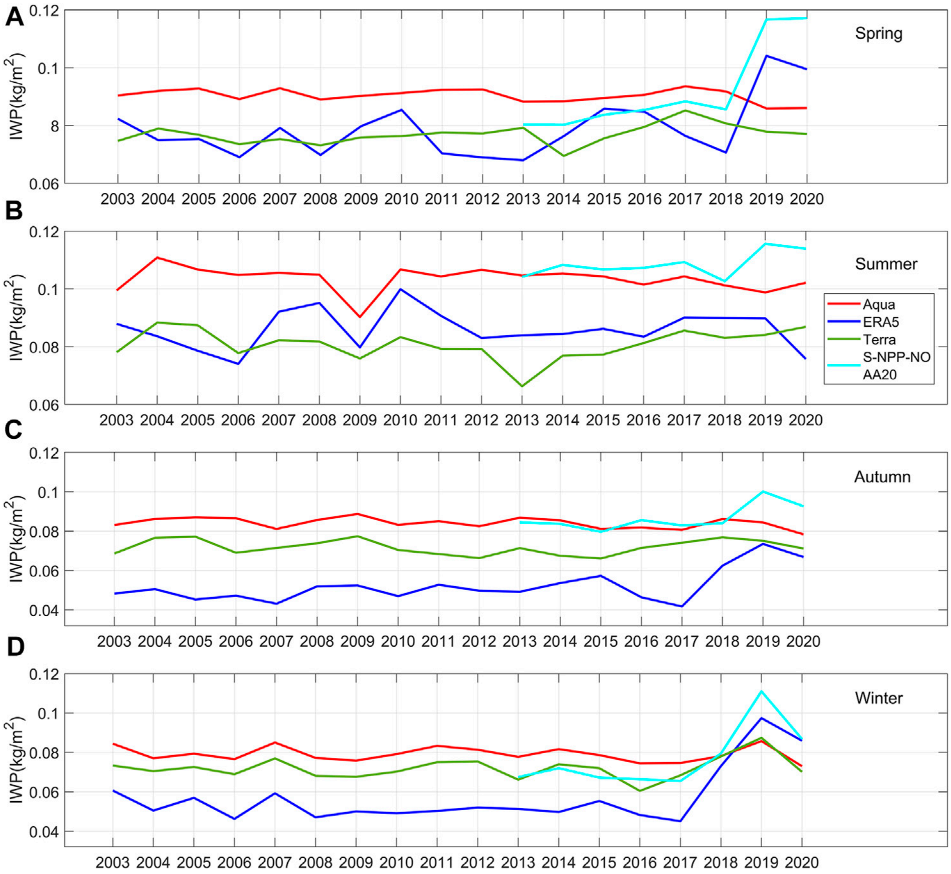

FIGURE 6
Interannual variations of the seasonal variations over the TP from 2003 to 2020. **(A)** Spring (MAM), **(B)** summer (JJA), **(C)** autumn (SON), and **(D)** winter (DJF).

factors are the main reasons for the high-value center of atmospheric ice in southeast Tibet. The terrain blocking prevented water vapor from northward penetration, resulting in the low ice concentration in northern TP.

Affected by southwest monsoon, the content of atmospheric ice in summer and autumn was generally higher than that in the other two seasons, especially for the eastern TP (Figure 3). This led to higher annual mean ice concentrations in the eastern TP. The seasonal distributions of the ice content derived from various satellite retrieval products were also consistent, only with slight differences in the central and western TP inland areas (Figure 3, Supplementary Figure S1, S2). For example, the IWP of the Aqua satellite in winter was slightly higher than those of Terra and Suomi NPP-NOAA-20 in this region during the same period (Figure 3D; Supplementary Figures S1D, S2D).

ERA5 reanalysis could basically capture the seasonal variations of the atmospheric ice content derived from satellite retrieval products, although there were still some discrepancies in the amount of ice. In summer, the ice content tended to decrease from the east to west but that from the ERA5 reanalysis tended to decrease from southeast to northwest, and the IWP was overestimated by −0.02 kg/m2 in the southeast Tibet (Figure 2B, Figure 3B, Supplementary Figures S1B, S2B). However, in winter, ERA5 underestimated the IWP value in most areas of the TP, except for the northwest TP (Figure 2D, Figure 3D, Supplementary Figures S1D, S2D).

3.3 Annual variability and long-term trend

As shown in Figure 5, the variability of the atmospheric ice content over the TP within a year presented a distinct single peak structure, with an upward tendency in the first half of the year, peaked in summer, and then began to decline. Among them, the growth of atmospheric ice was more "twists and turns" than its reduction process (a tiny maximum would arise around March–May), and this pattern was noticeable across all satellite products. For the annual maximum value of the ice content, Aqua was close to Suomi

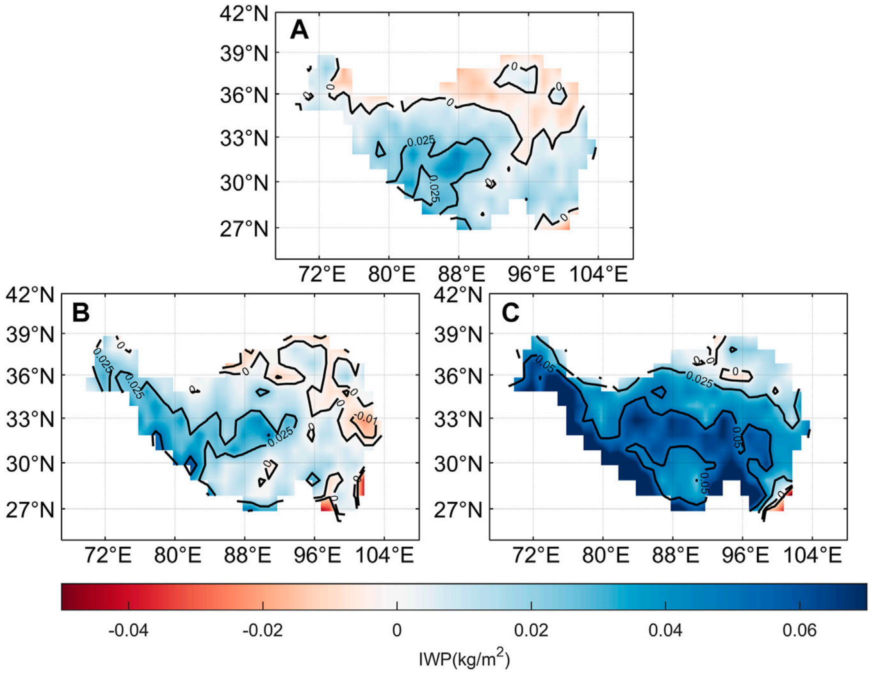

FIGURE 7
Spatial difference of atmospheric ice in winter between 2017 and 2019 retrieved by the three products. **(A)** Aqua, **(B)** Terra, and **(C)** Suomi NPP-NOAA-20.

NPP-NOAA-20 and ERA5, and higher than Terra. As for the minimum value, the three sets of satellite data were relatively close and significantly higher than ERA5 (Figure 5), indicating that the underestimation of the atmospheric ice content over the TP by ERA5 was mainly caused by the simulation deviation of ice growth in winter due to the underestimation of water vapor over the TP during this season.

The atmospheric ice content showed no obvious trend over the TP before 2017 whether for satellite products or reanalysis data, while the annual minimum ice content has increased in recent years (Figure 5). Similarly, the annual average ice content also increased from 2017, except for the result of Aqua (Figure 5). Dou et al. (2020)pointed out that the total mass of the global atmospheric ice showed an increasing trend with climate warming in the past decades. However, this study indicated that the mass of atmospheric ice in the TP had not completely followed this law but showed certain regional characteristics, although it seemed to have increased over the last few years.

From the time series of the atmospheric ice content in different seasons, there were great differences between various datasets, which were not only reflected in the IWP value but were also reflected in the change trend. In general, Aqua was close to Suomi NPP-NOAA-20 and higher than the other two datasets. Terra was close to ERA5 in spring and summer, while it is significantly higher than ERA5 in autumn and winter (Figure 6). The interannual variability of various datasets was relatively consistent in autumn and winter, but there were obvious discrepancies in the other seasons. Additionally, all sets of data showed a consistent increasing trend in winter in recent years, although there were some differences in the ice mass. In spring and autumn, Suomi NPP-NOAA-20 and ERA5 showed a consistent increasing trend, while the other two datasets showed a weak decreasing trend (Figure 6).

In view of the increasing trend of the atmospheric ice content in winter in the past few years, we further analyzed the spatial manifestation and the possible causes of this trend. By comparing the spatial distribution of the atmospheric ice content in 2017 (low-value year) and 2019 (high-value year), it can be seen that the increase of atmospheric ice was reflected in most areas except the northeast TP (Figure 7). Specifically, the increase in the ice content based on Suomi NPP-NOAA-20 is the most significant, with an increase of 0.08 kg/m^2 in the central and southwest regions of the TP. It can be seen from the moisture flux in winter that the water vapor convergence was clearly intensified over the TP since 2017 (Supplementary Figure. S3), which provided sufficient water vapor for the growth of ice crystals, resulting in the overall increase of the atmospheric ice content in winter during recent years.

4 Discussion and conclusion

This study applied four sets (Suomi NPP was merged with NOAA-20, and there are actually three datasets) of satellite retrieval products and ERA5 reanalysis to estimate the total mass, spatial-temporal distribution, and long-term trend of atmospheric ice over the TP, analyzed the causes of spatial differences, and discussed the uncertainties of the results. This study indicates for the first time that the total mass of atmospheric ice over the TP was to be 0.26 ± 0.03 Gt, with the maximum in summer (0.32 ± 0.05 Gt) and the lowest in winter (0.22 ± 0.01 Gt). This result was obtained from three sets of satellite data, and there were some differences among them. For two datasets using the MODIS instruments, according to the quality summary, the Aqua satellite did not have calibration anomalies, but Terra's band 1 (central wavelength of 0.65 μm) had two calibration anomalies in 2003 and 2009 and one in band 5 (central wavelength of 1.2 μm) in 2002 (CERES, 2021). Coupled with the difference of their orbits, these factors will result in the difference of retrieval values of the IWP. In comparison with ground-based, ship-based, and airborne observations and other high-quality satellite data (e.g., CALIPSO data), Aqua-MODIS satellite data showed the highest performance, and Suomi NPP-VIIRS data were overall comparable to Aqua-MODIS and would gradually replace Aqua and Terra MODIS retrieval data completely in the future (Minnis et al., 2016; CERES, 2021). In conclusion, although there are some differences among various datasets, the total mass of atmospheric ice over the TP estimated based on them is close and thus, has high reliability.

Under the influence of monsoon, the water vapor on the TP is more abundant in summer and autumn, especially in southeast Tibet, resulting in a higher atmospheric ice content in these two seasons and a spatial pattern of low concentration in the west and high concentration in the east. The high-value center (0.15 ± 0.035 kg/m^2) was located in Linzhi City and its surrounding area, which could be well captured by ERA5 reanalysis. In terms of spatial distribution, the results of different satellite data and ERA5 reanalysis are consistent, although the latter slightly underestimates the spatial heterogeneity. For the ice content, the value given by Aqua is comparable with that of Suomi NPP-NOAA-20 and is larger than those of the other two datasets in the eastern TP. ERA5 is close to Terra in the description of the atmospheric ice content.

From the time series of atmospheric ice over the TP, it can be seen that the annual variation is unimodal. Since 2017, the annual minimum increased, and the annual amplitude declined. This might affect the frequency and distribution of ice clouds over the TP, which needed further study. There was no evident long-term trend before 2017, while after that, apart from Aqua, the other datasets showed that the mass of atmospheric ice has increased over the TP in recent years. It is to be noted that, in winter, all four datasets show a consistent increasing trend since 2017, and this trend is reflected in most areas except the small area of the northeast TP. Since 2017, there is a significant increase in the moisture convergence over the TP, which promotes the growth of atmospheric ice, leading to an increasing trend of the ice content during this period. The largest uncertainty of this study comes from the discrepancies among different satellite products. Next, it is necessary to verify the reliability of the present satellite products by using the *in situ* measurement, ground radar observations, or other high-quality satellite data. It is also necessary to use the new generation of weather radar, terahertz sensors, and lidar to retrieve more advanced atmospheric ice products.

Data availability statement

The original contributions presented in the study are included in the article/Supplementary Material. Further inquiries can be directed to the corresponding author. The boundary data of the TP was downloaded from the National Tibetan Plateau Scientific Data Center (TPDC) (http://data.tpdc.ac.cn/zh-hans/), and the topographic data was downloaded from the website of GEBCO Project (https://download.gebco.net/). Remote sensing data was downloaded from the NASA Langley Research Center CERES ordering tool at (https://ceres.larc.nasa.gov/data/). ERA5 reanalysis data was downloaded from Copernicus Climate Change Service (C3S) Climate Date Store (https://cds.climate.copernicus.eu/cdsapp#!/search).

Author contributions

TD and CX jointly conceived the study; YY, GX, and TD performed the analyses; all of the authors discussed the results, contributed to interpretations, and wrote the manuscript.

Funding

This study was funded by the National Key Research and Development Program of China (2018YFC1406104) and the National Nature Science Foundation of China (NSFC 41401079).

Acknowledgments

The authors thank the National Tibetan Plateau Scientific Data Center, GEBCO Project, NASA CERES project, and European Centre for Medium-Range Weather Forecasts for providing access to the boundary and topography data on the TP, CERES_SSF_1deg-Month L3 data and ERA5 reanalysis used in this study. The authors also thank the reviewers for valuable comments that led to improvements in the analysis and clarifications in the text.

Conflict of interest

The authors declare that the research was conducted in the absence of any commercial or financial relationships that could be construed as a potential conflict of interest.

Publisher's note

Supplementary material

The Supplementary Material for this article can be found online at: https://www.frontiersin.org/articles/10.3389/feart.2022.998603/full#supplementary-material

References

Barnes, W. L., Xiong, X., and Salomonson, V. V. (2003). Status of terra MODIS and aqua MODIS. *Adv. Space Res.* 32, 2099–2106. doi:10.1016/s0273-1177(03)90529-1

Cao, C., Blonski, S., Wang, W., Uprety, S., Shao, X., Choi, J., et al. (2018). "NOAA-20 VIIRS on-orbit performance, data quality, and operational Cal/Val support," in *Earth observing missions and sensors: Development, implementation, and characterization V* (Honolulu, Hawaii, United States: International Society for Optics and Photonics). doi:10.1117/12.2324329

Cao, C., De Luccia, F. J., Xiong, X., Wolfe, R., and Weng, F. (2014). Early on-orbit performance of the visible infrared imaging radiometer suite onboard the Suomi national polar-orbiting partnership (S-NPP) satellite. *IEEE Trans. Geosci. Remote Sens.* 52, 1142–1156. doi:10.1109/tgrs.2013.2247768

CERES (2021). CERES_SSF1deg-Hour/Day/Month_Ed4A data quality summary. Available at: https://ceres.larc.nasa.gov/documents/DQ_summaries/CERES_SSF1deg_Ed4A_DQS.pdf.

Dou, T., Xiao, C., Huang, Y., Yue, H., and Han, W. (2020). Estimation of the atmospheric ice content mass, spatial distribution, and long-term changes based on the ERA5 reanalysis. *Geophys. Res. Lett.* 47. doi:10.1029/2020gl088186

Duncan, D. I., and Eriksson, P. (2018). An update on global atmospheric ice estimates from satellite observations and reanalyses. *Atmos. Chem. Phys.* 18, 11205–11219. doi:10.5194/acp-18-11205-2018

ECMWF (2021). "IFS documentation CY47R3 - Part IV physical processes," in *IFS documentation CY47R3* (Reading: ECMWF). doi:10.21957/cpmkqvhja

Group, G. C. (2019). *The GEBCO_2019 grid: A continuous terrain model of the global oceans and land.* NERC Liverpool: British Oceanographic Data Centre, National Oceanography Centre.

Hersbach, H., Bell, B., Berrisford, P., Hirahara, S., HORáNYI, A., MUñOZ-Sabater, J., et al. (2020). The ERA5 global reanalysis. *Q. J. R. Meteorol. Soc.* 146, 1999–2049. doi:10.1002/qj.3803

Holl, G., Eliasson, S., Mendrok, J., and Buehler, S. (2014). SPARE-ICE: Synergistic ice water path from passive operational sensors. *J. Geophys. Res. Atmos.* 119, 1504–1523. doi:10.1002/2013jd020759

Horváth, Á., and Davies, R. (2007). Comparison of microwave and optical cloud water path estimates from TMI, MODIS, and MISR. *J. Geophys. Res.* 112, D01202. doi:10.1029/2006jd007101

Khanal, S., Wang, Z., and French, J. R. (2020). Improving middle and high latitude cloud liquid water path measurements from MODIS. *Atmos. Res.* 243, 105033. doi:10.1016/j.atmosres.2020.105033

Lebsock, M., and Su, H. (2014). Application of active spaceborne remote sensing for understanding biases between passive cloud water path retrievals. *J. Geophys. Res. Atmos.* 119, 8962–8979. doi:10.1002/2014jd021568

Li, W., Li, X., Zhang, L., and Cheng, D. (2018). Climatic characteristic analysis of cloud water over the Tibetan Plateau. *Clim. Environ. Res.* 23, 574–586.

Li, X., Guo, X., and Zhu, J. (2008). Climatic distribution features and trends of cloud water resources over China. *Chin. J. Atmos. Sci.* 32, 1.

Liljegren, J. C., Clothiaux, E. E., Mace, G. G., Kato, S., and Dong, X. (2001). A new retrieval for cloud liquid water path using a ground-based microwave radiometer and measurements of cloud temperature. *J. Geophys. Res.* 106, 14485–14500. doi:10.1029/2000jd900817

Liu, X., and Chen, B. (2000). Climatic warming in the Tibetan Plateau during recent decades. *Int. J. Climatol.* 20, 1729–1742. doi:10.1002/1097-0088(20001130)20:14<1729::aid-joc556>3.0.co;2-y

Long, L. (2016). *Analysis of variation characteristics of cloud and influence factors over the Tibetan plateau from 2007 to 2014.* Yunnan: Yunnan University.

Minnis, P., Sun-Mack, S., Bedka, K., Yost, C., Trepte, Q., Smith, W., et al. (2016). *Validation of Cloud Parameters Derived from Geostationary Satellites, AVHRR, MODIS, and VIIRS Using SatCORPS Algorithms.* Lille: Workshop of the International Cloud Working Group (ICWG) 2016.

O'Dell, C. W., Wentz, F. J., and Bennartz, R. (2008). Cloud liquid water path from satellite-based passive microwave observations: A new climatology over the global oceans. *J. Clim.* 21, 1721–1739. doi:10.1175/2007jcli1958.1

Qi, P., Guo, X., Chang, Y., Tang, J., and Li, S. (2022). Cloud water path, precipitation amount, and precipitation efficiency derived from multiple datasets on the Qilian Mountains, Northeastern Tibetan Plateau. *Atmos. Res.* 274, 106204. doi:10.1016/j.atmosres.2022.106204

Qin, D., Ding, Y., Xiao, C., Kang, S., Ren, J., Yang, J., et al. (2018). Cryospheric science: Research framework and disciplinary system. *Natl. Sci. Rev.* 5, 255–268. doi:10.1093/nsr/nwx108

Tian, J., Dong, X., XI, B., Minnis, P., Smith, W. L., Sun-Mack, S., et al. (2018). Comparisons of ice water path in deep convective systems among ground-based, GOES, and CERES-MODIS retrievals. *JGR. Atmos.* 123, 1708–1723. doi:10.1002/2017jd027498

Wielicki, B. A., Barkstrom, B. R. H., Edwin, F., Lee, R. B., Louis, G. S., and Cooper, J. E. (1996). Clouds and the Earth's radiant energy system (CERES): An Earth observing system experiment. *Bull. Am. Meteorol. Soc.* 77, 853–868. doi:10.1175/1520-0477(1996)077<0853:catere>2.0.co;2

Xu, G., Dou, T., Yang, Y., Yue, H., Husi, L., Ma, L., et al. (2022). The total mass and spatio-temporal structure of the aerial cryosphere. *Chin. Sci. Bull.* 47, e2020GL088186. doi:10.1029/2020GL088186

Yue, B., Yi, W., Jiamin, L., and Chenghai, W. (2016). Temporal and spatial variation features of cloud water and its relation to precipitation over the Tibetan Plateau. *J. Glaciol. Geocryol.* 38, 1.

Zhang, Y., Li, B., Liu, L., and Zheng, D. (2021a). Redetermine the region and boundaries of Tibetan Plateau. *Geogr. Res.* 40, 1.

Zhang, Y., Li, B., and Zheng, D. (2002). A discussion on the boundary and area of the Tibetan Plateau in China. *Geogr. Res.* 21, 1.

Zhang, Y., Liu, L., Li, B., and Zheng, D. (2021b). Comparison of boundary datasets covering Tibetan plateau between 2021 and 2014 versions. *J. Glob. Change Data Discov.* 5, 1.

Zhao, P., Xiao, H., Liu, J., and Zhou, Y. (2021). Precipitation efficiency of cloud and its influencing factors over the Tibetan plateau. *Int. J. Climatol.* 42, 416–434. doi:10.1002/joc.7251

frontiers | Frontiers in Earth Science

TYPE Original Research
PUBLISHED 09 January 2023
DOI 10.3389/feart.2022.1007384

Extensive responses of lake dynamics to climate change on northeastern Tibetan Plateau

Wenhui Liu[1,2], Hairui Liu[3]*, Qingpeng Li[1], Changwei Xie[4], Zhijun Zhang[5], Guanghao Zhou[1], Qi Zhang[1] and Qinhao Zhao[1]

[1]Department of Geological Engineering, Qinghai University, Xining, China, [2]Key Lab of Cenozoic Resource and Environment in North Margin of the Tibetan Plateau, Qinghai University, Xining, China, [3]College of Eco-Environmental Engineering, Qinghai University, Xining, China, [4]Cryosphere Research Station on the Qinghai-Tibet Plateau, State Key Laboratory of Cryosphere Sciences, Northwest Institute of Eco-Environment and Resources, Chinese Academy of Sciences, Lanzhou, China, [5]Qinghai Eco-Environmental Monitoring Center, State Environmental Protection Key Laboratory of Tibetan Plateau Eco-Environmental Monitoring and Assessment, Xining, China

OPEN ACCESS

EDITED BY
Chunqiao Song,
Nanjing Institute of Geography and Limnology (CAS), China

REVIEWED BY
Haijun Deng,
Fujian Normal University, China
Jing Zhou,
Institute of Tibetan Plateau Research (CAS), China

*CORRESPONDENCE
Hairui Liu,
lhrbotany@163.com

SPECIALTY SECTION
This article was submitted to Cryospheric Sciences, a section of the journal Frontiers in Earth Science

RECEIVED 30 July 2022
ACCEPTED 27 September 2022
PUBLISHED 09 January 2023

CITATION
Liu W, Liu H, Li Q, Xie C, Zhang Z, Zhou G, Zhang Q and Zhao Q (2023), Extensive responses of lake dynamics to climate change on northeastern Tibetan Plateau.
Front. Earth Sci. 10:1007384.
doi: 10.3389/feart.2022.1007384

The lakes on the Qinghai–Tibetan Plateau have undergone substantial changes. As intensive cryospheric components change, the response of the lake dynamics to climatic factors, glacier-snow melting, and permafrost thawing has been complex. Based on Landsat images, meteorological data, and glacier and permafrost data, the spatial-temporal changes in the lake area on the northeastern Tibetan Plateau between 1988 and 2019 were analyzed and the driving factors behind the lake changes were further explored. The results suggest that the regional lake area increased from 1988 to 2019 at rates of 0.01–16.03 km^2/yr. It decreased during 1988–2000, quickly increased during 2000–2012, and rapidly increased during 2012–2019. The most significant lake expansion occurred in sub-region I, which is the source region of the Yangtze River Basin. There was a sharper increase during 2012–2019 than during 2000–2012 in sub-region II (the source region of the Yellow River Basin and the Qinghai Lake Basin) and sub-region III (the Qaidam Basin). The significant lake expansion occurred about 12 years earlier in sub-region I than in sub-regions II and III. This dramatic change in the lake area was closely associated with the annual precipitation, and precipitation was the primary driving factor. Although serious glacier retreat occurred, most of the lakes in the sub-regions were non-glacier-fed lakes. The correlation between glacier ablation and the change in the lake area was poor, which suggests that glacial meltwater was not the replenishment source of most of the lakes in this region. A more accelerated increase in the active layer thickness occurred (1.90 cm/yr), which was consistent with the more rapid lake expansion, and the permafrost degradation further intensified the lake expansion.

KEYWORDS

lake area, spatial-temporal changes, influencing factors, northeastern Tibetan Plateau, permafrost impact

1 Introduction

The Qinghai–Tibetan Plateau (QTP) is the source of several large rivers in China and east Asia, and therefore, it is known as the Asian water tower (Zhang et al., 2019; Wang et al., 2021). It contains more than 1,000 lakes (areas of >1 km^2), with a total lake area of about 41,800 km^2. These lakes account for 39.2% and 51.4% of the total number of lakes and lake area in China, respectively (Zhang et al., 2014). They play a crucial role in regulating the balance between the regional surface water and groundwater. In recent decades, the QTP has experienced significant changes, which were mainly characterized by climate warming-wetting (Yang et al., 2011; Duan et al., 2015), glacier melting (Bolch et al., 2010; Yao et al., 2012), and permafrost thawing (Wu et al., 2010; Cheng et al., 2019; Zhao et al., 2020). Due to cloud-radiation feedback, an accelerated warming trend occurred on the Tibetan Plateau during 1998–2013 (0.25°C decade^{-1}), compared with that during 1980–1997 (0.21°C decade^{-1}) (Duan and Xiao, 2015). The annual retreat rate of the Basu Glacier in the Karakorum Mountains is nearly 50 m/yr and that of the Large Dongkemadi Glacier in the Tanggula Mountains is 4.6 m/yr (Yao et al., 2012). With continued climate warming, as well as accelerated glacier ablation and permafrost degradation, a succession of hydrological changes is anticipated to occur, which will have intensive impacts on the hydrological processes (Cheng et al., 2021; Ding et al., 2021; Gao et al., 2021). In particular, the lakes on the QTP have undergone substantial changes, including significant lake expansion, since 2000 (Lei et al., 2013; Li et al., 2014; Song et al., 2014; Yang et al., 2017; Zhang et al., 2019, 2021; Liu et al., 2021). The relationship between the lake dynamics and climate mechanism has been explored in many studies, but the dominant driver behind these lake changes is still under debate (Phan et al., 2013; Song and Sheng, 2016; Yao et al., 2018). Furthermore, the permafrost was not taken into consideration in these studies.

Permafrost is widely distributed on the QTP, with a total area of 1.06 × 10^6 km^2 (Zou et al., 2017), and the total volume of the ground ice in the permafrost regions is 9,528 km^3 (Zhao et al., 2010). Permafrost degradation has accelerated due to the rising air temperature, resulting in reduced permafrost coverage (Zou et al., 2017), increased permafrost ground temperature (Wu et al., 2010), thickening of the active layer (Li et al., 2012), a decrease in the depth of the zero annual amplitude of the ground temperature of the permafrost (Xie et al., 2015; Liu et al., 2016), intensified thawing-freezing processes in the active layer (Zhu et al., 2022), and even a decrease in the ground ice content (Zhao et al., 2010). Long-term monitoring data have revealed that the Active Layer Thickness (ALT) along the Qinghai–Tibet Highway has increased at a rate of 1.33–1.90 cm/yr (Li et al., 2012). Permafrost temperatures at a depth of 15 m have decreased at a rate of 0.57°C per 100 m of altitude increase and 0.79°C per degree latitude northward (Wu et al., 2010). The effect of the presence of ice-rich permafrost and its thawing on the hydrological regimes of catchments has been commonly detected in the sub-basins in the QTP (Song et al., 2020) and typical basins in northwestern China (Niu et al., 2011; Li et al., 2016; Wang et al., 2018). Permafrost degradation has caused increases in the amount of ground ice meltwater, aquifer thicknesses, and the amount of surface water infiltration, which has impacted the movement patterns of the surface water and groundwater and enhanced the hydraulic exchange between the surface water and groundwater, further resulting in an important contribution to rive runoff (Kurylyk et al., 2014; Walvoord and Kurylyk, 2016). An increasing number of studies have suggested that the spatial trend in the lake changes in recent years has been closely related to the existence of permafrost and its accelerated degradation, which have contributed to the increase in lake volume in permafrost catchments (Zhang et al., 2017a; Liu et al., 2020).

In addition, intensive changes in cryospheric components and increases in climate extremes, especially accelerated glacier ablation and permafrost degradation, are playing increasingly significant roles in influencing the hydrological regimes and water resources in cold regions. Lake changes are one consequence of these influencing factors; and they may be related to the permafrost and glacier melting distribution rather than to a direct climatic mechanism such as increased precipitation. Many previous studies have extensively explored the lake variation across the endorheic basin on the QTP (Song et al., 2014; Yang et al., 2017; Yao et al., 2018; Liu et al., 2021) or focused on single large lakes (Qinghai Lake, Selin Co, Num Co) (Lei et al., 2013; Tang et al., 2018; Liu et al., 2022), but less research focuses on that on the northeast QTP. In fact, the northeastern QTP contains many lakes, and most of these lakes are distributed in the Yangtze River Basin (489 lakes, 38.29%), the Yellow River Basin (265 lakes, 20.75%), and the Qaidam Basin (164 lakes, 12.8%). Due to the large differences in the landforms, climate, hydrological conditions, and topography at the basin scale, as well as significant human interventions on lakes, especially lakes in the Qaidam Basin, the responses of the lake dynamics to climatic factors, glacier-snow melting, permafrost thawing, and water input from other lakes have been more complex. Therefore, a comprehensive analysis of many factors behind lake change for different geomorphologic units is necessary and of importance. In this study, the spatial-temporal trend of the lake area across the northeastern QTP between 1988 and 2019 was analyzed, and the potential driving factors were further explored. The results of this study provide a comprehensive understanding of the major mechanism controlling the lake dynamics.

2 Data and methods

2.1 Study area

The northeastern QTP (89°35′–103°04′N, 31°39′–39°19′E), the coverage of the whole Qinghai Province in this paper, has a total area of 72.23 × 10^4 km^2, a west-east length of 1,200 km, and

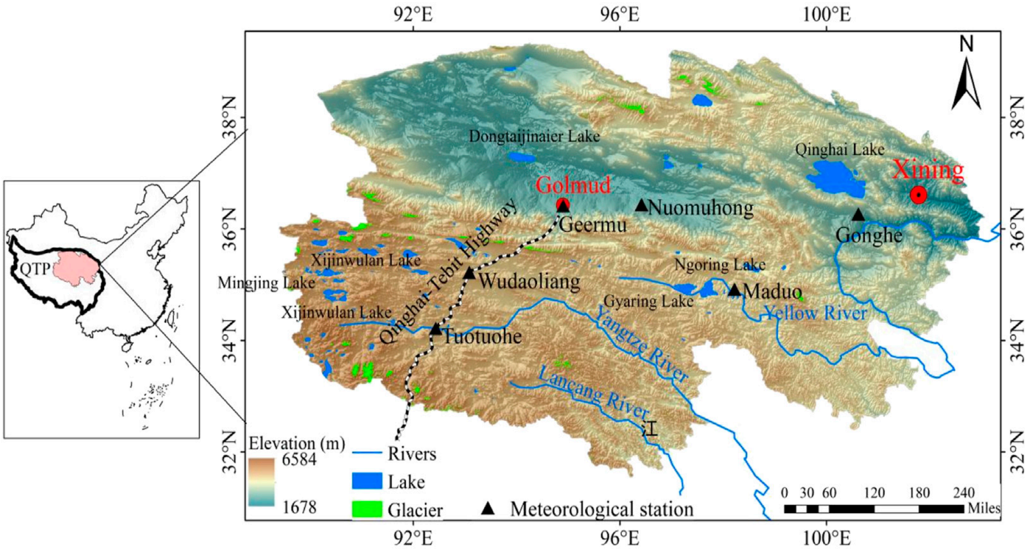

FIGURE 1
Schematic representation of the study area. The digital elevation model was obtained from the Advanced Spaceborne Thermal Emission and Reflection Radiometer (ASTER) Global Digital Elevation Model (GDEM) version 2.0, with a spatial resolution of 30 m; the glacier area shown is from the Second Glacier Inventory Dataset of China; the drainage networks and drainage basins were extracted from the HydroSHEDS dataset to calculate the glacier area in each basin; and the lake areas shown in 2019 are from this paper.

a north-south width of 800 km. It is characterized by an alpine continental climate with a Mean Annual Air Temperature (MAAT) of −5.6°C to 8.6°C and a mean Annual Precipitation (AP) of 15–750 mm. The precipitation mainly occurs from May to September. As shown in Figure 1, the average elevation is 3,000 m above sea level (a.s.l.). The areas with elevations of <3,000 m a.s.l., 3,000–5,000 m a.s.l., and >5,000 m a.s.l. account for 26.3%, 67%, and 5% of the total area, respectively. The terrain is high in the southwest and low in the east. It is the source region of the Yangtze River, Yellow River, and Lancang River; so, it is also known as the river source region. There are 1,277 lakes with areas greater than 0.01 km^2, with a total area of 14,370.2 km^2, accounting for 1.99% of the total area of Qinghai Province (Pi et al., 2018). Qinghai Lake (99°37′–100°44′N, 36°33′–37°14′E) is the largest inland salt lake on the QTP, with a lake area of 4,165 km^2, a surface elevation of 3,193 m, and a water volume of 71.6 km^3 (Tang et al., 2018). It has a maximum length of 101 km, a width of 76 km, and a depth of 25.5 m. The annual river runoff in the region is 63.34 km^3, accounting for 2.34% of the total annual river runoff in China. Modern glaciers have grown, covering an area of 5,225.38 km^2 and having a glacial storage of 3,705.92 km^3, accounting for 9.2% and 12.5% of the total glacier area and storage in China, respectively (Pi et al., 2018). Permafrost is widely distributed with coverage of 336,783 km^2, its area accounts for 46.6% of the entire study region and 31.7% of the total permafrost area on the QTP, respectively. The permafrost temperature is low, with a lowest value of −13.58°C; and the permafrost thickness is large, with a maximum value of 139 m in the Qilian Mountains, which may provide the occurrence conditions and resource background for the formation of a large amount of natural gas hydrates. The region studied is classified as alpine meadow, alpine steppe, and alpine desert.

2.2 Satellite images

Landsat data (http://glovis.usgs.gov) are widely used to delineate lakes. Landsat Thematic Mapper (TM), Enhanced Thematic Mapper Plus (ETM+), and Operational Land Imager (OLI) images with no or small fractions of cloud coverage (<10%) were selected to extract the lake surface areas to create a continuous time series of the area changes from 1998 to 2019. All of these images had a 30 m spatial resolution and were acquired each October because the lake areas were relatively stable in October. The data window was also extended to September and November if insufficient data were available for October (Zhang et al., 2017b). Manual visual interpretation was used to delineate the lakes. The false color compositions of the raw Landsat images for each lake using the ENVI 5.3 software were processed to identify lake boundary (bands 5, 4, and 3 as red, green, and blue, respectively, for Landsat TM/ETM+ and bands 7, 6, and 5 for Landsat OLI), which satisfactorily distinguished the water areas from the non-water areas. Then, visual examination and manual editing of the lake boundaries based on false color compositions images (also called lake digitization) were conducted to delineate the lakes and the calculated geometry of lake boundary shapes were subsequently carried out in ArcGIS 10.2 software. The accuracy of the manual digitization was controlled within one pixel. All image data were projected into the UTM coordinate system Zone 45 using the WGS-84 geodetic datum.

2.3 Climate data

The air temperature and precipitation recorded at the Wudaoliang (93.08°E, 35.21°N, 4,612 m a.s.l.), Tuotuohe (92.43°E, 34.21°N, 4,433 m a.s.l.), Maduo (98.21°E, 34.91°N, 4,272 m a.s.l.), Gonghe (100.61°E, 36.26°N, 2,835 m a.s.l.), Geermu (94.9°E, 36.41°N, 2,807 m a.s.l.), and Nuomuhong (96.41°E, 36.43°N, 2,790 m a.s.l.) meteorological stations, as well as the pan evaporation from a 20-cm pan by using a data set recorded at the Tuotuohe, Maduo, and Geermu meteorological stations on the QTP, were used to analyze the influences of the climatic condition on the lake changes. These climate data were provided by the National Meteorological Information Center (NMIC), China Meteorological Administration (CMA) (http://cdc.cma.gov.cn).

2.4 Glacier and permafrost data

The glacier and permafrost data were used to analyze the influence of the cryosphere changes on the lake dynamics under the background of climate warming. The glacier areas (http://www.tpedatabase.cn/portal/Login.jsp) in 1980 and 2010 were extracted from the First Glacier Inventory of China (images taken during 1950–1980) and the Second Glacier Inventory of China (images taken during 2006–2010), respectively. The spatial distribution of the permafrost types, Mean Annual Ground Temperature (MAGT), and ground ice content over the study area, as well as the long-term averaged ALT along the Qinghai–Tibet Highway (available at http://www.crs.ac.cn/), were provided by the Cryosphere Research Station on the QTP, Chinese Academy of Sciences. The MAGT and ground ice content over the study region were extracted from the MAGT and ground ice content across the QTP calculated by Zhao and Sheng. (2019). The spatial distribution MAGT was modeled by using an improved Noah land surface model (LSM). The ground ice content was calculated by the formula:$Gi = \int \rho_d(Z)\theta(Z)dzDs$, where Gi was ground ice content (kg), $\rho_d(Z)$ was bulk density of the soil (kg·m^{-3}), $\theta(Z)$ was gravimetric water content of the soil (%), Z was permafrost thickness (m) and S was permafrost area (m^2). Based on the parameters from borehole drilling and permafrost area of 1.06×10^6 km^2, the calculated ground ice content in permafrost on the QTP was 12,700 km^3. The long-term averaged ALT during 1981–2017 was calculated by Li et al. (2012) using active-layer monitoring data recorded at more than 10 observation sites and a long sequence of meteorological variables using a multiple regression method.

The freezing and thawing depths were subsequently calculated using Stefan's equation, as follows:

$$\begin{aligned} Z &= \sqrt{\frac{2K \cdot DDF/DDT}{Q_L}} = \sqrt{\frac{2K \cdot DDF/DDT}{L\rho(\omega - \omega_u)}}, \\ DDF &= \sum_{t=0}^{t} (T_0 - T_t), \quad T_t < T_0, \\ DDT &= \sum_{t=0}^{t} (T_t - T_0), \quad T_t > T_0, \end{aligned} \tag{1}$$

where Z is the depth of the frost or thaw (m), K is the appropriate frozen or thawed thermal conductivity (W·m^{-1}°C^{-1}), ρ is the dry soil density (kg·m^{-3}), ω is the soil's water content (%), ω_u is the unfrozen water content (%), L is the latent heat of the fusion of ice (3.3×10^5 Jkg^{-1}), and DDF/DDT stands for the annual degree-days of freezing/thawing, i.e., the sum of the daily mean temperatures below (above) 0°C. In this study, these physical parameters in equation were derived from soil profile borehole and field investigation data during summer for a site around Maduo meteorological station; ω and ω_u are 19% and 5% respectively, ρ is 1,240 kgm^{-3}, K is 0.88 W·m^{-1}°C$^{-1.}$

3 Results

3.1 Spatial-temporal changes in lake areas

Figure 2 shows the spatial-temporal changes in the areas of the lakes in the northeastern Tibetan Plateau from 1988 to 2019. Overall, the lakes experienced dramatic changes. Although the shrinkage of some of the lakes weakened, the regional lake area tended to increase. The areas of 75.7% of the lakes increased at rates of 0.01–16.03 km^2/yr; and the areas of only 24.2% of the lakes decreased at rates of 0.01–3.52 km^2/yr (Figure 2D). Specifically, this change trend exhibited three stages between 1988 and 2019. During 1988–2000, the lake area decreased sharply; and the areas of 54.5% of the lakes decreased slightly at rates of 0.01–2.27 km^2/yr. In addition, the areas of 45.6% of the lakes increased at rates of 0.01–8.53 km^2/yr (Figure 2A). However, after 2000, the lake area increased quickly. The areas of 75.7% of the lakes increased at rates of 0.01–20.74 km^2/yr from 2000 to 2012 (Figure 2B), and the areas of 72.7% of the lakes increased at high rates of 0.01–32.80 km^2/yr from 2012 to 2019 (Figure 2C). The prevailing lake expansion in this region since 2000 was also commonly observed for the inland lakes in the endorheic basin on the QTP and has been reported in many studies (Li et al., 2014; Song et al., 2014; Yang et al., 2017; Liu et al., 2021).

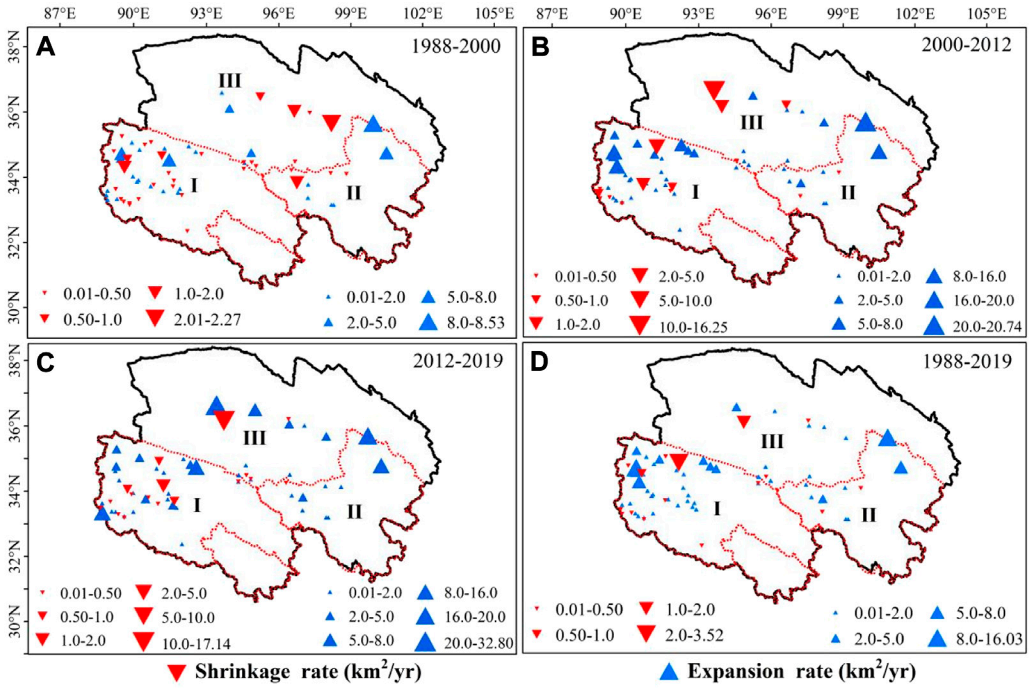

FIGURE 2
Spatial patterns of the trends in the lake area from **(A)** 1988 to 2000, **(B)** from 2000 to 2012, **(C)** from 2012 to 2019, and **(D)** from 1988 to 2019. The blue and red dots indicate lake expansion and lake shrinkage, respectively. The red line is the boundary of the drainage-basin of the river source region.

Figure 2 also shows the large spatial differences in the lake area changes in the three sub-regions (I–III). These large spatial differences in the lake area changes were observed during the same period. Generally, from 1988 to 2019, the most significant lake expansion occurred in sub-region I, which is the source region of the Yangtze River Basin (Figure 2D). In sub-region I, most of the lakes are mainly distributed in the northwestern part of the source region of the Yangtze River in the unpopulated, high-altitude area. The areas of most of the lakes exhibited an obvious decreasing trend during 1988–2000, an abrupt increasing trend during 2000–2012, and a relatively slow increasing trend during 2012–2019. Similar to sub-region I, most of the lakes in sub-regions II and III have increased since 2000, with significant area increases and rates. However, in sub-region II, which is the source region of the Yellow River and the Qinghai Lake Basin, the lakes exhibited sharper increases during 2012–2019 than during 2000–2012. In sub-region III, in the northern part of Qinghai Province (mainly the Qaidam Basin), the lake area shrunk dramatically before 2000, but it began to expand rapidly and substantially in 2012. There was a more rapid increasing trend during 2012–2019 than during 2000–2012. The lake expansion occurred in sub-region I about 12 years earlier than in sub-regions II and III. Compared with the results for the period before 2000 obtained by Huang et al. (2011), widespread decreases occurred in the abundance and areas of inland lakes in the entire source area of the Yellow River and the southeastern part of the source area of the Yangtze River, while the western and northern parts of the source area of the Yangtze River exhibited completely opposite trends. The spatial difference in the lake expansion and contraction in sub-region II was not fully reflected, which may be related to the delimitation of only the large lakes (>10 km^2) and not the small lakes (<10 km^2) in this study.

3.2 Changes in typical lakes

Seven typical expanding large-lakes with great area-increase from 1988 to 2019 in the three sub-regions were selected to present dramatic lake changes, and the annual area changes of these lakes are shown in Figure 3. Overall, in spite of the small lake areas in some years, the trends in the areas of the seven lakes were highly consistent with the overall trend in the lake area on the northeastern QTP, which decreased before 2000 and increased after 2000. In detail, during 1988–2019, Qinghai Lake experienced the greatest increase of 452.11 km^2 at a rate of 15.96 km^2/yr. The areas of the Xijinwulan Lake, the

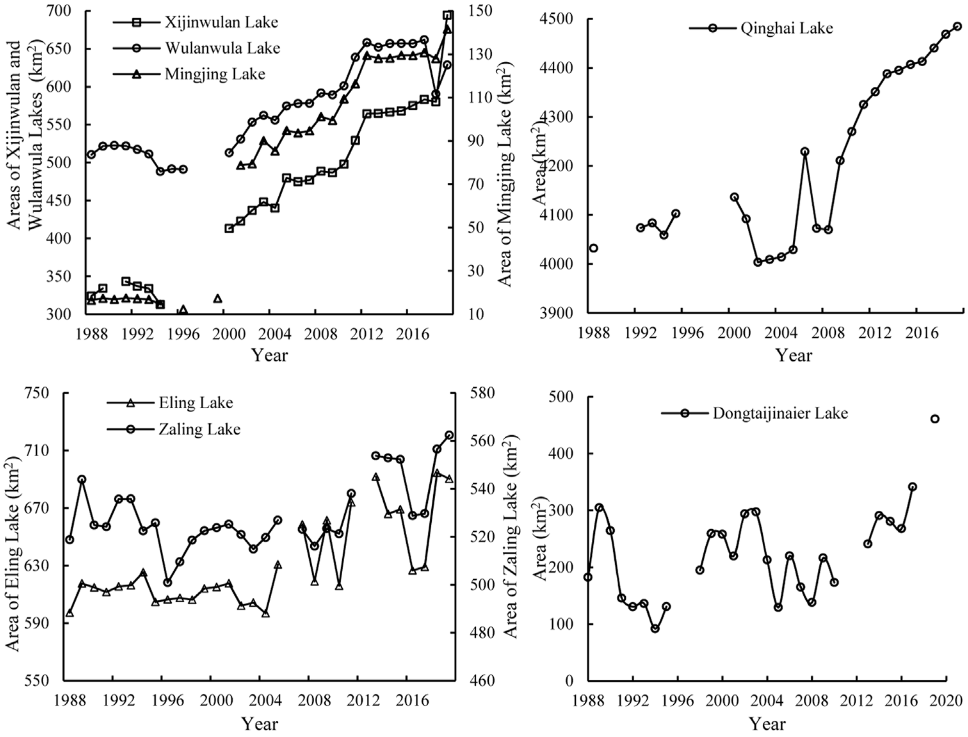

FIGURE 3
The annual area changes of seven typical lakes that expanded from 1988 to 2019.

Wulanwula Lake, and the Mingjing Lake increased by 370.17 km^2, 118.36 km^2, and 125.09 km^2, respectively, at rates of increase of 10.31 km^2/yr, 5.46 km^2/yr, and 4.70 km^2/yr, respectively. The areas of these three lakes exhibited similar trends, and the changes occurred in three stages: decreasing during 1988–2000, sharply increasing during 2000–2012, and increasing since 2012. The areas of the Gyaring Lake and the Ngoring Lake increased by 43.58 km^2 and 92.97 km^2, respectively, at rates of 0.77 km^2/yr and 2.27 km^2/y, respectively. Their areas decreased obviously during 1988–1996, rapidly increased during 1996–2012, and slightly decreased during 2012–2019. In addition to increased precipitation, the expansion of the lakes' surface areas was primarily due to the construction of a hydropower station near the outlet of the Ngoring Lake. The areas of the Dongtaijinaier Lake increased by a large amount (278.23 km^2) but at a slow rate of 4.33 km^2/yr. Its change trend was different from those of the other lakes, was mainly attributed to increasing imbalance between precipitation and evaporation, with Annual Evaporation (AE) of 3,560 mm and AP of 21.9 mm. The area change was W-shaped: decreasing during 1988–1996, increasing during 1996–2003, decreasing during 2003–2012, and decreasing more rapidly during 2012–2019. Similar to the Qinghai Lake, a sustainable expansion has occurred in recent years (since 2012). The Zonag, Kusai, Hedin Noel, and Yanhu lakes are independent inland lakes in the Hoh Xil region of the QTP. After the outburst of the Zonag Lake in September 2011, the flood waters flowed through the Kusai Lake and the HedinNoel Lake and eventually into the Yanhu Lake, leading to rapid shrinkage of the Zonag Lake and the continuous expansion of the Yanhu Lake. The temporal changes of the four lakes involved in this event were examined and discussed in detail by Liu et al. (2019).

3.3 Controlling mechanism of lake changes

3.3.1 Influence of climatic conditions

Both the AP and MAAT recorded at the meteorological stations exhibited overall increasing trends, with rates of 2.37 mm/yr and 0.06°C/yr, respectively, from 1988 to 2018 (Figures 4A, 5A). The AE exhibited a decreasing trend (14.31 mm/yr) during the same period (Figure 6A). During the same period, the P/E (the ratio of annual precipitation to annual evaporation) tended to increase continuously (Figure 7A). The climate has exhibited a warming and wetting trend with significant accelerated increases in the MAAT, AP and P/E over the last 30 years. These climatic characteristics are consistent with the warming-wetting of the climate in most regions of the QTP in recent decades (Yang et al., 2011). In

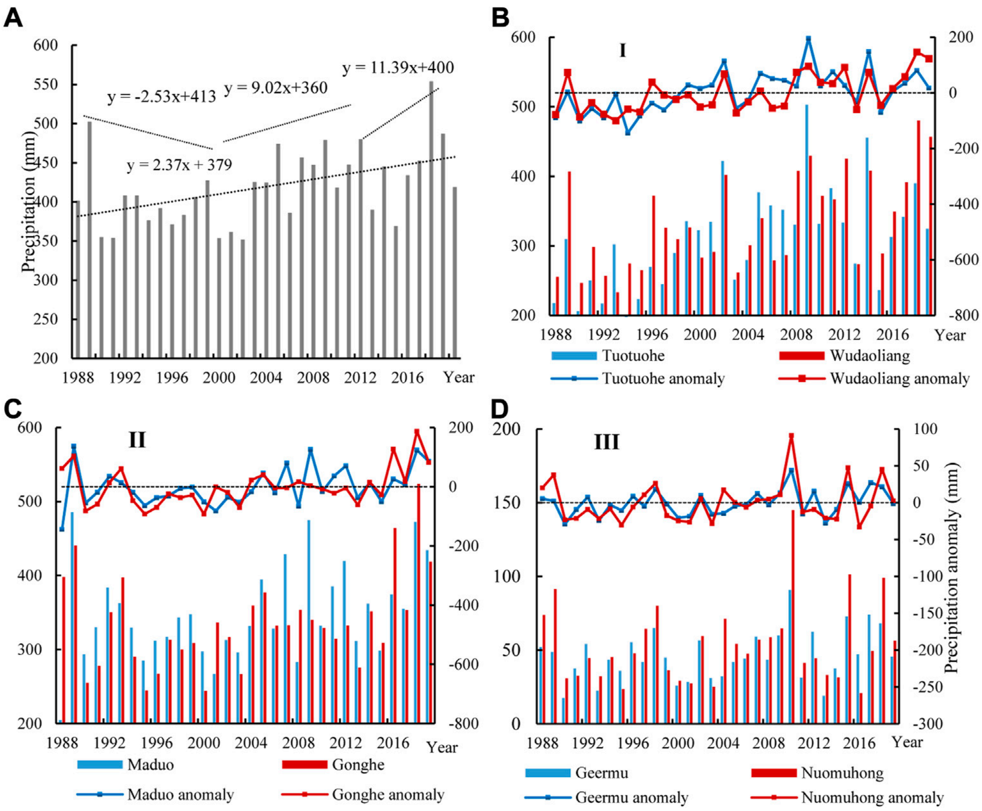

FIGURE 4
The changes in the average values of annual precipitation for the meteorological stations **(A)** and the annual precipitation recorded at meteorological stations in the three sub-regions from 1988 to 2019 **(B–D)**.

general, the AP and P/E decreased before 2000 but rapidly increased after 2000, which well explains the lake shrinkage during 1988–2000 and the lake expansion during 2000–2019 in the study area. The continuous decrease in the AE indicates an actual increase in potential evaporation, which suggests that the lake evaporation and the evaporation in the lake basin increased, theoretically exerting a positive effect on the lake water budget and contributing to the enhanced lake growth. However, it appears that the decrease in the AE was not significantly correlated with the change in the lake area. Under the continuous decrease in the AE, the lake area significantly decreased before 2000 and significantly increased after 2012.

More importantly, the large spatial variations in the AP, MAAT, and AE resulted in a regional discrepancy in the lake area changes. In sub-region I, the lake area responded well to the decrease in the AP and increase in the AE as reducing MAAT during 1988–2000, the significant increase in the AP and decrease in the AE during 2000–2012, and the increase in the AP during 2012–2019 (Figures 4B2212;Figures 6B). Slightly different from that in sub-region I, the lakes in sub-region II expanded more rapidly during 2012–2019 in response to the most significant increase in the AP, in spite of no obvious trend in the AE and MAAT (Figures 4C2212;Figures 6C). Most of the lakes in sub-region III have expanded before 2012 was mainly attributed to significant increase in the AP (0.47 mm/yr) and sharp rising MAAT (0.04–0.05°C/yr), in spite of the decreasing AE (−39.69 mm/yr) (Figures 4D2212;Figures 6D). Since 2012, the accelerated lake expansion was mainly caused by climate change and human activities, such as water consumption in the catchment, blocking rivers and lakes connection around the lake, brine mining utilization, constructions of solar ponds. What's more, a strong positive relationship between lake area change and precipitation increase was observed; lake area increases more than 0.5 km^2/yr agrees fairly well with precipitation increase rates (R^2=0.18, p<0.05). These results suggest that the expansion of most of the lakes in the study area was more closely related to the changes in the AP than the changes in the AE, and precipitation was the primary factor influencing the lake area changes. The good correlation between the regional precipitation and the changes in the areas of the lakes in the study area, as well as over the entire QTP, has also been confirmed by other researchers (Li et al., 2010; Huang et al., 2011; Duan et al., 2015).

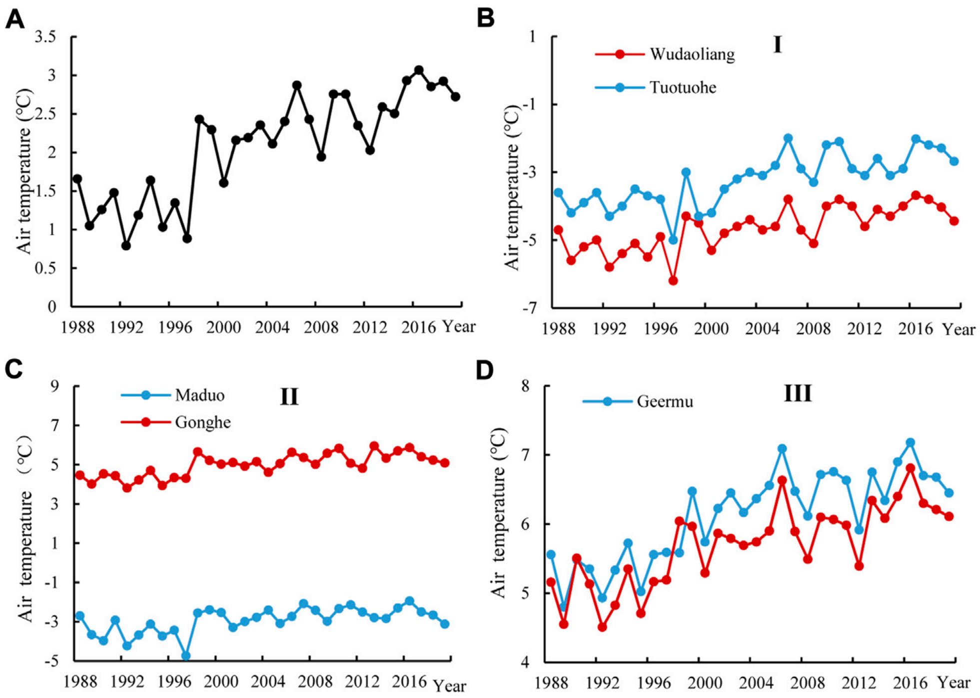

FIGURE 5
The changes in the average values of mean annual air temperature for the meteorological stations **(A)** and the mean annual air temperature recorded at meteorological stations in the three sub-regions from 1988 to 2019 **(B–D)**.

3.3.2 Glacier melting

The total glacier area in Qinghai Province was 5,381.56 km^2 in 1980 and 4,464.93 km^2 in 2010, i.e., a significant decrease of 916.62 km^2 (17.03%). The spatial variation in the glacier area differed obviously in the sub-regions of Qinghai Province. The glacier area in sub-region II decreased the most (22%), followed by that in sub-region III (19%) (Figure 8). The glacier area in sub-region I decreased relatively little (14%). This spatial pattern of the change in the glacier area did not agree well with the spatial pattern of the lake area changes in the three sub-regions due to the presence of glacier-fed lakes and non glacier-fed lakes, as well as the different responses of the glacier-fed lakes to the regional glacial meltwater. In sub-region I, only four large lakes (Lexiewudan Lake, Kekexili Lake, Xijinwulan Lake and Wulanwula Lake) that expanded were glacier-fed lakes, which were fed by the Malan Glacier and the Hantaishan Glacier, respectively, with accelerated area decreases of 6.04% and 5.4%, respectively, from 1973 to 2010 (Jiang et al., 2012). The Xijinwulan Lake and Wulanwula Lake, the glacier-fed lakes, glacier areas in basins greatly decrease by 58.492 km^2 (39.7%) and 23.193 km^2 (48.8%) from 1988 to 2019, but the Mingjing Lake, the non-glacier-fed lakes, its area change exhibited same trends as theses two lakes. This was not consistent with the significant lake expansion, and this further suggests that glacial meltwater was not the replenishment source of most of the lakes in the source area of the Yangtze River. Similarly, in sub-regions II and III, although significant glacier retreat occurred, all of the lakes were non-glacier-fed lakes, except for the Qinghai Lake. In spite of large glacier shrinkage in the Qinghai Lake basin, i.e., a decrease of 19.191 km^2 (29.12%), the recharge from the glacier meltwater was small (5×10^6 m^3/yr), contributing <2% of the water supply and a small increase in the lake volume (297.67×10^6 m^3/yr). This suggests that the glacier melting caused by the rising temperature contributed little to the recent lake expansion in this region, and it was not the dominant driving factor of the recent lake expansion in Qinghai Province.

3.3.3 Permafrost degradation

The study area has a total permafrost area of 0.336×10^6 km^2, accounting for approximately 31.7% of the total permafrost area on the QTP. The total volume of ground ice in the permafrost is 4,142 km^3, with contents of 2.0–185.8 km^3, accounting for 32.6% of the total ground ice content in the QTP. The permafrost in the study area was mainly distributed in sub-region I (the hinterland of continuous permafrost on the QTP), followed by sub-region II (the eastern boundary of continuous permafrost on the QTP). 81.3% of the total expanding lakes were distributed in continuous permafrost region, and the area increased by 1,673.85 km^2, accounting for 74.3% of the total area increase. A dramatic lake expansion was observed in the continuous permafrost

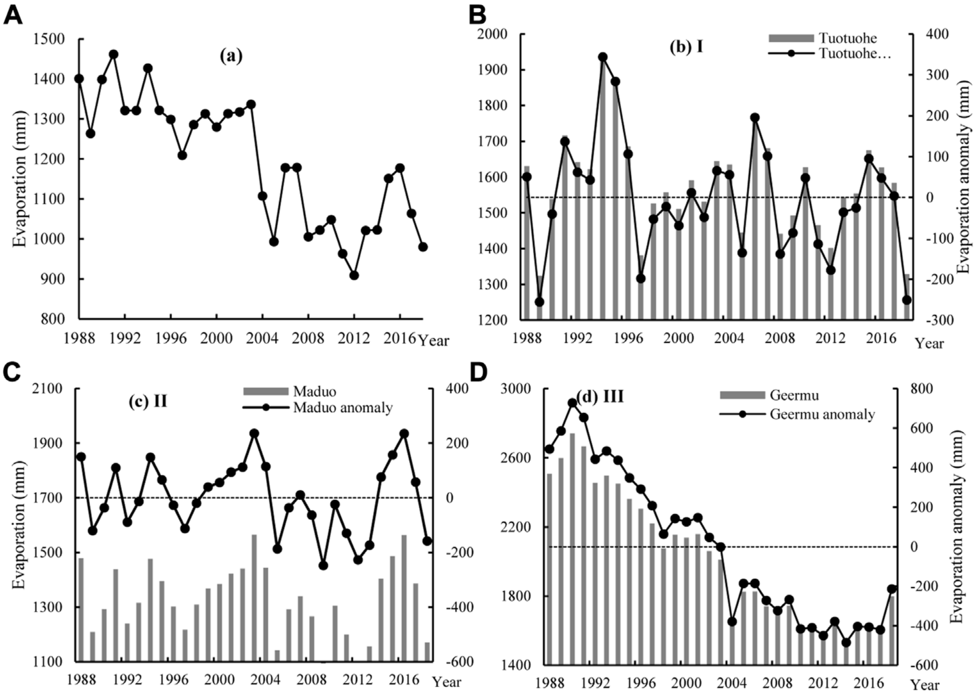

FIGURE 6
The changes in the average values of annual evaporation for the meteorological stations **(A)** and the annual evaporation recorded at meteorological stations in the three sub-regions from 1988 to 2019 **(B–D)**.

region, which has exhibited large spatial differences. (Figure 9A). The spatial pattern of the lake expansion in the continuous permafrost region agreed well with the spatial patterns of the MAGT and the ground ice content of the continuous permafrost. The lakes in the continuous permafrost region with a large amount of ground ice and a low MAGT expanded significantly, whereas the lakes in the continuous permafrost with little ground ice and a high MAGT only expanded slightly (Figures 9B,C). The statistical result showed that 79.5% of the total expanding lakes and even all lakes with increase rate larger than 5 km^2/yr in continuous permafrost region distributed in cold permafrost (MAGT<−1.5°C) with high-ground ice content (>10×10^6 m^3). This is also supported by the fact that the permafrost characteristics and degradation trends were closely related to the lake changes in the endorheic basin in the QTP (Liu et al., 2020). The lake expansion in the continuous permafrost region was mainly due to the presence of ice-rich permafrost with a high permafrost coverage, which acted as a barrier layer due to its low hydraulic conductivity and permeability. This layer impeded the infiltration of liquid water and the interaction between the surface water and groundwater, which finally resulted in more direct surface runoff of both rain and snow-melt and the lack of a water storage buffer effect compared to the non-permafrost regions. This was followed by the melting of the ground ice in the shallow permafrost due to the accelerated permafrost degradation, which was a significant potential source in the water balance of the lakes in this cold region.

The permafrost was significantly degraded in the continuous permafrost region, as well as on the QTP, due to the increase in temperature in recent decades. Long-term monitoring data collected along the Qinghai–Tibet Highway reveal that the average ALT increased from 181 cm in 1981 to 238 cm in 2017 at a rate of 1.90 cm/yr. Notably, an accelerated increase has been observed since 2000. The rate of increase during 2000–2017 (2.60 cm/yr) was higher than that during 1981–2000 (1.44 cm/yr). Specifically, the rate during 2000–2012 (2.89 cm/yr) was higher during 2012–2019 (2.29 cm/yr) (Figure 9D), which is consistent with the more rapid lake expansion during 2000–2012 than during 2012–2019 in sub-region I. The calculated thawing index and ALT of the permafrost in the source area of the Yellow River Basin also exhibited increasing trends, with rates of 7.50°Cd/yr and 0.13 m/yr, respectively (Figure 10). Due to the permafrost degradation, the larger amount of meltwater from the ground ice due to permafrost degradation was a major supply of water for the lake growth. In addition, as the ground ice began to melt, the permeability of the soil increased and the hydraulic exchange between the surface water and the suprapermafrost groundwater was enhanced. Thus, aquifer activation arising from permafrost degradation may have increased the recharge and groundwater

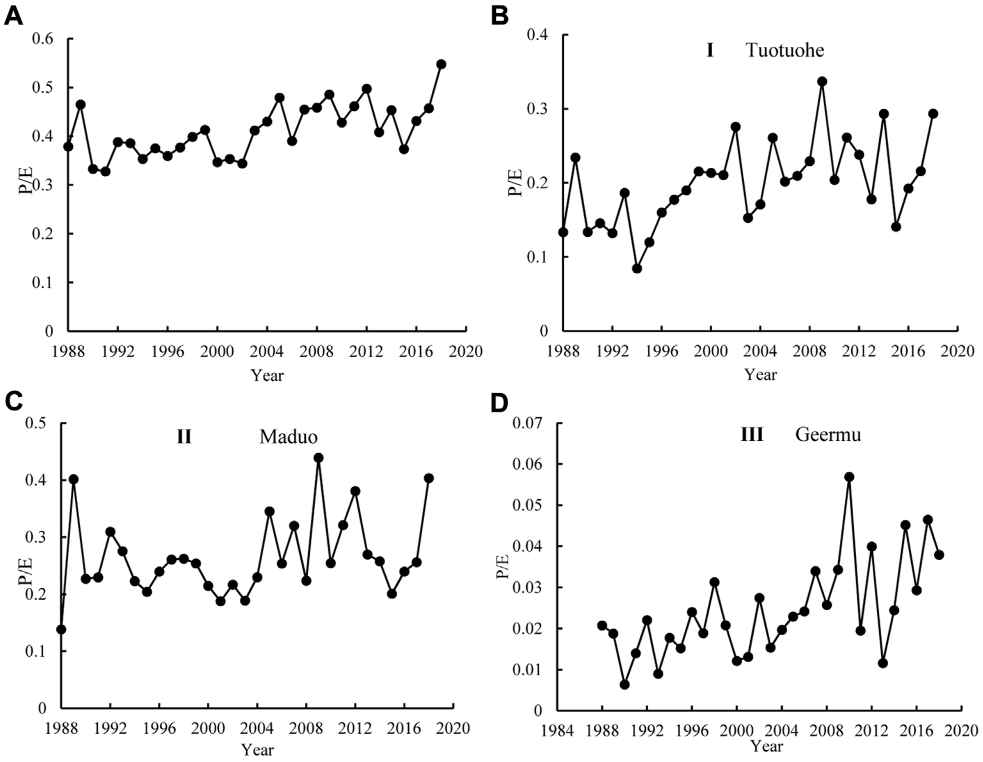

FIGURE 7
The changes in the average values of the P/E for the meteorological stations **(A)** and the P/E based on annual precipitation and evaporation recorded at meteorological stations in the three sub-regions from 1988 to 2019 **(B–D)**.

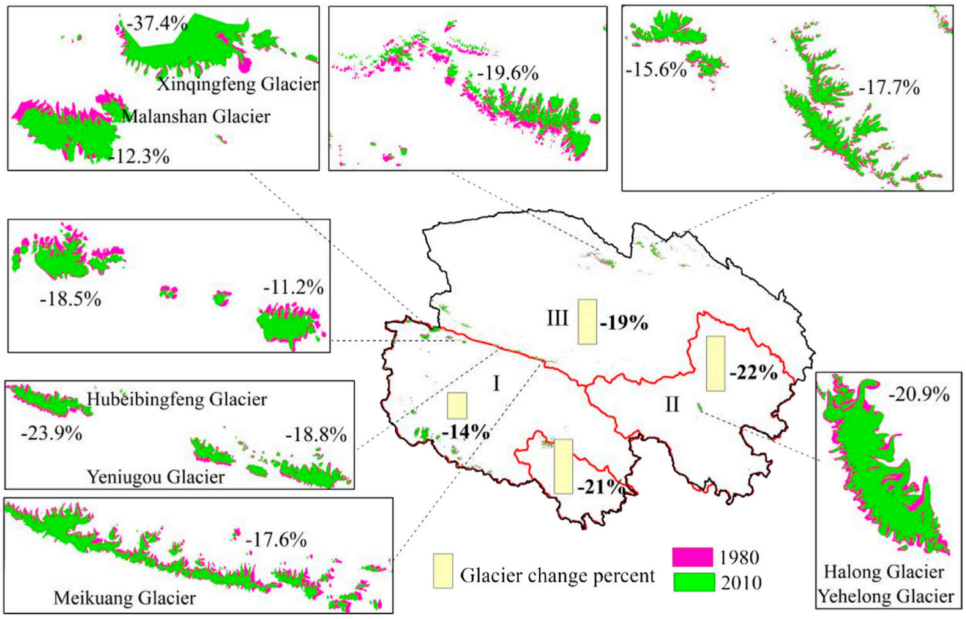

FIGURE 8
The changes in the total glacier area in the different sub-regions.

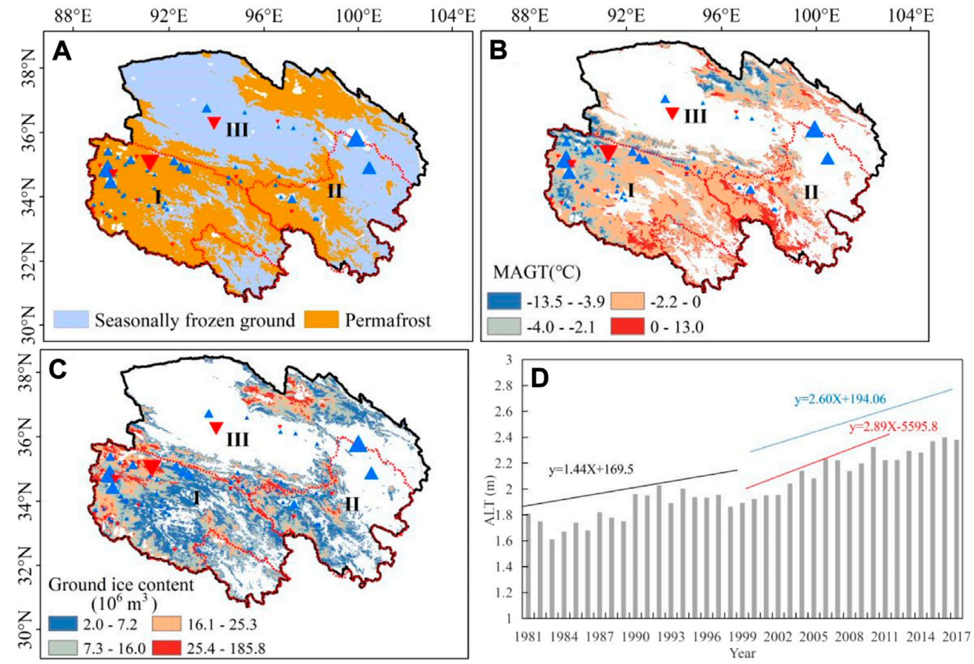

FIGURE 9
(A) The permafrost distribution; **(B–C)** the spatial patterns of the mean annual ground temperature and the ground ice content of permafrost, respectively; **(D)** the annual change in the active layer thickness from 1981 to 2017 along the Qinghai–Tibet Highway.

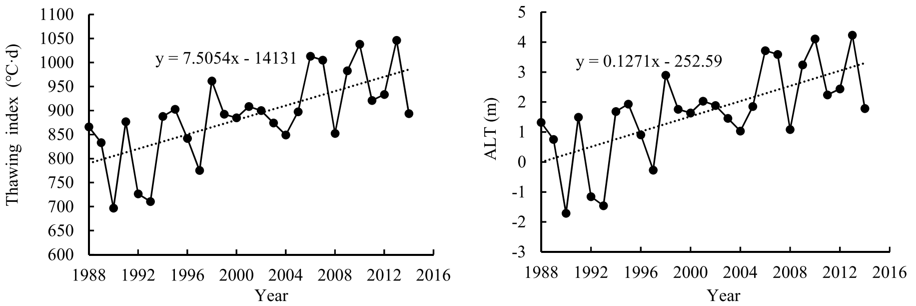

FIGURE 10
The annual changes in the thawing index and active layer thickness of the permafrost from 1988 to 2014 in the source region of the Yellow River Basin.

discharge to the rivers and lakes, further accelerating the lake expansion. Thus, the permafrost degradation may have partially contributed to the increase in the lake surface area in the study area, especially in sub-region I.

Moreover, the analysis of infuential factors in basins for several typical lakes showed that lake changes were mostly related to AP. The Xijinwulan Lake and Wulanwula Lake, the glacier-fed lakes with large decrease in glacier area, presented same area-change trends as the Mingjign Lake, which was consistent with the decrease in the AP and increase in the AE during 1988–2000, the significant increase in the AP and decrease in the AE during 2000–2012, and the increase in the AP in spite of slight decreasing AE during 2012–2019 recorded at Tuotuohe meteorological station. Similar to the Gyaring Lake and Ngoring Lake, the area-change trends also showed well corresponding response to AP. For the Qinghai Lake, with little contribution of glacial meltwater to water budget, its sustainable expansion, especially in recent years (since 2012) showed closer covariation with significant increasing AP (226 mm/yr) and MAAT (0.03°C/yr) than with slight decreasing AE (−0.98 mm/yr) from 1988 to 2019 recorded at Gangcha meteorological station.

4 Discussion

4.1 Impact of permafrost degradation on lake changes

The source region of the Yellow River is underlain by seasonally frozen ground, as well as continuous, discontinuous, and sporadic permafrost in the northeastern QTP. Since the 1980s, significant regional permafrost degradation due to warming has occurred, along with decreased permafrost area, decreased permafrost thickness, and expansion of taliks. The lower limit of the permafrost has risen by 50–80 m. The average maximum depth of the frost penetration has decreased by 12 cm in the areas of seasonally frozen ground (Jin et al., 2010). The maximum frozen soil depth decreased from 3.2 m in 1980 to 2.8 m in 2000 and further decreased to 2.4 m in 2008. The temperature at the depth of the zero annual amplitude of the permafrost increased by 0.03–0.20°C during 2010–2017 (Luo et al., 2020). Thermokarst ponds (ground subsidence induced by the degradation of ice-rich permafrost causes the formation of thermokarst lakes) (French, 1974), which are a significant sign of local permafrost degradation, are the most widespread evidence of accelerating permafrost thawing in the source region of the Yellow River. There are a variety of thermokarst ponds dotting the predominantly continuous permafrost region. There are 477,518 thermokarst lakes in the permafrost region in 2021 with a total area of $190.22\times10^6\ m^2$. Water bodies consisting of lakes, thermokarst ponds, and depressions are widely distributed in this region and occasionally form clusters of ponds in the same geographical unit. Adjacent thermokarst ponds and depressions are sometimes interconnected by ditches and troughs, indicating the melting of ground ice in the permafrost table.

Moreover, due to the thawing of discontinuous permafrost under the present climate and warmer climate conditions, the evolution of the hydrogeological conditions also dramatically affects the lake dynamics. Although most of the lakes in the source region of the Yellow River are still distributed in the continuous permafrost region, these lakes may still shrink or disappear when the permafrost in the lake region and its surrounding area undergoes a transition from continuous to discontinuous-isolated permafrost, and some isolated permafrost areas may have already been converted to seasonally frozen ground. Further intensified permafrost degradation will lead to thinning and eventual breakage of the permafrost beneath the lakes, greatly facilitating their drainage into the subsurface zone *via* taliks (Smith et al., 2005). Newly formed open taliks can facilitate groundwater movement into subpermafrost aquifers at lower heads and can thereby drain lakes, leading to decreased groundwater levels and lake shrinkage. The phenomenon of significant lake expansion in the continuous permafrost region is in sharp contrast to the lake shrinkage in the island-discontinuous permafrost region that is widespread throughout the endorheic basin in the QTP (Liu et al., 2020) and the Mongolian Plateau (Zhou et al., 2019). Lake shrinkage has become a common feature in the island-discontinuous permafrost region, especially, the shrinkage or disappearance of thermokarst lakes in the discontinuous permafrost region in the Arctic and in subarctic regions (Yoshikawa and Hinzman, 2003). This phenomenon was well described by Smith et al. (2005) and Riordan et al., 2015: initial permafrost warming led to the development of thermokarst lakes and lake expansion, followed by lake drainage as the permafrost degraded further.

In addition, the groundwater in the island-discontinuous permafrost region and the adjacent area became connected and was mutually transformed. The increased recharge and discharge supplied the groundwater in the adjacent regions at low heads with a low elevation through taliks (activated aquifers), which caused lake expansion instead. Thus, the coexistence of lake expansion and shrinkages in one geographic unit in this region, and even over the entire QTP, will occur and become a common feature of the permafrost region. This is manifested as the broad geographic pattern, in which permanently drained lakes are commonly found alongside unchanged neighboring lakes. In the island-discontinuous permafrost region, Southern Seling Co has expanded, while in the continuous permafrost boundary, Northern Seling Co has expanded (Liu et al., 2022). Lake expansion in the continuous permafrost region and losses where the permafrost is thinner and less contiguous have been observed in Siberia (Smith et al., 2005). This also suggests a spatially patchy process, rather than a direct climatic mechanism such as increased precipitation and decreased evaporation.

4.2 Effect of lake changes on regional climate conditions and permafrost

Even though regional climate conditions were the main drivers of the dynamic changes of the lakes, recent research has also revealed that the lakes have had an important influence on the local temperature and precipitation and are also regulators of the regional climate. The lakes are strong heat sinks in the daytime and heat sources at night in summer, and they are weak heat sinks in the daytime and strong heat sources at night in autumn (Dai et al., 2020). After the outburst of the Zonag Lake on 14 September 2011, the influences of this event on the permafrost surrounding it and the permafrost surrounding the Yanhu Lake were investigated. Observations revealed that new permafrost had formed in the exposed lake bottom, accompanied by various periglacial landscapes. The permafrost aggradation in the exposed bottom of the lake was rapid, and the permafrost base reached 4.9, 5.4, and 5.7 m in the first 3 years. The simulated results indicate that the permafrost in the exposed lake bottom is likely to continue to develop, quickly at first and then slowly (Zhang et al., 2022). In contrast, the continuous expansion of the Yanhu Lake significantly accelerated the degradation of the surrounding permafrost. It resulted in the obvious thermal disturbance of the underlying permafrost and lateral thermal erosion of the surrounding permafrost. Such degradation may have been due to the thermal alteration of the thawing-freezing cycle of the permafrost and the melting of the ground ice, along with the resulting changes in the hydrological connectivity and soil permeability (Lu et al., 2020).

The permafrost hydrological processes on the QTP are complex, and they affect soil water movement, rainfall-runoff, base flow, and evaporation (Gao et al., 2021). Although several *in situ* observation stations have been established to gather long-term measurements, given the vast area of the QTP, the permafrost hydrology research in this region remains far from adequate. Due to the different scales of the permafrost coverage, the thermal conditions and the amount of ground ice melting in the different watersheds in the study area, and the different changes in the streamflow characteristics, it is difficult to determine the specific contribution of the permafrost degradation to the lake changes in each lake basin, as well as those of the glacier ablation and climate factors. Therefore, permafrost hydrological modeling is a powerful tool for quantifying the effects of the spatiotemporal variations in the permafrost on the basin-scale hydrology because it can incorporate landscape and topographical data in order to sufficiently represent the horizontal heterogeneities. There are some developing hydrological models which considers both snow and frozen ground processes describe interactions between cryosphere, hydrosphere, biosphere, and atmosphere. These model have been applied in many river basins in cold regions and performed very well. The HydroSiB2-SF model coupled snow and frozen ground physics was developed based on a hydrologically improved land surface model (HydroSiB2), and indicated good performance at two typical sites on the QTP (Zhou et al., 2015; Wang et al., 2017). Based on the Water and Energy Budget-based Distributed Hydrological Model (WEB-DHM), the WEB-DHM-SF model incorporating both three-layer snow and frozen ground physics successfully reproduced the basin-wide daytime and nighttime land surface temperature as well as snow depth in basin-averaged time series and spatial distributions at the upper Yangtze River Basin under widespread snow cover and frozen ground (Qi et al., 2019). The cryosphere-hydrology-lake-dam model was recently used to quantify the different contributors to the rising water levels at Lake Yanhu. This well-performing model reproduce the volume of Lake Zonag satisfactorily, with an RMSE (root mean square error) of 0.012–0.062 km^3, which can well used for reproduce the following simulations and predictions of lake change (Wang et al., 2022). Determining the balance point between model simplicity and catchment complexity is likely one of the most important scientific challenges yet to be resolved in permafrost hydrological modeling on the QTP, which will be investigated in our next study.

5 Conclusion

Overall, from 1988 to 2019, the lakes in the northeastern Tibetan Plateau experienced rapid expansion. The total area of 75.7% of the lakes increased at rates of 0.01–16.03 km^2/y. In detail, the lake area generally decreased during 1988–2000, quickly increased during 2000–2012, and rapidly increased from 2012 to 2019. Large spatial differences in the lake area changes were observed in the three sub-regions, and the most significant lake expansion occurred in sub-region I. In sub-region I, the lake area significantly decreased during 1988–2000, quickly increased during 2000–2012, and slowly increased during 2012–2019. Similarly, most of the lakes in sub-regions II and III have continued to increase since 2000, with significant lake area increases and rates of increase. The lakes in sub-region II exhibited sharper increasing trends during 2012–2019 than during 2000–2012. In sub-region III, the lakes shrank dramatically before 2000 but have expanded rapidly and substantially since 2012. There was a sharper increasing trend during 2012–2019 than during 2000–2012. The lake expansion occurred in sub-region I about 12 years earlier than in sub-regions II and III.

The AP decreased before 2000 but rapidly increased after 2000, which explains the lake shrinkage during 1988–2000 and the lake expansion since 2000 in the study area. The expansion of most of the lakes in the study area was closely related to the AP, and precipitation was the primary factor influencing the lake area changes. Although significant glacier retreat occurred, most of the lakes in the sub-regions were non-glacier-fed lakes. This is inconsistent with the significant lake expansion, further suggesting that glacial meltwater was not the replenishment source of most of the lakes in the study area. An accelerated increase in the ALT has occurred since 2000. The increase rate was higher during 2000–2017 (2.60 cm/yr) than during 1981–2000 (1.44 cm/yr). Specifically, the rate was higher during 2000–2012 (2.89 cm/yr), which is consistent with the more rapid lake expansion during 2000–2012 than during 2012–2019 in sub-region I. Permafrost degradation further intensified the lake expansion.

Data availability statement

The raw data supporting the conclusions of this article will be made available by the authors, without undue reservation.

Author contributions

Conceptualization and writing (original draft) for WL and QL, supervision and editing for HL and CX, data curation for ZZ, QZ, QHZ, methodology and software for GZ.

Funding

This study was supported by the Natural Science Foundation of Qinghai Province, China (No. 2021-ZJ-940Q). Significant thanks to all author for their contributions; conceptualization and writing (original draft) for WL and QL, supervision and editing for HL and CX, data curation for ZZ, QZ, QHZ, methodology and software for GZ.

Acknowledgments

Special thanks to all the staff of the Cryosphere Research Station on the Qinghai-Tibet Plateau, Chinese Academy of Sciences for their hard work in obtaining field permafrost data.

Conflict of interest

The authors declare that the research was conducted in the absence of any commercial or financial relationships that could be construed as a potential conflict of interest.

Publisher's note

References

Bolch, T., Yao, T. D., Kang, S. C., Buchroithner, M. F., Scherer, D., Maussion, F., et al. (2010). A Glacier Inventory for the Western nyainqentanglha range and the nam Co basin, tibet, and glacier changes 1976-2009. *Cryosphere* 4 (3), 419–433. doi:10.5194/tc-4-419-2010

Cheng, G. D., Zhao, L., Li, R., Wu, X. D., Sheng, Y., Hu, G. J., et al. (2019). Characteristic, changes and impacts of permafrost on Qinghai-Tibet Plateau. *Chin. Sci. Bull.* 64, 2783–2795. doi:10.1360/tb-2019-0191

Cheng, J., Song, C. Q., Liu, K., Ke, L. H., Chen, T., and Fan, C. Y. (2021). Regional assessment of the potential risks of rapid lake expansion impacting on the Tibetan human living environment. *Environ. Earth Sci.* 80 (4), 166. doi:10.1007/s12665-021-09470-4

Dai, Y., Yao, T., Wang, L., Li, X., and Zhang, X. (2020). Contrasting Roles of a large alpine lake on Tibetan Plateau in shaping regional precipitation during Summer and Autumn. *Front. Earth Sci.* 8, 358. doi:10.3389/feart.2020.00358

Ding, Y. J., Mu, C. C., Wu, T. H., Hu, G. J., Zou, D. F., Wang, D., et al. (2021). Increasing cryospheric hazards in a warming climate. *Earth. Sci. Rev.* 213, 103500. doi:10.1016/j.earscirev.2020.103500

Duan, A. M., and Xiao, Z. X. (2015). Does the climate warming hiatus exist over the Tibetan Plateau? *Sci. Rep.* 5, 13711. doi:10.1038/srep13711

Duan, S. Q., Fan, S. X., Cao, G. C., Liu, X. S., and Sun, Y. S. (2015). The changing features and cause analysis of the lakes in the source regions of the Yellow River from 1976 to 2014. *J. Glaciol. Geocryol.* 37 (3), 745–756.

French, H. M. (1974). Active thermokarst processes, eastern banks island, western Canadian arctic. *Can. J. Earth Sci.* 11, 785–794. doi:10.1139/e74-078

Gao, H. K., Wang, J. J., Yang, Y. Z., Pan, X. C., Ding, Y. J., and Duan, Z. (2021). Permafrost hydrology of the Qinghai-Tibet Plateau: A review of processes and modeling. *Front. Earth Sci.* 8, 576838. doi:10.3389/feart.2020.576838

Huang, L., Liu, J. Y., Shao, Q. Q., and Liu, R. G. (2011). Changing inland lakes responding to climate warming in Northeastern Tibetan Plateau. *Clim. Change* 109, 479–502. doi:10.1007/s10584-011-0032-x

Jiang, S., Yang, T. B., and Tian, H. Z. (2012). Glacier shrinkage and its dependence on climate in the Malan Mountain in the past 40 years based on RS and GIS. *J. Glaciol. Geocryol.* 34 (3), 522–529.

Jin, H. J., Wang, S. L., lv, L. Z., He, R. X., Chang, X. L., and Luo, D. L. (2010). Features and degradation of frozen ground in the sources area of the Yellow River, China. *J. Glaciol. Geocryol.* 32 (1), 10–17.

Kurylyk, B. L., MacQuarrie, K. B., and McKenzie, J. M. (2014). Climate change impacts on groundwater and soil temperatures in cold and temperate regions: Implications, mathematical theory, and emerging simulation tools. *Earth. Sci. Rev.* 138, 313–334. doi:10.1016/j.earscirev.2014.06.006

Lei, Y. B., Yao, T. D., Bird, B. W., Yang, K., Zhai, J. Q., and Sheng, Y. W. (2013). Coherent lake growth on the central Tibetan plateau since the 1970s: Characterization and attribution. *J. Hydrol. X.* 483, 61–67. doi:10.1016/j.jhydrol.2013.01.003

Li, H., Xiao, P. F., Feng, X. Z., Wan, W., Ma, R. H., and Duan, H. T. (2010). Lake changes in spatial evolution and area in source region of Three Rivers in recent 30 years. *J. Lake .Sci.* 22 (6), 862–873. doi:10.18307/2010.0608

Li, R., Zhao, L., Ding, Y. J., Wu, T. H., Xiao, Y., Du, E. J., et al. (2012). Temporal and spatial variations of the active layer along the Qinghai-Tibet Highway in a permafrost region. *Chin. Sci. Bull.* 57, 4609–4616. doi:10.1007/s11434-012-5323-8

Li, Y. K., Liao, J. G., Guo, H. D., Liu, Z. W., and Shen, G. Z. (2014). Patterns and potential drivers of dramatic changes in Tibetan lakes, 1972-2010. *PLoS ONE* 9, e111890. doi:10.1371/journal.pone.0111890

Li, Z. X., Feng, Q., Wang, Q. J., Yong, S., Cheng, A. F., and Li, J. G. (2016). Contribution from frozen soil meltwater to runoff in an in-land river basin under water scarcity by isotopic tracing in northwestern China. *Glob. Planet. Change* 136, 41–51. doi:10.1016/j.gloplacha.2015.12.002

Liu, G. Y., Zhao, L., Xie, C. W., Pang, Q. Q., Du, E. J., and Qiao, Y. P. (2016). Variation characteristics and impact factors of the depth of zero annual amplitude of ground temperature in permafrost regions on the Tibetan Plateau. *J. Glaciol. Geocryol.* 38, 1189–1200. doi:10.7522/j.issn.1000-0240.2016.0139

Liu, W. H., Liu, H. R., Xie, C. W., Zhao, J. Y., Liu, G. Y., Wang, W., et al. (2022). Dynamic changes in lakes and potential drivers within the Selin Co basin, Tibetan Plateau. *Environ. Earth Sci.* 81, 84. doi:10.1007/s12665-021-10155-1

Liu, W. H., Xie, C. W., Wang, W., Yang, G. Q., Zhang, Y. X., Wu, T. H., et al. (2020). The impact of permafrost degradation on lake changes in the endorheic basin on the Qinghai–Tibet Plateau. *Water* 12, 1287. doi:10.3390/w12051287

Liu, W. H., Xie, C. W., Zhao, L., Li, R., Liu, G. Y., Wang, W., et al. (2021). Rapid expansion of lakes in the endorheic basin on the Qinghai-Tibet Plateau since 2000 and its potential drivers. *Catena* 197, 104942. doi:10.1016/j.catena.2020.104942

Liu, W. H., Xie, C. W., Zhao, L., Wu, T. H., Wang, W., Zhang, Y. X., et al. (2019). Dynamic changes in lakes in the Hoh Xil region before and after the 2011 outburst of Zonag Lake. *J. Mt. Sci.* 16, 1098–1110. doi:10.1007/s11629-018-5085-0

Lu, P., Han, J. P., Li, Z. S., Xu, R. G., Li, R. X., Hao, T., et al. (2020). Lake outburst accelerated permafrost degradation on Qinghai-Tibet Plateau. *Remote Sens. Environ.* 249, 112011. doi:10.1016/j.rse.2020.112011

Luo, D. L., Jin, H. J., Du, H. Q., Li, C., Ma, Q., Duan, S. Q., et al. (2020). Variation of alpine lakes from 1986 to 2019 in the headwater area of the Yellow River, Tibetan plateau using google Earth engine. *Adv. Clim. Change Res.* 11 (1), 11–21. doi:10.1016/j.accre.2020.05.007

Niu, L., Ye, B. S., Li, J., and Sheng, Y. (2011). Effect of permafrost degradation on hydrological processes in typical basins with various permafrost coverage in Western China. *Sci. China Earth Sci.* 54, 615–624. doi:10.1007/s11430-010-4073-1

Phan, V. H., Lindenbergh, R. C., and Menenti, M. (2013). Geometric dependency of Tibetan lakes on glacial runoff. *Hydrol. Earth Syst. Sci.* 17, 4061–4077. doi:10.5194/hess-17-4061-2013

Pi, Y. N., Liu, S. Y., Li, Z. R., Xin, R. F., and Zhang, X. (2018). Remote-sensing survey and dynamic change analysis on lakes in Qinghai Province based on GF-1 and Landsat satellite data. *J. Ningxia Univ. Nat. Sci. Ed.* 39, 170–176.

Qi, J., Wang, L., Zhou, J., Song, L., Li, X. P., Zeng, T., et al. (2019). Coupled snow and frozen ground physics improves cold region hydrological simulations: An evaluation at the upper Yangtze River basin (Tibetan plateau). *JGR. Atmos.* 124, 12985–13004. doi:10.1029/2019JD031622

Riordan, B., Verbyla, D., and Mcguire, A. D. (2015). Shrinking ponds in subarctic Alaska based on 1950-2002 remotely sensed images. *J. Geophys. Res.* 111 (G4), 277–305. doi:10.1029/2005JG000150

Smith, L. C., Sheng, Y., Macdonald, G. M., and Hinzman, L. D. (2005). Disappearing arctic lakes. *Science* 308, 1429. doi:10.1126/science.1108142

Song, C. L., Wang, G. X., Mao, T. X., Dai, J. C., and Yang, D. Q. (2020). Linkage between permafrost distribution and river runoff changes across the Arctic and the Tibetan Plateau. *Sci. China Earth Sci.* 63, 292–302. doi:10.1007/s11430-018-9383-6

Song, C. Q., Huang, B., Richards, K., Ke, L. H., and Phan, V. (2014). accelerated lake expansion on the Tibetan plateau in the 2000s: Induced by glacial melting or other processes? *Water Resour. Res.* 50, 3170–3186. doi:10.1002/2013WR014724

Song, C. Q., and Sheng, Y. W. (2016). Contrasting evolution patterns between glacier-fed and non-glacier-fed lakes in the Tanggula Mountains and climate cause analysis. *Clim. Change* 135, 493–507. doi:10.1007/s10584-015-1578-9

Tang, L. Y., Duan, X. F., Kong, F. J., Zhang, F., Zheng, Y. F., Li, Z., et al. (2018). Influences of climate change on area variation of Qinghai Lake on Qinghai-Tibetan plateau since 1980s fluences of climate change on area variation of Qinghai Lake on Qinghai-Tibetan plateau since1980s. *Sci. Rep.* 8, 7331. doi:10.1038/s41598-018-25683-3

Walvoord, M. A., and Kurylyk, B. L. (2016). Hydrologic impacts of thawing permafrost-a review. *Vadose Zone J.* 15, 1–20. doi:10.2136/vzj2016.01.0010

Wang, L., Liu, H., Zhong, X. Y., Zhou, J., Zhu, L. P., Yao, T. D., et al. (2022). Domino effect of a natural cascade alpine lake system on the Third Pole. *PNAS Nexus* 1, 1–9. doi:10.1093/pnasnexus/pgac053

Wang, L., Song, C. Q., Conradt, T., Rasmy, M., and Li, X. P. (2021). Editorial: Climatic and associated cryospheric and hydrospheric changes on the third Pole. *Front. Earth Sci.* 8, 638371. doi:10.3389/feart.2020.638371

Wang, L., Zhou, J., Qi, J., Sun, L. T., Yang, K., Tian, L. D., et al. (2017). Development of a land surface model with coupled snow and frozen soil physics. *Water Resour. Res.* 53, 5085–5103. doi:10.1002/2017WR020451

Wang, X. Q., Chen, R. S., Han, C. T., Yang, Y., Liu, J. F., Liu, Z. W., et al. (2018). Changes in river discharge in typical mountain permafrost catchments, northwestern China. *Quat. Int.* 519, 32–41. doi:10.1016/j.quaint.2018.11.010

Wu, Q. B., Zhang, T. J., and Liu, Y. Z. (2010). Permafrost temperatures and thickness on the Qinghai-Tibet Plateau. *Glob. Planet. Change* 72 (1-2), 32–38. doi:10.1016/j.gloplacha.2010.03.001

Xie, C. W., William A, G., Zhao, L., Wu, T. H., and Liu, W. H. (2015). Temperature-dependent adjustments of the permafrost thermal profiles on the Qinghai-Tibet Plateau, China. *Arct. Antarct. Alp. Res.* 47, 719–728. doi:10.1657/AAAR00C-13-128

Yang, K., Ye, B. S., Zhou, D. G., Wu, B. Y., Foken, T., Qin, J., et al. (2011). Response of hydrological cycle to recent climate changes in the Tibetan Plateau. *Clim. Change* 109, 517–534. doi:10.1007/s10584-011-0099-4

Yang, R. M., Zhu, L. P., Wang, J. B., Ju, J. T., Ma, Q. F., Turner, F., et al. (2017). Spatiotemporal variations in volume of closed lakes on the Tibetan plateau and their climatic responses from 1976 to 2013. *Clim. Change* 140, 621–633. doi:10.1007/s10584-016-1877-9

Yao, F. F., Wang, J. D., Yang, K. H., Wang, C., Walter, B. A., and Crétaux, J. F. (2018). Lake storage variation on the endorheic Tibetan Plateau and its attribution to climate change since the new millennium. *Environ. Res. Lett.* 13, 064011. doi:10.1088/1748-9326/aab5d3

Yao, T. D., Thompson, L., Yang, W., Yu, W. S., Gao, Y., Guo, X. J., et al. (2012). Different glacier status with atmospheric circulations in Tibetan Plateau and surroundings. *Nat. Clim. Chang.* 2, 663–667. doi:10.1038/nclimate1580

Yoshikawa, K., and Hinzman, L. D. (2003). Shrinking thermokarst ponds and groundwater dynamics in discontinuous permafrost near Council, Alaska. *Permafr. Periglac. Process.* 14, 151–160. doi:10.1002/ppp.451

Zhang, G. Q., Bolch, T., Chen, W. F., and Crétaux, J. F. (2021). Comprehensive estimation of lake volume changes on the Tibetan Plateau during 1976–2019 and basin-wide glacier contribution. *Sci. Total Environ.* 772, 145463. doi:10.1016/j.scitotenv.2021.145463

Zhang, G. Q., Li, J. L., and Zheng, G. X. (2017b). Lake-area mapping in the Tibetan plateau: An evaluation of data and methods. *Int. J. Remote Sens.* 38, 742–772. doi:10.1080/01431161.2016.1271478

Zhang, G. Q., Yao, T. D., Chen, W. F., Zheng, G. X., Shum, C. K., Yang, K., et al. (2019). Regional differences of lake evolution across China during 1960s-2015 and its natural and anthropogenic causes. *Remote Sens. Environ.* 221, 386–404. doi:10.1016/j.rse.2018.11.038

Zhang, G. Q., Yao, T. D., Shum, C. K., Yi, S., Yang, K., Xie, H. J., et al. (2017a). Lake volume and groundwater storage variations in Tibetan Plateaus endorheic basin. *Geophys. Res. Lett.* 44, 5550–5560. doi:10.1002/2017GL073773

Zhang, G. Q., Yao, T. D., Xie, H. J., Zhang, K. X., and Zhu, F. J. (2014). Lakes' state and abundance across the Tibetan Plateau. *Chin. Sci. Bull.* 59, 3010–3021. doi:10.1007/s11434-014-0258-x

Zhang, Y. X., Xie, C. W., Wu, T. H., Zhao, L., Wu, J. C., Wu, X. D., et al. (2022). New permafrost is forming on the exposed bottom of Zonag Lake on the Qinghai-Tibet Plateau. *Sci. Total Environ.* 815, 152879. doi:10.1016/j.scitotenv.2021.152879

Zhao, L., Ding, Y. J., Liu, G. Y., Wang, S. L., and Jin, H. J. (2010). Estimates of the reserves of ground ice in permafrost regions on the Tibetan Plateau. *J. Glaciol. Geocryol.* 32, 1–9.

Zhao, L., and Sheng, Y. (2019). *Permafrost and its changes on the Qinghai-Tibetan plateau (in Chinese)*. Beijing: Science Press, 200–237.

Zhao, L., Zou, D. F., Hu, G. J., Du, E. j., Pang, Q. Q., Xiao, Y., et al. (2020). Changing climate and the permafrost environment on the qinghai-tibet (xizang) plateau. *Permafr. Periglac. Process.* 31, 396–405. doi:10.1002/ppp.2056

Zhou, J., Wang, L., Zhang, Y. S., Guo, Y. H., Li, X. P., and Liu, W. B. (2015). Exploring the water storage changes in the largest lake (Selin Co) over the Tibetan Plateau during 2003–2012 from a basin-wide hydrological modeling. *Water Resour. Res.* 51, 8060–8086. doi:10.1002/2014WR015846

Zhou, Y., Dong, J. W., Xiao, X. M., Liu, R. G., Zou, Z. H., Zhao, G. S., et al. (2019). Continuous monitoring of lake dynamics on the Mongolian Plateau using all available Landsat imagery and Google Earth Engine. *Sci. Total Environ.* 689, 366–380. doi:10.1016/j.scitotenv.2019.06.341

Zhu, X. F., Wu, T. H., Ni, J., Wu, X. D., Hu, G. J., Wang, S. J., et al. (2022). Increased extreme warming events and the differences in the observed hydrothermal responses of the active layer to these events in China's permafrost regions. *Clim. Dyn.* 59, 785–804. doi:10.1007/s00382-022-06155-x

Zou, D. F., Zhao, L., Sheng, Y., Chen, J., Hu, G. J., Wu, T. H., et al. (2017). A new map of permafrost distribution on the Tibetan Plateau. *Cryosphere* 11, 2527–2542. doi:10.5194/tc-11-2527-2017

frontiers | Frontiers in Earth Science

TYPE Original Research
PUBLISHED 18 January 2023
DOI 10.3389/feart.2022.1084540

OPEN ACCESS

EDITED BY
Xiuping Li,
Institute of Tibetan Plateau Research (CAS),
China

REVIEWED BY
Yufeng Dai,
Institute of Tibetan Plateau Research (CAS),
China
Yanbin Lei,
Institute of Tibetan Plateau Research (CAS),
China

*CORRESPONDENCE
Jifu Liu,
✉ liujifu@bnu.edu.cn

SPECIALTY SECTION
This article was submitted to Hydrosphere, a section of the journal Frontiers in Earth Science

RECEIVED 30 October 2022
ACCEPTED 28 December 2022
PUBLISHED 18 January 2023

CITATION
Wang R, Guo L, Chen B, Yang Y, Zheng H, Deng F and Liu J (2023), Spatiotemporal variations and overflow risk analysis of the Salt Lake in the Hoh Xil Region using machine learning methods.
Front. Earth Sci. 10:1084540.
doi: 10.3389/feart.2022.1084540

Spatiotemporal variations and overflow risk analysis of the Salt Lake in the Hoh Xil Region using machine learning methods

Rui Wang[1,2], Lanlan Guo[2,3], Bo Chen[1,2,3], Yuting Yang[4], Hao Zheng[1,2], Fang Deng[5] and Jifu Liu[1,2]*

[1]Key Laboratory of Environmental Change and Natural Disasters, Ministry of Education, Beijing Normal University, Beijing, China, [2]Faculty of Geographical Science, Beijing Normal University, Beijing, China, [3]State Key Laboratory of Earth Surface Processes and Resource Ecology (ESPRE), Beijing Normal University, Beijing, China, [4]Faculty of Geomatics, Lanzhou Jiaotong University, Lanzhou, China, [5]Emergency Material Reserve Center of Hainan Province, Haikou, China

Global warming is inducing dramatic changes in fluvial geomorphology and reshaping the hydrological connections between rivers and lakes. The water level and area of the Salt Lake have increased rapidly since the outburst of the Zonag Lake in the Hoh Xil region of the Qinghai–Tibet Plateau in 2011, threatening the downstream infrastructure. However, fewer studies have focused on its spatiotemporal variation and overflow risk over long time series. Here, we used three machine learning algorithms: Classification and Regression Trees (CART), Random Forest (RF), and Support Vector Machine (SVM) to extract the area of the Salt Lake for a long time series, analyzed its spatiotemporal variation from 1973 to 2021, and finally assessed the overflow risk. The Kappa coefficient (KAPPA) and the overall accuracy (OA) were used to evaluate the performance of the models. The results showed that Random Forest performs superior in lake extraction (KAPPA = 0.98, overall accuracy = 0.99), followed by Classification and Regression Trees and Support Vector Machine. normalized difference water index is the relatively important feature variable in both RF and CART. Before the outburst event, the area change of the Salt Lake was consistent with the variation in precipitation; after that, it showed a remarkable area increase (circa 350%) in all orientations, and the main direction was the southeast. Without the construction of the emergency drainage channel, the simulation result indicated that the earliest and latest times of the Salt Lake overflow event are predicted to occur in 2020 and 2031, respectively. The results of this paper not only demonstrate that RF is more suitable for water extraction and help understand the water system reorganization event.

KEYWORDS

Salt Lake, spatiotemporal variation, overflow risk, remote sensing, machine learning

1 Introduction

The evolution of lakes is essential for a better understanding of regional climate change and anthropogenic factors (Vorosmarty et al., 2000; Subin et al., 2012; Tao et al., 2015). Additionally, lakes are considered important sources of greenhouse gases in the atmosphere (Wang et al., 2021). The Qinghai–Tibet Plateau (QTP), designated by scholars as the Third Pole (Qiu, 2008; Zhang et al., 2019; Zheng et al., 2021), has a large number of lakes widely spread over it. There are almost 1,200 lakes larger than 1 km^2 on the QTP, with a total area of 46,201.62 km^2 (Zhang et al., 2021), which is more than half the overall lake area in China (Ma et al., 2011). Because of the lack of direct human intervention and their predominant distribution in endorheic watersheds, these lakes are an important indicator of climate change (Zhang et al., 2020), and they have been regarded as research hotspots in studies of global surface water changes (Donchyts et al., 2016a; Pekel et al., 2016).

Global climate change has intensified and stimulated the global water cycle (Huntington, 2006; Huntington et al., 2018; Ficklin et al., 2019). Surface water systems in polar regions have been affected by these hydrological changes (Lu et al., 2021). As a region sensitive to global warming, the QTP (the Third Pole) warmed faster than other continental areas between 1970 and 2018, with a warming rate of 0.36°C/decade in contrast to the global average of 0.19°C/decade (Zhang et al., 2021). The hydrological characteristics in the region have experienced significant changes due to the warmer climate (Chen et al., 2015). Noticeable degradation of permafrost and accelerated glacier retreat has not only influenced the security of the local infrastructure but also provided ample water for glacial lakes, causing them to rupture to form glacial lake outburst floods (GLOFs) (Yao T. et al., 2012; Ran et al., 2018; Shean et al., 2020; Veh et al., 2020; Yin et al., 2021). The imbalance between liquid (lakes and rivers) and solid (snow and glaciers) water has augmented since the 1980s, together with glacier retreat, lake water gain, and increasing runoff (Yao et al., 2022). Changes in hydrology and geomorphology caused by this imbalance affect drainage pattern reorganization and trigger the endorheic-exorheic transition, threatening the ecosystem and infrastructures (Milner et al., 2017; Liu et al., 2021). For example, In mid-September 2011, the Zonag Lake in the Hoh Xil region burst, causing a large amount of lake water to overflow, resulting in a sharp reduction in the area of the Zonag Lake, accompanied by the formation of permafrost in the following years (Liu et al., 2016; Liu W. et al., 2019; Zhang et al., 2022). A large amount of lake water flowed into the Kusai Lake, causing its water to flow into the Haiding Nor Lake (Yao X. et al., 2012). The flood waters eventually flowed into the Salt Lake, accelerating permafrost degradation (Wu and Niu, 2013). The Salt Lake is predicted to overflow by 2026 based on data from 2014 to 2015 (Yao et al., 2018). The possibility of the Salt Lake overflowing needs to be reassessed because of its faster area growth in subsequent years. The expanded Salt Lake is less than 10 km from China's key infrastructure, like the Qinghai-Tibet Highway and Railway (Lu et al., 2020), a latent outburst of the Salt Lake may cause destructive floods and further destroy these two engineering structures that link Tibet and Qinghai Province (Yao et al., 2018). Therefore, it is crucial to analyze the spatiotemporal trends of the Salt Lake and evaluate the risk of lake water overflow.

The extraction of water bodies based on remote sensing technology first appeared 40 years ago (Work and Gilmer, 1976). Since then, the methods used to detect and extract surface water from space have expanded dramatically (Huang et al., 2018; Zhang et al., 2018; Zhang et al., 2020). The basis of extracting surface water from multispectral (satellite) imagery is the distinct lower reflectance of water in infrared channels because of its strong absorption compared to other land cover types. Hence, single-band methods based on infrared channels were initially used to derive a water map (Rundquist et al., 1987; Frazier and Page, 2000). Nevertheless, these kinds of methods may cause classification errors in topographically complex environments. Afterwards, multi-band methods such as water indices were widely developed, based on the calculation of two or more bands, to distinguish between water and non-water areas (Huang et al., 2018). Normalized difference vegetation index (NDVI), which is calculated from the red band (R) and near-infrared band (NIR) to improve water features, has been used to delineate the extent of water bodies in studies (Townshend and Justice, 1986; Domenikiotis et al., 2003). While NDVI is actually a vegetation index, it can only infer water's existence through identifying above-ground biomass but does not present direct information about water (McFeeters, 1996). To rectify this problem, normalized difference water index (NDWI) was introduced to preferably highlight water bodies considering its high and low values of spectral reflectance for the green band (G) and the NIR band (McFeeters, 1996). However, the NDWI cannot efficiently delineate water bodies in urban areas. Hanqiu Xu (Xu, 2006) found that the reflectance of water in the Short-wave Infrared (SWIR) band is lower than that in the NIR band and substituted the SWIR band for the NIR band and proposed the modified NDWI index (MNDWI). One disadvantage to MNDWI is that it cannot distinguish between water and snow because the reflectance of snow in all visible and infrared channels is generally higher than that of water (Huang et al., 2018). In general, NDWI and MNDWI are widely used for water extraction, but many researchers have tried to develop new spectral indices to better monitor surface water, such as $NDWI_3$ (Ouma and Tateishi, 2006), Automated Water Extraction Index (AWEI) (Feyisa et al., 2014), Water Index (WI_{2015}) (Fisher, 2016), and so on. Although the effect of water extraction has improved, all of these spectral indices face the threshold selection problem (Huang et al., 2018; Zhang et al., 2018). When using NDWI and MNDWI indices to extract water bodies, the threshold is usually greater than 0. However, static threshold values may lead to misclassification of surface water boundaries because the threshold values usually change with satellite sensor view angle, atmospheric conditions, topography, and image acquisition quality (Jain et al., 2005; Ji et al., 2009). It is challenging and time-consuming when thresholding either the planetary-scale analysis that covers a considerable amount of water bodies or a time series of images that include the same water body.

In recent decades, machine learning (ML) algorithms have become a prevalent method of solving hydrological problems recognized in previous research (Shen et al., 2018; Bijeesh and Narasimhamurthy, 2020; Yang et al., 2022). These ML methods include K-means clustering (Lu and Weng, 2007), Iterative Self-Organizing Data Analysis Technique (ISODATA) (Zhang et al., 2017), Maximum Likelihood Classification (MLC) (Frazier and Page, 2000; Manaf et al., 2016), Support Vector Machine (SVM) (Rokni et al., 2015; Paul et al., 2018; Liu et al., 2020), Artificial Neural Network (ANN) (Isikdogan et al., 2020), Tree-based classification (Donchyts et al., 2016b; Wang et al., 2018; Li and Niu, 2022), and so on. Several studies have demonstrated that Classification and Regression Trees (CART), Random Forest (RF), and SVM have performed well in surface water extraction (Huang et al., 2015; Donchyts et al., 2016b; Liu et al., 2020). For example, Donchyts et al. (2016b) used CART to remove the mountain shadows and snow/ice to refine the surface water map. Wang et al. (2018) analyzed the long-term dynamic changes of surface water based on RF in the middle Yangtze River Basin. Liu et al. (2020) designed a river water mapping algorithm based on SVM, which can quantify the uncertainties of its result.

In this paper, three advanced machine learning methods, namely CART, RF, and SVM, were applied to construct the monitoring models for the Salt Lake using remote sensing data in the Hoh Xil Region. We prepared separate training and testing sets for the construction of the models. Models were trained using randomly and repeatedly sampled training set, while accuracy evaluation used a testing set. Models were compared by accuracy evaluation metrics, and the most stable and reliable model was selected to generate water maps for the Salt Lake. Then, the spatiotemporal variations and the overflow risk for the Salt Lake were analyzed. Here, the main objectives of this paper are: (1) to develop an appropriate model for delineating water bodies; (2) to quantify the contributions of the feature variables to the extraction of lakes using ML methods; (3) to analyze the spatiotemporal variations of the Salt Lake from 1973 to 2021; (4) to judge the risk of the Salt Lake water overflow and simulate its scenario.

2 Materials and methods

2.1 Study area

The Salt Lake is located in Zhidoi County, Qinghai Province. It lies in the northeastern section of the Hoh Xil National Nature Reserve in the hinterland of QTP (**Figure 1**). The Hoh Xil region, recorded on the World Heritage Sites, is noted by an average elevation of about 4,600 m above sea level (Lu et al., 2020). The Salt Lake originates from the Tertiary continental down-faulted basin among the Kunlun Mountains, surrounded by monadnocks comprised of Tertiary-Pliocene continental strata (Yao et al., 2018). The topographic features vary remarkably within the drainage basin, characterized by high terrain in the west and low terrain in the east. An alpine semi-arid continental climate dominates the lake region with a mean annual air temperature and precipitation of -4.72°C and 320.42 mm, respectively (Liu W. et al., 2019). Alpine meadow, alpine steppe, and alpine desert comprise this region's three major types of vegetation. Permafrost and periglacial landforms are broadly developed around this neighborhood.

The Salt Lake was primarily supplied by seasonal rivers. Until September 2011, the Salt Lake's water volume remained stable. There are three lakes northwest of the Salt Lake: Haiding Nor, Kusai Lake, and Zonag Lake (**Figure 1**), which belonged to typical endorheic lakes before the outburst of the Zonag Lake in September 2011 (Liu et al., 2016). The Zonag Lake is mainly supplied by glacial melt water through the Zonag River. The Kusai River is the main water source of the Kusai Lake. The Haiding Nor is fed by the surface runoff and intermittent stream. After the outburst, the lake water flowed eastward successively through the Kusai Lake and the Haiding Nor. Finally, it flooded into the Salt Lake, resulting in the hydraulic connection of the four lakes with newly-formed channels. The Salt Lake has experienced rapid expansion since 2011. **Figure 2** shows the considerable growth of the Salt Lake area from 9 November 2011 to 11 November 2012 through the Landsat seven imageries, severely threatening the engineering constructions.

2.2 Data preparation

2.2.1 Lake inventory dataset

As one of the most eminent satellite series, Landsat has been observing the Earth for 50 years since 1972, which provides medium-resolution images for scientific research (Wulder et al., 2022). The Landsat eight is one of the newest Landsat satellites, and its data has been widely used for surface water detection (Donchyts et al., 2016a; Pekel et al., 2016; Albarqouni et al., 2022). Herein, the Landsat eight satellite imagery was used to obtain lake occurrences for machine learning modeling *via* visual interpretation. As a planetary-scale platform for geospatial analysis, Google Earth Engine (GEE) collects a large amount of remote sensing data and powerful algorithms (Gorelick et al., 2017) and was used for the preprocessing of Landsat eight satellite images in this research. Additionally, we specially prepared separate training data and testing data from different periods and regions to effectively evaluate the machine model's ability to resist overfitting. We selected the subset of the Inner Tibetan Plateau (Inner E), where the Salt Lake is located, as the sampling location for training

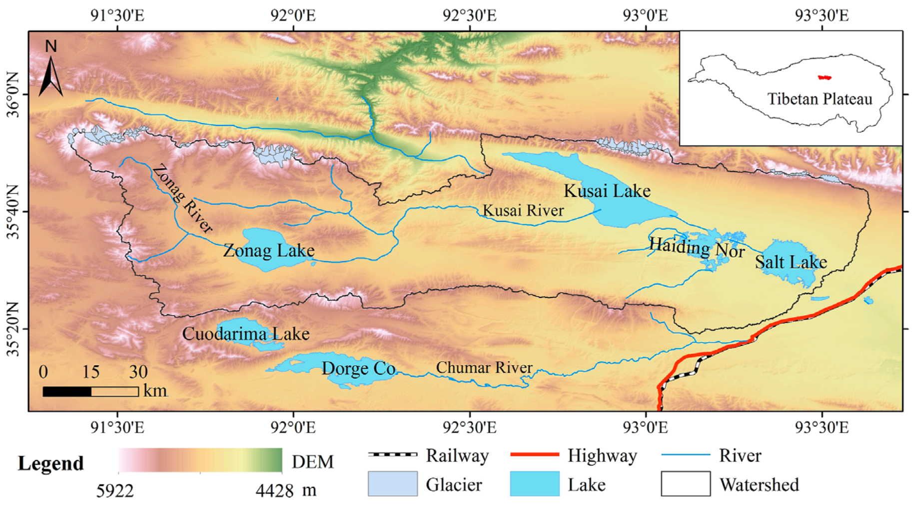

FIGURE 1
The spatial distribution of the Zonag Lake and the Salt Lake drainage basin.

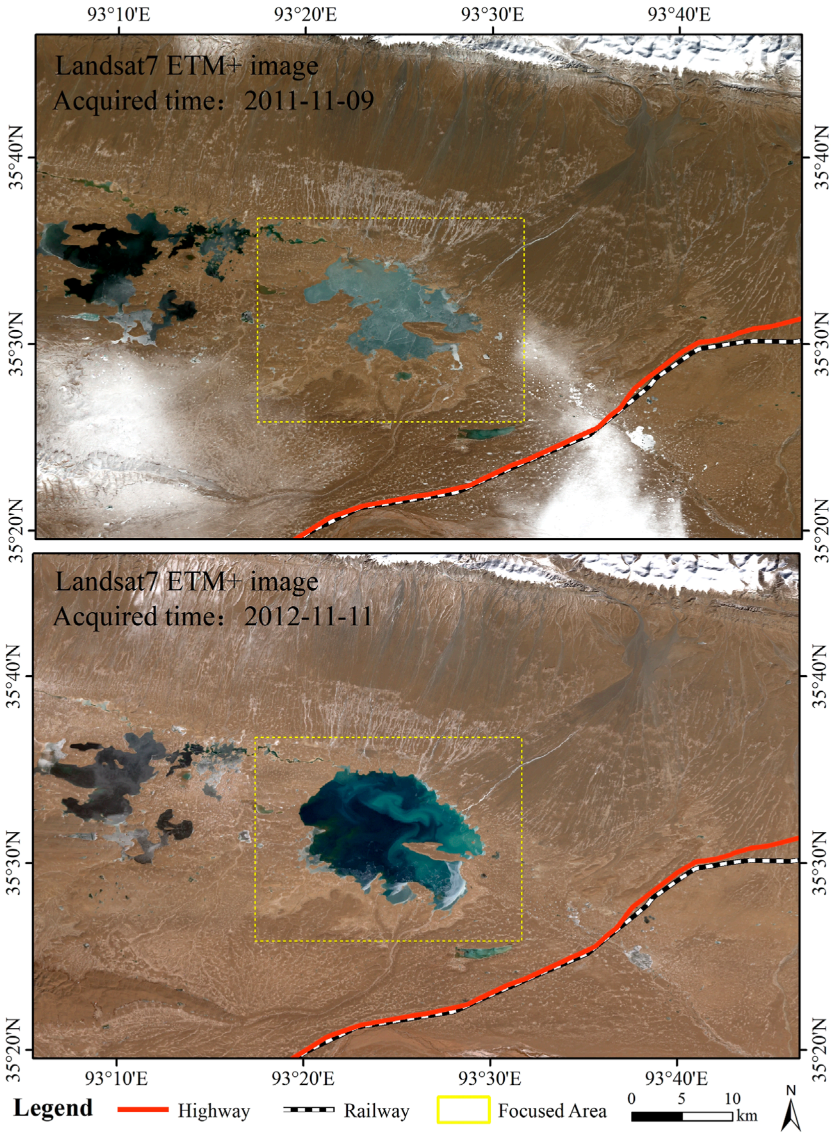

FIGURE 2
The variation of the Salt Lake (yellow box) as observed via the Landsat 7 images.

data. A detailed description of the area can be found in this paper (Wan et al., 2016). We obtained images with a cloud cover percentage of less than 5% in September and October in the Inner E from 2013 to 2021 and calculated the mean value of the images. Afterwards, the lakes were manually delineated and converted into sample points using the algorithm of GEE. Finally, the total number of lake points was 101,045. Likewise, we collected 124,580 non-lake points. For the testing data, the images from July to November 2020 in the central Tibetan Plateau were acquired for mosaicing, and then 537 lake points and 674 non-lake points were visually interpreted.

2.2.2 Feature variables

The feature variables are crucial for the training of machine learning models. The variables were selected considering the water characteristics and data availability. Image bands, water indices, and topographic variables were finally chosen, referring to the information in the existing literature (McFeeters, 1996; Frazier and Page, 2000; Ouma and Tateishi, 2006; Xu, 2006; Feyisa et al., 2014; Yin et al., 2021). A total of 13 feature variables were selected for surface water extraction—-namely, the blue band (B), G, R, NIR, SWIR$_1$, SWIR$_2$, NDWI, NDWI$_3$, MNDWI, AWEI$_{sh}$, AWEI$_{nsh}$, Slope, and Aspect. For quick reference, **Table 1** lists the water indices mentioned above. Note that Blue, Green, NIR, SWIR$_1$, and SWIR$_2$ represent top-of-atmosphere reflectance for corresponding Landsat eight bands. In this paper, the Landsat five and Landsat eight images from 1986 to 2021 (except 2011 and 2012) were acquired based on the principle of low cloud cover, and the water indices were calculated through GEE. All satellite images used in the study are listed in **Supplementary Table S1**. Without suitable data from the satellites mentioned above, we downloaded data from satellite seven in 2011 and 2012 *via* the United States Geological Survey (USGS, https://earthexplorer.usgs.gov/, accessed on 3 October 2021), whose imagery was partially missing due to the Scan Line Corrector (SLC) failure. Afterwards, the partial images were interpolated locally to obtain

TABLE 1 **Water index methods using Landsat OLI data.**

No	Index	Equation	Source
1	NDWI	(Green—NIR)/(Green + NIR)	McFeeters (1996)
2	$NDWI_3$	$(SWIR_1$—NIR)/$(SWIR_1$ + NIR)	Ouma and Tateishi (2006)
3	MNDWI	(Green—$SWIR_1$)/(Green + $SWIR_1$)	Xu (2006)
4	$AWEI_{sh}$	Blue +2.5 × Green—1.5 × (NIR + $SWIR_1$)—0.25 × $SWIR_2$	Feyisa et al. (2014)
5	$AWEI_{nsh}$	4 × (Green—$SWIR_1$)—0.25 × NIR +2.75 × $SWIR_2$	Feyisa et al. (2014)

the complete images, and the lake vector polygons were delineated through visual interpretation. In addition, we downloaded the earliest imagery covering the Salt Lake (acquired in 1973) from the USGS website and visually interpreted it. The Shuttle Radar Topography Mission (SRTM) data was employed to calculate topographic variables (i.e., Slope and Aspect).

2.3 Methods

In this study, we used three machine learning models–exactly CART, RF, and SVM–to extract water. Lake volume and the likelihood of lake water overflow were calculated using the SRTM data. The flowchart for the water extraction and analysis is presented in **Figure 3**. The main steps are described as follows.

1) Firstly, we constructed a lake inventory using GEE. This inventory included separate training and testing data. Five strata were introduced for better separation of lake samples from non-lake samples (i.e., cloud, glacier, shadow, land, snow). Regarding feature selection, SRTM DEM and satellite images were prepared to construct 13 feature variables. Then, Pearson's correlation (r) was employed to assess the correlations between these variables.
2) Secondly, the training and testing data were created according to a binary variable, where one and 0 represent the lake point and non-lake point, respectively. The training data was first shuffled and then randomly sampled at a percentage ratio of 10%. The testing data was used to measure the performance of the three models. The models were run 100 times with different sample combinations using CART, RF, and SVM, and each time, the training samples were split randomly with a ratio of 10%. After the models were trained, accuracy evaluation and model comparison was performed using KAPPA and OA.
3) Thirdly, after the model capabilities were compared, evaluation metrics for the three models were calculated, the relative importance of the feature variables for the tree-based models was obtained, and the best performing model was used to extract the water body extent.
4) Finally, we conducted a spatiotemporal analysis of the Salt Lake to assess its changes from 1973 to 2021. Climate characteristics were analyzed using temperature and precipitation data. In addition, the watershed in the basin where the Salt Lake is located was derived through hydrology analysis. The maximum boundary of the Salt Lake was simulated by iterating DEM until its water overflowed the watershed. The overflow potential of the Salt Lake was assessed by calculating the increment of the water volume.

CART, RF, and SVM were employed for lake extraction by relating the lake inventory dataset to feature variables. All the machine learning algorithms were implemented using the cloud-based platform–GEE. Hydrology analysis of the Salt Lake was performed *via* the geographic information system (GIS) software. Detailed depictions of the three machine learning models and hydrology analysis are presented as follows.

2.3.1 Classification and regression trees

CART belongs to a kind of Decision Trees (DTs) algorithm, which was first proposed by Breiman et al. (1984). CART is a supervised classification algorithm whose input data can be continuous or discrete variables. Unlike other decision tree algorithms (i.e., ID3, C4.5), CART can handle both classification and regression tasks (Quinlan, 1986; Salzberg, 1994). In the classification problem, a simple decision rule is learned from features in the data to develop a model that predicts the target variable. Compared to other machine learning techniques, the principle of CART is simple to understand, and its decision tree can be visualized. In addition, the input data for CART requires little data preparation, such as normalization, blank values removal, and dummy variables creation. In the process of dealing with classification problems, CART can also yield the importance of each input variable by the Gini index.

2.3.2 Random forest

RF is an ensemble learning approach that aggregates a large number of CART decision trees to generate a single model with a more accurate prediction (Breiman, 2001). RF has been a widely used model in both classification and regression tasks (Belgiu and Drăguţ, 2016). When handling classification tasks, these CART decision trees are generated based on different subsets of the training dataset, which contain randomly selected features and samples (i.e., bootstrap sample with replacement) (Yin et al., 2021). After RF is established, samples are first evaluated individually by each decision tree in the model and then determined by the majority of those decision trees. As a frequently used bagging model, RF is resistant to overfitting by combining ensemble learning and bootstrap sample (Guan et al., 2013). Like the decision tree algorithm, RF can also generate the importance of each feature variable by the Information Gain (IG), Information Gain Ratio (IGR), or Gini index when dealing with classification problems.

2.3.3 Support vector machine

SVM is one of the supervised learning methods widely used for classification and regression tasks (Cortes and Vapnik, 1995; Vapnik, 1999). The optimal classification hyperplane and the kernel function

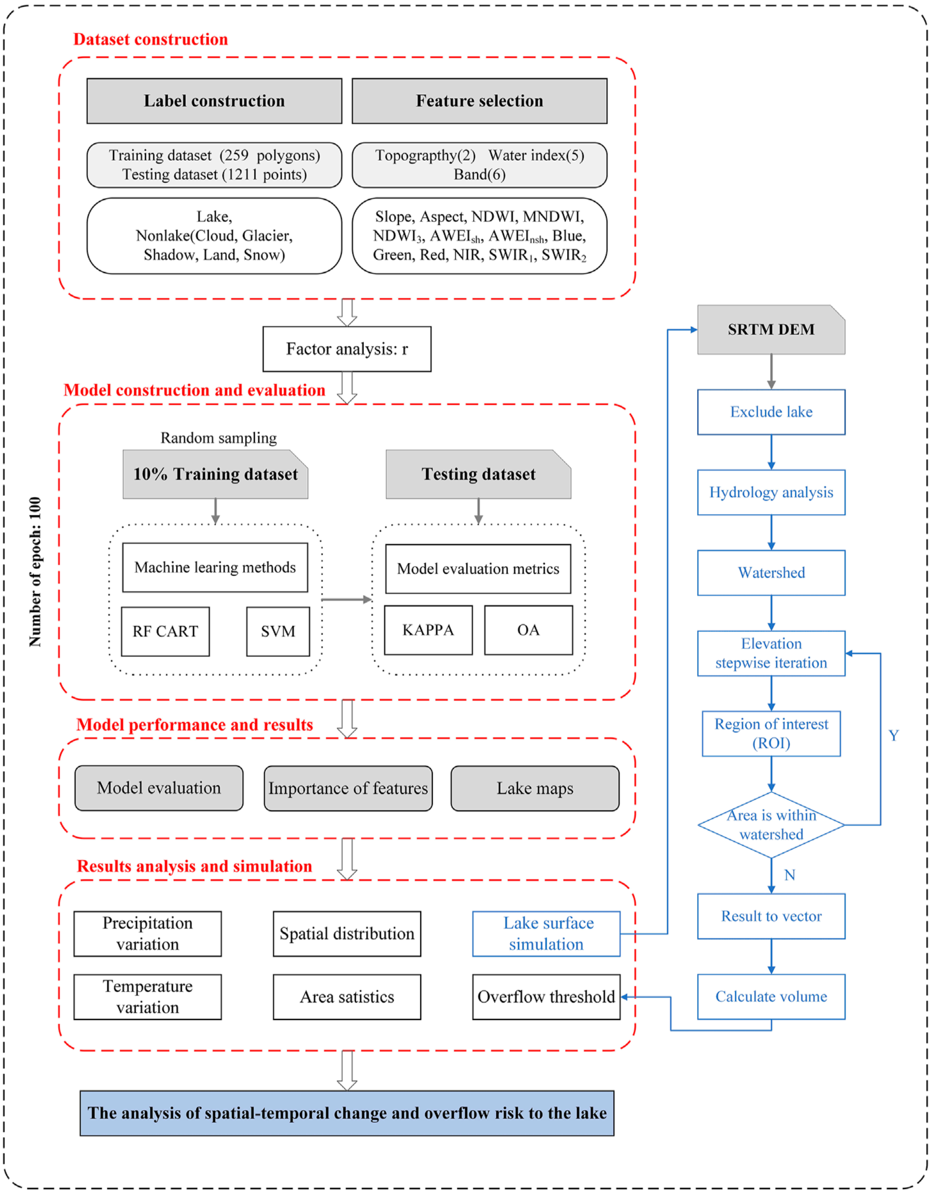

FIGURE 3
Flowchart of the proposed methodology for water extraction in this work.

are the two central principles of SVM (Yao et al., 2008). Optimizing the classification hyperplane aims to correctly differentiate between the positive and negative samples while maximizing the classification margin. The role of the kernel function is to transform the initially non-separable data into linearly separable data in a higher dimensional feature space. During the training process, SVM can ignore outliers and focus on the maximum margin by adjusting the regularization parameter (Sarp and Ozcelik, 2017). Additionally, SVM can also effectively handle datasets with more features than samples.

2.3.4 Lake water volume calculation

In order to assess the risk of Salt Lake water overflow, the SRTM DEM was employed to construct equations between the area and the volume. In the calculation formula, ΔV represents the change of lakewater volume in two periods, A_1 and A_2 represent the area of the lake in different periods, respectively, with lake area A_1 and level H_1 for the previous period and lake area A_2 and level H_2 for the later period. This method has been frequently used in estimating lake water volume (Liu et al., 2021; Lu et al., 2021).

$$\Delta V = \frac{1}{3}\left(A_1 + A_2 + \sqrt{A_1 \times A_2}\right) \times (H_2 - H_1) \qquad (1)$$

2.4 Factor importance

Factor importance refers to the relative importance of each feature variable, indicating the role of each variable in the modeling process. Measuring the relative importance of each factor is crucial to understand the modeling process. RF can be utilized to assess the relative importance of each feature variable (Yin et al., 2021), as can CART. In this paper, the relative importance of factors was obtained according to 100 rounds of RF and CART output results, accumulating the normalized results of factor importance for the modeling in each round.

2.5 Model performance and accuracy assessment

The performance of the three models was evaluated through 100 rounds of accuracy evaluation results. In this study, the extraction of the Salt Lake based on machine learning models is a classification problem with binary results of the presence and absence of lake pixels. In classification problems, a confusion matrix, which combines the actual class of the sample and the model's predicted class, is obtained to compute evaluation metrics such as commission error and omission error (Liu et al., 2020). In this paper, the Kappa coefficient (KAPPA) and the overall accuracy (OA), derived from the confusion matrix, were mainly considered indicators to measure the overall model performance (Warrens and Pratiwi, 2016; Liu et al., 2020).

3 Results

3.1 Evaluation of the models

According to the accuracy evaluation results in **Figure 4**, the RF model had the best outcome in terms of KAPPA and OA, followed by CART and SVM. The mean KAPPA for the 100-round RF model was 0.9876, and the mean OA was 0.9939. The higher values of the two evaluation indicators mean the better accuracy of the model. As shown in **Figure 4**, the values of the evaluation indicators of the three models were all higher than 0.85, indicating that these models had good performance in water extraction. The distribution of the two evaluation indicators for the RF model was very concentrated, which proved that it was very stable in 100 rounds of modeling. Although the results of the two evaluation indicators showed good accuracy for the CART model, the distribution of the results was not concentrated, indicating that it was not as stable as the RF model. The SVM model had relatively low accuracy and its accuracy distribution approximated a normal distribution. After the comprehensive evaluation, the RF model was selected for the extraction of the Salt Lake.

3.2 Factor contribution analysis

In this paper, the Pearson correlation coefficient was calculated between the feature variables to check the multicollinearity of the data (**Figure 5**). The result shows that there was strong collinearity between the feature variables (absolute value greater than 0.7). For example, NDWI and MNDWI, which are widely employed in water body extraction, had a correlation coefficient value of 0.84, indicating that these two water indices could be used as substitutes for each other.

In the factor contribution analysis experiment, if there are strongly correlated feature variables, any one of them can be used as an excellent feature to participate in the construction of the model. Once one of these correlated feature variables is selected, the mean decrease impurity is occupied by this variable, resulting in the reduction of the importance of other feature variables. In order to solve this problem, we randomly sampled the training dataset to set up the machine learning models. In addition, we also accumulated the results of the machine learning models for 100 experiments because the results of a single experiment cannot indicate whether the experimental results are reliable. According to the relative importance analysis results in **Figure 6**, NDWI was considered the most important feature variable

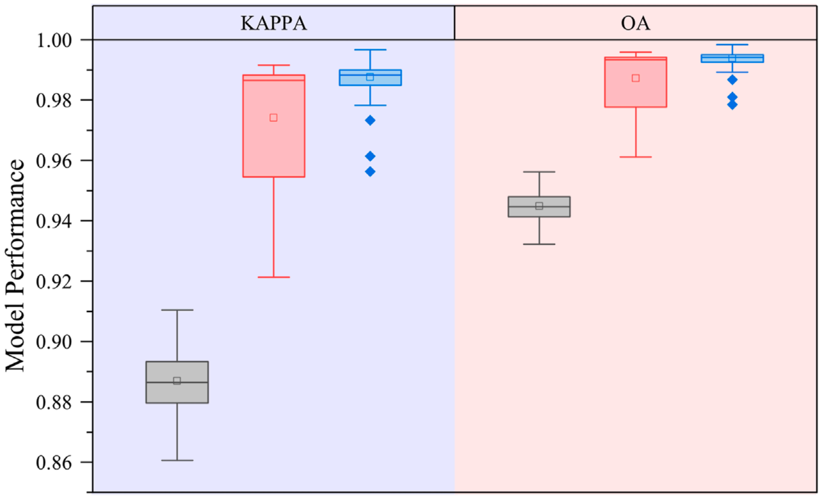

	SVM	CART	RF	SVM	CART	RF
Median	0.8865	0.9866	0.9883	0.9447	0.9934	0.9942
Mean	0.8870	0.9742	0.9876	0.9449	0.9873	0.9939

FIGURE 4
Evaluation metrics regarding the performances of different models.

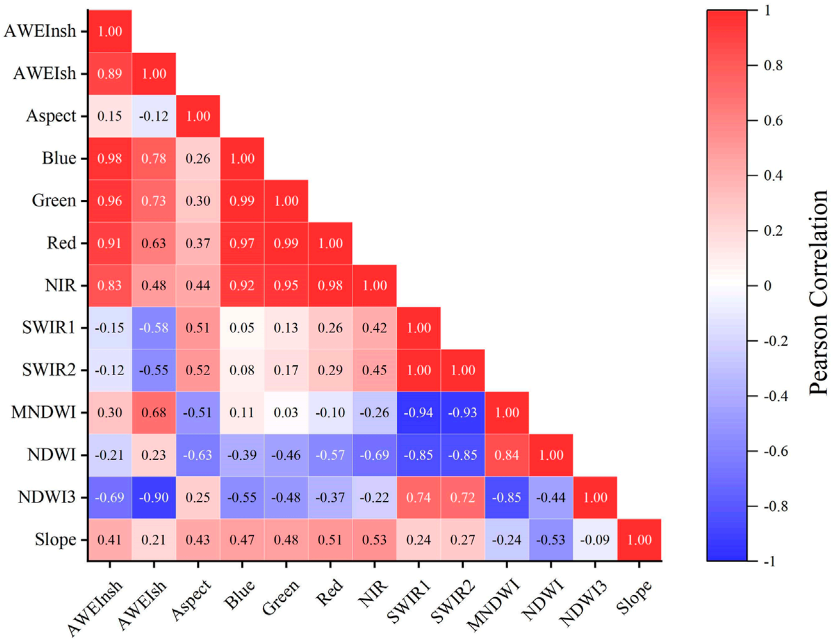

FIGURE 5
Pearson's correlations between feature variables.

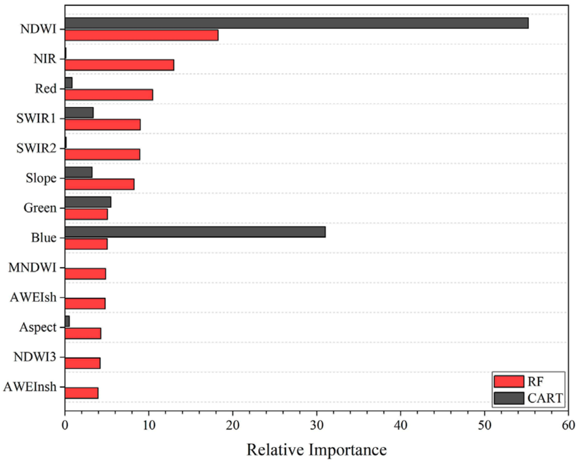

FIGURE 6
The relative importance of each feature variable from RF and CART.

in the lake extraction by RF and CART models, while AWEI$_{nsh}$ seemed to be the least important feature variable.

3.3 Spatiotemporal variations of the Salt Lake

The long-term evolution of the Salt Lake between 1973 and 2021 is shown in **Figure 7**. During the period 1973–1987, the Salt Lake area showed an enormous 53% reduction, from 41.09 in 1973 to 19.30 km^2 in 1987. Until 1989, the Salt Lake area went back to its previous size. Between 1989 and 1995, the Salt Lake area declined in a linear fashion, almost to its area value in 1989. Slow growth in the Salt Lake area occurred from 1995 to 2010. After the outburst of the Zonag Lake in September 2011, the Salt Lake area reached 73.32 km^2 in November 2011, showing a 57% area increase compared to the 46.54 km^2 of the Salt Lake area in November 2010. From 2010 to 2019, the Salt Lake area experienced a dramatic expansion, then a steady increase, and finally a rapid expansion, and eventually, it reached a maximum area value of 209.43 km^2 in 2019, showing an astonishing 350% area increase. The most recent 3 years (2019–2021) were relatively stable periods with a slight decline, possibly due to the construction of the artificial drainage channel.

Temperature and precipitation data from the nearest China meteorological station (Wudaoliang) to the Salt Lake are shown in **Figure 8**. Temperature observations from 1980 to 2017 revealed a warming rate of 0.05°C/a (p <0.05), with annual average temperatures almost always higher than the multi-year average temperature since 1998 (**Figure 8A**). Precipitation also showed an overall increasing trend (p <0.05), especially after 1996 (**Figure 8B**). After the collapse of the Zonag Lake (circa 2011), the Salt Lake, as a tailwater lake, was heavily recharged by the upstream lakes. Therefore, the response of the Salt Lake to climate was mainly focused on the period from 1986 to 2010. Overall, the fluctuation of precipitation matched the change in the Salt Lake area well, compared with the temperature (**Figure 9**). For example, high precipitation in 1989 and 2008–2010 was associated with high lake areas, whereas low precipitation from 1990 to 1995 coincided with small lake areas. Pearson's correlation analysis was conducted between the lake area variable and the precipitation variable from 1986 to 2010. A correlation coefficient value of 0.603 (p <0.01) indicated a significant correlation between the variables.

Maps of the Salt Lake in 1973 and 2010 were selected as reference data before and after the Zonag Lake outburst, and the area changes of Salt Lake in different directions were analyzed based on the geometric

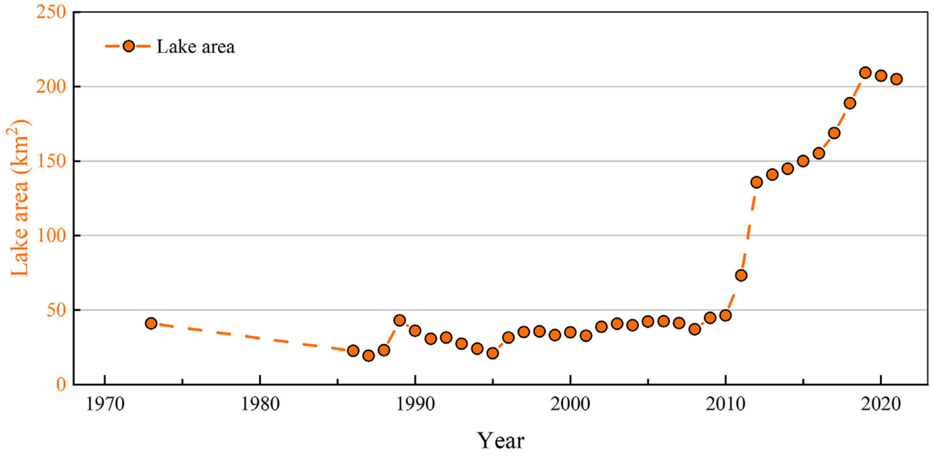

FIGURE 7
Changes in the Salt Lake area from 1973 to 2021.

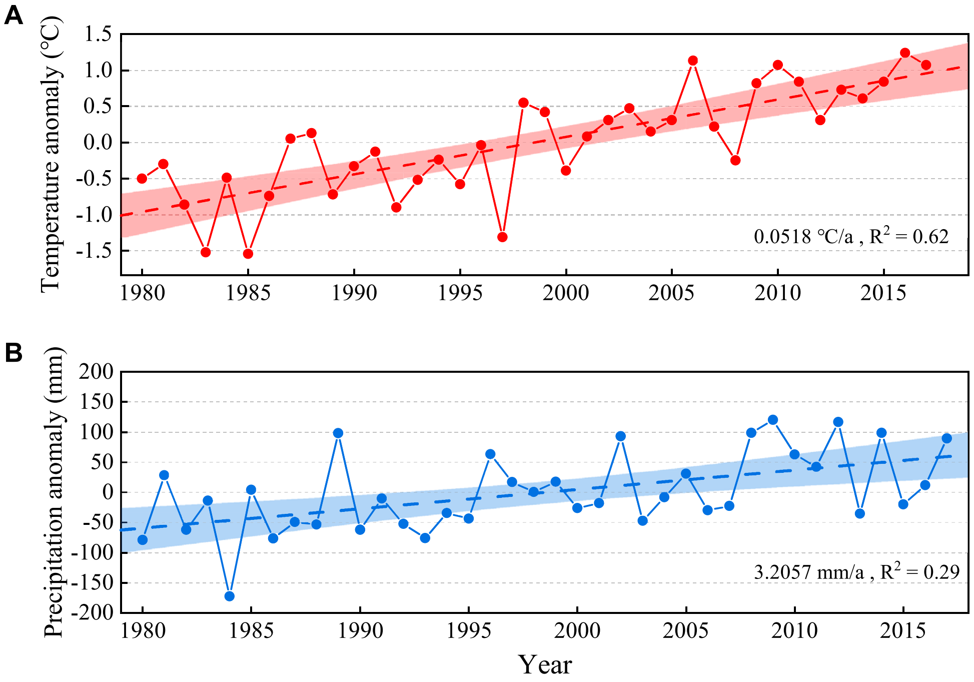

FIGURE 8
Climate variations from 1980 to 2017: **(A)** time series of annual average temperature change and **(B)** time series of annual precipitation change.

center of these reference maps (**Figure 10**). From 1973 to 2010, the Salt Lake area increased from 41.09 km^2 to 46.54 km^2, and the main directions of area expansion were the east, south, north, and northwest, but the area growth did not exceed 1 km^2. Between 2010 and 2012, the Salt Lake, affected by the lake overflow, expanded in all directions by more than 5 km^2, of which the main expansion direction was the southeast, and the expansion area reached 17.80 km^2, followed by the southwest, west, and south, with an expansion area of all more than 10 km^2. During the period from 2012 to 2019, the Salt Lake area reached a maximum value of 209.43 km^2 and expanded in all directions, with the main orientations including southeast, south, and west. In the last 2 years (2019–2021), the area of the Salt Lake decreased slightly in all directions, with an area of no more than 1 km^2.

3.4 Scenario of water overflow from the Salt Lake

The overflow condition of the Salt Lake is that its boundary crosses the watershed between the Salt Lake and Qingshui Lake, which can be simulated through the iteration of the lake water level. The water

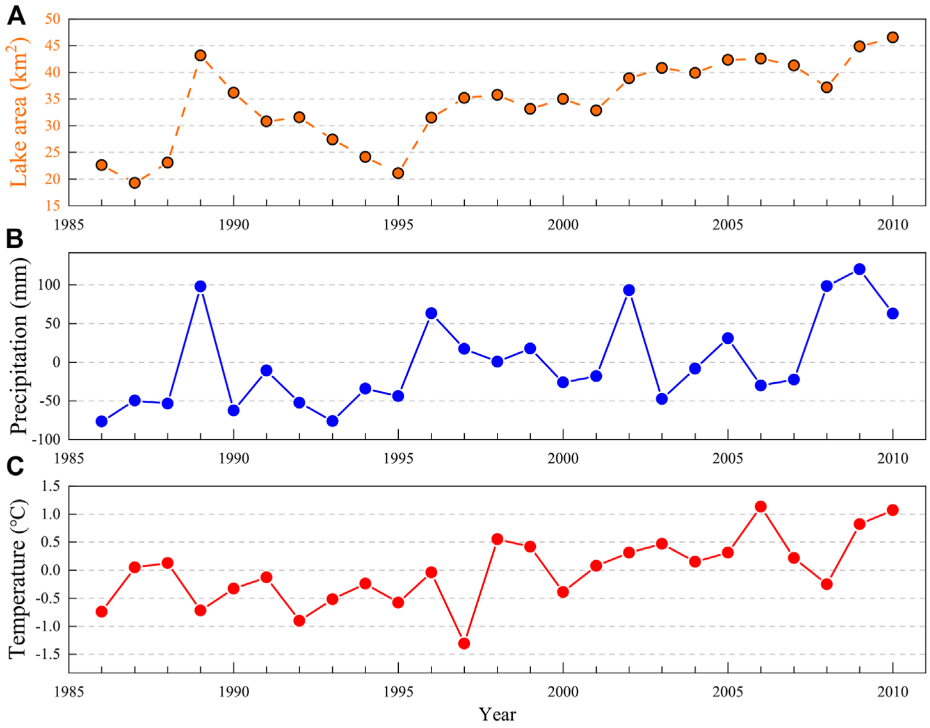

FIGURE 9
Changes in lake area and climate fluctuations from 1986 to 2010: **(A)** lake area, **(B)** precipitation and **(C)** temperature.

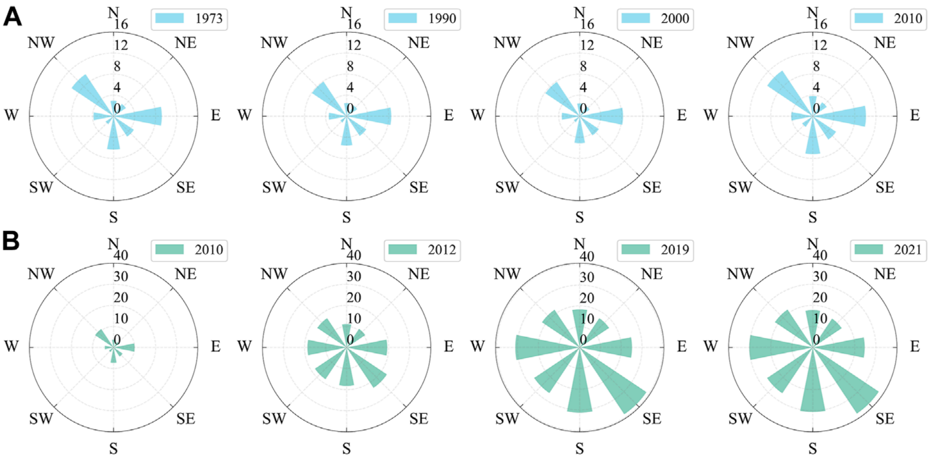

FIGURE 10
Changes in different directions of the Salt Lake before **(A)** and after **(B)** the outburst of the Zonag Lake.

level corresponding to the inundation area was calculated as the mean value of the SRTM DEM grids intersecting the lake shoreline. To minimize the uncertainty of SRTM DEM, three times the Normalized Median Absolute Deviation (NMAD) was employed to filter out outliers (Höhle and Höhle, 2009; Leys et al., 2013). **Figure 11** shows the maximum expansion area of the Salt Lake when it meets the overflow condition. The area and elevation of the overflowed Salt Lake-simulated were 220.09 km^2 and 4,471.42 m, respectively. According to the lake area time series in **Figure 7**, the lake area changes from 2012 to 2019 were selected to assess the risk of Salt Lake water overflow. In the case of slow growth in the area of the Salt Lake (from 2012 to 2016), the water level continued to rise at a vertical rate of 0.84 m/a (0.12 billion m^3/a), and the water level is predicted to reach its watershed overflow elevation of 4,471.4 m by 2031 (assuming the 0.12 billion m^3/a rate keeps the same). From 2016 to 2019, the water level of the Salt Lake rose rapidly at a rate of 2.96 m/a (0.54 billion m^3/a), and the Salt Lake is projected to reach its maximum water capacity in 2020. Fortunately, the emergency drainage channel between the Salt Lake and Qingshui

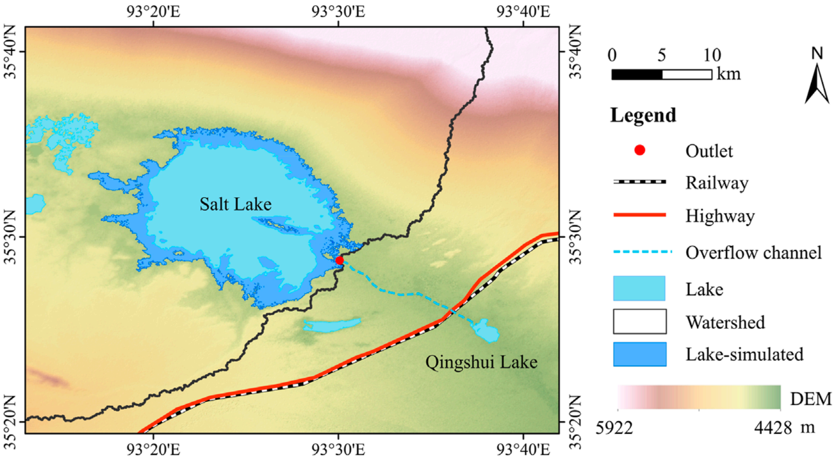

FIGURE 11
The maximum expansion area of the Salt Lake before overflow.

Lake was completed in 2019 (**Figure 11**) (Lu et al., 2021). Since then, this artificial channel has been connected with the tributary of the Yangtze River, resulting in the endorheic-exorheic transition of the Salt Lake catchment.

4 Discussion

4.1 Comparison between the machine learning methods

The three applied methods, CART, RF, and SVM, are very popular machine learning methods in the field of earth sciences (Huang et al., 2015; Donchyts et al., 2016b; Liu et al., 2020). In this paper, the results showed that tree-based algorithms, especially the RF model, outperformed the SVM model in terms of KAPPA and OA, and the excellent capability of the RF model has been facilitated by other studies (Huang et al., 2015; Belgiu and Drăguț, 2016). Compared with the SVM model, tree-based models (i.e., CART and RF) can directly output the importance order of feature variables, which can help researchers explore the relationship between feature variables and target variables. The difference between SVM and tree-based models is mainly the basic framework. SVM is developed from statistical learning theory, with structural risk minimization as its principle (Chapelle et al., 1999). SVM is appropriate for image classification with a small number of training samples and a high-dimensional feature space (Melgani and Bruzzone, 2004). Tree-based algorithms, one of the most frequently used supervised classification methods (Rokach and Maimon, 2005; Belgiu and Drăguț, 2016), have multiple interior nodes and leaf nodes, representing the feature and target variables, respectively (Huang et al., 2015).

In this study, both the CART algorithm and RF algorithm had high accuracy and output the importance ranking of feature variables. There are two differences between the two algorithms: one is that the results of the RF algorithm were more robust, and the other is that the relative importance results of the RF algorithm were more reasonable without the bias of feature variables. This is because the RF method is based on the idea of ensemble learning, integrates multiple decision trees to construct a model, and has two aspects of randomness. In comparison to a single decision tree, it can improve prediction accuracy (Ho, 1998). Taking multiple aspects of the model into consideration, RF is recommended for the extraction of lakes in the Hoh Xil region.

4.2 Implications of the endorheic-exorheic transition

Since the lake outburst event in 2011, the four lakes (i.e., the Salt Lake, Haiding Nor, Kusai Lake, and Zonag Lake) have been hydrologically connected with newly-formed channels (Liu W. et al., 2019). Although these reorganization events occurred in the endorheic basins, the results showed that the significant increase in the Salt Lake water volume could overflow to the adjacent exorheic basin, seriously threatening the engineering construction. In the worst-case scenario, the outburst flood from Salt Lake can destroy engineering infrastructure within 6 hours (Liu et al., 2021). In the end, to reduce the impact of the potential Salt Lake outburst, the local government constructed a drainage channel to divert the lake water into the Qingshui River, which also led to the endorheic-exorheic transition (Lu et al., 2021).

The construction of the emergency drainage channel can reduce the potential damage of an outburst flood, and the impact of the endorheic-exorheic transition requires special attention. The highly mineralized lake water is continuously discharged into the Qingshui River, which not only influences the stability of the permafrost around the water system but also impacts the northernmost source of the Yangtze River water quality (Liu M. et al., 2019; Liu et al., 2021; Lu et al., 2021). In addition, studies have shown that the total area of lakes on the Inner Tibetan Plateau will continue to expand from 2016 to 2035 (Yang et al., 2018; Zhang et al., 2020). Therefore, it is indispensable to monitor whether the drainage of the artificial channel is sufficient to cope with the large amount of water from the Salt Lake. Further, it is necessary to consider whether there are similar cases in other basins.

4.3 Limitations and future works

In this work, three machine learning models were implemented 1,000 times to compare performance using different subsets of the training dataset. Finally, the best performing random forest model was trained using 70% of the entire training data and applied to the long-term lake extraction. The current research also has some limitations. Our study area is located on the QTP, where there is less human activity. For this reason, the training samples were selected on the QTP, and the machine learning model was trained using these samples. Therefore, the results of the relative importance of features may not be suitable for lakes in urban areas.

The QTP is distributed in numerous lakes, which are an important part of the Asian Water Tower (Zhang et al., 2021; Yao et al., 2022). These lakes are subject to little human intervention and respond exceptionally quickly to climate change (Zhang et al., 2020). Abnormal climate events such as El Niño and La Niña significantly impact the global climate. However, the response of lakes on the QTP to abnormal climate events is less involved (Lei et al., 2019). In addition, water system reorganization events are expected to increase by 20 from 2019 to 2030 (Liu et al., 2021), and these accelerated evolutions and impacts should be continuously monitored and confirmed in future work. Currently, research on lake area changes on the QTP mainly focuses on inter-annual changes (Zhang et al., 2020; 2021). With the launch of remote sensing satellites in the future, the intra-annual variations of the lake should be studied to understand its response to climate change better.

5 Conclusion

In this study, we used machine learning models to extract the Salt Lake area in the Hoh Xil region. Meanwhile, based on the long-term lake area data, we analyzed its response to meteorological data and simulated the Salt Lake water overflow scenario. The conclusions are as follows.

1) This study used KAPPA and OA to evaluate model performance and found out that RF is the best performing model compared to CART and SVM. The mean accuracy of KAPPA and OA for the 100-round RF model were 0.9876 and 0.9939, respectively.
2) There was a strong correlation between most water indices. Through the factor contribution analysis, it was found that NDWI was the most important feature selected by RF and CART for the area extraction of the Salt Lake.
3) Before the Zonag Lake outburst, the area change of the Salt Lake was consistent with the variation of precipitation, and the correlation coefficient value reached 0.603. After that, the area of the Salt Lake expanded at an alarming rate in all orientations, and the primary expansion directions were southeast, west, southwest, and south.
4) The area of the overflowed Salt Lake-simulated was 220.09 km^2. The simulation result indicated that the earliest and latest times for the Salt Lake to overflow were 2020 and 2031, respectively.

The results of this paper improve the understanding of the impact of water system reorganization on downstream lakes. Continued research in this region is required due to the endorheic-exorheic transition in the future. In addition, the intra-annual variation of the Salt Lake needs to be considered, and the reasons for the variation need to be quantitatively analyzed. Herein, we suggest that other areas of the QTP with water system reorganization need to be studied to gain a better understanding and reduce the disasters caused by lake outbursts.

Data availability statement

The raw data supporting the conclusion of this article will be made available by the authors, without undue reservation.

Author contributions

RW, LG and JL contributed to conception and design of the study. RW, BC and YY processed and analyzed data. RW wrote the first draft of the manuscript. HZ and FD wrote sections of the manuscript. All authors have read and agreed to the published version of the manuscript.

Funding

This research was funded by the Second Tibetan Plateau Scientific Expedition and Research Program (STEP, Grant No. 2019QZKK0906).

Acknowledgments

We would like to thank the editor and reviewers for their suggestions.

Conflict of interest

The authors declare that the research was conducted in the absence of any commercial or financial relationships that could be construed as a potential conflict of interest.

Publisher's note

Supplementary material

The Supplementary Material for this article can be found online at: https://www.frontiersin.org/articles/10.3389/feart.2022.1084540/full#supplementary-material

References

Albarqouni, M. M. Y., Yagmur, N., Bektas Balcik, F., and Sekertekin, A. (2022). Assessment of spatio-temporal changes in water surface extents and lake surface temperatures using google earth engine for lakes region, türkiye. *Int. J. Geo-Inf.* 11, 407. doi:10.3390/ijgi11070407

Belgiu, M., and Drăguţ, L. (2016). Random forest in remote sensing: A review of applications and future directions. *Isprs J. Photogramm.* 114, 24–31. doi:10.1016/j.isprsjprs.2016.01.011

Bijeesh, T. V., and Narasimhamurthy, K. N. (2020). Surface water detection and delineation using remote sensing images: A review of methods and algorithms. *Sustain. Water Resour. Manag.* 6, 68. doi:10.1007/s40899-020-00425-4

Breiman, L., Friedman, J. H., Olshen, R. A., and Stone, C. J. (1984). Classification and regression trees (CART). *Biometrics* 40, 358.

Breiman, L. (2001). Random forests. *Mach. Learn.* 45, 5–32. doi:10.1023/a:1010933404324

Chapelle, O., Haffner, P., and Vapnik, V. (1999). Support vector machines for histogram-based image classification. *IEEE Trans. Neural Netw.* 10, 1055–1064. doi:10.1109/72.788646

Chen, D., Xu, B., Yao, T., Guo, Z., Cui, P., Chen, F., et al. (2015). Assessment of past, present and future environmental changes on the Tibetan Plateau. *Chin. Sci. Bull.* 60, 3025–3035. doi:10.1360/N972014-01370

Cortes, C., and Vapnik, V. (1995). Support-vector networks. *Mach. Learn.* 20, 273–297. doi:10.1007/BF00994018

Domenikiotis, C., Loukas, A., and Dalezios, N. R. (2003). The use of NOAA/AVHRR satellite data for monitoring and assessment of forest fires and floods. *Nat. Hazard Earth Syst.* 3, 115–128. doi:10.5194/nhess-3-115-2003

Donchyts, G., Baart, F., Winsemius, H., Gorelick, N., Kwadijk, J., and van de Giesen, N. (2016a). Earth's surface water change over the past 30 years. *Nat. Clim. Change* 6, 810–813. doi:10.1038/nclimate3111

Donchyts, G., Schellekens, J., Winsemius, H., Eisemann, E., and van de Giesen, N. (2016b). A 30 m resolution surface water mask including estimation of positional and thematic differences using landsat 8, SRTM and OpenStreetMap: A case study in the murray-darling basin, Australia. *Remote Sens-Basel* 8, 386. doi:10.3390/rs8050386

Feyisa, G. L., Meilby, H., Fensholt, R., and Proud, S. R. (2014). Automated water extraction index: A new technique for surface water mapping using landsat imagery. *Remote Sens. Environ.* 140, 23–35. doi:10.1016/j.rse.2013.08.029

Ficklin, D. L., Abatzoglou, J. T., and Novick, K. A. (2019). A new perspective on terrestrial hydrologic intensity that incorporates atmospheric water demand. *Geophys Res. Lett.* 46, 8114–8124. doi:10.1029/2019GL084015

Fisher, A. (2016). Comparing Landsat water index methods for automated water classification in eastern Australia. *Remote Sens. Environ.* 175, 167–182. doi:10.1016/j.rse.2015.12.055

Frazier, P. S., and Page, K. J. (2000). Water body detection and delineation with landsat TM data. *Photogramm. Eng.* 66, 1461–1467.

Gorelick, N., Hancher, M., Dixon, M., Ilyushchenko, S., Thau, D., and Moore, R. (2017). Google earth engine: Planetary-scale geospatial analysis for everyone. *Remote Sens. Environ.* 202, 18–27. doi:10.1016/j.rse.2017.06.031

Guan, H., Li, J., Chapman, M., Deng, F., Ji, Z., and Yang, X. (2013). Integration of orthoimagery and lidar data for object-based urban thematic mapping using random forests. *Int. J. Remote Sens.* 34, 5166–5186. doi:10.1080/01431161.2013.788261

Ho, T. K. (1998). The random subspace method for constructing decision forests. *IEEE T Pattern Anal.* 20, 832–844. doi:10.1109/34.709601

Höhle, J., and Höhle, M. (2009). Accuracy assessment of digital elevation models by means of robust statistical methods. *Isprs J. Photogramm.* 64, 398–406. doi:10.1016/j.isprsjprs.2009.02.003

Huang, X., Xie, C., Fang, X., and Zhang, L. (2015). Combining pixel- and object-based machine learning for identification of water-body types from urban high-resolution remote-sensing imagery. *IEEE J-Stars* 8, 2097–2110. doi:10.1109/JSTARS.2015.2420713

Huang, C., Chen, Y., Zhang, S., and Wu, J. (2018). Detecting, extracting, and monitoring surface water from space using optical sensors: A review. *Rev. Geophys.* 56, 333–360. doi:10.1029/2018RG000598

Huntington, T. G., Weiskel, P. K., Wolock, D. M., and McCabe, G. J. (2018). A new indicator framework for quantifying the intensity of the terrestrial water cycle. *J. Hydrol.* 559, 361–372. doi:10.1016/j.jhydrol.2018.02.048

Huntington, T. G. (2006). Evidence for intensification of the global water cycle: Review and synthesis. *J. Hydrol.* 319, 83–95. doi:10.1016/j.jhydrol.2005.07.003

Isikdogan, L. F., Bovik, A., and Passalacqua, P. (2020). Seeing through the clouds with DeepWaterMap. *IEEE Geosci. Remote S* 17, 1662–1666. doi:10.1109/LGRS.2019.2953261

Jain, S. K., Singh, R. D., Jain, M. K., and Lohani, A. K. (2005). Delineation of flood-prone areas using remote sensing techniques. *Water Resour. Manag.* 19, 333–347. doi:10.1007/s11269-005-3281-5

Ji, L., Zhang, L., and Wylie, B. K. (2009). Analysis of dynamic thresholds for the normalized difference water index. *Photogramm. Eng. Rem. S* 75, 1307–1317. doi:10.14358/PERS.75.11.1307

Lei, Y., Zhu, Y., Wang, B., Yao, T., Yang, K., Zhang, X., et al. (2019). Extreme Lake level changes on the Tibetan plateau associated with the 2015/2016 El Niño. *Geophys Res. Lett.* 46, 5889–5898. doi:10.1029/2019GL081946

Leys, C., Ley, C., Klein, O., Bernard, P., and Licata, L. (2013). Detecting outliers: Do not use standard deviation around the mean, use absolute deviation around the median. *J. Exp. Soc. Psychol.* 49, 764–766. doi:10.1016/j.jesp.2013.03.013

Li, Y., and Niu, Z. (2022). Systematic method for mapping fine-resolution water cover types in China based on time series Sentinel-1 and 2 images. *Int. J. Appl. Earth Obs.* 106, 102656. doi:10.1016/j.jag.2021.102656

Liu, B., Li, L., Du, Y., Liang, T., Duan, S., Hou, F., et al. (2016). Causes of the outburst of Zonag Lake in Hoh Xil, Tibetan plateau, and its impact on surrounding environment. *J. Glaciol. Geocryol.* 38, 305. doi:10.7522/j.issn.1000-0240.2016.0033

Liu, M., Zhao, W., Wang, Q., Huang, S., and Shi, K. (2019). Compatibility issues with irregular current injection islanding detection methods and a solution. *Energies* 12, 1467. doi:10.3390/en12081467

Liu, W., Xie, C., Zhao, L., Wu, T., Wang, W., Zhang, Y., et al. (2019). Dynamic changes in lakes in the Hoh Xil region before and after the 2011 outburst of Zonag Lake. *J. Mt. Sci-Engl* 16, 1098–1110. doi:10.1007/s11629-018-5085-0

Liu, Q., Huang, C., Shi, Z., and Zhang, S. (2020). Probabilistic river water mapping from landsat-8 using the support vector machine method. *Remote Sens-Basel* 12, 1374. doi:10.3390/rs12091374

Liu, K., Ke, L., Wang, J., Jiang, L., Richards, K. S., Sheng, Y., et al. (2021). Ongoing drainage reorganization driven by rapid lake growths on the Tibetan plateau. *Geophys Res. Lett.* 48, e2021GL095795. doi:10.1029/2021GL095795

Lu, D., and Weng, Q. (2007). A survey of image classification methods and techniques for improving classification performance. *Int. J. Remote Sens.* 28, 823–870. doi:10.1080/01431160600746456

Lu, P., Han, J., Li, Z., Xu, R., Li, R., Hao, T., et al. (2020). Lake outburst accelerated permafrost degradation on Qinghai-Tibet Plateau. *Remote Sens. Environ.* 249, 112011. doi:10.1016/j.rse.2020.112011

Lu, S., Jin, J., Zhou, J., Li, X., Ju, J., Li, M., et al. (2021). Drainage basin reorganization and endorheic-exorheic transition triggered by climate change and human intervention. *Glob. Planet Change* 201, 103494. doi:10.1016/j.gloplacha.2021.103494

Ma, R., Yang, G., Duan, H., Jiang, J., Wang, S., Feng, X., et al. (2011). China's lakes at present: Number, area and spatial distribution. *Sci. China Earth Sci.* 54, 283–289. doi:10.1007/s11430-010-4052-6

Manaf, S. A., Mustapha, N., Sulaiman, M. N., Husin, N. A., and Hamid, M. R. A. (2016). Comparison of classification techniques on fused optical and SAR images for shoreline extraction: A case study at northeast coast of peninsular Malaysia. *J. Comput. Sci.* 12, 399–411. doi:10.3844/jcssp.2016.399.411

McFeeters, S. K. (1996). The use of the Normalized Difference Water Index (NDWI) in the delineation of open water features. *Int. J. Remote Sens.* 17, 1425–1432. doi:10.1080/01431169608948714

Melgani, F., and Bruzzone, L. (2004). Classification of hyperspectral remote sensing images with support vector machines. *IEEE T Geosci. Remote* 42, 1778–1790. doi:10.1109/TGRS.2004.831865

Milner, A. M., Khamis, K., Battin, T. J., Brittain, J. E., Barrand, N. E., Füreder, L., et al. (2017). Glacier shrinkage driving global changes in downstream systems. *Proc. Natl. Acad. Sci.* 114, 9770–9778. doi:10.1073/pnas.1619807114

Ouma, Y. O., and Tateishi, R. (2006). A water index for rapid mapping of shoreline changes of five East African Rift Valley lakes: An empirical analysis using Landsat TM and ETM+ data. *Int. J. Remote Sens.* 27, 3153–3181. doi:10.1080/01431160500309934

Paul, A., Tripathi, D., and Dutta, D. (2018). Application and comparison of advanced supervised classifiers in extraction of water bodies from remote sensing images. *Sustain. Water Resour. Manag.* 4, 905–919. doi:10.1007/s40899-017-0184-6

Pekel, J.-F., Cottam, A., Gorelick, N., and Belward, A. S. (2016). High-resolution mapping of global surface water and its long-term changes. *Nature* 540, 418–422. doi:10.1038/nature20584

Qiu, J. (2008). China: The third pole. *Nature* 454, 393–396. doi:10.1038/454393a

Quinlan, J. R. (1986). Induction of decision trees. *Mach. Learn.* 1, 81–106. doi:10.1007/BF00116251

Ran, Y., Li, X., and Cheng, G. (2018). Climate warming over the past half century has led to thermal degradation of permafrost on the Qinghai–Tibet Plateau. *Cryosphere* 12, 595–608. doi:10.5194/tc-12-595-2018

Rokach, L., and Maimon, O. (2005). Top-down induction of decision trees classifiers - a survey. *IEEE Trans. Syst. Man, Cybern. Part C Appl. Rev.* 35, 476–487. doi:10.1109/TSMCC.2004.843247

Rokni, K., Ahmad, A., Solaimani, K., and Hazini, S. (2015). A new approach for surface water change detection: Integration of pixel level image fusion and image classification techniques. *Int. J. Appl. Earth Obs.* 34, 226–234. doi:10.1016/j.jag.2014.08.014

Rundquist, D. C., Lawson, M. P., Queen, L. P., and Cerveny, R. S. (1987). The relationship between summer-season rainfall events and lake-surface AREA[1]. *JAWRA J. Am. Water Resour. Assoc.* 23, 493–508. doi:10.1111/j.1752-1688.1987.tb00828.x

Salzberg, S. L. (1994). C4.5: Programs for machine learning by J. Ross quinlan. *Mach. Learn.* 16, 235–240. doi:10.1007/BF00993309

Sarp, G., and Ozcelik, M. (2017). Water body extraction and change detection using time series: A case study of lake burdur, Turkey. *J. Taibah Univ. Sci.* 11, 381–391. doi:10.1016/j.jtusci.2016.04.005

Shean, D. E., Bhushan, S., Montesano, P., Rounce, D. R., Arendt, A., and Osmanoglu, B. (2020). A systematic, regional assessment of high mountain Asia glacier mass balance. *Front. Earth Sci.* 7, 363. doi:10.3389/feart.2019.00363

Shen, C., Laloy, E., Elshorbagy, A., Albert, A., Bales, J., Chang, F.-J., et al. (2018). HESS Opinions: Incubating deep-learning-powered hydrologic science advances as a community. *Hydrol. Earth Syst. S. C.* 22, 5639–5656. doi:10.5194/hess-22-5639-2018

Subin, Z. M., Riley, W. J., and Mironov, D. (2012). An improved lake model for climate simulations: Model structure, evaluation, and sensitivity analyses in CESM1. *J. Adv. Model Earth Syst.* 4, M02001. doi:10.1029/2011MS000072

Tao, S., Fang, J., Zhao, X., Zhao, S., Shen, H., Hu, H., et al. (2015). Rapid loss of lakes on the Mongolian Plateau. *P Natl. Acad. Sci. U. S. A.* 112, 2281–2286. doi:10.1073/pnas.1411748112

Townshend, J. R., and Justice, C. (1986). Analysis of the dynamics of African vegetation using the normalized difference vegetation index. *Int. J. Remote Sens.* 7, 1435–1445. doi:10.1080/01431168608948946

Vapnik, V. N. (1999). An overview of statistical learning theory. *IEEE Trans. neural Netw.* 10, 988–999. doi:10.1109/72.788640

Veh, G., Korup, O., and Walz, A. (2020). Hazard from Himalayan glacier lake outburst floods. *Proc. Natl. Acad. Sci.* 117, 907–912. doi:10.1073/pnas.1914898117

Vorosmarty, C. J., Green, P., Salisbury, J., and Lammers, R. B. (2000). Global water resources: Vulnerability from climate change and population growth. *Science* 289, 284–288. doi:10.1126/science.289.5477.284

Wan, W., Long, D., Hong, Y., Ma, Y., Yuan, Y., Xiao, P., et al. (2016). A lake data set for the Tibetan Plateau from the 1960s, 2005, and 2014. *Sci. Data* 3, 160039. doi:10.1038/sdata.2016.39

Wang, C., Jia, M., Chen, N., and Wang, W. (2018). Long-term surface water dynamics analysis based on landsat imagery and the Google Earth engine platform: A case study in the middle Yangtze River basin. *Remote Sens-Basel* 10, 1635. doi:10.3390/rs10101635

Wang, L., Du, Z., Wei, Z., Xu, Q., Feng, Y., Lin, P., et al. (2021). High methane emissions from thermokarst lakes on the Tibetan Plateau are largely attributed to ebullition fluxes. *Sci. Total Environ.* 801, 149692. doi:10.1016/j.scitotenv.2021.149692

Warrens, M. J., and Pratiwi, B. C. (2016). Kappa coefficients for circular classifications. *J. Classif.* 33, 507–522. doi:10.1007/s00357-016-9217-3

Work, E. A., and Gilmer, D. S. (1976). Utilization of satellite data for inventorying prairie ponds and lakes. *Photogramm. Eng. Remote Sens.* 42, 685–694.

Wu, Q., and Niu, F. (2013). Permafrost changes and engineering stability in Qinghai-Xizang Plateau. *Chin. Sci. Bull.* 58, 1079–1094. doi:10.1007/s11434-012-5587-z

Wulder, M. A., Roy, D. P., Radeloff, V. C., Loveland, T. R., Anderson, M. C., Johnson, D. M., et al. (2022). Fifty years of Landsat science and impacts. *Remote Sens. Environ.* 280, 113195. doi:10.1016/j.rse.2022.113195

Xu, H. (2006). Modification of normalised difference water index (NDWI) to enhance open water features in remotely sensed imagery. *Int. J. Remote Sens.* 27, 3025–3033. doi:10.1080/01431160600589179

Yang, K., Lu, H., Yue, S., Zhang, G., Lei, Y., La, Z., et al. (2018). Quantifying recent precipitation change and predicting lake expansion in the Inner Tibetan Plateau. *Clim. Change* 147, 149–163. doi:10.1007/s10584-017-2127-5

Yang, L., Driscol, J., Sarigai, S., Wu, Q., Chen, H., and Lippitt, C. D. (2022). Google Earth engine and artificial intelligence (AI): A comprehensive review. *Remote Sens-Basel* 14, 3253. doi:10.3390/rs14143253

Yao, X., Tham, L., and Dai, F. (2008). Landslide susceptibility mapping based on support vector machine: A case study on natural slopes of Hong Kong, China. *Geomorphology* 101, 572–582. doi:10.1016/j.geomorph.2008.02.011

Yao, T., Thompson, L., Yang, W., Yu, W., Gao, Y., Guo, X., et al. (2012). Different glacier status with atmospheric circulations in Tibetan Plateau and surroundings. *Nat. Clim. Change* 2, 663–667. doi:10.1038/nclimate1580

Yao, X., Liu, S., Sun, M., Guo, W., and Zhang, X. (2012). Changes of Kusai Lake in Hoh Xil region and causes of its water overflowing. *Acta Geogr. Sin.* 67, 689. doi:10.11821/xb201205011

Yao, X., Sun, M., Gong, P., Liu, B., Li, X., An, L., et al. (2018). Overflow probability of the Salt Lake in Hoh Xil region. *J. Geogr. Sci.* 28, 647–655. doi:10.1007/s11442-018-1496-7

Yao, T., Bolch, T., Chen, D., Gao, J., Immerzeel, W., Piao, S., et al. (2022). The imbalance of the Asian water tower. *Nat. Rev. Earth Environ.* 3, 618–632. doi:10.1038/s43017-022-00299-4

Yin, G., Luo, J., Niu, F., Zhou, F., Meng, X., Lin, Z., et al. (2021). Spatial analyses and susceptibility modeling of thermokarst lakes in permafrost landscapes along the Qinghai–Tibet engineering corridor. *Remote Sens-Basel* 13, 1974. doi:10.3390/rs13101974

Zhang, G., Zheng, G., Gao, Y., Xiang, Y., Lei, Y., and Li, J. (2017). Automated water classification in the Tibetan plateau using Chinese GF-1 WFV data. *Photogramm. Eng. Rem. S* 83, 509–519. doi:10.14358/PERS.83.7.509

Zhang, F., Li, J., Zhang, B., Shen, Q., Ye, H., Wang, S., et al. (2018). A simple automated dynamic threshold extraction method for the classification of large water bodies from landsat-8 OLI water index images. *Int. J. Remote Sens.* 39, 3429–3451. doi:10.1080/01431161.2018.1444292

Zhang, G., Luo, W., Chen, W., and Zheng, G. (2019). A robust but variable lake expansion on the Tibetan Plateau. *Sci. Bull.* 64, 1306–1309. doi:10.1016/j.scib.2019.07.018

Zhang, G., Yao, T., Xie, H., Yang, K., Zhu, L., Shum, C., et al. (2020). Response of Tibetan Plateau lakes to climate change: Trends, patterns, and mechanisms. *Earth-Sci Rev.* 208, 103269. doi:10.1016/j.earscirev.2020.103269

Zhang, G., Ran, Y., Wan, W., Luo, W., Chen, W., Xu, F., et al. (2021). 100 years of lake evolution over the Qinghai–Tibet Plateau. *Earth Syst. Sci. Data* 13, 3951–3966. doi:10.5194/essd-13-3951-2021

Zhang, Y., Xie, C., Wu, T., Zhao, L., Wu, J., Wu, X., et al. (2022). New permafrost is forming on the exposed bottom of Zonag Lake on the Qinghai-Tibet Plateau. *Sci. Total Environ.* 815, 152879. doi:10.1016/j.scitotenv.2021.152879

Zheng, G., Allen, S. K., Bao, A., Ballesteros-Cánovas, J. A., Huss, M., Zhang, G., et al. (2021). Increasing risk of glacial lake outburst floods from future Third Pole deglaciation. *Nat. Clim. Change* 11, 411–417. doi:10.1038/s41558-021-01028-3

frontiers | Frontiers in Earth Science

TYPE Brief Research Report
PUBLISHED 27 February 2023
DOI 10.3389/feart.2023.1134910

OPEN ACCESS

EDITED BY
Weili Duan,
Xinjiang Institute of Ecology and Geography (CAS), China

REVIEWED BY
Zhaofei Liu,
Institute of Geographic Sciences and Natural Resources Research (CAS), China
Hongyi Li,
Northwest Institute of Eco-Environment and Resources (CAS), China

*CORRESPONDENCE
Lei Wang,
✉ wanglei@itpcas.ac.cn

SPECIALTY SECTION
This article was submitted to Hydrosphere,
a section of the journal Frontiers in Earth Science

RECEIVED 31 December 2022
ACCEPTED 15 February 2023
PUBLISHED 27 February 2023

CITATION
Li X, Wang L, Hu B, Chen D and Liu R (2023), Contribution of vanishing mountain glaciers to global and regional terrestrial water storage changes. *Front. Earth Sci.* 11:1134910.
doi: 10.3389/feart.2023.1134910

Contribution of vanishing mountain glaciers to global and regional terrestrial water storage changes

Xiuping Li[1], Lei Wang[1,2]*, Baoyi Hu[1], Deliang Chen[3] and Ruishun Liu[1,2]

[1]State Key Laboratory of Tibetan Plateau Earth System, Environment and Resources (TPESER), Institute of Tibetan Plateau Research, Chinese Academy of Sciences, Beijing, China, [2]The University of Chinese Academy of Sciences, Beijing, China, [3]Department of Earth Sciences, University of Gothenburg, Gothenburg, Sweden

Mountain is called the water towers of the world. Due to high sensitivity and vulnerability to climate change, more attention is paid to the change of water resources in mountain regions, where provide water for environmental and human demands downstream. Mountains glacier, as one of the most important components of terrestrial water storage (TWS), effectively regulates and stabilizes surface water resources. TWS appears to be trending below previous ranges in recent years, and glacier retreating is becoming the primary cause of TWS depletion in mountain regions. However, how much mountain glacier changes contribute to TWS changes around mountain regions is unknown. Here, we combine multi-source datasets to quantify the contribution rate over high-elevation mountain regions. On a global scale, the glacial melting is equivalent to about 49% of the total TWS decline during 2006–2015. TWS and glacier show decreasing trends in most of mountain regions and watersheds of the Third Pole and surroundings (TPs), but the contribution ranges from −23% to 728% in mountain regions and −21% to 99% in watersheds of TPs. There are larger contributions in regions with more glaciers, while smaller in less glacier-covered regions. Glacier together with other storage components play diverse roles across different mountain regions and watersheds, but factors with great influence are glacier, groundwater, soil water, reservoirs and lakes.

KEYWORDS

terrestrial water storage, mountain glacier, global hydrological model, GRACE satellite, contribution

1 Introduction

As the water towers of the world, mountains provide water for environmental and human demands downstream. Mountains have high sensitivity and vulnerability to climate change (Viviroli et al., 2011) and are experiencing faster warming than low-elevation areas. Glacier, one of the most important components of mountains terrestrial water storage (TWS), effectively regulates and stabilizes surface water resources. TWS appears to be trending below previous ranges around the global regions and is dominated by different factors (Rodell et al., 2018; Huang et al., 2021). Mountain glaciers retreating in response to climate change is becoming the primary cause of TWS depletion in mountain regions (e.g., Jacob et al., 2012). However, how much mountain glacier changes contribute to TWS changes around mountain regions is unknown. Therefore, quantifying the contribution of melting glaciers to TWS changes from regions to watersheds is important because TWS changes have important implications for water resources assessment, climate change, and ecosystem dynamics.

With the release of GRACE satellites, many studies have focused on TWS changes at varied spatial scales (e.g., Hu et al., 2020). TWS changes can exert influence on sea-level rise due to glacier melting, natural resources and disasters (e.g., groundwater depletion), ecological environment (e.g., vegetation dependent on groundwater) and construction projects (e.g., land subsidence). About 20%–35% of the recent decadal sea-level rise was attributed to the net TWS change that integrates changing mountain glacier, groundwater and mass in other stores (Reager et al., 2016). A study shows that the contribution of net TWS decline in endorheic basins to a potential sea level rise matched the contribution of nearly half of the land glacier retreat (excluding Greenland and Antarctica) (Wang et al., 2018). Generally speaking, mountain glacier melting and groundwater exploitation had positive contributions to sea-level rise, while changes in reservoir storage had negative effects (Wada et al., 2016; Zemp et al., 2019).

The contribution of storage components to TWS changes presents a remarkable regional difference. For inland river basins, TWS changes are mainly from surface waters, soil moisture and groundwater (Wang et al., 2018). The decline of water storage in arid and semi-arid areas is mainly due to groundwater overexploitation (Rodell et al., 2018). Snow also has an important impact on TWS changes, such as for the river basins of Canada (Bahrami et al., 2020). Groundwater overexploitation is one of the main factors affecting TWS changes around the plain areas. For the Tibetan Plateau, water storage is extremely sensitive to climate change (Wang et al., 2020), followed with a significantly spatial difference. TWS decline in exorheic basins is mainly caused by the glacier retreat and the decline of soil and groundwater reserves, while the increase in endorheic basins is mainly caused by the expansion of lakes and the increase of glaciers in the Karakoram-West Kunlun Mountains (Li et al., 2022).

Mountain glaciers are key indicators of climate change for high-elevation mountain areas (Immerzeel et al., 2020), and their mass changes can alter the Earth's hydrological cycles at multiple scales, by regulating and stabilizing runoff. Recent studies have discovered mountain glaciers are diminishing in response to climate change, affecting the TWS changes and water availability. Because of the accelerated melting rate of most mountain glaciers around the world, the mountain glacier mass budget estimates have raised more concerns about the sustainability of water supply in many parts of the world. Therefore, clarifying the contribution of mountain glaciers to TWS is conducive to the quantity of the impact of glacier changes on freshwater availability.

Owing to existing data's coarse spatial resolution and availability, attribution of the TWS changes, especially from mountain glaciers, has been challenging. Here, we investigate the contributions of mountain glaciers changes to the total TWS changes from a global perspective to a watershed scale, aiming to enhance the understanding of the spatial differences of TWS's contributing factors. We combine multiple GRACE products, glacier mass balance data and global hydrological model outputs to investigate the mass-budget changes of storage components, and focus on the impacts of glacier changes on water storage over high-elevation mountain regions on the Earth.

2 Materials and methods

2.1 Study area

The study regions include Western Canada and United States (WCA), Central Europe (CE), Caucasus and the Middle East (CME), the Third Pole and surroundings (TPs), Low Latitudes (LL) and Southern Andes (SA) except for Antarctica and Greenland periphery (Figure 1). This region has an area of about 483,155 km^2 and total glacier volume is equal to about 221 ± 23 mm sea level (Hock et al., 2019). The glaciers range from the sea level (e.g., southeast Alaska) to the Himalayas and Karakoram mountains with an altitude of more than 8,000 m across the different climatic regions. Therefore, their mass budget largely depends on the balance between snow accumulation and melt at the glacier surface, driven primarily by atmospheric conditions. In the past 10 years, annual total precipitation has changed (Table 1), which will affect the TWS changes.

As the Asian water tower, TPs contain the largest number of glaciers outside the Polar Regions (Vaughan et al., 2013). These glaciers are at the headwaters of many prominent Asian rivers and are an important contributor to river flow. TPs has 95,536 glaciers with an area of about 97,605 ± 7,935 km^2 (Pfeffer et al., 2014; RGI Consortium, 2017). Eight typical river basins are chosen to study the contribution of mountain glacier changes to TWS changes. And they are the Syr Darya, Ili, Tarim, Amu Darya, Ganges, Brahmaputra, Indus, and Yangtze basins, respectively (Figure 2). The first four belong to endorheic basins, and the others are the exorheic basins.

2.2 Data

Data used in the study include the TWS from GRACE, storage components from WaterGAP Global Hydrology Model (WGHM) outputs and glacier mass-budget data (Table 2). In addition, global monthly precipitation products from GPCP (Adler et al., 2018), CMAP (Huffman et al., 1997), ERA5-Land (Muñoz Sabater, 2019), GPCC (Markus et al., 2011) and Princeton (Sheffield et al., 2006) are used to investigate the possible reasons of TWS changes.

Eight GRACE products are used to calculate TWS changes, including GRAVIS, MASCON_CSR05, MASCON_CSR06, MASCON_JPL05, MASCON_JPL06, SH_JPL, SH_CSR, and SH_GFZ (Table 2). Considering the continuity and quality of data, we selected TWS anomaly (TWSA, which represents the TWS deviation relative to the 2004–2009 time-mean baseline) from January 2003 to December 2015 from eight products. All GRACE products were resampled from 1° or 0.5° to 0.1° by nearest neighbor interpolation to calculate domain-averaged TWS changes.

Data from the WaterGAP Global Hydrology Model (WGHM) (v2.2d; Müller et al., 2021) was used to analyze the variations of TWS components and explore the contribution of storage components to TWS changes except for glaciers. The WaterGAP WGHM not only can simulate human use of groundwater and surface water, but also can separately simulate each storage component, including canopy

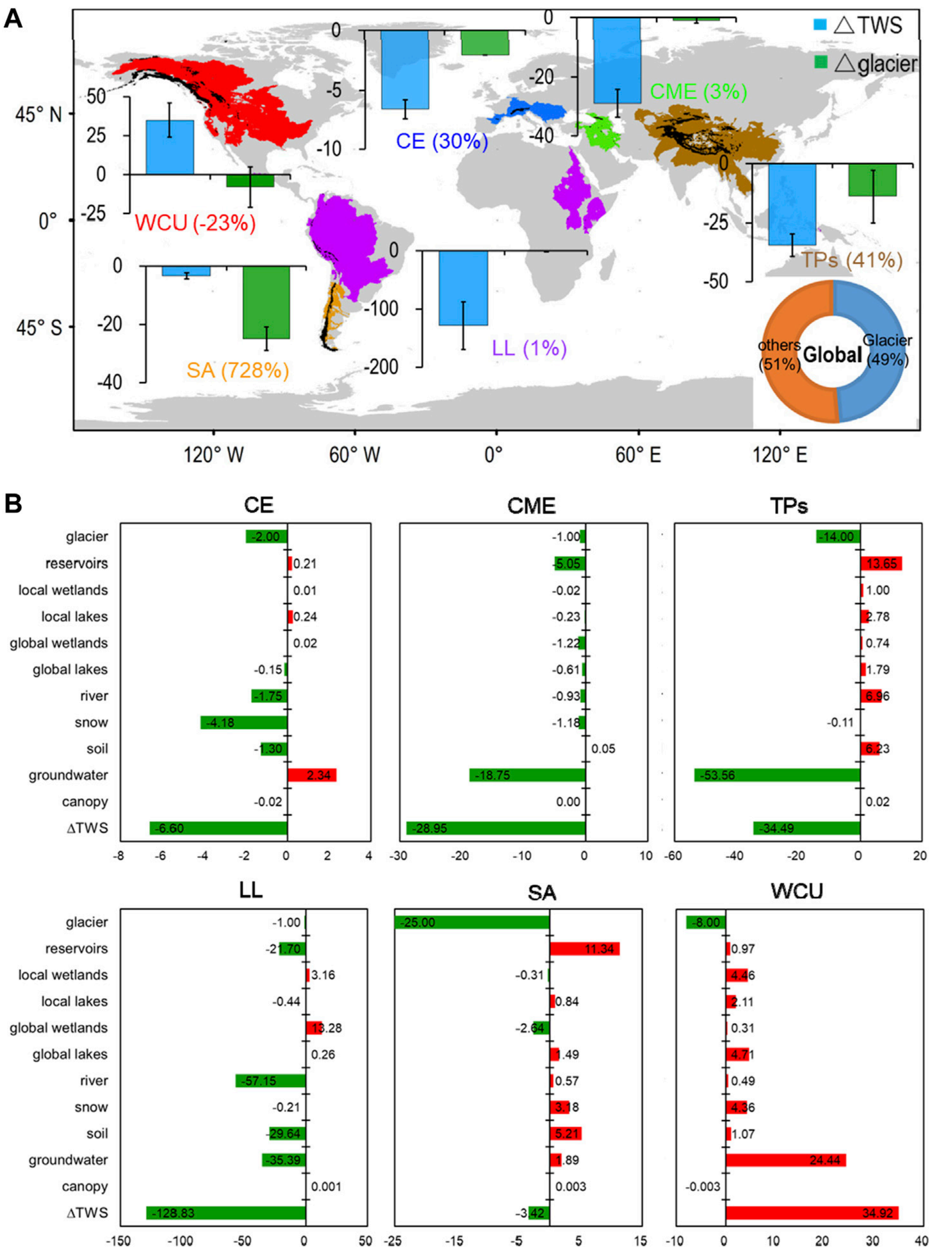

FIGURE 1
Locations of regions covered by mountain glacier and comparisons of estimated annual mean mass changes (Gt yr⁻¹) between the terrestrial water storage (△TWS) and the glacier (△glacier) **(A)** and the values of △TWS and all storage components (Gt yr⁻¹) **(B)** in six typical mountain regions. All storage components data except for glacier are bias-corrected from WaterGAP Global Hydrology Model (WGHM) outputs. Regional △TWS is average calculated from annual-averaged GRACE values after removing maximum and minimum during 2006–2015. Global △TWS is similar to regional ones, but for regions except for Greenland and Antarctic periphery. Global and regional glacier mass changes are from IPCC SROCC. The shaded black areas represent the glacier distribution. WCU, CE, CME, TPs, LL, SA represent Western Canada and United States, Central Europe, Caucasus and Middle East, the Third Pole and surroundings, Low Latitudes and Southern Andes, respectively. The figure in the lower right corner is from the global result.

interception (canopy), groundwater storage (groundwater), soil moisture (soil), snow water equivalent (snow), river runoff storage (river), global lake storage (global lakes), global wetland storage (global wetlands), local lake storage (local lakes), local wetland storage (local wetlands) and reservoir storage (reservoirs). Previous studies have proved that WGHM is a qualitatively good-performing global hydrological model, especially for quantifying global scale water resources and assessing water stress (Masaki et al., 2017; Zhao et al., 2017). More details about the WGHM products can be referenced in Döll et al. (2014) and Müller et al. (2021).

The glacier mass-budget estimates from the United Nation's Intergovernmental Panel on Climate Change (IPCC) report on the Ocean and Cryosphere in a Changing Climate (SROCC) (Hock

TABLE 1 Information of regions and river basins including the regional area, glacierized information with glacier area and ratio of glacier area to total area, and linear trends (mm decade^{-1}) of annual total precipitation during the study period. The study period is 2006–2015 for six regions, 2003–2015 for eight river basins. Glacierized areas are from IPCC SROCC (Hock et al., 2019) and Brun et al. (2017). Data of precipitation come from ERA5-Land, the Princeton Global Meteorological Forcing Dataset, GPCP, CMAP, and GPCC.

Region/basin name	Region/basin information			Trend of precipitation (mm yr^{-1})				
	Total area (10^4 km^2)	Glacierized area (10^4 km^2)	Ratio (%)	ERA5-land	Princeton	GPCP	CMAP	GPCC
Central Europe	192	0.21	0.11	2.09	0.87	0.12	0.11	1.05
Caucasus and the Middle East	189	0.13	0.07	1.66	−1.81	−2.08	−2.84	0.14
the Third Pole and surroundings	1299	9.77	0.75	1.18	0.12	−1.86	4.23	2.98
Low Latitudes	1462	0.23	0.02	1.75	−0.92	−7.64	−4.60	−4.11
Southern Andes	154	2.94	1.91	1.89	−1.19	2.48	3.21	0.65
Western Canada and United States	1464	1.45	0.10	1.59	6.10	−3.46	−3.14	−0.56
Brahmaputra	61	0.95	1.56	−3.14	−3.38	−13.91	−13.24	−10.08
Amu Darya	104	1.08	1.04	−1.97	−1.50	3.79	−4.67	−0.20
Ganges	105	0.83	0.79	−2.24	7.19	−5.18	−4.98	1.45
Ili	79	0.43	0.55	−3.20	0.54	4.95	2.18	1.72
Indus	102	2.47	2.42	6.25	4.79	13.86	4.87	13.98
Yangtze	223	0.14	0.06	0.72	4.90	5.14	4.77	5.30
Tarim	120	1.84	1.53	−1.26	−2.60	0.72	1.02	0.28
Syr Darya	162	0.23	0.14	−3.36	−0.45	2.93	−0.21	−0.74

et al., 2019) are used to study the contribution of the changes of mountain glaciers to the changes of TWS on the global and regional scales, and from Brun et al. (2017) using time series of DEM derived from satellite stereo-imagery for the typical river basins of TP.

2.3 Methods

The primary TWS anomaly from GRACE and TWS components from WaterGAP WGHM reflect the monthly variations in TWS and its each storage component in the Earth's climate system. For TWS from GRACE, the difference in mass balance between the last month of the last year (here it is December) and the first month of the first year (here it is January) is regarded as the mass changes of TWS during the study period, which is then used to compare with the glacier mass-balance changes. Different GRACE products have different performances. To eliminate the extreme influence from GRACE products and reflect the reasonable amplitude, we firstly remove the maximum and minimum from eight calculated TWS changes, and the remaining values are then used to calculate the TWS mean TWS and its standard deviation for global, regions and river basins. Similar method is used to monthly TWS and components from WaterGAP WGHM to calculate the mass changes in the study period.

Bias-correction method is used to correct TWS components from WaterGAP WGHM. Both of GRACE and WaterGAP WGHM simultaneously output TWS anomaly. Müller et al. (2021) found the underestimation phenomenon among WaterGAP WGHM outputs. So in this study, we regard the TWS change averaged from GRACE as the true value to correct the TWS change from WaterGAP WGHM, and then correct each storage component assuming that the simulation of components is reasonable in WaterGAP WGHM. In addition, linear regression is used to calculate the trends of precipitation.

3 Data comparison and bias correction

3.1 Comparison of mass balance from eight GRACE products

In this study, eight GRACE products are chosen to reveal the mass-balance changes of TWS. To validate the performance of eight GRACE products over the same region, we compare their ability in reproducing annual variability. We calculate the mass-balance changes of global averaged TWS except for Greenland and Antarctica during 2006–2015 (Supplementary Figure S1). All GRACE products show consistent decreasing trends but with different amplitudes of variation, ranging from 1411.08 to 224.70 Gt yr^{-1}. Removing the maximum (1411.08 Gt yr^{-1}) and minimum (224.70 Gt yr^{-1}), the calculated global mean mass change is −452.67 ± 310.52 Gt yr^{-1} during 2006–2015.

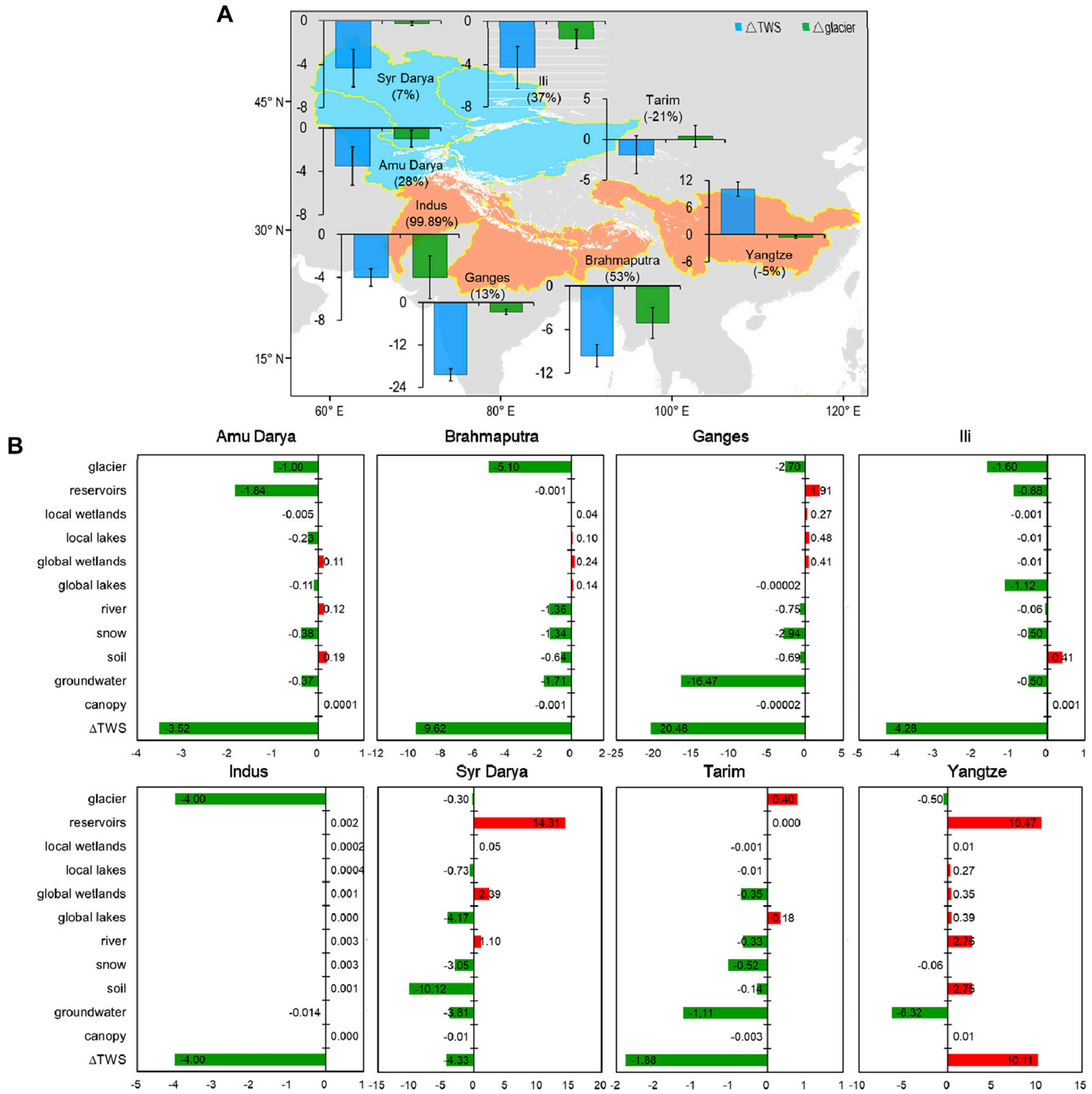

FIGURE 2
Locations of river basins around the Third Pole and surroundings covered by mountain glacier and comparisons of estimated annual mean mass changes (Gt yr^{-1}) between the terrestrial water storage (△TWS) and the glacier (△glacier) **(A)** and the values of △TWS and all storage components (Gt yr^{-1}) **(B)** in eight river basins of the Third Pole. All storage components data except for glacier are from WaterGAP Global Hydrology Model (WGHM) outputs. Eight river basins are Yangtze, Brahmaputra, Ili, Tarim, Ganges, Amu Darya, Syr Darya and Indus. The endorheic basins are in blue and the exorheic basins are in red. The shaded black areas represent the glacier distribution. △TWS is average calculated from annual-averaged GRACE values after removing maximum and minimum during 2003–2015. The shaded white areas represent the glacier distribution. Glacier mass balance are from Brun et al. (2017) in the Supplementary Material.

The mass budget estimates of TWS from eight GRACE products in six typical regions covered by mountain glaciers are shown in Supplementary Figure S1. Eight products show consistent results except for the Third Pole and surroundings and Southern Andes. Most of the mountain regions have mass losses indicated by all GRACE products except for Western Canada and United States. Removing the maximum and minimum at each region, the calculated mean mass change is shown in Figure 1. Similar comparison based on river basins is investigated (Supplementary Figure S2). We also can find that nearly all products display consistent results except for GRAVIS and SH_GFZ, which mainly happens in the northwest of TP (Tarim, Syr Darya and

TABLE 2 Data sources of the terrestrial water storage, storage components, glaciers, precipitation used in this study.

Datasets		Data source	Temporal extent	Spatial resolution
GRACE	GFZ GravIS RL06 Level-3	http://gravis.gfz-potsdam.de/land	2003–2015	1.0° × 1.0°
	CSR GRACE RL05 mascons	http://www2.csr.utexas.edu/grace		0.5° × 0.5°
	CSR GRACE RL06 mascons			
	JPL GRACE RL05 mascons	http://podaac.jpl.nasa.gov/grace		0.5° × 0.5°
	JPL GRACE RL06 mascons			
	JPL GRACE RL05 SH	https://grace.jpl.nasa.gov		1.0° × 1.0°
	CSR GRACE RL05 SH			
	GFZ GRACE RL05 SH			
WaterGAP WGHM		http://www.watergap.de	2003–2015	0.5° × 0.5°
Glacier mass balance		https://www.ipcc.ch/srocc/	2006–2015	\
		Published reference in Brun et al. (2017)	2000–2016	
Precipitation	GPCP	https://gpcp.umd.edu	2003–2015	2.5° × 2.5°
	ERA5-Land	https://cds.climate.copernicus.eu/cdsapp#!/dataset/reanalysis-era5-land-monthly-means?tab=overview		0.1° × 0.1
	GPCC	https://opendata.dwd.de/climate_environment/GPCC/html/download_gate.html		1.0° × 1.0°
	Princeton	http://hydrology.princeton.edu/data.php		0.25° × 0.25°
	CMAP	https://psl.noaa.gov/data/gridded/data.cmap.html		2.5° × 2.5°

Amu Darya). Around the southern TP (Ganges, Brahmaputra and Yangtze), results from eight GRACE products are consistent. The mean mass changes are calculated and shown in Figure 2 after removing the maximum and minimum. In short, eight GRACE products give consistent results and the ensemble mean can be used to reveal the TWS changes in the glacier-covered mountain areas.

3.2 Bias correction of TWS from WaterGAP WGHM

During the process of model evaluation and validation, the underestimation phenomenon among WaterGAP WGHM outputs was discovered (Müller et al., 2021). The comparison between TWS changes from GRACE and the sum of TWS changes from WGHM and glacier mass budget is shown in Supplementary Figure S3. Both results are comparable and WGHM underestimates the TWS changes compared with GRACE in most of the regions. And GRACE considers glacier changes while WaterGAP does not simulate glaciers. To ensure accuracy, a bias-correction method is used to correct all storage components among WaterGAP WGHM outputs. Firstly, we assume that the TWS changes from GRACE products (except for glaciers) are reasonable and reliable and regarded as true values to correct the storage changes among WaterGAP WGHM outputs. In addition, we believe that the proportion among all storage components is reasonable in WaterGAP WGHM outputs. Thus, the ratio of TWS changes between the GRACE products after removing glaciers and the WaterGAP WGHM outputs is used for each storage component to eliminate the underestimation or overestimation phenomenon. After the bias correction, all storage components in WaterGAP WGHM outputs are improved and then applied to investigate the contribution of storage components to TWS changes in the regions and river basins.

4 Results

4.1 Global contribution

On a global scale, TWS changes have obvious spatial heterogeneity and locations where TWS appears to be decreasing, where glaciers are diminishing and groundwater is being withdrawn (Rodell et al., 2018). The calculated global mean mass changes of TWS is -452.67 ± 310.52 Gt yr^{-1} during 2006–2015, while the globally-averaged glacier mass change from IPCC SROCC is -220.00 ± 30.00 Gt yr^{-1} with a glacier area of 483,155 km^2 (excluding Greenland and Antarctic). Thus, the glacial melting is equivalent to about 49% of the total TWS decline on a global scale during 2006–2015 (Figure 1A). In other words, mountain glacier melting accounts for almost half of the TWS decline in the major mountains of the Earth. Other storage factors (groundwater, rivers, global wetlands, local lakes and reservoirs and so on) account for 51% of TWS changes (Figure 1A), but each storage factor plays a different role in various regions (Rodell et al., 2018).

4.2 Regional contribution

Glaciers are mainly distributed in high-altitude mountain areas. To better understand the impact of glaciers on TWS, we choose six mountain regions to quantitatively assess the contribution of glaciers to TWS changes (Figure 1A). All mountain regions have mass losses indicated by most of GRACE products (Supplementary Figure S1). The impact of glacier melting on TWS changes shows significant spatial heterogeneity. There are greater contributions of glacier changes to TWS changes in the Third Pole and surroundings (TPs, 41%) and in Central Europe (CE, 30%) owing to a large proportion of glaciers, while smaller in Caucasus and Middle East (CME, 3%) and Low Latitudes (LL, 1%) due to less glacier coverage. In Western Canada and United States (WCU), both TWS and glacier changes display opposite variability, so the contribution of glacier changes to TWS changes is negative (−23%). In the Southern Andes (SA), the glacier and TWS changes are −25 and −3.43 Gt yr^{-1}, respectively. The TWS changes are far less than the changes in glacier mass due to a large glacier coverage, appeared in Rodell et al. (2018). So the contribution is 728% in this region. The glacier melting can be converted to storage of soil, lakes and reservoirs (Figure 1B). In short, the contribution of glaciers to TWS is not negligible in the glacier-covered mountain regions.

To better clarify the relationship between TWS and each storage component in the mountain regions, mass-budget estimates of storage components are bias corrected based on GRACE TWS results. Bias-corrected storage components in six regions are shown in Figure 1B. Each storage component plays different roles in different regions (Supplementary Figure S4). In CE, the glacier and snow are the main factors to cause a TWS decrease as indicated by a positive effect (Supplementary Figure S4), but the opposite is true for groundwater. The soil moisture increases together with river runoff increase caused by precipitation increase offset the TWS decrease. The glacier mass decrease, far greater than other factors, is the main factor to influence TWS decline in SA, and then supporting the increase of other storage components and offsetting the TWS decline. In CME, a significant decline in the groundwater, resulted from a combination of recent drought and consequent increases in groundwater demand, is the main factor of TWS decrease, and the glacier and other factors have a small influence on the TWS decline. In TPs, except for the glacier melting, the sharp decline in groundwater is an important factor for the TWS decrease, while the increased storage in rivers, reservoirs and soil were most likely caused by the glacier melting. The influence of glacier changes in LL seems to be negligible, while the water storage decline in rivers, groundwater, soils and reservoirs, due to decreased precipitation (Table 1), is the main factor for the TWS decrease. Previous studies find that the groundwater changes, drought and glacier retreating lead to TWS changes in parts of WCU (Rodell et al., 2018), which is demonstrated again in this study. Both glacier and TWS have opposite variations, and nearly all storage factors except for glaciers display increase trends and are helpful to TWS increase. The changes in groundwater, lakes and wetlands are the main factors for TWS changes.

4.3 Watershed contribution

TPs, covered with the largest number of glaciers outside the Polar Regions, has unusually high spatial variability of glaciers induced by climate change (Huang et al., 2022), which affects the water discharge of large rivers (e.g., Liu et al., 2020) and the TWS changes (e.g., Wang et al., 2021). More and more attention has been paid to the influence of glacier melting on the surface water resources. Eight glacier-covered river basins are chosen to compare mass-budget changes of TWS and glaciers during 2003–2015 (Figure 2A). The mass changes of TWS display a decrease except for the Yangtze. And the mass changes of glaciers are negative except for the Tarim. Except for the Tarim and Yangzte basins, the glacier mass changes in other basins show positive effects on TWS changes. There are greater contributions of glacier changes to TWS changes in the Brahmaputra (53%), Indus (99.89%), Amu Darya (28%) and Ili (37%) basins than in the Ganges (13%) and Syr Darya (7%). For the Tarim and Yangtze basins, there are opposite trends in glaciers and TWS, which may be related to the glacier increase in the Kunlun Mountain and decreased precipitation in the Tarim basin, and less glacier melting and more increased precipitation in the Yangtze basin (Table 1), respectively. In addition, we find that the groundwater plays a key role in most of the river basins, especially around the southern TPs.

Bias-corrected mass changes of other storage components are presented in Figure 2B. The glacier mass changes have great contributions to TWS changes in most of the river basins, although the contribution rates vary with basins (Supplementary Figure S5). In the Amu Darya basin, the glacier-snow melting and storage decrease in lakes and reservoirs are an important factor in the TWS decline, likely owing to the decreased precipitation (Table 1). Conversely, the glacier-snow melting can replenish the increased water storage in rivers and soils in this basin. The mass budget changes in Ili are mainly influenced by glacier melting and decreased water storage in reservoirs and lakes. Storage decreases in soils, lakes and groundwater are the main reasons for TWS changes in the Syr Darya basin, while storage increase in reservoirs induced by human activities offsets the TWS decreases. For the Brahmaputra basin, the main influence factor is glacier melting, and others (groundwater, rivers, and snow) play a limited role. In the Ganges basin, the groundwater decline, extracted to irrigate crops (Rodell et al., 2018), is the main factor for TWS decreases, and the second is glacier-snow melting. In the Tarim basin, the glacier increases dictated the TWS decline, and the decrease of water storage in groundwater, snow and rivers had a positive influence on TWS decline. The influence of glacier changes on TWS is negligible in the Yangtze basin, while the reservoirs are the main factor to the TWS increases, and other factors induced by precipitation increases also contributed to the TWS increases. The TWS appears a decrease trend in the Indus basin in 2003–2015, agree well with results from Zhu et al. (2021), and the glacier mass changes are nearly equal to TWS decline and the influence from other factors is negligible (Supplementary Figure S5). In the other words, the glacier melting dominates the changes of TWS in this basin.

5 Conclusion and discussion

This work quantified the effect of glacier changes on TWS changes using multi-source datasets over mountain regions. TWS and glacier mainly present decreasing trends in the mountains, but the contribution rates of glacier changes to TWS changes are spatially heterogeneous. On a global scale, the glacial melting is equivalent to nearly half of the total TWS decline during 2006–2015. For regions and watersheds, the contribution rates range from −23% to 728%, −21% to 99%, respectively. There are larger contributions in more glacier-covered regions, while smaller in less glacier-covered regions. Except for glaciers, other storage components play a significant role in TWS changes.

Accurate accounting of changes surface water resources availability is essential for environmental and human demands, regionally sustainable development of society, especially for mountain regions and its downstream. With the global warming, mountain glacier has gradually become a non-ignorable factor affecting surface water resources. Previous studies projected that glaciers could almost disappear in some mountain ranges in this century with the present mass-loss rates, and thus, its contribution to TWS changes will become more and more important and then influences the changes in surface water resources.

It is worth mentioning that our study is limited by several factors. First, the glacier data and TWS data, although an improvement derived from reliable data and reasonable method, are still uncertain due to the lack of the validation from a large number of field observations. Second, our study period focuses on recent 10 years, which is not long enough to allow for an investigation into interannual or decadal variations. Third, the main factor to influence TWS changes is precipitation for most of regions. In our study, we investigated the influence from domain-averaged annual precipitation. But due to the different performance of precipitation data, five datasets display different trends. In the future research, precipitation data should be validated and then conclude the quantitative and unified precipitation trends. Fourth, the application of results is limited due to the restriction of our research in of space and time. The current results only give a quantitative understanding about the contribution of glacier changes to TWS changes around the mountain regions. Despite these limitations, our study improved accounting of changes in freshwater availability, providing new knowledge for integrated water resources management for mountain regions in the context of global changes.

Data availability statement

The original contributions presented in the study are included in the article/Supplementary Material, further inquiries can be directed to the corresponding author.

Author contributions

XL, methodology, data processing, writing—original draft. LW, conceptualization, methodology, review and editing. BH, methodology, and data processing. DC, review and editing. RL, data processing.

Funding

This study was supported by the National Natural Science Foundation of China (Grant Nos 41988101 and 92047301), and the Second Tibetan Plateau Scientific Expedition and Research Program (2019QZKK0206).

Conflict of interest

The authors declare that the research was conducted in the absence of any commercial or financial relationships that could be construed as a potential conflict of interest.

Publisher's note

Supplementary material

The Supplementary Material for this article can be found online at: https://www.frontiersin.org/articles/10.3389/feart.2023.1134910/full#supplementary-material

References

Adler, R. F., Sapiano, M., Huffman, G. J., Wang, J. J., Gu, G., Bolvin, D., et al. (2018). The global precipitation climatology project (GPCP) monthly analysis (new version 2.3) and a Review of 2017 global precipitation. *Atmosphere* 9 (4), 138. doi:10.3390/atmos9040138

Bahrami, A., Goïta, K., and Magagi, R. (2020). Analysing the contribution of snow water equivalent to the terrestrial water storage over Canada. *Hydrol. Process.* 34, 2007–2008. doi:10.1002/hyp.13725

Brun, F., Berthier, E., Wagnon, P., Kaab, A., and Treichler, D. (2017). A spatially resolved estimate of high mountain Asia glacier mass balances from 2000 to 2016. *Nat. Geosci.* 10, 668–673. doi:10.1038/ngeo2999

Döll, P., Müller Schmied, H., Schuh, C., Portmann, F. T., and Eicker, A. (2014). Global-scale assessment of groundwater depletion and related groundwater abstractions: Combining hydrological modeling with information from well observations and GRACE satellites. *Water Resour. Res.* 50, 5698–5720. doi:10.1002/2014wr015595

Hock, R., Rasul, G., and Adler, C. (2019). "High Mountain areas," in *IPCC special report on the Ocean and Cryosphere in a changing climate.* Editors D. C. Roberts, V. Masson-Delmotte, P. Zhai, M. Tignor, E. Poloczanska, K. Mintenbeck, et al. (Beijing: China Press).

Hu, B. Y., Wang, L., and Li, X. P. (2020). Divergent changes in terrestrial water storage across global arid and humid basins. *Geophys. Res. Lett.* 47, e2020GL091069.

Huang, L., Hock, R., Li, X., Bolch, T., Yang, K., Wang, N., et al. (2022). Winter accumulation drives the spatial variations in glacier mass balance in High Mountain Asia. *Sci. Bull.* 67, 1967–1970. doi:10.1016/j.scib.2022.08.019

Huang, W., Duan, W., and Chen, Y. (2021). Rapidly declining surface and terrestrial water resources in Central Asia driven by socio-economic and climatic changes. *Sci. Total Environ.* 784, 147193.

Huffman, G. J., Adler, R. F., Arkin, P., Chang, A., Ferraro, R., Gruber, A., et al. (1997). The global precipitation climatology project (GPCP) combined precipitation dataset. *Bull. Amer. Meteor. Soc.* 78, 5–20. doi:10.1175/1520-0477(1997)078<0005:tgpcpg>2.0.co;2

Immerzeel, W. W., Lutz, A. F., Andrade, M., Bahl, A., Biemans, H., Bolch, T., et al. (2020). Importance and vulnerability of the world's water towers. *Nature* 577, 364–369. doi:10.1038/s41586-019-1822-y

Jacob, T., Wahr, J., Pfeffer, W. T., and Swenson, S. (2012). Recent contributions of glaciers and ice caps to sea level rise. *Nature* 482, 514–518. doi:10.1038/nature10847

Li, X. Y., Long, D., Scanlon, B. R., Mann, M. E., and Tian, F. (2022). Climate change threatens terrestrial water storage over the Tibetan Plateau. *Nat. Clim. change* 12, 801–807. doi:10.1038/s41558-022-01443-0

Liu, Z. F., Yao, Z. J., Wang, R., and Yu, G. A. (2020). Estimation of the Qinghai-Tibetan Plateau runoff and its contribution to large Asian rivers. *Sci. Total Environ.* 749, 141570. doi:10.1016/j.scitotenv.2020.141570

Markus, Z., Andreas, B., and Peter, F. (2011). GPCC first guess product at 1.0°: Near real-time first guess monthly land-surface precipitation from rain-gauges based on SYNOP data. *Theor. Appl. Climatol.* 115, 15–40. doi:10.5676/DWD_GPCC/FG_M_100

Masaki, Y., Hanasaki, N., Biemans, H., Schmied, H. M., Tang, Q., Wada, Y., et al. (2017). Intercomparison of global river discharge simulations focusing on dam operation-multiple models analysis in two case-study river basins, Missouri–Mississippi and Green–Colorado. *Environ. Res. Lett.* 12, 055002. doi:10.1088/1748-9326/aa57a8

Müller, S. H., Cáceres, D., and Eisner, S. (2021). The global water resources and use model WaterGAP v2.2d: Model description and evaluation. *Geosci. Model Dev. Discuss.* 14, 1037–1079. doi:10.5194/gmd-14-1037-2021

Muñoz Sabater, J. (2019). *ERA5-Land monthly averaged data from 1981 to present, copernicus climate change service (C3S) climate data store (CDS).* Berlin, Germany: Springer. doi:10.24381/cds.68d2bb3

Pfeffer, W., Arendt, A., Bliss, A., Bolch, T., Cogley, J. G., Gardner, A. S., et al. (2014). The randolph glacier inventory: A globally complete inventory of glaciers. *J. Glaciol.* 60, 537–552. doi:10.3189/2014jog13j176

Reager, J. T., Gardner, A. S., Famiglietti, J. S., Wiese, D. N., Eicker, A., and Lo, M. H. (2016). A decade of sea level rise slowed by climate-driven hydrology. *Science* 351, 699–703. doi:10.1126/science.aad8386

RGI Consortium (2017). *Randolph Glacier inventory – a dataset of global glacier outlines: Version 6.0: Technical report, global land ice measurements from space.* Colorado, USA: Digital Media. doi:10.7265/N5-RGI-60

Rodell, M., Famiglietti, J. S., Wiese, D. N., Reager, J. T., Beaudoing, H. K., Landerer, F. W., et al. (2018). Emerging trends in global freshwater availability. *Nature* 557, 651–659. doi:10.1038/s41586-018-0123-1

Sheffield, J., Goteti, G., and Wood, E. F. (2006). Development of a 50-year high-resolution global dataset of meteorological forcings for land surface modeling. *J. Clim.* 19 (13), 3088–3111. doi:10.1175/jcli3790.1

Vaughan, D. G., Comiso, J. C., and Allison, I. (2013). "Observations: Cryosphere," in *Climate change 2013: The physical science basis, contribution of working group I to the fifth assessment report of the intergovernmental Panel on climate change* (Cambridge: Cambridge University Press), 317–382.

Viviroli, D., Archer, D. R., Buytaert, W., Fowler, H. J., Greenwood, G. B., Hamlet, A. F., et al. (2011). Climate change and mountain water resources: Overview and recommendations for research, management and policy. *Hydrology Earth Syst. Sci.* 15, 471–504. doi:10.5194/hess-15-471-2011

Wada, Y., Lo, M., Yeh, P. J. F., Reager, J. T., Famiglietti, J. S., Wu, R. J., et al. (2016). Fate of water pumped from underground and contributions to sea-level rise. *Nat. Clim. Change* 6, 777–780. doi:10.1038/nclimate3001

Wang, J., Song, C., Reager, J. T., Yao, F., Famiglietti, J. S., Sheng, Y., et al. (2018). Recent global decline in endorheic basin water storages. *Nat. Geosci.* 11, 926–932. doi:10.1038/s41561-018-0265-7

Wang, J. R., Chen, X., Hu, Q., and Liu, J. (2020). Responses of terrestrial water storage to climate variation in the Tibetan Plateau. *J. Hydrology* 584, 124652. doi:10.1016/j.jhydrol.2020.124652

Wang, L., Yao, T. D., Chai, C. H., Cuo, L., Su, F., Zhang, F., et al. (2021). TP-River: Monitoring and quantifying total river runoff from the Third Pole. *Bull. Am. Meteorological Soc.* 102, 948–965. doi:10.1175/bams-d-20-0207.1

Zemp, M., Huss, M., Thibert, E., Eckert, N., McNabb, R., Huber, J., et al. (2019). Global glacier mass changes and their contributions to sea-level rise from 1961 to 2016. *Nature* 568, 382–386. doi:10.1038/s41586-019-1071-0

Zhao, F., Veldkamp, T., Frieler, K., Schewe, J., Ostberg, S., Willner, S., et al. (2017). The critical role of the routing scheme in simulating peak river discharge in global hydrological models. *Environ. Res. Lett.* 12, 075003. doi:10.1088/1748-9326/aa7250

Zhu, Y., Liu, S. Y., Yi, Y., Xie, F., Grunwald, R., Miao, W., et al. (2021). Overview of terrestrial water storage changes over the Indus River Basin based on GRACE/GRACE-FO solutions. *Sci. Total Environ.* 799, 149366. doi:10.1016/j.scitotenv.2021.149366

Frontiers in
Earth Science

Investigates the processes operating within the major spheres of our planet

Advances our understanding across the earth sciences, providing a theoretical background for better use of our planet's resources and equipping us to face major environmental challenges.

Discover the latest Research Topics

See more →

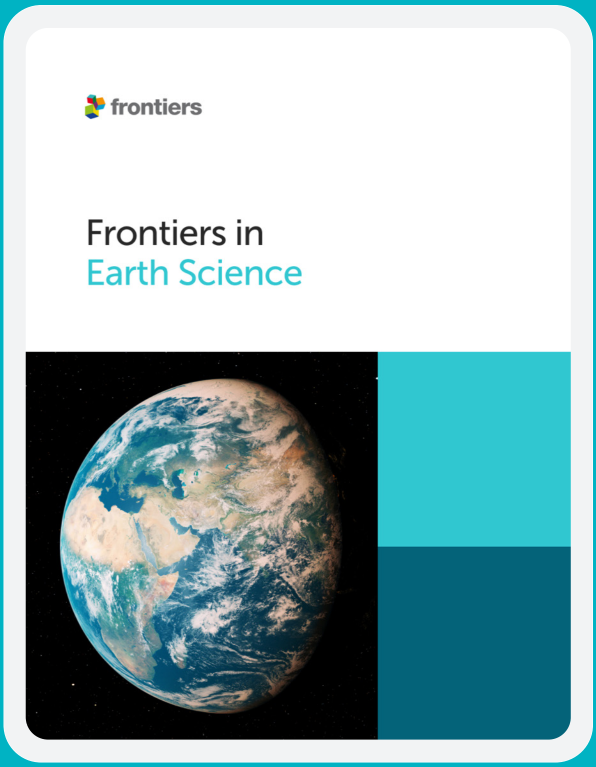

frontiers

Frontiers in
Earth Science

Frontiers

Avenue du Tribunal-Fédéral 34
1005 Lausanne, Switzerland
frontiersin.org

Contact us

+41 (0)21 510 17 00
frontiersin.org/about/contact

frontiers | Research Topics